Chlorite Diagenesis in Reservoir Sandstones of the Lower Missisauga Formation, Offshore Nova Scotia

By

Kathleen Gould

A Thesis Submitted in Partial Fulfillment of the

Requirements for the Degree of Master of Science

In

The Faculty of Graduate Studies

Department of Geology, Saint Mary's University

Halifax, Nova Scotia, Canada

Your file Votre référence
ISBN: 978-0-494-41695-2
Our file Notre référence
ISBN: 978-0-494-41695-2

Certification

Chlorite Diagenesis in Reservoir Sandstones
of the Lower Missisauga Formation,
Offshore Nova Scotia

By

Kathleen Gould

A Thesis Submitted to Saint Mary's University, Halifax, Nova Scotia,
in Partial Fulfillment of the Requirements for the
Degree of Master of in Applied Science

November 23rd, 2007

Examining Committee:

Approved:	Dr. Duncan McIlroy, External Examiner Canada Research Chair in Petroleum Geosciences Department of Earth Sciences Memorial University of Newfoundland
Approved:	Dr. Georgia Pe-Piper, Senior Supervisor Department of Geology
Approved:	Dr. David Piper, Supervisory Committee Geological Survey of Canada (Atlantic)
Approved:	Ms. Colleen Reimer, Supervisory Committee Exxon Mobil
Approved:	Dr. Andrew MacRae, Supervisory Committee Department of Geology
Approved:	Dr. Kathy Singfield, Supervisory Committee Department of Chemistry
Approved:	Dr. Pierre Jutras, Program Representative
Approved:	Dr. Kevin Vessey, Dean of Graduate Studies

Chlorite diagenesis in reservoir sandstones of the Lower Missisauga Formation, offshore Nova Scotia

By Kathleen Gould

ABSTRACT

Diagenetic chlorite rims on quartz grains preserve porosity by preventing the formation of secondary, pore-filling quartz overgrowths in wells from the Venture and Thebaud fields. Elsewhere, in the Norwegian Sea and the US Gulf Coast, such chlorite rims have been interpreted as an early burial diagenetic feature related to the input of iron from rivers or volcanic activity, or to later diagenesis by basinal fluids. The purpose of this study is to evaluate which hypothesis is applicable to the Scotian Basin.

A set of 45 sandstone samples from conventional cores were analyzed for mineralogy in thin section, mineral composition by electron microprobe, whole-rock chemistry, and X-ray diffraction.

From analytical data, it can be argued that a precursor iron-rich clay has diagenetically altered to form chlorite rims during early burial diagenesis, before widespread precipitation of pore-filling kaolinite and quartz overgrowths.

The depositional environment, including the degree of bioturbation, may influence formation of early Fe-rich clay coatings. The quality of the final chlorite rim depends on the sea floor diagenetic environment, apparent from the correlation between the quality of chlorite rims and phosphorus. The conditions that favour precipitation of phosphate must also result in Fe-rich clay coatings and may also make some coatings a better precursor than others for the conversion to chlorite during burial diagenesis. The presence of other Fe-rich minerals may also indicate an abundant supply of iron in the early diagenetic environment.

ACKNOWLEDGEMENTS

I would like to thank my supervisors, Georgia Pe-Piper and David Piper for providing me the opportunity to work on this project. Both are outstanding mentors and their advice and feedback through draft after draft enabled me to learn more than I thought I could by completing this thesis.

Thank you to Colleen Reimer and Exxon Mobil for generously providing the samples and digital data that made analytical work for this thesis possible! Colleen, thank you for your feedback and for being so helpful from beginning of the project to the very end. Thank you also to the ladies of the Canada Nova Scotia Petroleum Board for arranging time in the lab, often last minute, and for providing samples.

Thank you to Pengrowth and the Nova Scotia Department of Energy for making financial support possible through the Petroleum Innovation Grant.

Owen Brown of the Geological Survey of Canada (Bedford Institute of Oceanography) was crucial in the X-ray diffraction analyses. He both helped create and modify the method required for our samples. He contributed his time, energy and equipment to ensure we were successful, and for that I am very grateful.

Thank you to Andrew MacRae for help with stratigraphy, figures and supportive words. Thank you to Dave Dudus of Imperial Oil for lending his petrophysical skills to understanding my well logs, and to Vanessa Kavanagh for software and technical support. I also feel extremely grateful to have had the support network of other graduate students and friends.

My family, Ryan, Bridget, Mom and Dad for their love and positive words, especially during this last and most difficult year, you are all nothing short of amazing.

Lastly to Colin Garroway whose constant love, encouragement, support and kind words enabled me both start and finish my thesis.

TABLE OF CONTENTS

LIST OF TABLES

LIST OF FIGURES

CHAPTER 1: INTRODUCTION

1.1 Introduction

An ideal petroleum reservoir is defined by the ability of the reservoir rocks to hold hydrocarbons in their pore spaces (porosity) and the ease with which hydrocarbons can flow between pore spaces (permeability). To evaluate the quality of a reservoir, the controls on porosity and permeability must be well understood. Usually, porosity in a given rock has an inverse relationship with burial depth. As depth increases, the pore space becomes reduced as a result of pressure and temperature factors, including compaction of framework grains, mineral growth, diagenesis and low grade metamorphism.

It has been previously documented that higher than normal porosity is observed in reservoirs where early diagenetic chlorite rims on detrital grains are present. The chlorite rims seem to isolate quartz surfaces from interstitial pore water (e.g., Pittman and Lunsden, 1968, Ehrenberg, 1993) and precipitation of later pore-filling quartz overgrowths is retarded or prevented (Figure 1.1A). Porosities in these intervals are higher than would be expected for that depth (Figure 1.1B).

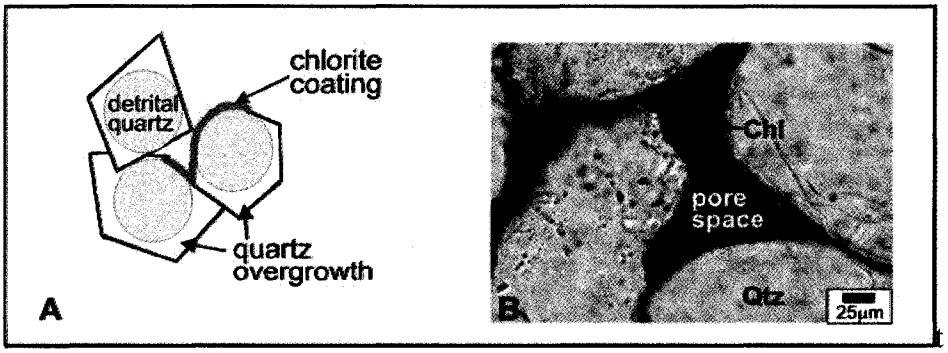

Figure 1.1: A) Diagram of chlorite rims preventing the nucleation of pore-filling quartz cement (modified from Ketzer, 2002)**; B)** microphotograph of chlorite-coated quartz grains (arrows); blue staining of the pore space indicates excellent porosity (Venture 4, plug sample SP74).

Early diagenesis of chlorite requires an early influx of labile iron. Previous studies have attributed the iron supply to tropical weathering (Odin, 1988; Ehrenberg, 1993; Ehrenberg et al., 1998; Aagaard et al., 2000) or volcanic supply (Ryan and Reynolds, 1996; Grigsby, 2001). The presence of chlorite rims within overpressured reservoirs has been documented in the Sable Subbasin, within the Scotian Basin in offshore Nova Scotia, and in particular within the Missisauga Formation of the Venture and Thebaud fields (Drummond, 1992; Canada Nova Scotia Offshore Petroleum Board, 1997; Reimer, 2002). Although the stratigraphy of the Scotian Basin is reasonably well understood, the relationships between diagenesis, porosity and sedimentary facies have not been well established. A better understanding may help to predict the distribution of chlorite rims in the Sable Subbasin, allowing better prediction of reservoir quality and management of hydrocarbon reservoirs.

1.2 Early diagenesis of chlorite rims in sandstones

The diagenetic growth of chlorite within deeply buried sandstone reservoirs requires the availability of an iron-rich precursor. Currently, there are two hypotheses for the source of an iron precursor (Ehrenberg et al., 1998): mafic igneous detrital grains (Ryan and Reynolds, 1996; Grigsby, 2001) or a depositional setting that favours the concentration of an Fe-rich clay mineral, such as a shallow marine verdine facies, characterized by a variety of authigenic green clays including odinite and berthierine (Odin, 1988; Ehrenberg, 1993; Aagaard et al., 2000; Al-Ramadan et al., 2004). Several studies support the latter theory: a study of five Lower to Middle Jurassic sandstones reservoirs from the Veslefrikk and Smørbukk fields (Norwegian continental shelf) show that where grain-coating chlorite is present porosities are 10-15 % higher than would be

expected from normal depth to porosity ratios (Ehrenberg, 1993). Petroleum reservoirs in the North Sea (Ehrenberg, 1993) host chlorite ooids, pellets and expanded chloritized micas, all indicators that chlorite, or more likely, other Fe-rich clay precursors, such as berthierine (average composition $Fe^{2+}_{1.5}$ Al $Fe^{3+}_{0.2}$ $Mg_{0.2}$ $Si_{1.1}$ $Al_{0.9}$ O_5 $(OH)_2$) or odinite (average composition: $(Fe,Mg,Al,Fe,Ti,Mn)_{2.4}$ $(Si,Al)_2$ O_5 (OH) (Odin, 1988), were present within the sedimentary environment at the time of burial. Both precursor minerals, berthierine and odinite, form in similar settings and are structurally akin to chlorite (Ryan and Reynolds, 1996). Studies by Ehrenberg (1993) and Hillier (1994) noted that verdine facies sediments containing berthierine convert during diagenesis to grain-coating chlorite. Experimental testing Aagaard et al. (2000) show that grains with thin, discontinuous coatings of berthierine, recovered from shallow low temperature reservoir intervals, when subjected to conditions replicating shallow burial temperatures and pressures, will recrystallize at about 100°C to form thick, continuous coatings of authigenic iron-rich chlorite (chamosite) that is similar to naturally formed Fe-rich chlorite seen in other parts of the reservoir. The understanding that berthierine forms in certain depositional environments and can recrystallize to form diagenetic chlorite may help geologists to pinpoint possible reservoirs containing higher porosity due to this unique grain-coating feature. It has also been proposed by Ryan and Reynolds (1996) that odinite acts as the precursor of chlorite within the depositional setting sandstone reservoirs that contain abundant iron-rich volcanic clasts (27 % of bulk rock) along the US Gulf Coast. It has also been shown experimentally that the Fe-rich clay coating (berthierine) can be produced in the gut of a polychaete worm, *Arenicola marina*, during ingestion, digestion and excretion of metamorphic primary minerals (mica and chlorite)

of the sediment (McIlroy et al., 2003; Needham et al., 2005). The excreted material, clay-sized grains in a quartz sand matrix, occur within fecal casts period of just over one day. These casts break down and form authigenic Fe-clay rims on grains in sediments after one month of bioturbation. These clay coatings strongly resemble those found within reservoir sandstones. It appears that the low pH and digestion process within the stomach of *A. marina* hasten degradation of the ingested minerals and the formation of rims on grains (McIlroy et al., 2003). The bioturbation of sands and shales by organisms may thus play a vital part in the origin of the Fe-rich clay coating on grains, the precursor to diagenetic chlorite.

Although grain-coating chlorite can help to preserve high porosity, its presence within a reservoir may also have a negative effect. Water can become trapped within the clay structure and create high irreducible water saturations within the rock. On a wireline log, this is characterized by lower than normal electrical resistivity values (Ketzer, 2002; Reimer, 2002; Rossi et al., 2003; Salem et al., 2005). However, hydrocarbons generated from these low resistivity, chlorite-rimmed sandstones are water free since the water is bound to the clay making it immobile (Rossi et al., 2003).

1.3 Research Setting: The Scotian Basin

The Scotian Basin, in particular the Sable Subbasin, has been the focus of extensive exploration for oil and gas reservoirs. Most of the inferred geological history is from the interpretation of well and seismic data. The variation in diagenetic cements, which can either improve or degrade reservoir quality, is insufficiently predictable in the Sable Subbasin. Petroleum geologists are interested in improving reservoir management by understanding and predicting the distribution of cements and reservoir architecture of

cemented zones.

1.3.1 Regional stratigraphy of the Scotian Basin

The following is a review of the general stratigraphy of the Scotian Basin, mostly based on Wade and MacLean (1990). The lithologies are based exclusively on well log interpretation. The Scotian Basin lies along the eastern coast of Canada, stretching from George's Bank to the Grand Banks and covering about 300,000 km^2. There are five associated subbasins, with maximum sediment thicknesses reaching over 18 km: the Shelburne, Sable, Abenaki, Laurentian and South Whale subbasins (Figure 2.1).

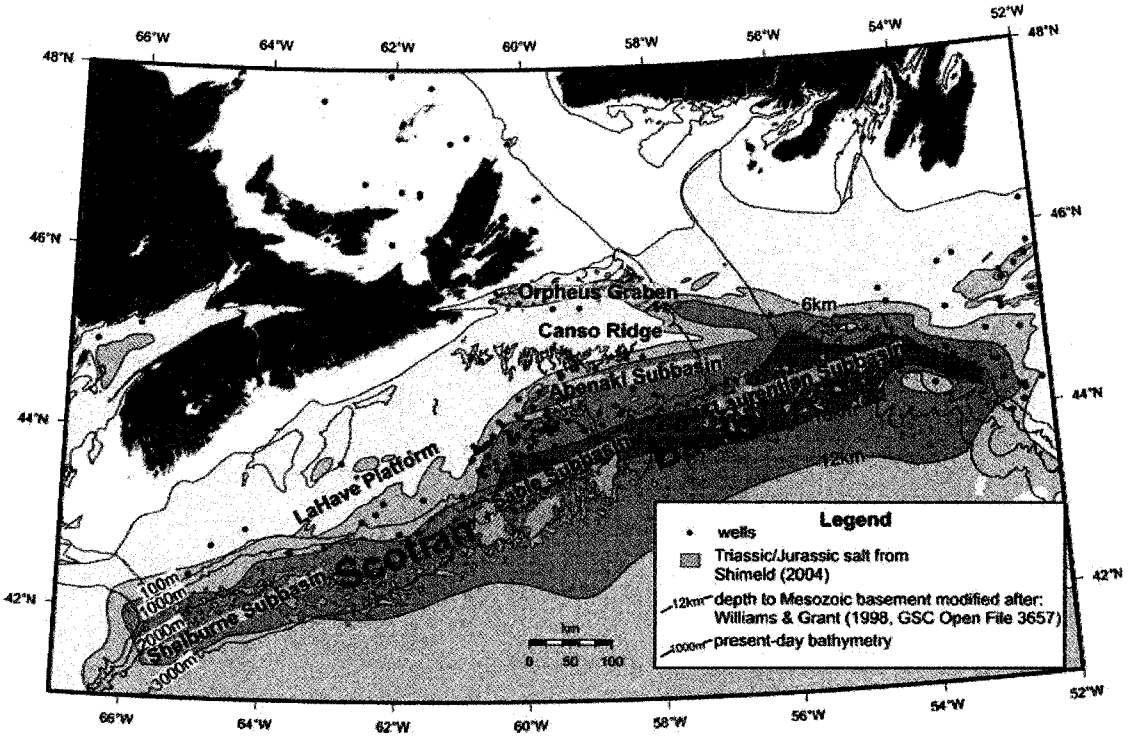

Figure 1.2: Map showing the location of the Scotian Basin and associated subbasins (modified from Wade and MacLean, 1990; Williams and Grant, 1998 and Shimeld, 2004)

The Scotian Basin is composed of Mesozoic to Cenozoic sediments (Figure 1.3) overlying basement rocks mainly composed of Cambrian to Ordovician metasediments of the Meguma Group and Devonian granites.

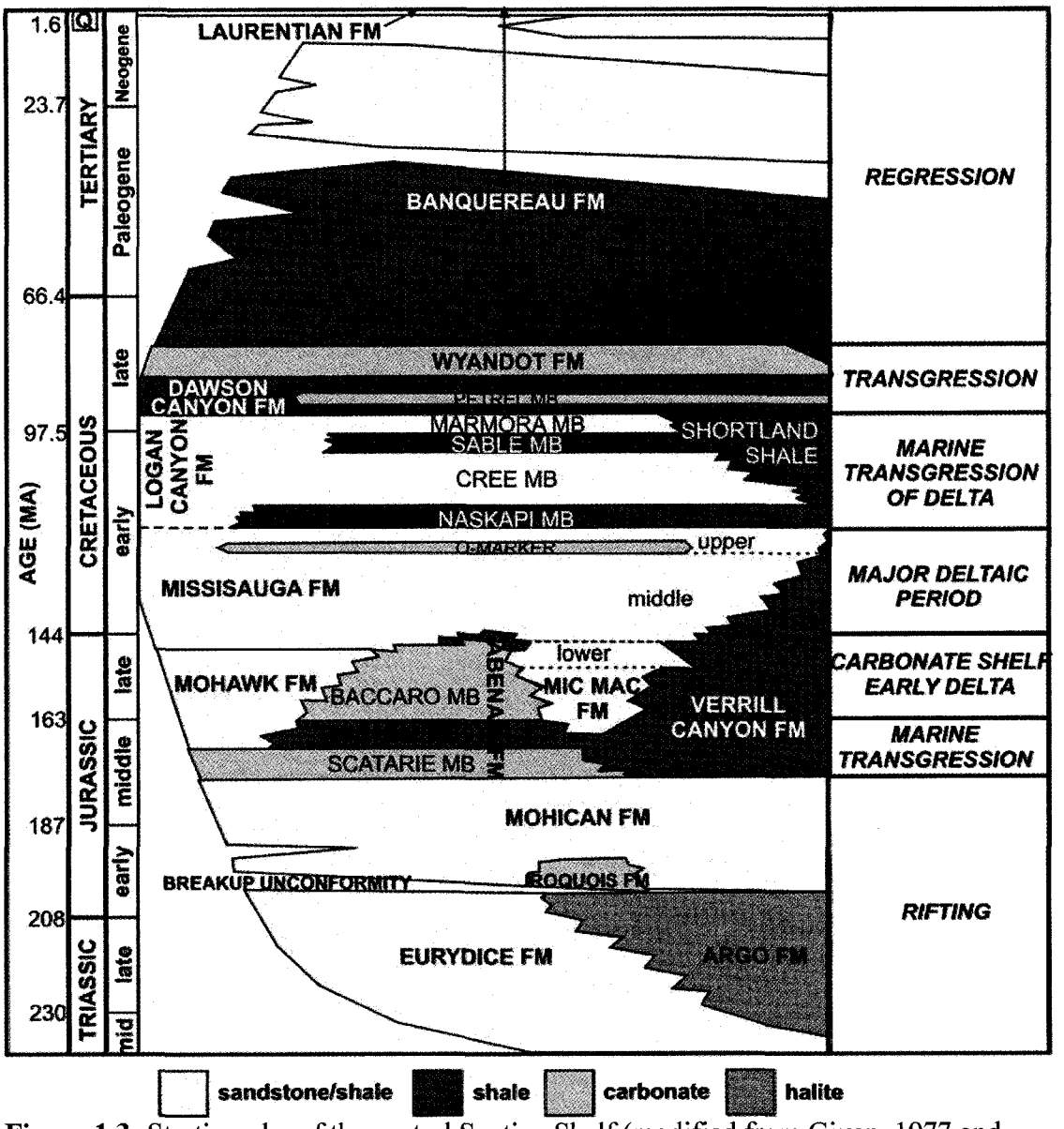

Figure 1.3: Stratigraphy of the central Scotian Shelf (modified from Given, 1977 and Wade and MacLean, 1990).

The Scotian Basin is a passive margin formed in the Mesozoic during the break-up of Pangaea and the opening of the Northern Atlantic Ocean. The continents began to separate during the Middle Triassic, creating northeast trending horst and graben structures. In the deeper graben, the Triassic to earliest Jurassic Eurydice (red clastic rocks) and Argo formations (evaporites) interdigitate. It is interpreted that these

formations were deposited in arid conditions in fluvial and lacustrine environments and are time-equivalent to the Wolfville and Blomidon formations that outcrop onland in western Nova Scotia. In the Early Jurassic, a phase between syn-rift and post-rift sedimentation, known as the Breakup Unconformity, separates the Eurydice and Argo formations from the dolostones, sandstones and shales of the Iroquois and Mohican formations, respectively. The succession is described as a very thick series associated with the rapid basin subsidence. The age of the Mohican Formation makes it the offshore equivalent to the Scots Bay and McCoy Brook formations of inland Nova Scotia.

Post-rift deposition occurred during the Middle and Upper Jurassic resulting in a series of four formations deposited in a deep marine environment. The Abenaki Formation is a distinct platform carbonate succession mainly composed of limestone and forming a prominent marker in seismic sections. The Mic Mac Formation is the siliclastic counterpart to the Abenaki Formation, and represents delta progradtion (McIver, 1972). It is mostly composed of shales with some sandstone and limestone units. Continental sandstones of the Mohawk Formation are contemporaneous with the Mic Mac Formation and include continental facies. Shales of the Verrill Canyon Formation represent the Middle Jurassic to Early Cretaceous deep-water, distal equivalent of the Abenaki, Mohawk, Mic Mac and Missisauga formations.

The Missisauga Formation was deposited during the latest Jurassic to Early Cretaceous periods. It is a thick, broadly regressive, siliclastic succession deposited by at least three rivers supplying sediment from multiple bedrock sources (Pe-Piper and Mackay, 2006). The Missisauga Formation contains many of the petroleum reservoirs in the basin and consists mainly of sandstones with mudstone and some limestone

successions. It reaches a maximum thickness of 3.5 km in the Sable Subbasin. Within this formation, a distinct horizon of carbonate and sandstone, known as the "O" marker, is indicative of a widespread but probably brief transgressive phase during the Lower Cretaceous. Distally, the Missisauga Formation changes into turbidites and shales of the Early Cretaceous Verrill Canyon Formation. Overlying the Missisauga Formation, are the sediments of the Logan Canyon Formation, at the boundary between the Early and Late Cretaceous. Within this formation are two shale units, the Naskapi and Sable Members, and two sandstone units, the Cree and Marmora members. The Upper Cretaceous Dawson Canyon Formation was deposited during a marine transgression and consists of shales and limestones. Also deposited in the Late Cretaceous, the Wyandot Formation is a distinct chalk unit which includes marls and chalky mudstones. Sedimentation in the latest Cretaceous and Tertiary resulted in the deposition of the Banquereau Formation, a broadly coarsening upward sequence representing several cycles of relative sea level changes (Figures 1.5 and 1.6).

1.4 Venture and Thebaud fields

This study focused on wells from the Venture and Thebaud fields (Figures 1.4, 1.5 and 1.6). Both fields penetrate sandstones containing grains with diagenetic chlorite rims. Thebaud C-74 is an exploration well drilled in 1986, Venture 1, 3 and 4 are production wells drilled in the late 1990's.

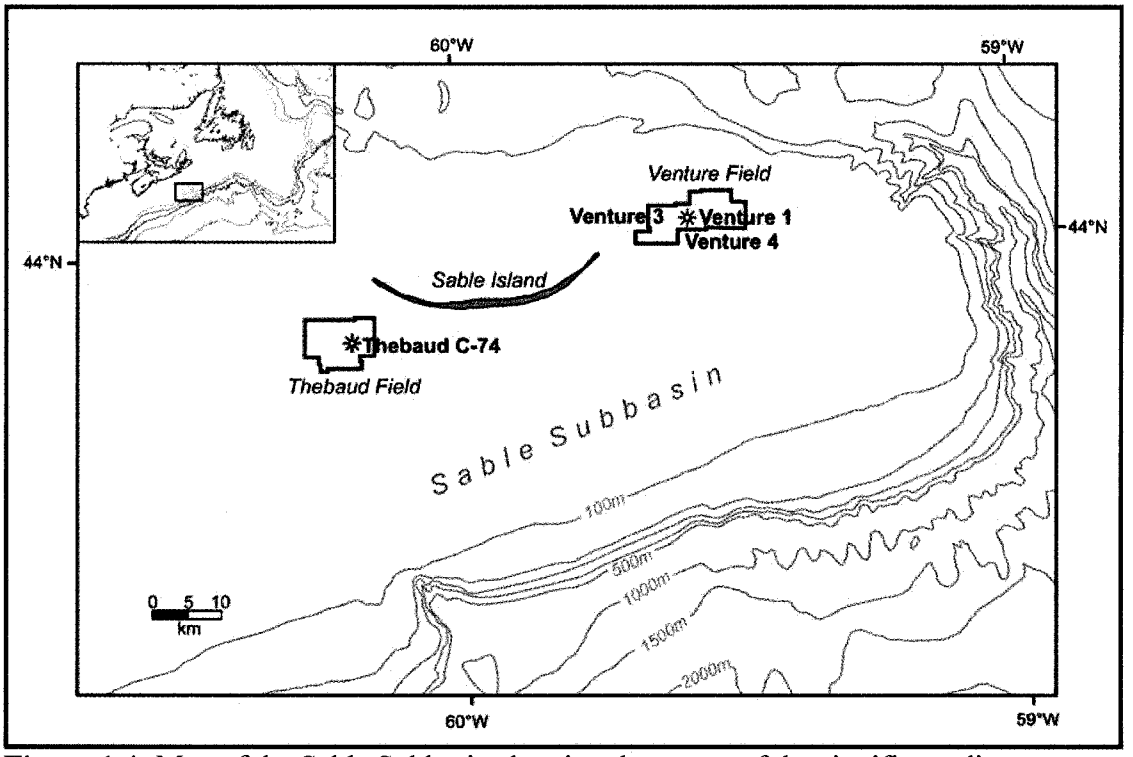

Figure 1.4: Map of the Sable Subbasin showing the extent of the significant discovery licenses of Thebaud and Venture fields and the specific locations of the wells used in this study. The Venture wells were drilled from one platform and deviate subbottom (aerial extent of fields from http://www.cnsopb.ns.ca/maps/index.html).

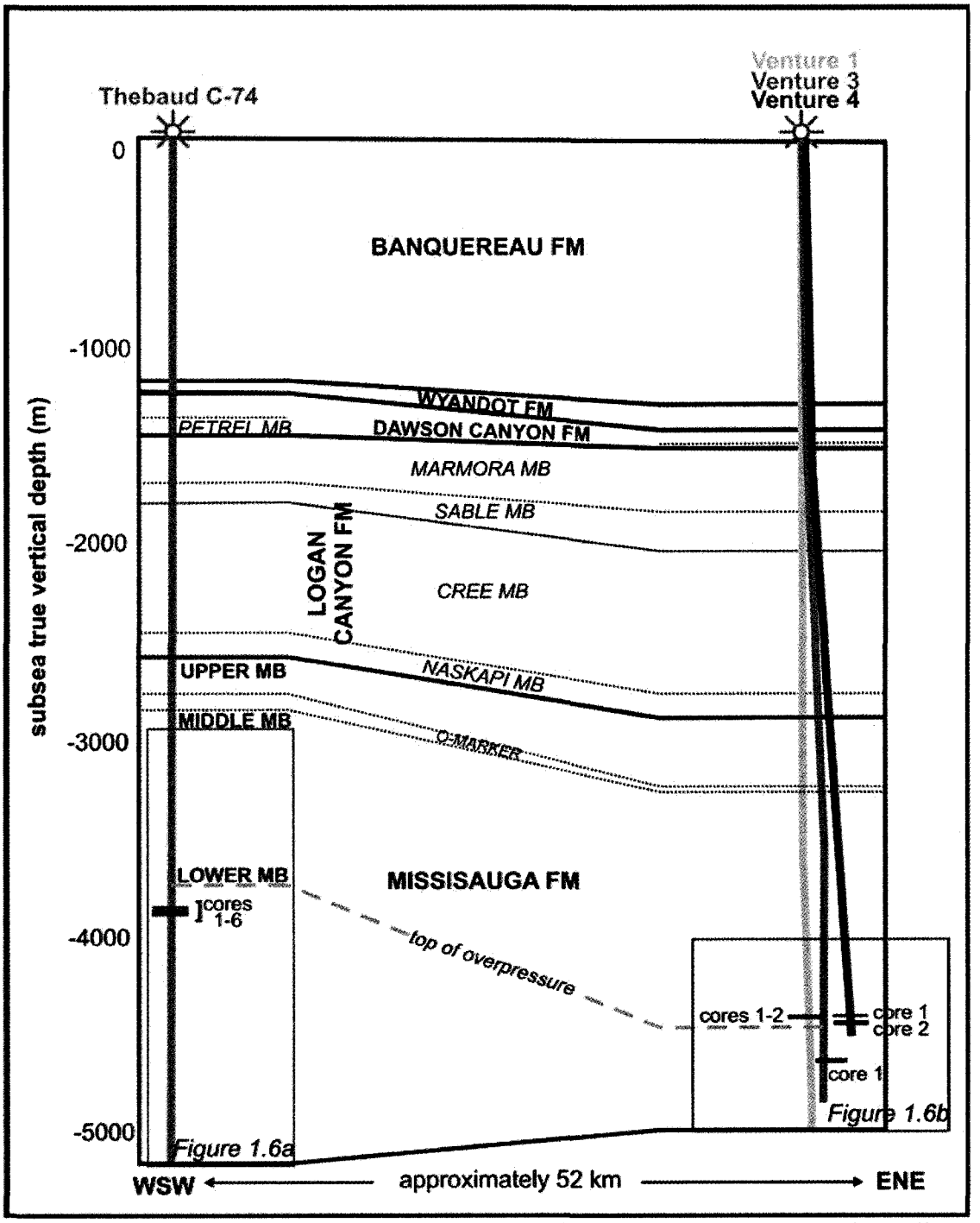

Figure 1.5: Regional cross section through Thebaud C-74 and Venture 1, 3 and 4 wells showing the location of cores relative to the regional stratigraphy. Similar terminology for sandstone units does not imply direct correlation between unit in Thebaud and Venture. Core locations and lithostratigraphic picks for the Venture wells are from Baker Hughes (1999a; 1999b; 1999c) and for Thebaud are from Mobil Oil Canada Limited (1986). Data was plotted and cores were depth corrected using Schlumberger Petrel well logging software.

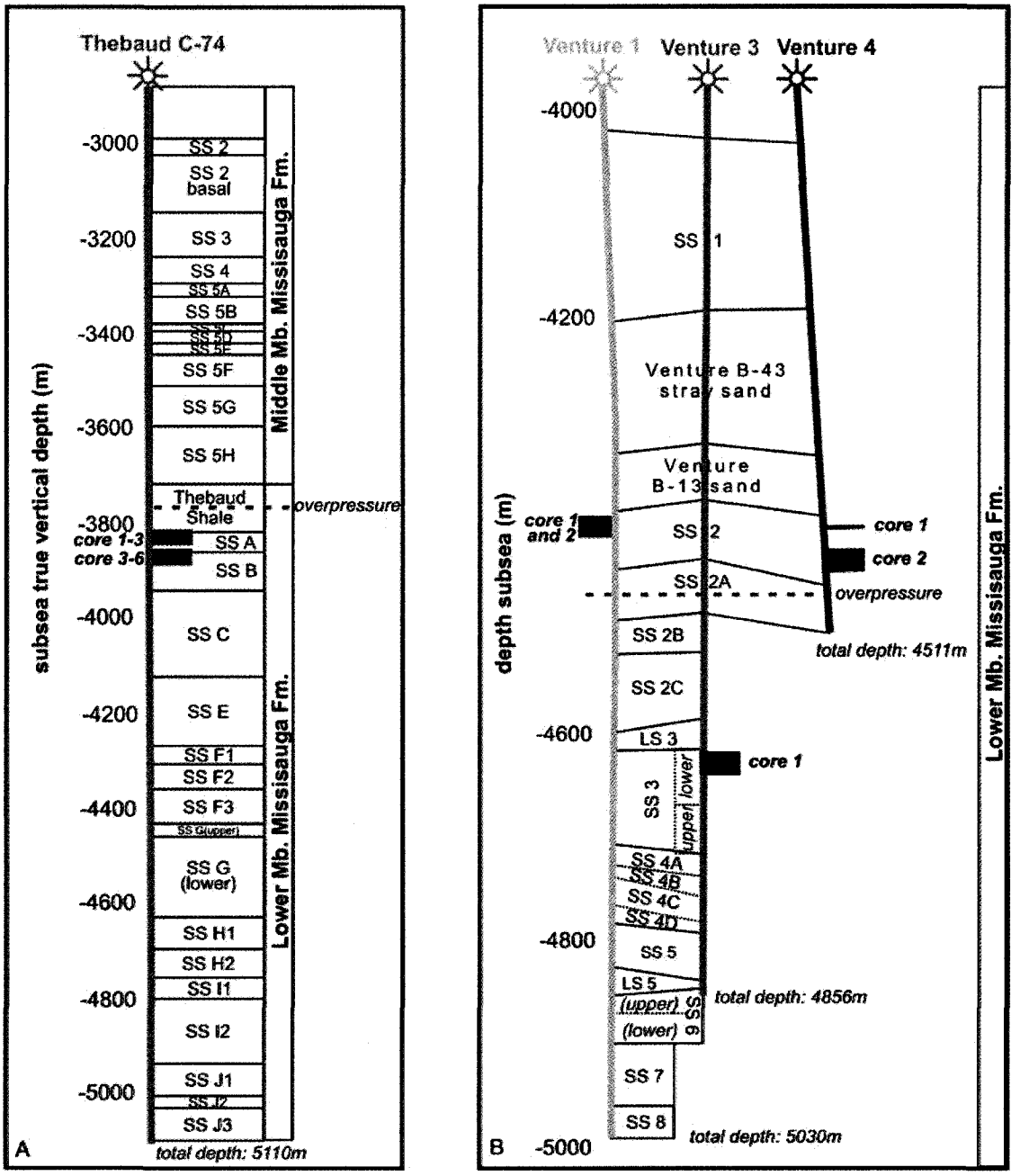

Figure 1.6: Inset to regional cross section through Thebaud C-74 (A) and Venture 1,3 and 4 wells (B) showing the location of cores relative to industry-picked sandstones (SS), shales and limestones (LS). Core locations and lithostratigraphic picks for the Venture wells are from Baker Hughes (1999a; 1999b; 1999c) and for Thebaud are from Mobil Oil Canada Limited (1986). Data was plotted and cores were depth corrected using Schlumberger Petrel well logging software. Data was plotted and cores were depth corrected using Schlumberger Petrel well logging software.

1.4.1 The Venture Field

The Venture Field is located close to the Sable depocentre, approximately 15 kilometres east of Sable Island (Figure 1.4) (Sable Offshore Energy, 1996; Wade and MacLean, 1990). The field structure is a deep rollover anticline developed on normal listric growth faults that terminate in the Lower Cretaceous (Figure 1.7) (Jansa and Noguera-Urrea, 1990; Drummond, 1992; Sable Offshore Energy, 1996; Canada Nova Scotia Offshore Petroleum Board, 1997).

The field was discovered in 1979 by Mobil-Texaco-Pex after drilling Venture D-23. Four additional exploration wells were drilled during 1978-1983: Venture B-13, B-43, B-52 and H-22, located between two - five kilometres from the discovery site (Canada Nova Scotia Offshore Petroleum Board, 1997). Since the exploration phase, seven development wells (Venture 1 to 7) have been drilled between 1998 and 2005.

The producing intervals of the reservoir are located within the Upper Jurassic Mic Mac Formation and the Lower Cretaceous, Lower and Middle members of the Misissauga Formation (Canada Nova Scotia Offshore Petroleum Board, 1997). The reservoirs are composed of several stacked deltaic successions, strandplain deposits and marine shales and oolitic limestones (Sable Offshore Energy, 1996; Canada Nova Scotia Offshore Petroleum Board, 1997). The Mic Mac Formation reflect distributary channel and delta front deposition, with the frequency of channel incisions increasing up section (Sable Offshore Energy, 1996). Zonal average porosities within the reservoir sands range from nine to 23 percent. Successive reservoir sandstones within the Missisauga Formation are well-sorted and coarsen upward, indicating a continued progradation of the delta, and of its associated strandplain (Canada Nova Scotia Offshore Petroleum Board,

1997; Sable Offshore Energy, 1996).

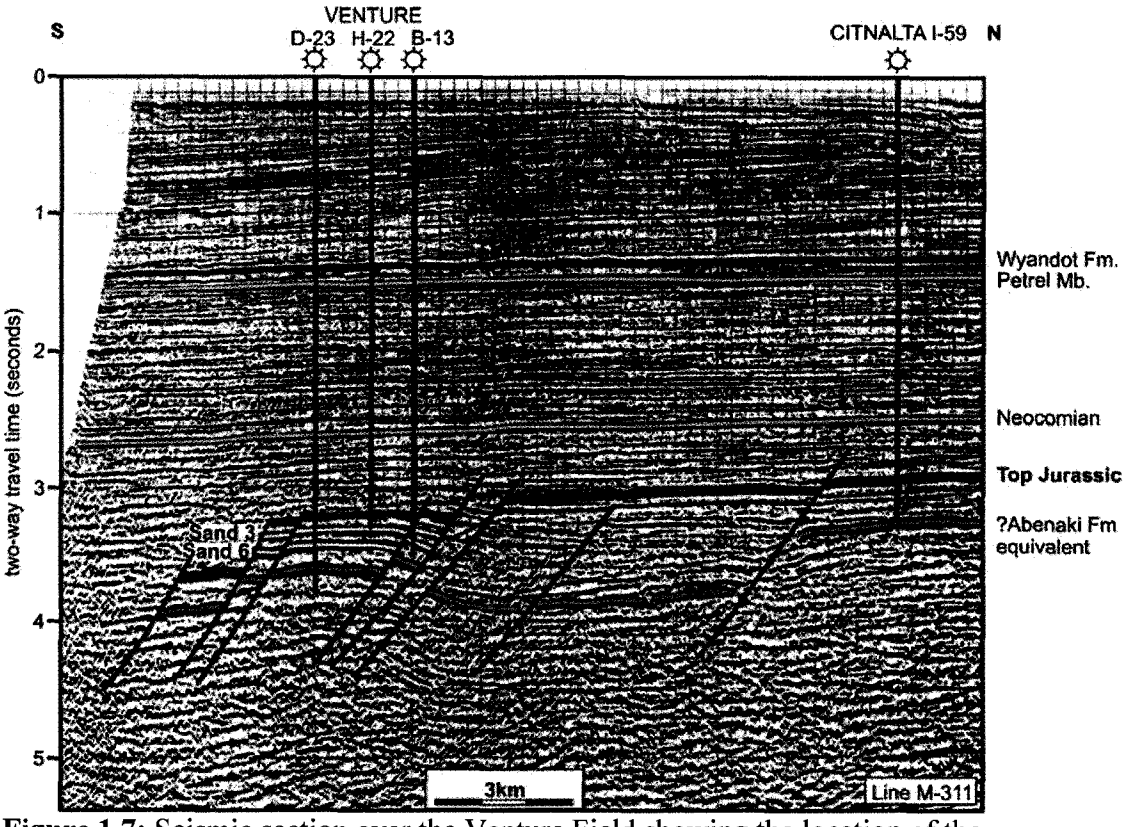

Figure 1.7: Seismic section over the Venture Field showing the location of the exploration wells and the deep rollover anticline structure, developed along several listric growth faults that terminate in the Lower Cretaceous (modified from Drummond, 1992)

Gas accumulations in the Venture Field are present from 4045 to 5825m true vertical depth (TVD). The principal gas reservoirs lie between 4406 to 5101m, within Sands 2, 3, 5 and 6 (upper) (Sable Offshore Energy Project, 1996).

Samples used in this study are from the production wells Venture 1, 3 and 4 and from cores recovered from Sand 2, Sand 3 (upper) and Limestone 3 (Figure 1.6B). These wells were drilled on an inclination and gyroscopically surveyed every 5 metres to determine the angle of deviation. Venture 1 and 4 were directionally drilled at an angle 34° to a total depth of 5030 and 4543m TVD respectively and 2 cores were recovered for each well from Sand 2. Venture 3 is deviated at an average angle of 12° and drilled to a

total depth of 4894m TVD. One core was recovered sampling the base of Limestone 3 and Sand 3 (Upper) (Sable Offshore Energy, 1996).

1.4.2 The Thebaud Field

The Thebaud Field, discovered in 1972, is located near the western edge of the Sable Delta complex, about ten kilometres SW of Sable Island (Figure 1.4) (Sable Offshore Energy, 1996; Canada Nova Scotia Offshore Petroleum Board, 1997). Like the Venture Field, Thebaud is located within a rollover anticline structure, bounded by two large east-west listric growth faults that extend down to the basin (Figure 1.8). The fault systems were active for significantly longer than those at Venture, with evidence of growth well into the Tertiary Period (Sable Offshore Energy, 1996: Canada Nova Scotia Offshore Petroleum Board, 1997).

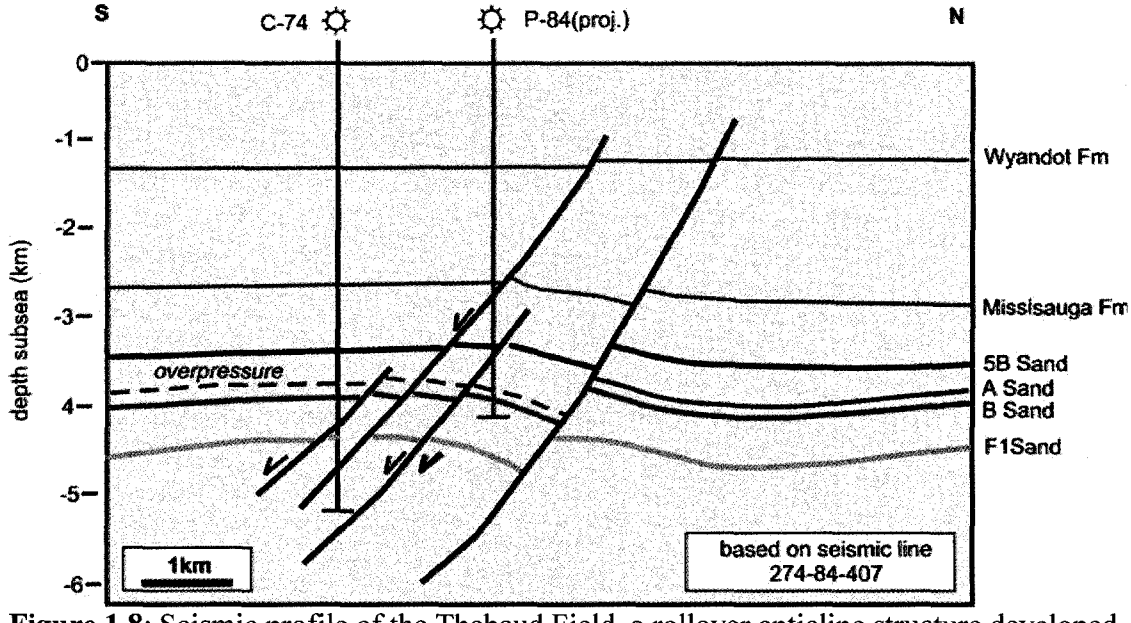

Figure 1.8: Seismic profile of the Thebaud Field, a rollover anticline structure developed along listric growth faults. Faults continued well into the Tertiary period (modified from Canada Nova Scotia Offshore Petroleum Board, 1997).

The discovery well, Thebaud P-84, was drilled by Mobil –Texaco in 1972 to test for the presence of hydrocarbons within the structure. Three additional exploration wells,

Thebaud I-94 (in 1978), I-93 (in 1985) and C-74 (in 1986), were drilled two to three kilometres from Thebaud P-84 (Canada Nova Scotia Offshore Petroleum Board, 1997). These exploration wells penetrate gas within normal and overpressured sands. Producing reservoirs are all overpressured occurring below the Thebaud Shale, a regional seal.

The principal reservoir sandstones are within the Lower and Middle members of Missisauga Formation (Early Cretaceous). The reservoir consists of stacked, upward coarsening units indicative of a prograding delta and strandplain sands passing distally into marine shales (Sable Offshore Energy, 1996).

Thebaud C-74 was drilled to further investigate Sand A, a gas bearing interval previously discovered in the field. Sand A was the first gas-bearing overpressured reservoir encountered in the Thebaud Field. Sand A varies from 14 to 26m in thickness, increasing from north to south across the structure. C-74 also evaluated the hydrocarbon potential and tested high gas flow-rates of the underlying overpressured Sand B (Sable Offshore Energy, 1996).

Six cores were recovered from Sand A and B, with the shallowest core sampling the very base of the informal Thebaud Shale (Figure 1.6A). Thebaud C-74 reached a total drilling depth of 5150.21m TVD. It was plugged and abandoned on September 25, 1986 (Sable Offshore Energy, 1996).

1.5 Overpressure in the Sable Subbasin

A reservoir is overpressured if it has pore fluid pressures higher than hydrostatic pressure, averaging 0.433 psi/ft (9.795 kPa/m) for fresh water (Ferlt, 1976). The deep petroleum reservoirs of the Sable Subbasin, particularly in the Venture Field, are overpressured (Drummond, 1992; Jansa and Noguera-Urrea, 1990; Mudford and Best,

1989; Wade and MacLean, 1990; Williamson, 1995) (Figure 1.9). Overpressures in reservoirs have been previously ascribed to: uneven compaction, clay diagenesis, aquathermal pressuring, tectonism, and hydrocarbon generation. Overpressured zones in the Sable Subbasin at the Venture Field are limited to the Mic Mac and Missisauga formations (Wade and MacLean, 1990). Core samples used in this study are from overpressured intervals, with the exception of core recovered from Sand 2 in the Venture Field. Fluid pressure within the Venture reservoirs increases in a stepwise fashion with depth, revealing six separate overpressure zones (Mudford and Best, 1989) (Figure 1.9). The excessive pressure has been associated with prograding regressive system tracts, and it is often seen together with high water saturations and high salinities (Drummond, 1992). Chlorite rimming seems connected to the areas of high porosities in the overpressured zones, which include interbeds of shales that show characteristics of undercompaction relative to their depth. However, chlorite rims are also observed in Sand 2 in the Venture field, a normally pressured interval.

It appears that shale units within the reservoirs act as pressure seals at the top of the overpressured sands, preventing reservoir pore pressures from equilibrating with the external hydrostatic pressures. Regionally, the onset of overpressure cuts across formation boundaries and Jansa and Noguera-Urrea (1990) showed that the overpressuring is diagenetically driven. The pore space was pressurized 50 Ma or earlier, helping to preserve create the excellent preservation of porosity (up to 32%) in these overpressured zones. This is similar to observations made by Drummond (1992), who concluded that reservoirs were sealed early in their burial history, preserving abnormally high porosities. The trapped fluids in the pore spaces supported the overburden weight

above the reservoir, preventing excessive compaction of the grains. Mudford and Best (1989) simulated pore-pressure relationships in the Sable Subbasin using one-dimensional, single phase models. From the combination of lithological and petrophysical data, the overpressure is thought to be caused by uneven compaction within the reservoirs.

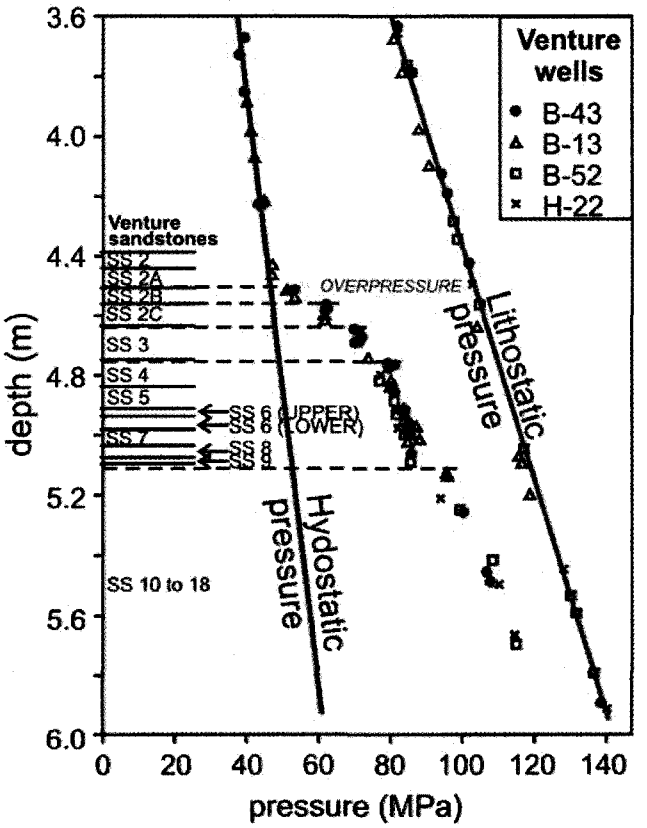

Figure 1.9: Fluid and overburden pressure versus depth for several wells in the Venture Field. Note that the pressure increases down depth in steps (modified from Mudford and Best, 1989).

1.6 Research Objectives

The heterogeneity of diagenetic cements within reservoirs of the Scotian Basin has made the task of predicting diagenetic cements (such as chlorite rims) very challenging. A rigorous study characterizing the mineral diagenesis, in particular the different types of chlorite, the origin of the chlorite-rich zones and their overall

relationship to the sedimentary facies scheme within cores from the Venture and Thebaud fields was undertaken to provide important additional input for reservoir modeling and management within the Scotian Basin.

This project involves a systematic examination of diagenesis within the producing intervals of the Lower Member of the Missisauga Formation in the Sable Subbasin, using samples from conventional cores of the Venture and Thebaud fields. Analytical work was conducted on a suite of representative plug samples obtained from Exxon Mobil Canada (Figure 1.10). A portion of each plug was removed for <2 μm separation and X-ray diffraction analysis, for bulk whole rock geochemical analyses and for a microprobe thin section.

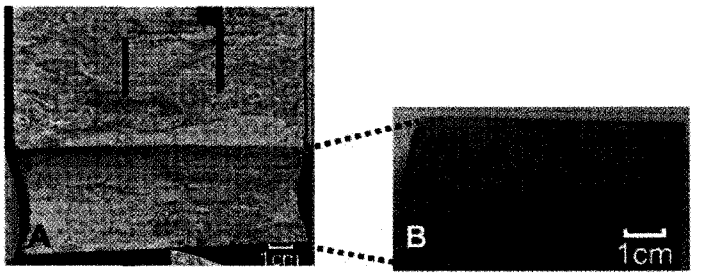

Figure 1.10: A) Core section showing small plug sample hole; **B)** Plug sample used for analysis.

Analytical findings on the diagenetic minerals are related to plug porosity measurements, wireline logs and depositional facies from the core to evaluate the importance of diagenesis for reservoir quality within the basin. This allows the testing of hypotheses for the origin of chlorite rims and its effect on porosity. The results are used to establish a relationship between diagenetic processes and sedimentary facies to aid reservoir prediction quality in the Sable gas fields.

Specific objectives of this thesis are:

1. Assign to cores sedimentary facies by using detailed core descriptions, core photographs and geophysical well logs;
2. characterize mineral diagenesis within cores from the Venture and Thebaud fields of the Sable Subbasin through petrography, X-ray diffraction (XRD), whole rock geochemistry, and electron microprobe analyses;
3. relate analytical findings on diagenetic minerals to porosity measurements and depositional facies;
4. test hypotheses for the origin of chlorite rim development and its effect on porosity;
5. apply the results to establish the relationship between diagenetic processes and sedimentary facies in order to help predict reservoir quality in the Sable gas fields.

Due to the lack of published studies on reservoir diagenesis in the Scotian Basin, it is anticipated that this project will improve our understanding of this topic, providing additional input for reservoir modeling. Results from this project will be applied by the East Coast petroleum industry and is anticipated to encourage more research to be conducted in the Nova Scotia offshore.

CHAPTER 2: STRATIGRAPHIC SETTING AND SEDIMENTOLOGY OF CONVENTIONAL CORES

2.1 Introduction

Conventional cores recovered from the Venture and Thebaud fields sample the Lower Missisauga Formation, and consist mainly of sandstone with some shale and carbonate intervals (Wade and MacLean, 1990). The sandstone units comprise the key petroleum reservoirs in the basin whereas the shale and carbonate lithologies often act as seals. All depths in text and on figures are measured below kelly bushing and uncorrected to wireline logs unless otherwise indicated.

2.2 Methods

2.2.1 Approach

Drill cores from the Venture and Thebaud fields, well history reports and paper copies of the wireline logs are held in the Canada-Nova Scotia Offshore Petroleum Board (CNSOPB) Data Archive, Core Storage and Laboratory Facility in Dartmouth Nova Scotia, where they are publicly available for viewing and limited sampling. Cores stored at the CNSOPB Core Lab were photographed and described in detail during the summer of 2005 (Table 2.1).

Table 2.1: Available conventional cores for study wells (from BASIN database, http://basin.gsca.nrcan.gc.ca).

Well	Sample	Top (m)	Bottom (m)	Sample Location	Formation	Industry Sand	Recovered (m)
Venture 1	Core 1	4590.00	4598.00	CNSOPB	Misissauga Fm. (Lower Mbr.)	Sandstone 2	8.00
	Core 2	4598.00	4615.50	CNSOPB	Misissauga Fm. (Lower Mbr.)	Sandstone 2	17.50
Venture 3	Core 1	4870.50	4896.50	CNSOPB	Misissauga Fm. (Lower Mbr.)	Sandstone 3	26.00
Venture 4	Core 1	5341.10	5345.00	CNSOPB	Misissauga Fm. (Lower Mbr.)	Sandstone 2	3.60
	Core 2	5369.00	5396.00	CNSOPB	Misissauga Fm. (Lower Mbr.)	Sandstone 2	27.00
Thebaud C-74	Core 1	3856.63	3873.26	CNSOPB	Misissauga Fm. (Lower Mbr.)	Sandstone A	16.63
	Core 2	3874.92	3883.86	CNSOPB	Misissauga Fm. (Lower Mbr.)	Sandstone A	8.94
	Core 3	3890.52	3891.08	CNSOPB	Misissauga Fm. (Lower Mbr.)	Sandstone A	0.56
	Core 4	3891.08	3903.92	CNSOPB	Misissauga Fm. (Lower Mbr.)	Sandstone B	12.84
	Core 5	3905.10	3909.35	CNSOPB	Misissauga Fm. (Lower Mbr.)	Sandstone B	4.25
	Core 6	3909.67	3926.83	CNSOPB	Misissauga Fm. (Lower Mbr.)	Sandstone B	17.16

Core photographs were compared with the drill operator's core photographs taken shortly after drilling to identify possible missing portions of the cores, upside down pieces and to check the accuracy of the cardboard filler lengths used as place holders for removed pieces of core. Plug sample locations were individually identified from the Operator's photographs.

2.2.2 Wireline logs

Access to digital wireline logs for the Thebaud C-74 well from the BASIN database (http://basin.gsca.nrcan.gc.ca) was possible due to the collaboration with D.J.W. Piper of the Geological Survey of Canada (Atlantic). Digital copies of wireline logs for Venture 1, 3 and 4 were provided by Exxon Mobil.

Wireline preparation and manipulation

Digital wireline data for Venture 1 and 3 required modification before displaying as a continuous well log. Wireline data was available as several runs for the same type of log, over different depth intervals (i.e., GR_1 and GR_2 for the first and second run of a gamma ray log, respectively). Logs with multiple runs were pieced together at overlapping depth intervals. Each type of log run was given an abbreviated nomenclature unique to the company who completed the test. These abbreviations differed for each of the wells and had to be defined before the data could be processed (Appendix 2). Wireline data for Thebaud C-74 were already spliced.

Compiling and display of logs and depth correction of cores.

Digital logs were compiled and displayed in Petrel well logging software (Schlumberger, 2004) with the well site Operator's picks for the major formations, members, and industry-named sands. Petrel was used to derive sub-sea true vertical

depth (SSTVD) for the production wells (Venture 1, 3 and 4) using deviation surveys. Analytical data (existing thin sections, samples, and point counting) and core measurements (core gamma ray, density, water saturation, measured porosity and permeability) provided by Mobil Oil Canada Limited (1986) and Core Laboratories (1999a, 1999b, 1999c), were also plotted and depth corrected using Petrel.

Cored intervals were depth corrected by comparing the spectral gamma log run over the cores to the corresponding wireline gamma log (Table 2.2).

Table 2.2: Depth correction applied to cores by comparing spectral core gamma to wireline gamma.

well	core	depth correction applied to cores	direction
Venture 1	core 1	2.00 m	deeper
	core 2	2.00 m	deeper
Venture 3	core 1	no correction needed	
Venture 4	core 1	3.50 m	deeper
	core 2	3.50 m	deeper
Thebaud C-74	core 1	3.25 m	deeper
	core 2	3.25 m	deeper
	core 3	3.25 m	deeper
	core 4	3.25 m	deeper
	core 5	3.25 m	deeper
	core 6	3.25 m	deeper

2.3 Lower Missisauga Stratigraphy

The Lower Missisauga Formation consists of interbedded sandstones, shales and rare limestones. Figure 2.1 is a stratigraphic cross section hung from an O-marker datum showing relevant wireline logs, stratigraphic markers and depths of the conventional cores for the wells used in this study.

The Lower Missisauga Formation is overlain by a thick mudstone package known informally as the Missisauga Shale. Within each field, Exxon Mobil (the operating company) has informally subdivided the Lower Member of the Missisauga Formation into sand packages, numbered from the top down. Exxon Mobil has identified 18 sands

with 22 potential gas bearing reservoirs recognized in the Venture Field. Within the Thebaud Field, 9 sands have been named informally by industry. The reservoirs at the Venture and Thebaud fields are not directly correlatable since each reservoir section was deposited within a growth fault setting, at different times. The general stratigraphy of the studied cores is outlined in the next paragraph, followed by more detailed descriptions in sections 2.4 and 2.5.

Conventional core from Venture 1 samples the upper part of Sand 2. The Venture 4 well has one core from the upper and one from the lower Sand 2 (Figures 1.5 and 1.6). The gamma logs show a general cleaning-upwards trend in Sand 2. The core consists of interbedded sandstone and mudstones packages. Just above the cored interval in both wells, a prominent increase in the gamma logs marks the top of Sand 2 and another cleaning-upwards succession in the overlying sandstone.

Conventional core from Venture 3 samples the upper part of Sand 3 and the very base of Limestone 3. The gamma logs show that Sand 3 is made up of an overall cleaning-upwards package of sandstone and shale. The base of the core is a series of fine sandstone interbedded with beds of mudstone that thin upsection. This is overlain by a single thick bed of coarsening-upward sandstone. The top of the core is composed of a poorly sorted, sandy bioclastic limestone that represents the very base of Limestone 3.

The six conventional cores from the Thebaud C-74 well also sample the Lower Member of the Missisauga Formation. Cores 5 and 6 represent the upper part of Sand B and consist of interbedded mudstones and some fining-upwards sandstones. The corresponding gamma ray logs over the cored interval shows a slight "dirtying upwards" trend, but overall there is no clear trend. The base of Sandstone A is marked by a sharp

increase in the gamma log followed by a slight cleaning-upward trend over cores 3 and 4. These cores are mostly composed of mudstone with minor sandstone beds. There is approximately seven metres of unsampled section between the top of core 3 and the base of core 2, in which the corresponding gamma log shows a sudden increase in values, suggesting that there is likely a change in lithology to shale that cleans upwards to the sandstone seen in core 2. These sandstones fine upwards and become interbedded with bioturbated mudstones in core 1, however the corresponding gamma ray log over this interval shows no distinct trend. Core 1 is dominated by silty mudstone passing into the base of the informal Thebaud Shale.

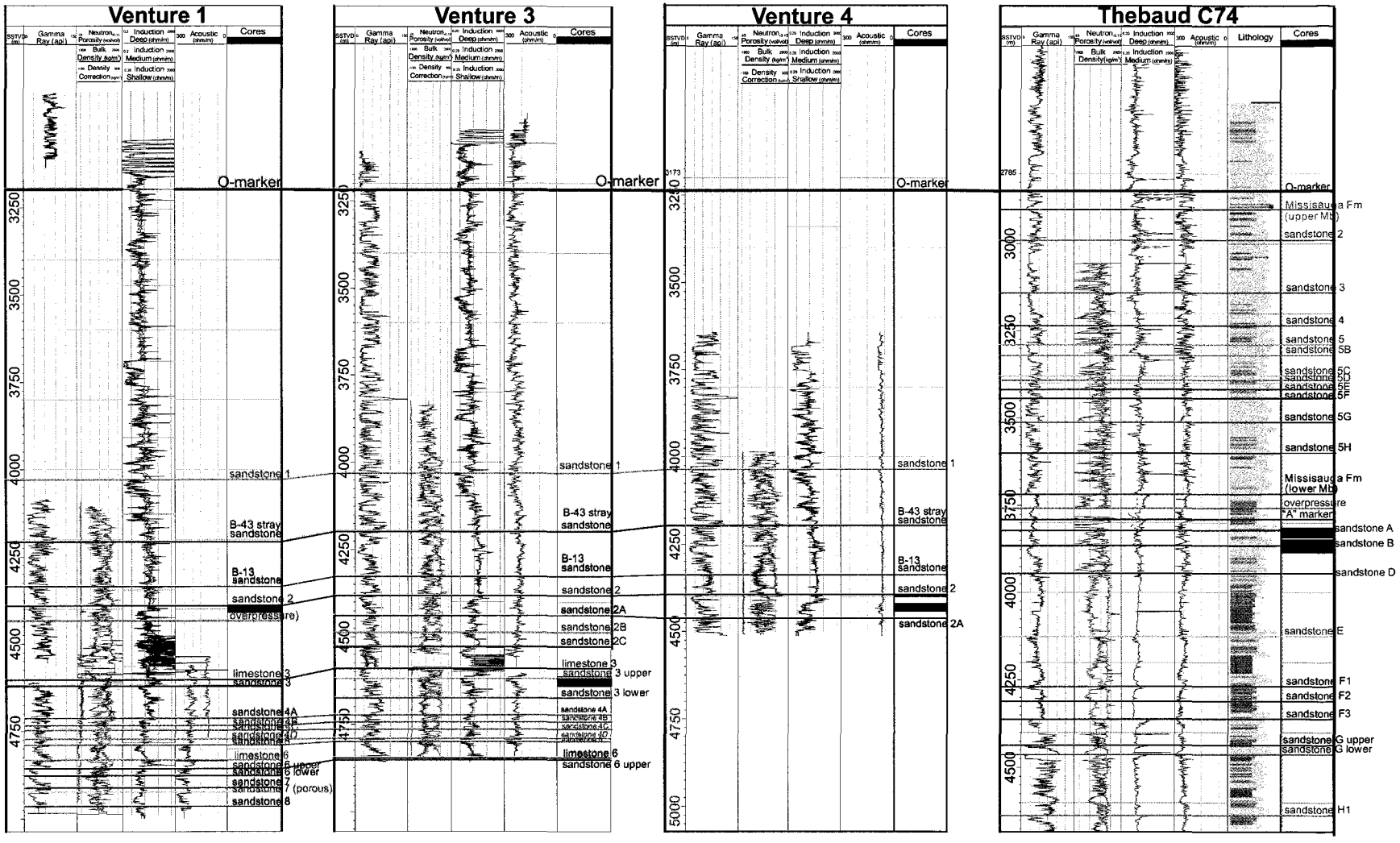

Figure 2.1: Stratigraphic cross-section hung from the O-marker datam showing lithostratigraphy, wireline logs, and correlation between wells (subsea true vertical depth (SSTVD) in metres).

2.4 Lithofacies Recognized in Core

Seven lithofacies have been distinguished in cores from the Venture and Thebaud fields, on the basis of grain size, sedimentary structures, biogenic structures and diagenetic features. They comprise: one bioclast-rich sandstone, two mudstones, and five sandstones (Table 2.4). The facies names reflect the dominant lithology: L for limestone, M for mudstone, and S for sandstone. The depths in text and on representative photographs are uncorrected measured depths unless otherwise indicated.

Facies L1: Bioclast-rich sandstone/limestone

Facies L1 is composed of poorly-sorted, bioclast-rich sandstone to sandy limestone with common parallel and cross laminae of silt and very fine sandstone. The unit is weakly bioturbated, with very rare vertical burrows (*Ophiomorpha)* (Figure 2.2).

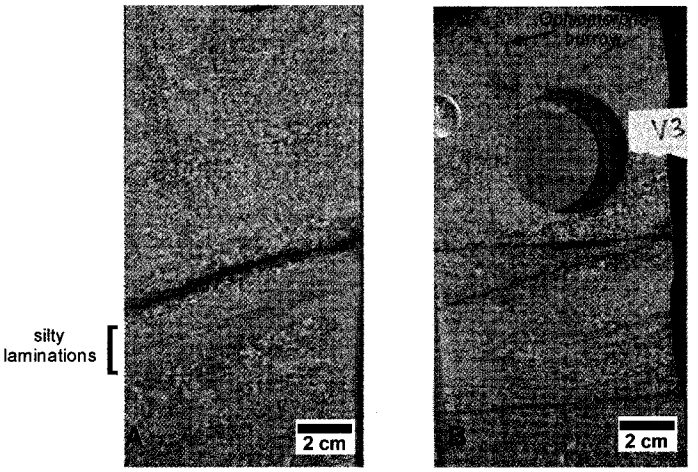

Figure 2.2: Facies L1 in core: **A)** Laminated bioclastic sandstone with silty laminae (depth at top of photograph is 4870.5 m, Venture 3, core 1); **B)** Top of facies L1, with rare bioturbation (depth at top of photograph is 4870.5 m, Venture 3 core 1).

Facies M1: Laminated mudstone

Facies M1 is a largely unbioturbated shale, with laminae composed of siltstone and fine sandstone. Very rarely, these sandstone laminae show intense bioturbation in siltier intervals, as in core 4 of Thebaud C-74 (Figure 2.3). In places there are spherical

concretions of calcite. This unit locally shows soft sediment deformation, in the form of slump blocks and folded strata (at 3894.5 to 3893.2 m in core 4, Thebaud C-74).

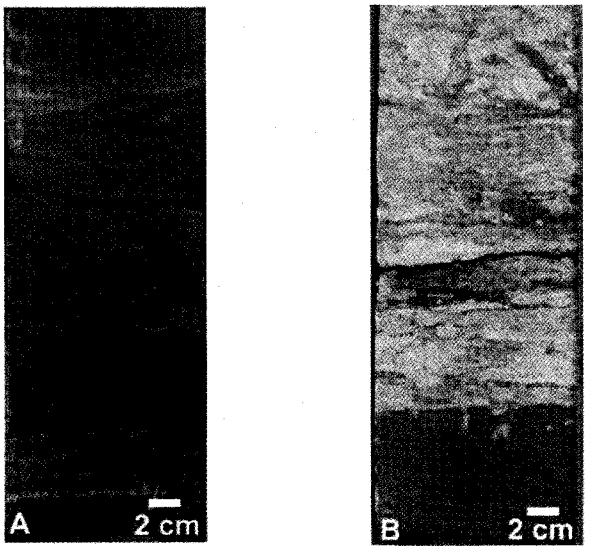

Figure 2.3: Facies M1. **A)** Laminated mudstone with moderate biotubation (depth at top of photograph is 3901.4 m, core 4, Thebaud C-74); **B)** Silty sandstone bed within facies M1 showing a high degree of bioturbation (depth at top of photograph is 3901 m, core 4, Thebaud C-74).

Facies M2: Siderite-cemented mudstone

Facies M2 is similar to facies M1, however it is patchily cemented with diagenetic siderite and is intensely bioturbated. It typically contains abundant shell fragments that decrease gradually upwards in abundance as the facies fines upwards (Figure 2.4).

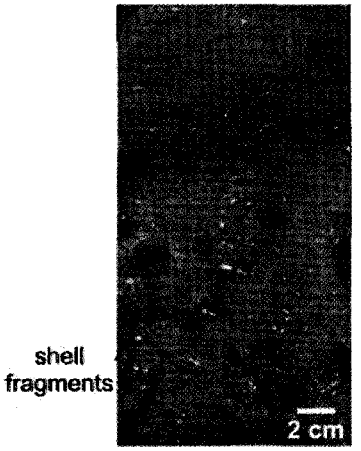

Figure 2.4: Facies M2. Siderite-cemented shale, with abundant shell fragments (depth at top of photograph is 3860 m, core 1, Thebaud C-74).

Facies S1: Mud-draped sandstone

Facies S1 consists of fine to coarse sandstones, organized into fining-upwards beds, 1 to 3 m thick. It contains abundant mudstone partings (Figure 2.5B) and beds of coarse, poorly sorted sand and granules, mud intraclasts and minor pyrite cement (Figure 2.5A). This facies is mostly unbioturbated, however minor bioturbation is seen in the upper part of core 1 at Venture 1.

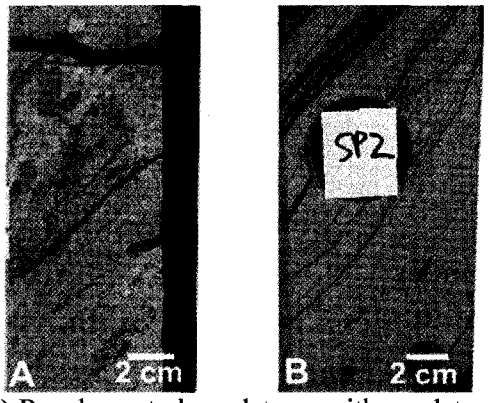

Figure 2.5: Facies S1. **A)** Poorly sorted sandstone with mudstone clasts and pyritized material (depth at top of photograph is 4595.80 m, core 1, Venture 1); **B)** Mud-draped fine sandstone with mud clasts and parallel laminae (depth at top of photograph, 5341.6 m, core 1, Venture 4).

Facies S2: Mudstone with laminated sandstone interbeds

This facies consists of interbedded mudstone and fine to coarse sandstones. The sandstone beds comprise from 35 to 95 % of the total facies, with bed thickness ranging from less than 5 cm to 6.25 m. Mudstone bed thicknesses vary from 5 cm to 2.25 m. This facies has been divided into three subfacies.

Subfacies S2a:

This facies consists of interbedded laminated mudstone and sandstone. The mudstone beds range from <5 cm to 0.75 m thick, making up 5 to 33 % of the total thickness. The laminae in the mudstone beds are faint and composed of siltstone. Bioturbation is absent to minor.

The sandstone beds are fine grained, and range from < 10 cm to 4.5 m in thickness and make up 67 to 95 % of the subfacies. In general, the sandstone beds tend to thicken upsection, for example at 5373.1 - 5380.1 in Venture 4 (Figure 2.14). They are either massive or show well-developed ripple cross laminae at the base, with parallel laminae of mudstone increasing in frequency upwards. The beds are generally sharp-based with erosive lower contacts, and the upper contacts of the beds may show wave ripples or very minor bioturbation (Figure 2.6).

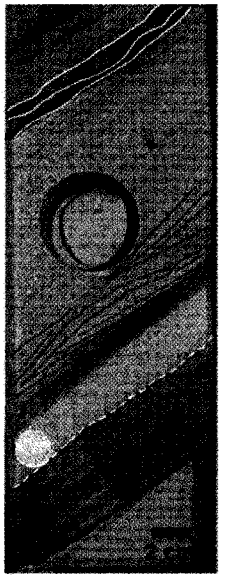

Figure 2.6: Facies S2a, interbedded mudstone and fine sandstone, showing scouring at the base of the sandstone beds (dashed white line), ripple cross laminae (dashed black lines), and wave ripples at the top of the sandstone bed (solid white line) (depth at top of photograph is 4615.7 m, core 2, Venture 1).

Subfacies S2b:

Like subfacies S2a, this consists of interbedded mudstone and sandstone. The thickness of mudstone beds ranges from < 10 cm to 2.25 m, and they make up 12 to 65 % of the subfacies. The mudstones are moderately to highly bioturbated and shell fragments are present at the base of beds of this subfacies, decreasing in abundance upwards (e.g., 4893.83 – 4895.71 m in Venture 3).

The sandstone beds vary in thickness from < 5 cm to 6.25 m, have thin parallel laminae, and become ripple cross bedded near the top of the beds. In places the beds have mudstone intraclasts. Similar to the mudstone beds, the sandstone beds have shell detritus at their base that decreases in abundance upwards. They have minor bioturbation, in particular at the upper contacts between sand and mud beds. Phytodetritus (broken and fine to coarse grained, coalified or pyritized plant material) is rarely present in some sandstone beds (Figure 2.7).

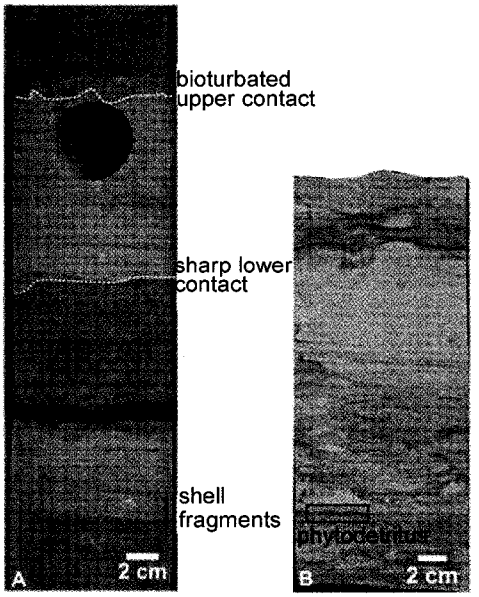

Figure 2.7: Facies S2B, bioturbated mudstone with laminated sandstone interbeds; **A)** Shell debris at the base (depth at the top of photograph 4891.9 m, core 1, Venture 3); **B)** Bioturbated sandstone and siltstone with pyritized plant fragments (depth at top of photograph 3871.95 m, core 2, Thebaud C-74).

Although this subfacies is also composed of interbedded sandstones and mudstones, several distinguishing features separate it from subfacies S2a. The mudstone beds in subfacies S2b show a high degree of bioturbation, whereas the mudstone beds in facies S2a show little to no bioturbation, with silty parallel laminae being preserved. In some intervals of subfacies S2b, particularly in Venture 3, both mudstone and sandstone beds have shell fragments at the base of the beds that decrease in abundance upwards.

Sandstone beds in subfacies S2b lack the low-angle inclined stratification interpreted as representing hummocky cross stratification and cross bedding seen in sandstone beds of subfacies S2a.

Subfacies S2c:

Subfacies S2c is composed of coarsening-upwards, generally well-sorted sandstone beds, 1.1 to 1.5 m thick. This facies is either massive or can be trough cross laminated at the base (Figure 2.8). Subfacies S2c is seen in gradational contact with the underlying subfacies S2a or S2b, and in sharp upper contact with the overlying facies C1.

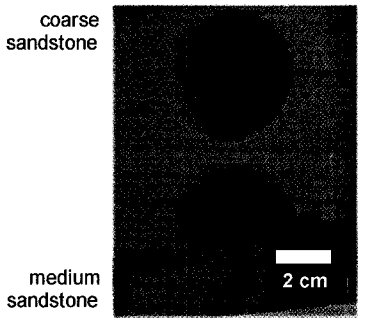

Figure 2.8: Coarsening-upwards sandstone of facies S2c, with trough cross laminae (depth at top of photograph is 4874.15 m, core 1, Venture 3).

Facies S3: Bioturbated fine sandstone

Facies S3 consists of bioturbated fine sandstone. It is has weak, silty laminae in places. Very rare shell fragments are present in Venture 3 (Figure 2.9). *Ophiomorpha* burrows are occasionally recognized in this facies.

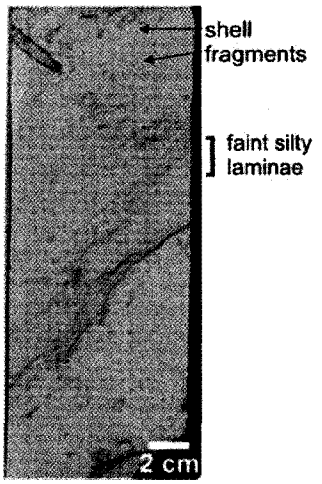

Figure 2.9: Facies S3, bioturbated fine sandstone with rare shell fragments and silty laminae. An *Ophiomorpha* burrow is seen in the upper left corner (depth at top of photograph is 4600 m, core 2, Venture 1).

Facies S4: Massive to laminated fining-upward coarse sandstones

The facies consists of stacked 1 to 5 m thick beds of sharp-based, very coarse-grained (sometime granular) sandstone that grade upwards to fine sandstone (Figure 2.10). The beds are generally massive at the base and become laminated and moderately bioturbated near the top of each bed. The series then repeats with sharp basal contacts that in some places are irregular and very steep, implying significant bottom relief. Complete oyster shell valves and fragments occur infrequently within the sandstone.

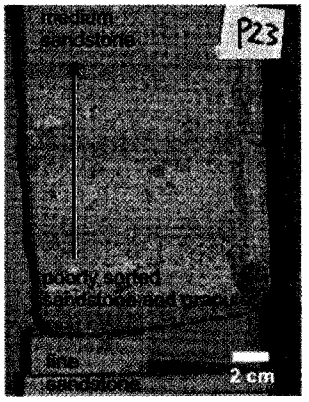

Figure 2.10: Facies S4 in conventional core, coarse grained sandstone with granules, in sharp contact with fine sandstone (dashed black line). The bed immediately fines upwards to a clean, medium grained sandstone above (depth at top of photograph is 3914.27 m, core 5, Thebaud C-74).

Facies C1: Poorly sorted sandstone and conglomerate

This facies consists of poorly sorted, fine to coarse-grained sandstone, and in some cases shows trough cross bedding. It is seen overlying facies S2c or S3 with gradational lower contacts. The upper contact is typically sharp and highly bioturbated with vertical burrows lined with diagenetic siderite and piping coarse sediment downwards (Figure 2.11A). Lithic clasts may be mixed into the overlying unit, which is generally facies M1 or M2 (Figure 2.11B).

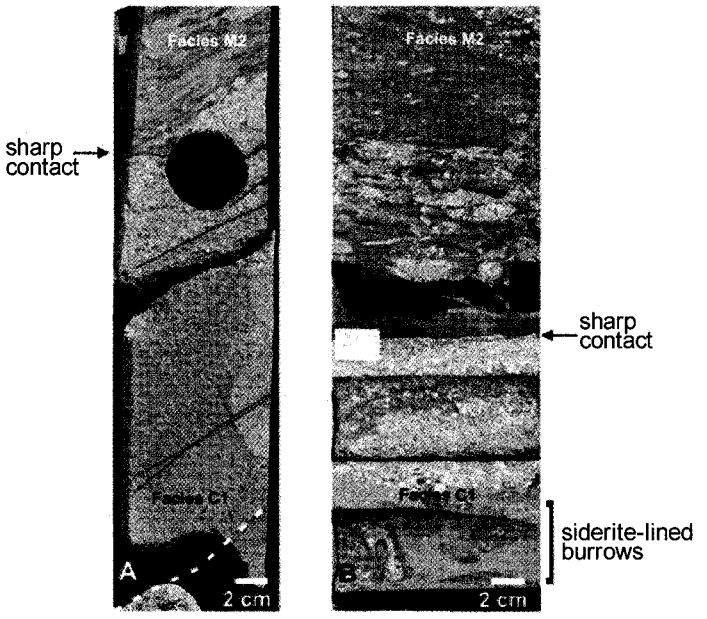

Figure 2.11: Two examples of the facies C1 seen in conventional core. **A)** Poorly sorted, trough cross bedded (black lines) granule conglomerate with gradational lower contact (dashed white line), and a sharp, slightly bioturbated upper contact with the overlying shale (depth at top of photograph is 5380.15 m, core 2, Venture 4); **B)** granule conglomerate with siderite-lined horizontal and vertical burrows. Lithic clasts are bioturbated into the overlying shale unit of facies M2 and coarser facies C1 is piped downwards by burrows (depth at top of photograph 3863.80 m, core 1, Thebaud C-74).

Table 2.3: Facies subdivisions for the Venture and Thebaud cores*.

Facies			Lithology	Sedimentary structures	Fossils	Visable diagenesis	Environmental Interpretation	Notes
L1	*bioclast-rich sandstone/ limestone*		f-c ss, bioclasts	poorly sorted; parallel and trough cross laminae of silty sand	common shell fragments, rare *Ophiomorpha* burrows at top of core 1, Venture 3	carbonate	reworking on shelf remote from distributary mouth	
M1	*laminated mudstone*		sh	thin beds and laminae of silt and vf ss	horizontal burrows in some silty laminae and beds; very rare beds with *abundant bioturbation*		distal prodelta	soft sediment deformation in core 4, Thebaud C-74
M2	*siderite-cemented mudstone*		sh	some coarse granules; typically fining upward	abundant shell fragments decreasing up section; highly bioturbated	siderite	open shelf during transgressive systems tract, extremely distal to active distributary (just below maximum flooding surface)	
S1	*mud-draped sandstone*		f-c ss	poorly sorted in places, generally fining upwards; mud drapes	rare phytodetritus	minor pyrite	tidally influenced distributary fluvial channel	mudstone intraclasts
S2	*ms with laminated ss interbeds*	***S2a***	f ss, sh	massive at base, parallel laminae at top (ss); ripple cross laminae of silty sand (sh)	very rare bioturbation, horizontal burrows (sh)		prodelta, distal hyperpycnal flood deposits	alternating sequence, sharp, erosive lower contact, bioturbated upper contacts (ss)
		S2b	f ss, sh	massive at base, parallel laminae at top (ss); ripple cross laminae of silty sand (sh)	rare phytodetritus, rare bioturbation (ss) highly bioturbated, diverse *?Skolithos* assemblage (sh), rare shell fragments in Venture 3 (sh)	minor pyrite (sh)	prodelta, storm influenced	sharp upper and lower bed contacts (ss)
		S2c	m-c ss	silty trough cross laminae; coarsening upward	rare horizontal burrows (*?Ophiomorpha*), rare shell fragments, mud intraclasts		prodelta	
S3	*bioturbated fine sandstone*		f ss	weakly laminated in places	low to high bioturbation, *?Ophiomorpha* horziontal burrows, very rare shell fragments in Venture 3		?mouth bar/delta front	dark buff coloured in places
S4	*massive to laminated fining-upward coarse sandstones*		f-c ss	structureless at base, faint silty clay parallel laminae near top of beds; repeating locally fining upward beds	whole oyster shells, other shell fragments		proximal hyperpycnal flood deposit	sharp upper and lower bed contacts
C1	*poorly sorted sandstone and conglomerate*		congl., ss	poorly sorted, generally coarsening upward; trough cross laminae	vertical burrows at upper contact	siderite lined burrows and cm thick beds of siderite at upper contact, commonly carbonate cemented	trangressive lag	

*ss=sandstone, sh=shale, ls=limestone, ms=mudstone; f=fine, c=coarse

2.5 Facies succession in the cores and paleoenvironmental interpretation

Lithofacies were identified in the cores logged from the Venture and Thebaud fields. The interpretation of depositional environment of these facies is loosely based upon Cummings (2004), and Cummings and Arnott (2005).

2.5.1 Venture 1

The base of the cored interval at 4616.65 m consists of facies S2a, mudstone beds with laminae of very fine silty sandstone, interbedded with sharp-based, laminated fine sandstones. The sandstone beds thicken from 10 cm to 4.5 m in this well.

At 4610.7 m facies S2a is overlain by facies S3, moderate to highly bioturbated fine sandstone. At 4609.1 m this passes upwards into another development of facies S2a, an overall fining-up sequence with a low percentage of interbedded mudstone near the top of the succession. At 4607.4 m this is again overlain by bioturbated fine sandstone of facies S3.

The uppermost unit, from 4596.35 to 4590 m is facies S1, sharp-based, fine to coarse sandstones. It is an overall fining-upwards sequence, with a poorly sorted interval of sandstone and granules at 4596 to 4595.7 m. The sandstones have common < 1 cm thick mud drapes, faint ripple cross laminae, and plant detritus. This facies generally lacks bioturbation, however minor bioturbation is present at the very top of core 1 (Figures 2.12 to 2.14).

Interpretation

In the lower part of the cores, the alternation of lithofacies S2a and S3 is interpreted as resulting from deposition in a predominantly prodelta environment with the a temporary progradation depositing a succession of mouth bar/delta front sandstones

based on the predominance of sand and the intensity of bioturbation in facies S3. The interbedded unbioturbated intervals of mudstone with siltstone laminae within facies S2a represent prodelta fluvial mud deposits with the sandstone beds representing distal hyperpycnal flood deposits with variations in salinity or the rapid deposition, temporarily suppressing bioturbation.

The sharp base and fining-upward character of facies S1 at the top of the core, together with its thickness, presence of ripple cross laminae and mudstone intraclasts, and the general lack of bioturbation, suggests it was deposited in a distributary fluvial channel. Thin mud drapes indicate that at least part of this channel was tidally influenced. The low abundance of bioturbation at the top of the interval indicates a return to marine conditions following deposition of channel sandstones.

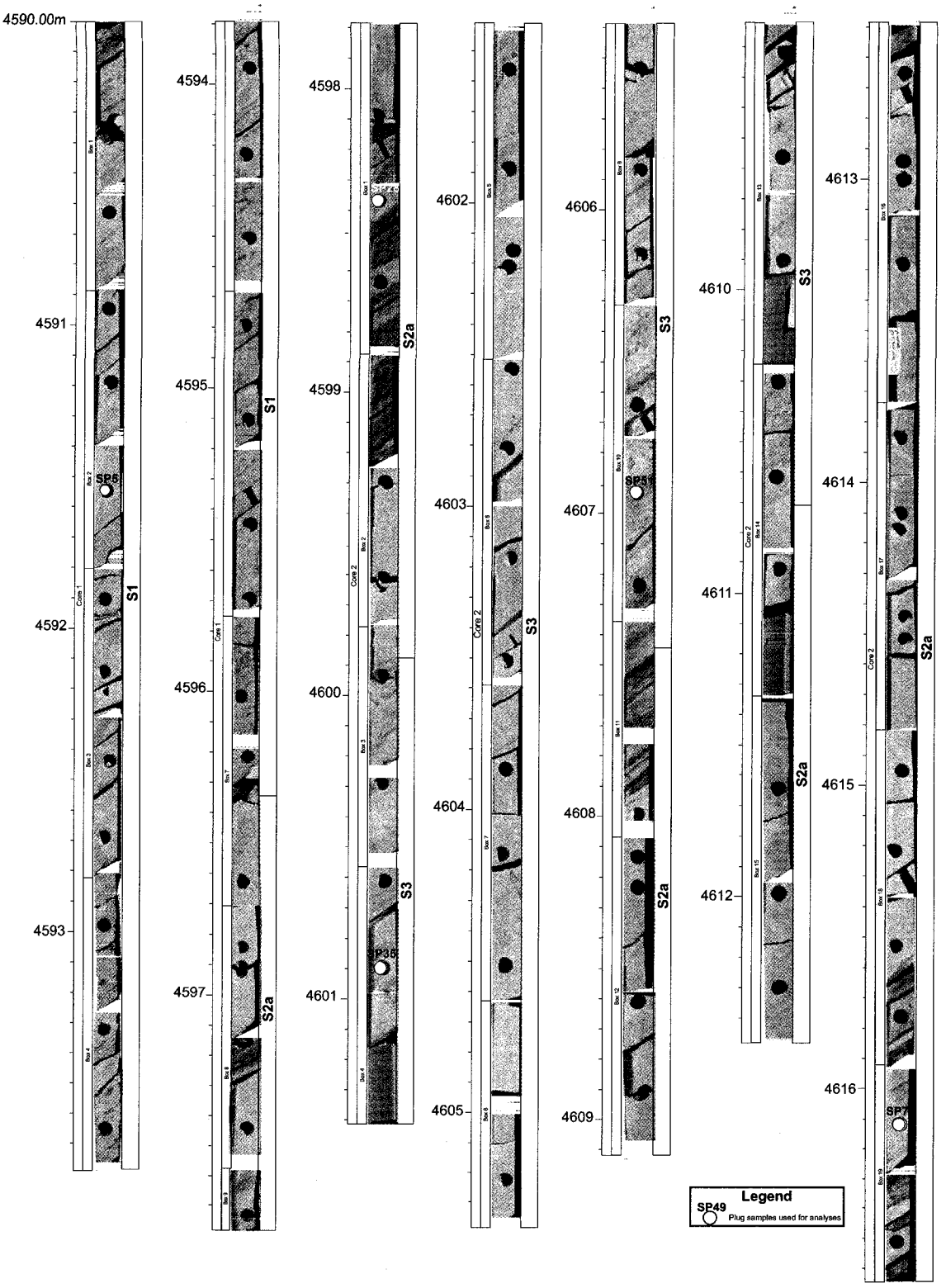

Figure 2.12: Core photos and facies interpretation for cores 1 and 2, Venture 1 (uncorrected measured depth in metres below kelly bushing).

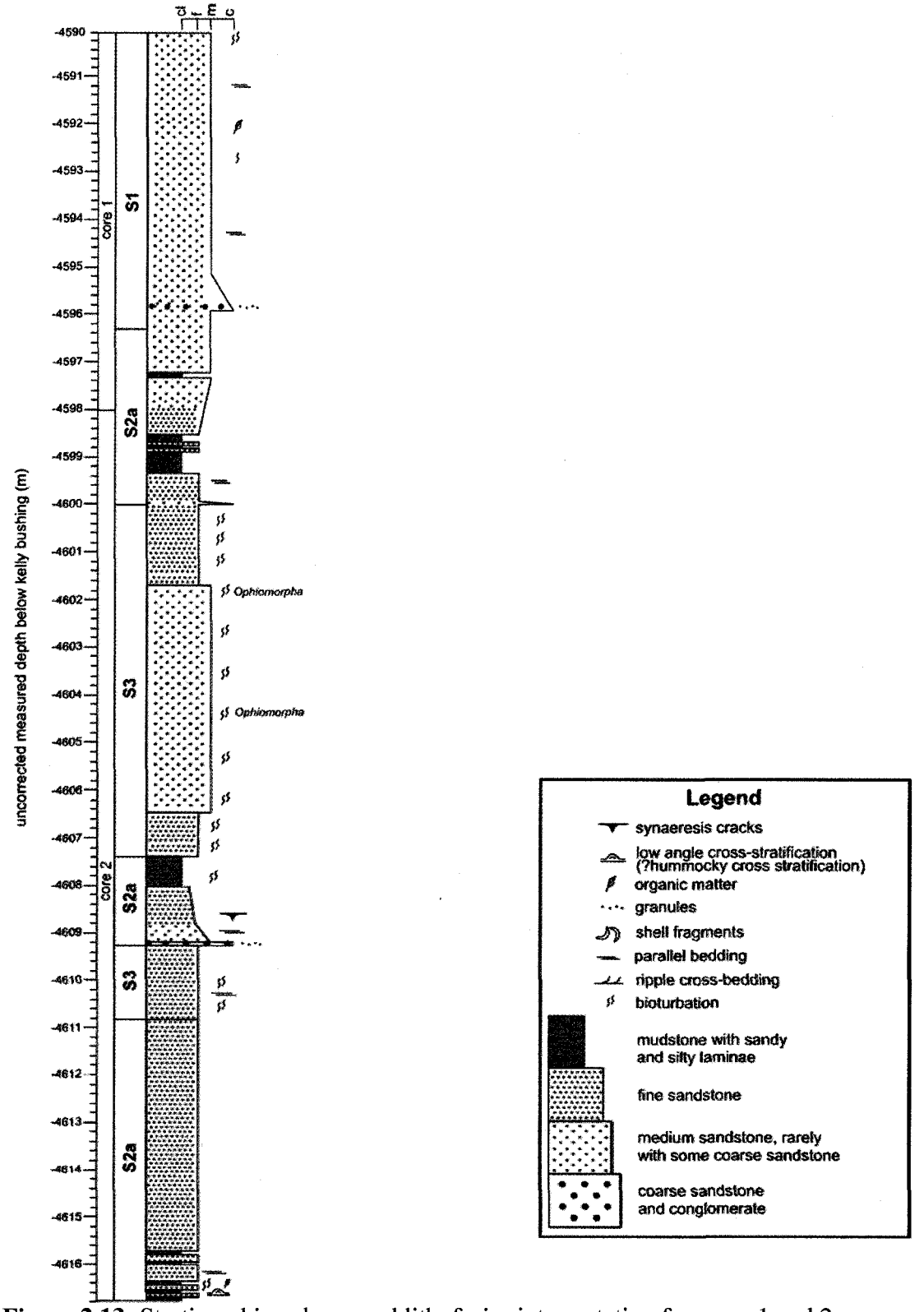

Figure 2.13: Stratigraphic column and lithofacies interpretation for cores 1 and 2, Venture 1 (uncorrected measured depth below kelly bushing).

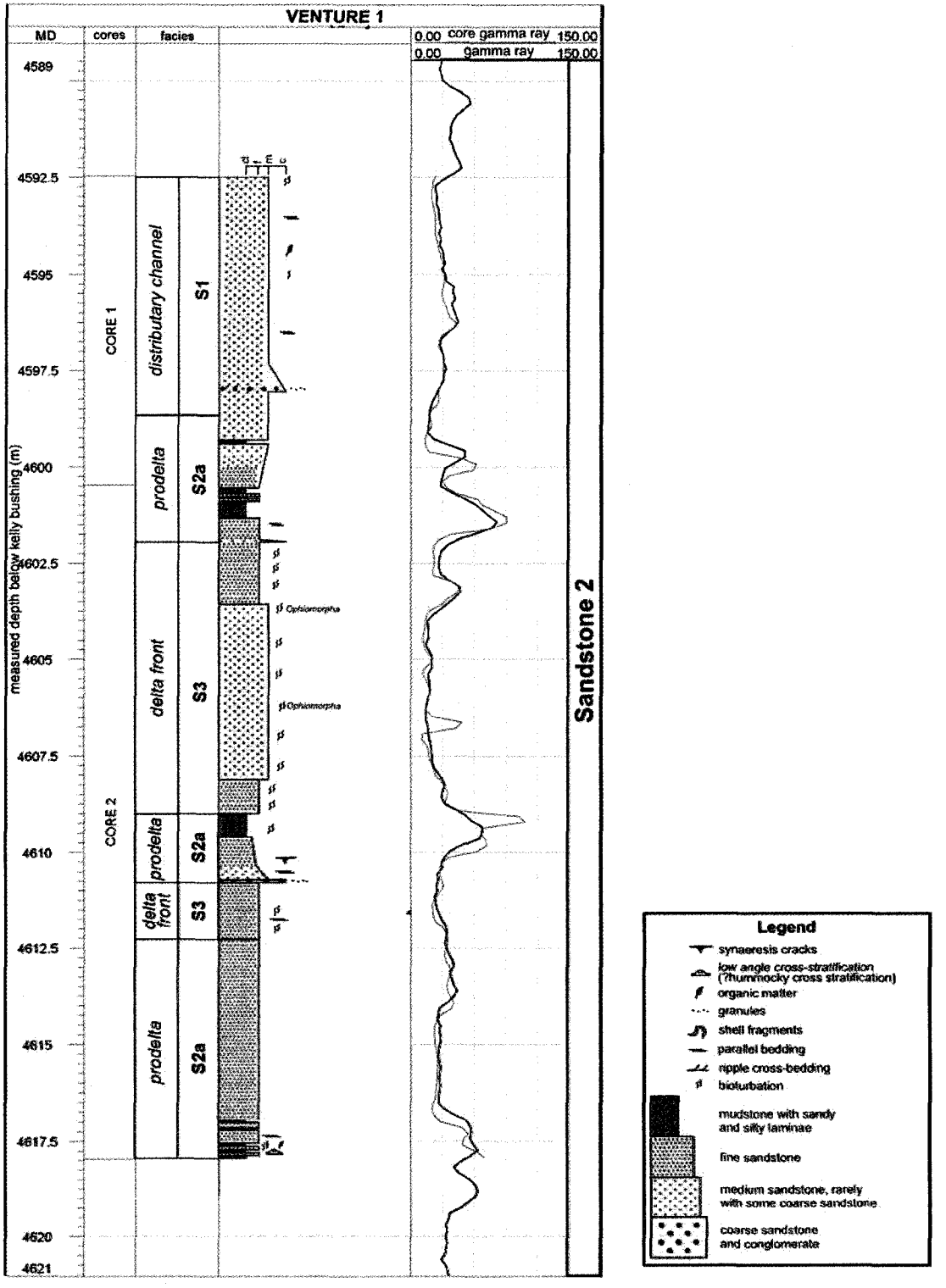

Figure 2.14: Lithostratigraphic plot for Venture 1 showing stratigraphic level, facies interpretation and gamma logs. Cored intervals were depth corrected to match wireline logs by comparing the core spectral gamma log (grey) to the wireline gamma log (black) and moving the core depths approximately 2.0 m down).

2.5.2 Venture 3

The base of the core at 4896.4 m is principally bioturbated mudstones alternating with beds of parallel laminated, fine-grained sandstone, interpreted as facies S2b. The mudstone bed thicknesses range from 5 cm to 2 m and are moderately to highly bioturbated. Shell fragments are common at the base of the beds but decrease in abundance upwards. The sandstone beds range from < 10 to 75 cm thick and contain rare phytodetritus. The lower contacts of the sandstone beds are sharp, the upper contacts bioturbated. At 4886.1 m, facies S3 is overlain by a thick, 3.8 m section of facies S2c. It is moderately bioturbated with rare silty laminae and shell fragments. At 4876.72 m the section becomes slightly coarser, passing into facies S2a. The mudstone beds in this interval are ~10 cm thick with parallel silty sandstone laminae and lack bioturbation. The sandstone beds are medium grained and ripple cross laminated, with sharp upper and lower contacts. Bed thickness increases upwards from 30 to 70 cm. At 4875 m, the sandstone beds thicken and coarsen gradually as the section enters facies S2c, coarse grained, trough cross laminated sandstone beds. Facies C1 sharply overlies facies S2c at 4873.5 m. It is a very poorly sorted bed of pebbles, granules and sandstone that fines upwards into moderately bioturbated sandstone. This bed is overlain by another bed of facies C1. The top of the core from 4872.1 to 4870.5 m consists of facies L1, a coarse-grained, shelly bioclastic sandstone unit with parallel laminae of silty sandstone (Figures 2.15 to 2.17).

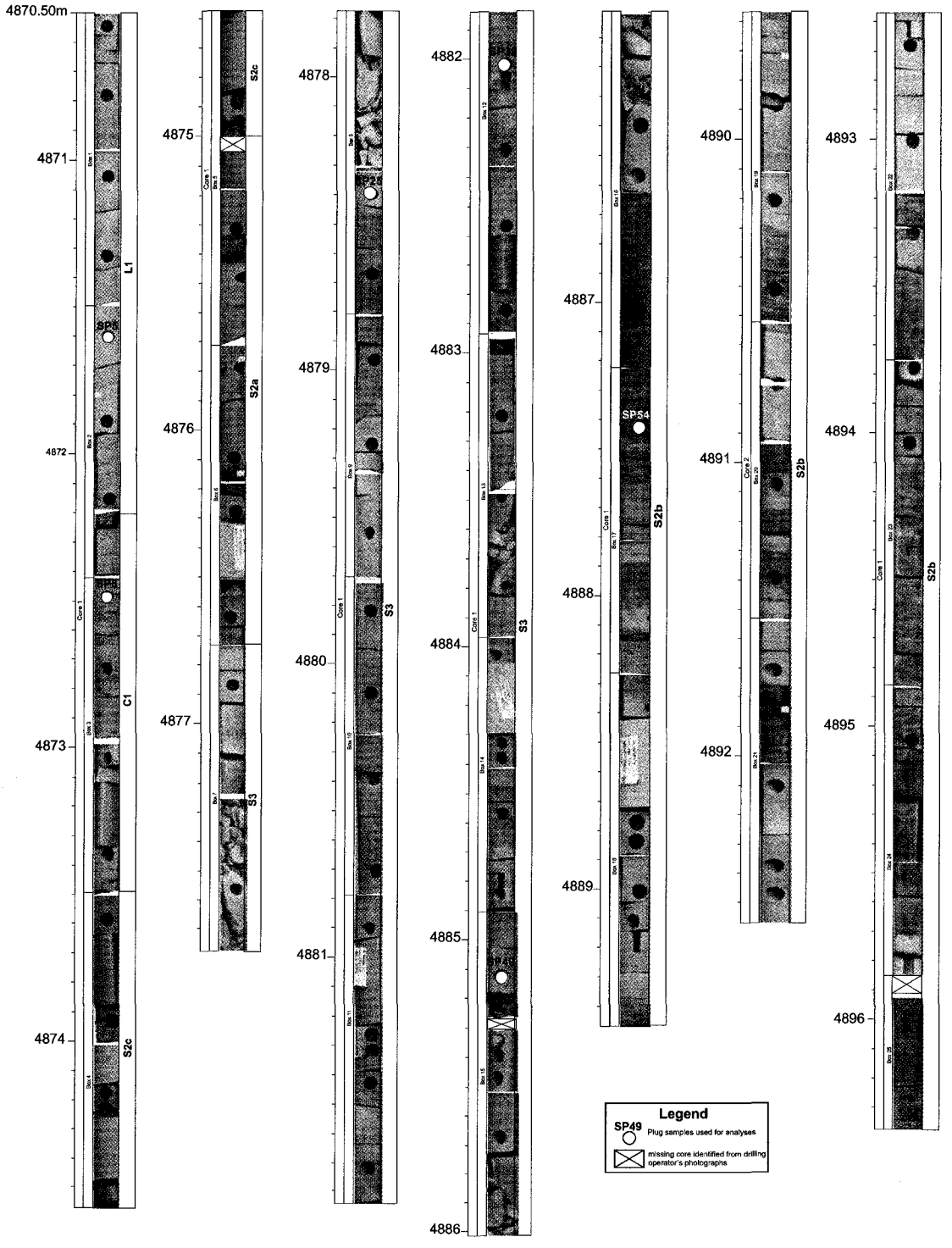

Figure 2.15: Core photos and facies interpretation for core 1, Venture 3 (uncorrected measured depth in metres below kelly bushing).

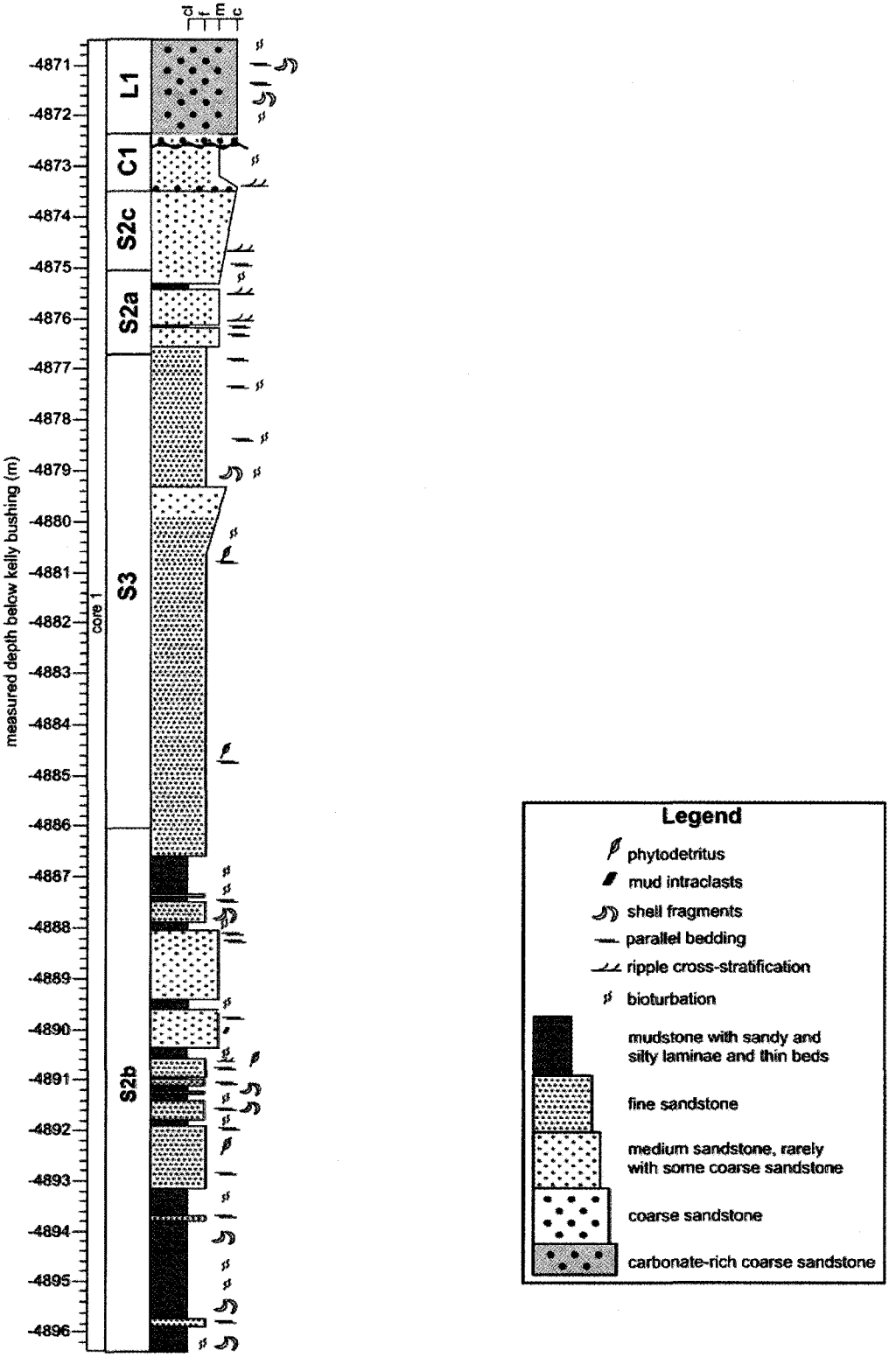

Figure 2.16: Stratigraphic column and lithofacies interpretation for core 1, Venture 3 (uncorrected measured depth below kelly bushing).

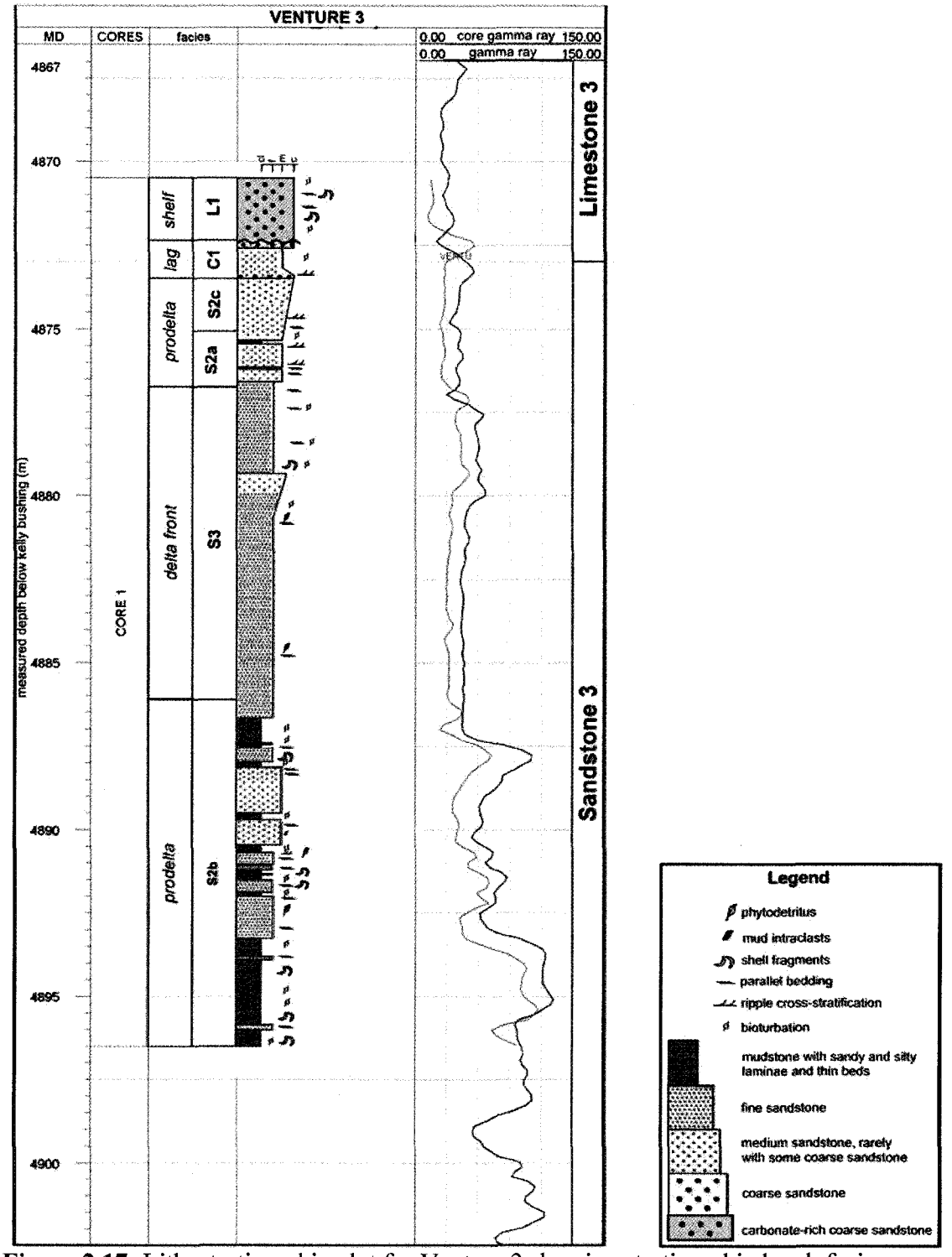

Figure 2.17: Lithostratigraphic plot for Venture 3 showing stratigraphic level, facies interpretation and gamma logs. Depth correction of cores was not necessary as the core spectral gamma log (grey) matched the wireline gamma log (black) fairly well.

Interpretation

On the basis of the gamma log, the cores represent a generally cleaning-upward, (coarsening-upward) succession, capped by a carbonate-rich sandstone. The interbedded mudstones and sandstone (subfacies S2b) in the lower part of the core are interpreted as representing a prodelta environment, as indicated by the high degree of bioturbation within the mudstones. The sandstone interbeds signify storm events of sand influx by the presence of reworked shelly material at the base of the beds. The general lack of plant material in the sandstone beds indicates this section was distal to the distributary channel. The section then passes into the predominantly sandy facies S3. This transition is interpreted as representing a shallowing due to river mouth progradation, on the basis of the increasing proportion of sandstones to shale and the slight decrease in the degree of bioturbation.

The section passes up gradually into another succession of interbedded mudstones and sandstone (facies S2a and S2c), representing prodeltaic muds and distal hyperpycnal flood deposits respectively. The lack of bioturbation of the mudstones and sandstones indicates either a salinity-stressed environment or rapid deposition. The gradual coarsening of the sandstone and the presence of trough cross laminae suggests there was significant shallowing of the system. The overlying poorly sorted pebble conglomerate is interpreted as representing a trangressive lag developed on top of an erosion surface, forming by reworking after abandonment of the delta distributary. The overlying poorly sorted bioclast-rich sandstone (facies L1) indicates a significant amount of reworking of biogenic carbonate material in shallow water on the shelf, remote from the delta and the siliclastic sediment source.

2.5.3 Venture 4

The base of core 1, samples facies S3 (5396.34 to 5381.85 m). From 5390.5 to 5389.43 m these sandstones are punctuated locally by coarse-grained, < 5 cm thick, parallel laminated beds. Above this, the succession abruptly coarsens upwards at 5381m to facies C1, a granule conglomerate with trough cross laminae and beds.

At 5380.2 m, facies C1 is sharply overlain by a succession of facies S2a, interbedded mudstones and sandstone. Mudstone bed thickness ranges from 10 to 80 cm. Sandstone beds are sharp-based, fine grained and laminated, ranging in thickness from 25 cm to 3 m. The very top of core 2 samples the bottom 10 cm of a sharp-based coarse sandstone (possibly the very bottom of facies C1).

There is approximately 24.7 m of uncored section between the top of core 2 and the base of core 1. The corresponding gamma log shows that this is an overall cleaning-upwards series with a sharp increase in values at 5356.75 m and a sharp decrease at 5356.75 m, possibly representing a sudden lithological change to shale in an otherwise cleaning-upwards sandstone.

Similar to core at Venture 1, the uppermost cored section from 5344.58 to 5341.1 m is made up of facies S1, poorly sorted, laminated fine to coarse sandstones. The beds are unbioturbated with mudstone intraclasts and plant detritus (Figure 2.18-2.20).

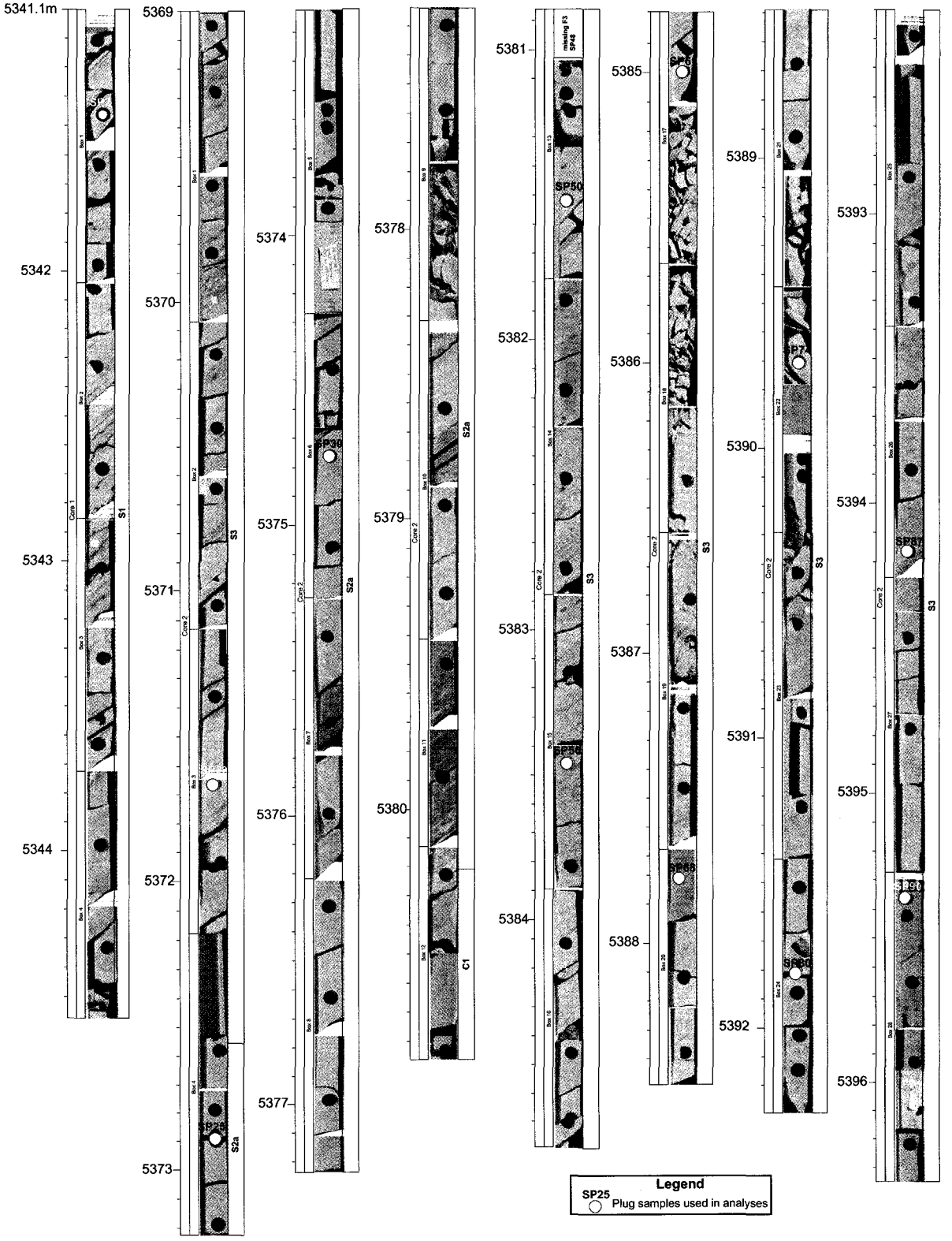

Figure 2.18: Core photos and facies interpretation for cores 1 and 2, Venture 4 (uncorrected measured depth in metres below kelly bushing).

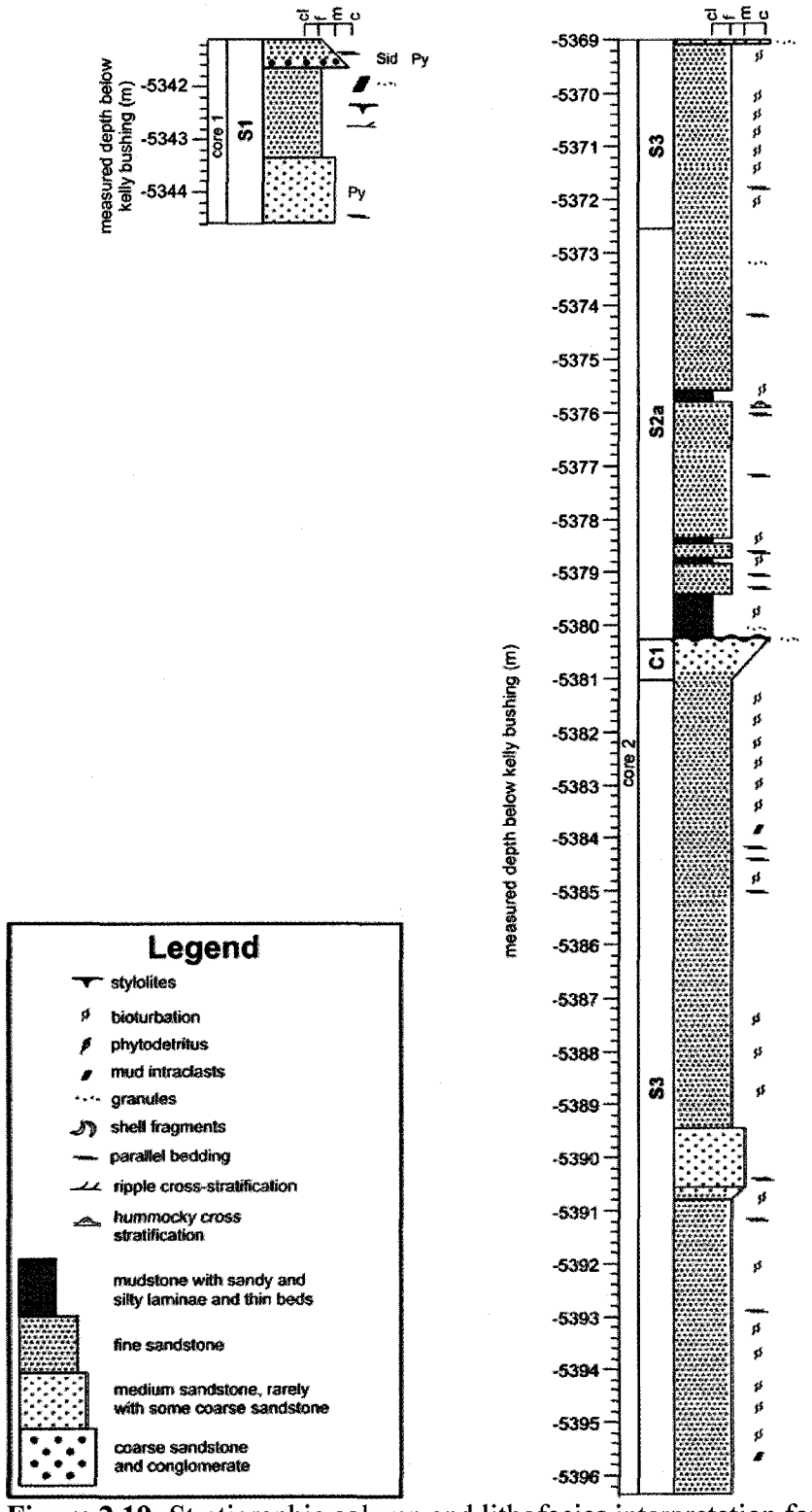

Figure 2.19: Stratigraphic column and lithofacies interpretation for cores 1 and 2, Venture 4 (uncorrected measured depth below kelly bushing).

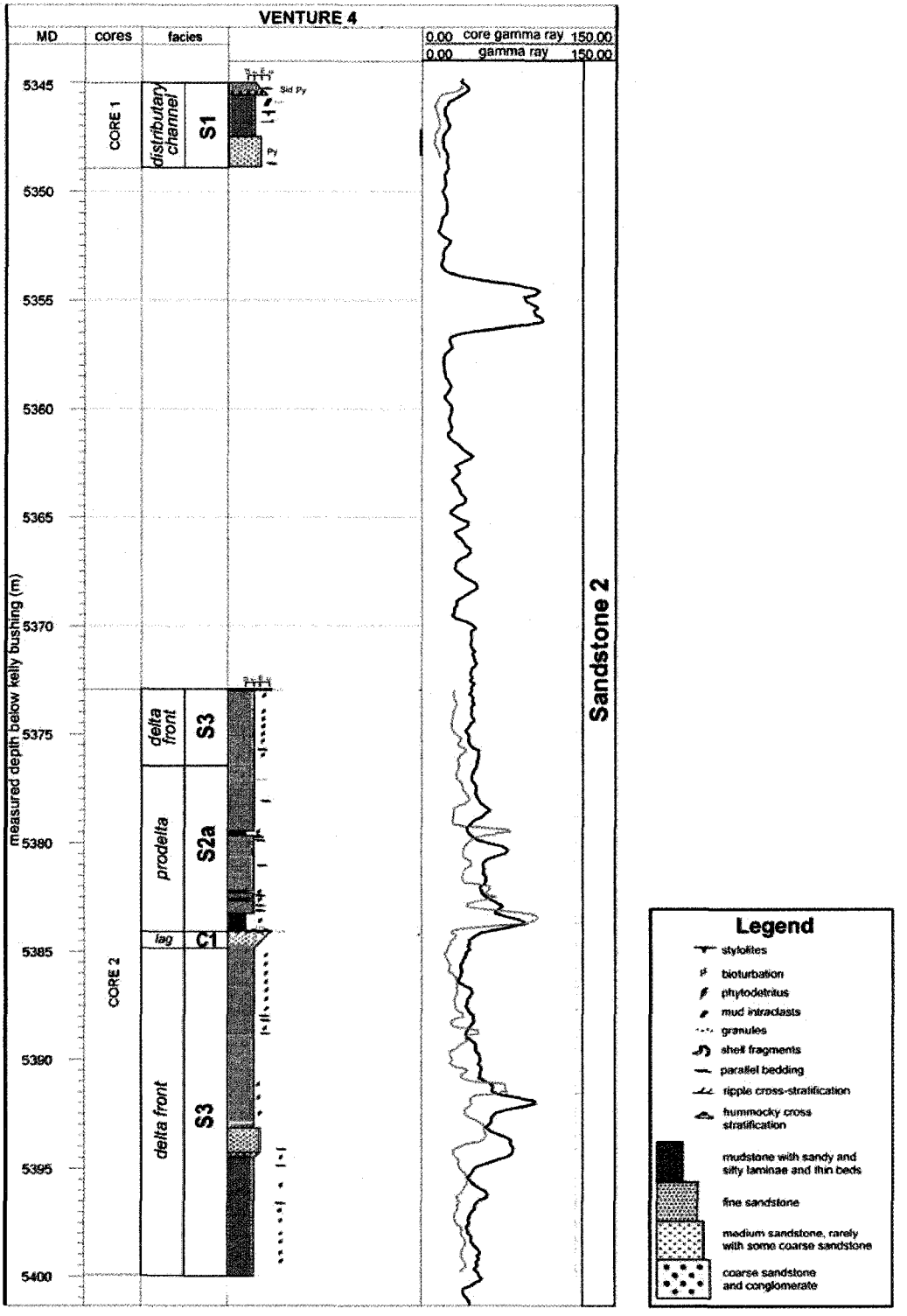

Figure 2.20: Lithostratigraphic plot for Venture 4 showing stratigraphic level, facies interpretation and gamma logs. Cored intervals were depth corrected to match wireline logs by comparing the core spectral gamma log (grey) to the wireline gamma log (black) and moving the core depths approximately 3.5 m down).

Interpretation:

The general cleaning-upward nature of the gamma logs in the lower part of the cored interval indicates a shallowing of the depositional system. Beginning in the delta front, a thick succession of bioturbated sandstones (facies S3) gradually coarsens upwards to 5365 m (wireline corrected depth) (Figure 2.20). The unit of Facies C1 capping this sandstone succession is interpreted as a trangressive lag on top of a probable erosion surface (in missing segment of core) based on the very coarse-grained lithology (with a coarsening-upwards character), lack of sorting, and the presence of trough cross beds.

The overlying interbedded mudstones and sandstone signify a deepening of the system to a prodelta depositional setting. The lack of bioturbation in the mudstone beds suggests a relatively stressed environment where these muds were deposited. The sharp, erosive based, fining-upward and sometimes massive nature of the sandstone interbeds indicates that these are distal hyperpycnal flood deposits. The overlying fine-grained, bioturbated sandstone (facies S3), indicates that the system is shallowing to a delta front depositional environment. The wireline logs imply a cleaning-upwards succession cumulating at 5356.5m (wireline corrected), probably representing shallowing to that point.

Similar to core at the upper part of Venture 1, the sandstone at the top of Venture 4 (core 1) is interpreted as being deposited in a distributary fluvial channel, possibly tidally influenced based on the lack of bioturbation, mudstone partings, the fining-upward nature of the bedsets, and the presence of mudstone intraclasts and plant detritus.

2.5.4 Thebaud C-74

Six cores were taken at Thebaud C-74. The base of the succession in core 6 at 3926.75 m consists of facies S2b, highly bioturbated mudstone beds between < 10 cm and 2.25 m thick. The mudstones are interbedded with massive to parallel laminated sandstones with thickness ranging from < 5 cm to 2.7 m. At 3924.98 m, it grades into facies S4, comprising repeating beds of sharp-based, coarse grained, granule-bearing sandstones that quickly fine upwards to parallel-laminated fine-grained sandstones near the top. The cycles range in thickness from 1.6 to 5 m. At 3911.3 m, facies S4 is overlain by an additional succession of facies S2b, similar in character to the succession seen at the base of the core. At 3908.73 m the section is overlain by weakly bioturbated, sand dominated facies S3 continuing to 3905.1m. There is 1.3 m of uncored section between the top of core 5 and the base of core 4 (Figures 2.21b, 2.21c, 2.22 and 2.23).

The lower part of core 4 is made up of facies S2c, coarsening-upward medium sandstone with minor discontinuous mudstone laminae. Facies S2c has a sharp and probably erosional upper contact with facies M2 at 3902.5m. The contact has erosive relief, is bioturbated and includes sideritized *Ophiomorpha, Teichichnus* and *Diplocraterion* burrows that pipe the overlying sediments into this interval. Overlying the contact is approximately 10 cm of facies M2, gradationally overlain by a thick succession of laminated mudstones (facies M1). Sandstone laminae and bed thicknesses range from 1-2 mm to 15 cm, occasionally showing minor bioturbation (horizontal burrows). Rare thick sandstone beds show intense bioturbation. Soft sediment deformation is present from 3893.1 to 3894.5 m in the upper part of core 4 in the form of slump blocks and folded sediments. Above the deformed interval, the sandstone

interbeds increase in frequency and thickness (facies S2a). Within the beds, the sandstones have fine siltstone laminae and sharp upper and lower contacts with the mudstones. The wavy shape of the beds is interpreted as ?hummocky cross stratification. The mudstone beds become highly bioturbated through core 3, from 3891.02 to 3890.52 m, returning to facies M1 at the top.

Core 2 samples facies S4, a section of repeating fining-upwards beds of medium to fine grained sandstones. The beds are massive at the base, with rare silty parallel laminae that increase in frequency upsection through each bed. The sandstones have very rare phytodetritus, coarse lithic grains and mudstone intraclasts chips. The beds range in thickness from 1 to 2.5 m. At 3877.65 m facies S4 passes into facies S2a, an unbioturbated interval of alternating beds of mudstone and lenticular sandstones, each 5 cm thick. The mudstones beds have parallel silty laminae and rare horizontal burrows. The sandstones have silty parallel laminae at the base, and wave ripple cross laminae near the top of the beds. Yellow (?pyrite) staining along laminae suggests that pyrite (favoured by phytodetritus) is present. At 3877.12 m the sandstone beds increase in thickness up to 50 cm. The top of core is comprised of well laminated and moderately bioturbated fine-grained sandstones.

The base of core 1 penetrates a poorly sorted sandstone with granules with abundant diagenetic siderite, interpreted as facies C1. At 3872.58 m the coarse-grained sandstone beds alternate with fine-grained sandstones, passing to a massive fine-grained sandstone bed at 3872.46 m. This is overlain by facies S2b, interbedded mudstones and laminated sandstones. The mudstones range in thickness from 5 cm to 2 m, and are highly bioturbated. The sandstone beds are sharp-based, laminated with siltstone and

range from < 5 cm to 75 cm thick. Upwards, sandstone beds become less common and the core is dominated by moderately bioturbated sandy mudstone. The succession gradually coarsens upwards, becoming sandier and less bioturbated, passing into facies S2c at 3863.91. At 3863.35 m it is overlain by poorly sorted sandy conglomerate of facies C1, with sideritized burrows and a 10 cm thick bed of lithic clasts at the upper contact. At 3862.88 m it is sharply overlain by a 2.5 m succession of facies S2b. Sandstone bed thicknesses in this interval vary from 2 to 15 cm, with the mudstones ranging in thickness from 12 to 75 cm. The lower 50 cm of the facies is highly bioturbated with reworked lithic clasts from the underlying beds of facies S2b. Above this, the mudstone beds contain rare shell fragments and become interbedded with sharp-based, parallel laminated sandstones. At 3860.38 m, the facies is abruptly overlain by 45 cm of facies M2, intensely bioturbated mudstone, with a large amount of diagenetic siderite cement. The remaining part of core 1 is laminated mudstone, with rare horizontal burrows in the silty laminae (Figures 2.21a, 2.22 and 2.23).

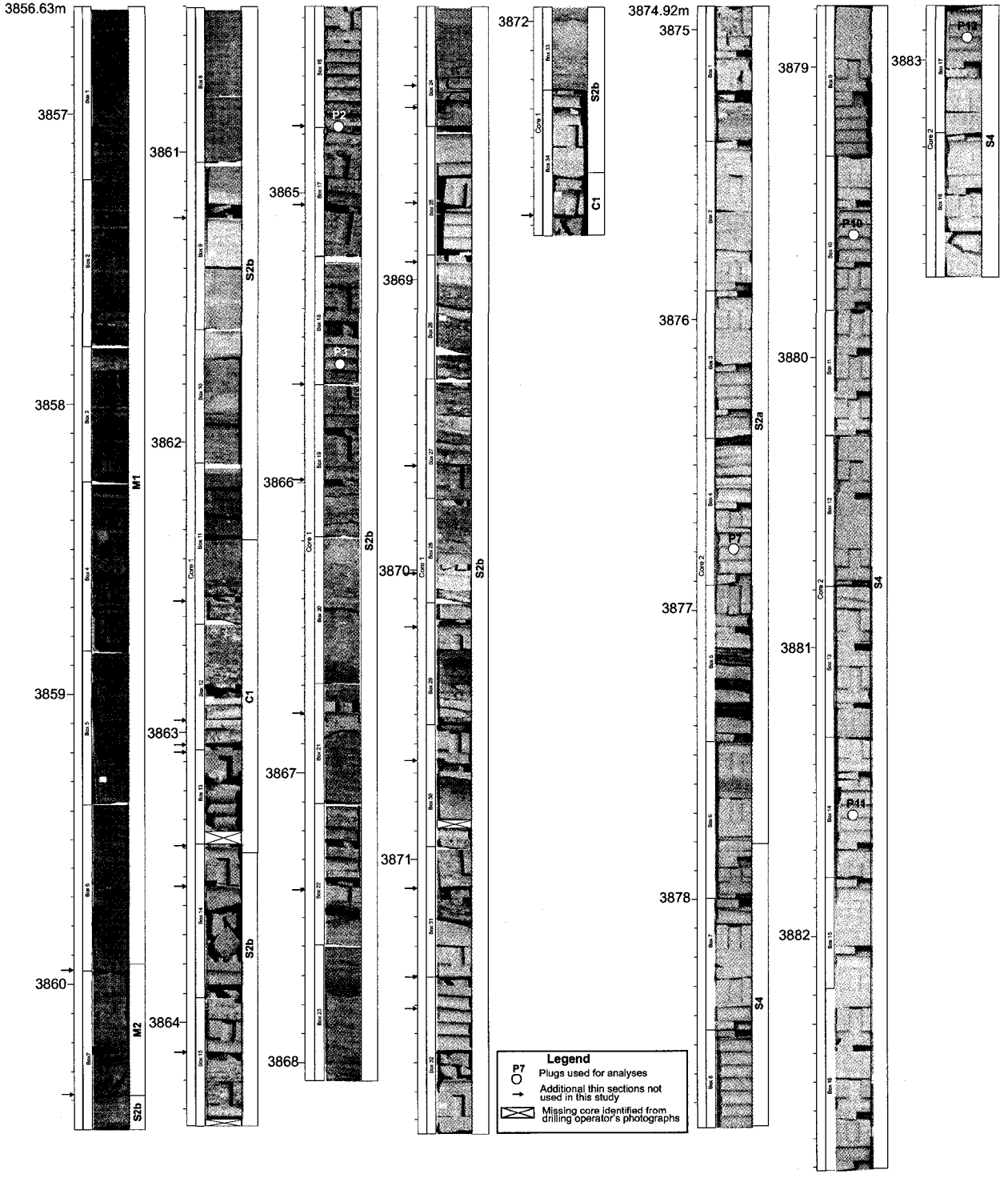

Figure 2.21a: Core photographs and facies interpretations for cores 1 and 2, Thebaud C-74 (uncorrected measured depth in metres below kelly bushing).

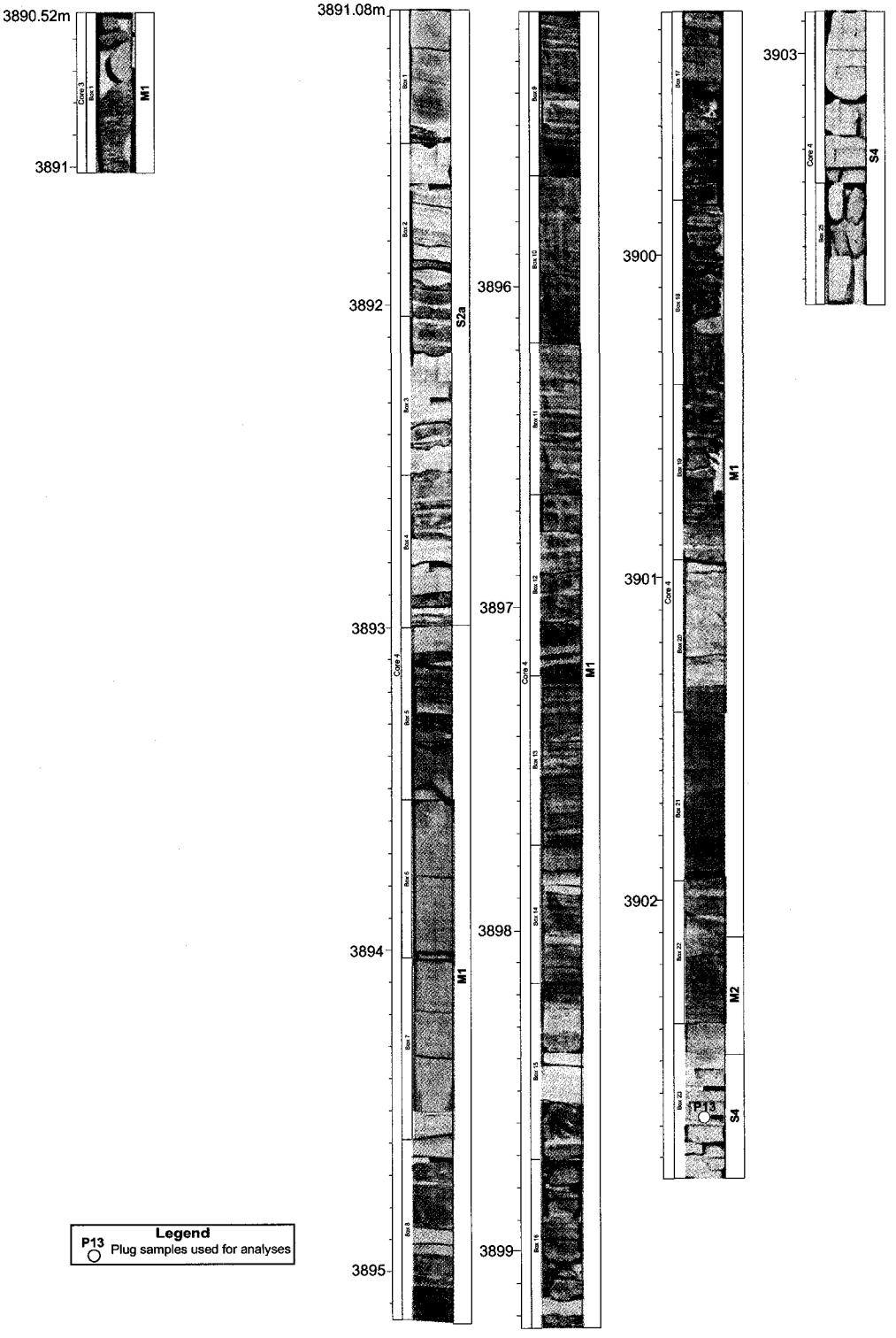

Figure 2.21b: Core photos and facies interpretation for cores 3 and 4, Thebaud C-74 (uncorrected measured depth in metres below kelly bushing).

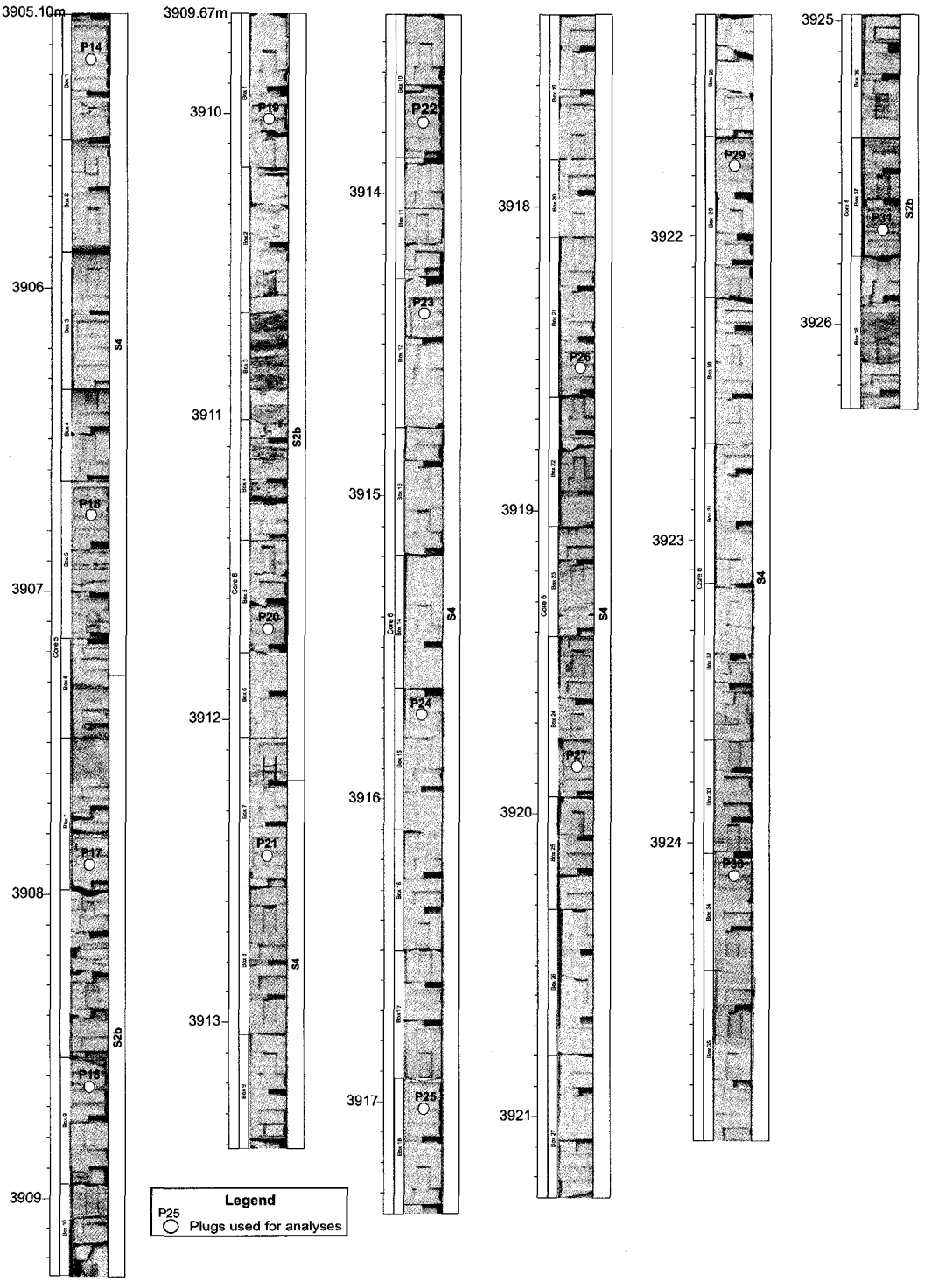

Figure 2.21c: Core photos and facies interpretation for cores 5 and 6, Thebaud C-74 (uncorrected measured depth in metres below kelly bushing).

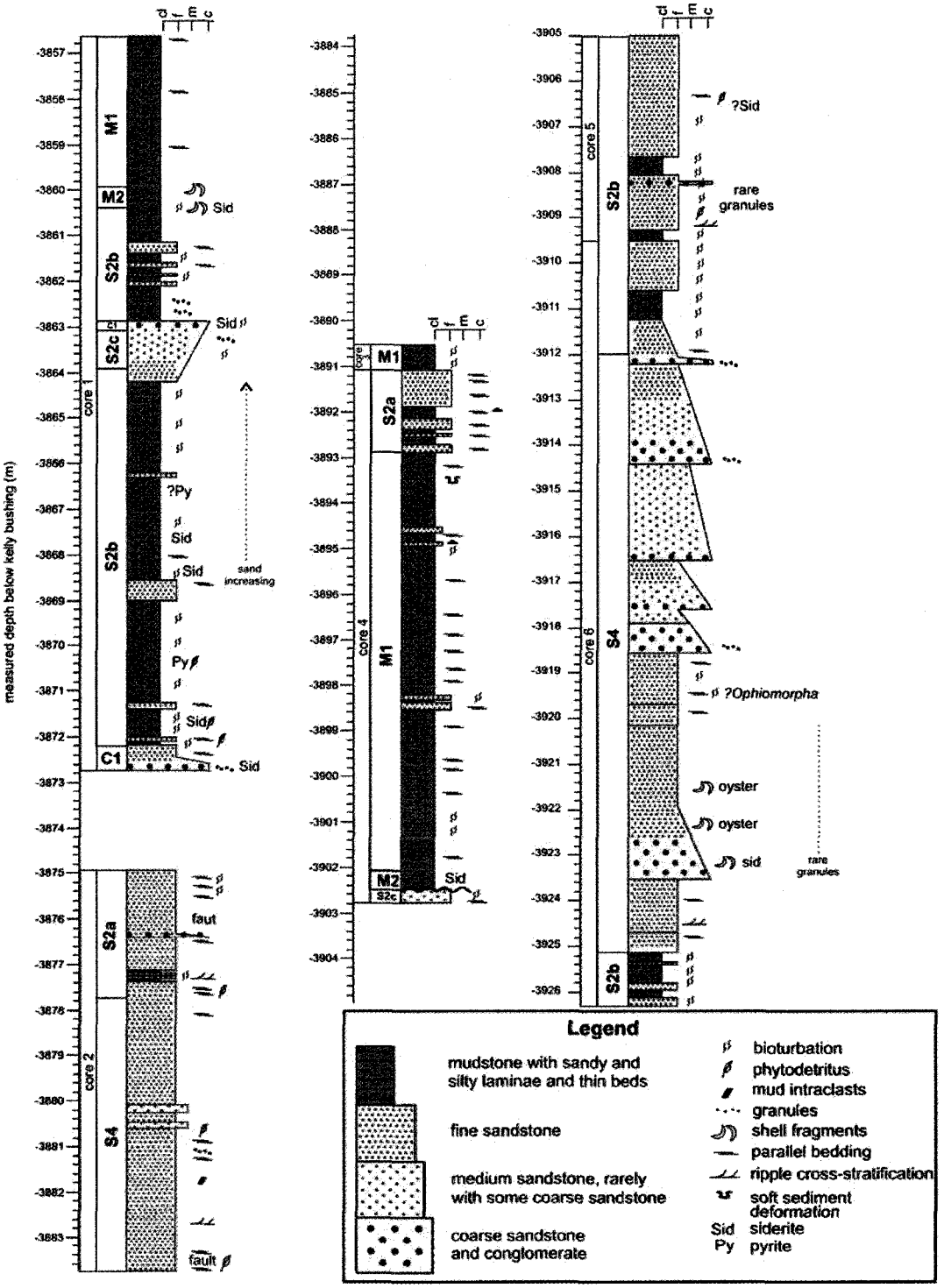

Figure 2.22: Stratigraphic column and lithofacies interpretation for cores 1 to 6, Thebaud C-74 (uncorrected measured depth below kelly bushing).

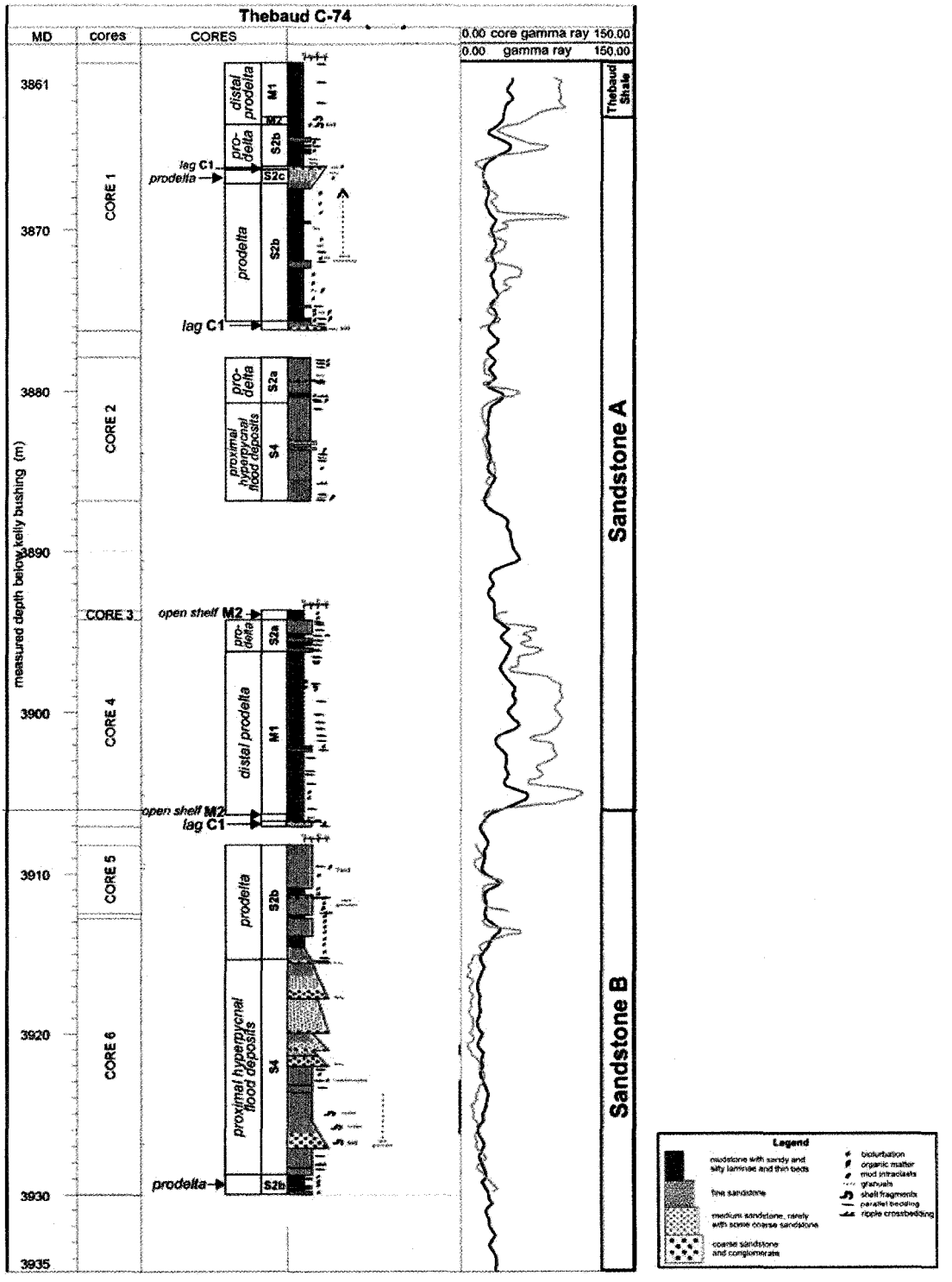

Figure 2.23: Lithostratigraphic plot for Thebaud C-74 showing stratigraphic level, facies interpretation and gamma logs. Cored intervals were depth corrected to match wireline logs by comparing the core spectral gamma log (grey) to the wireline gamma log (black) and moving the core depths approximately 3.25 m down).

Interpretation:

At the base of the succession, facies S2b is interpreted as being deposited in a predominantly prodelta environment based on the high degree of bioturbation in the mudstone beds. The sandstone interbeds represent distal hyperpycnal flood deposits, events that transported sand into the prodelta, resulting in sharp-based, fining-upward character seen in the beds.

Each bed in the overlying facies S4 represents more proximal hyperpycnal flood deposits, where sand from the mouth bar transported out to the delta front where there was adequate space to accommodate these deposits. This explains the sharp contacts, and why the lower parts of the beds are very poorly sorted, coarse grained, contain granules, and generally structureless. The beds fine upwards and silty laminae increase in frequency as a result of the depositional event loosing energy and finer material settled out in this quieter environment. Mud drapes, *Ophiomorpha* burrows and ?wave ripples near the upper contacts of the beds mark the last energy dissipation. The presence of whole intact oyster shells within several of the beds indicates that the source of the sand was coastal rather than fluvial. The succession of facies S2b overlying facies S4 signifies a deepening to a predominantly prodelta environment, again with periodic events of sand deposition.

The coarsening-upward sandstone at the base of core 4 and the lack of mudstone indicates the system was shallowing. The sharp, erosive nature of the contact between sandstones of facies C1 and siderite-cemented mudstones of facies M2 suggests that this contact is just below the maximum flooding surface, with Facies C1 forming by reworking after the abandonment of a delta distributary and facies M2 representing open

shelf deposition during the transgression. This contact marks the transition into the above facies M1 representing a distal prodelta environment through cores 3 and 4. The increase in frequency and thickness of sandstone beds (facies S2a) at the top of core 4 represents an increase in frequency of sand deposition events.

The gamma log suggests that the 6.77 m of uncored section between core 3 and core 2 units of cleaning-upward sandstone. The sudden increase in gamma values at 3890.12 m represents a sharp change in lithology from a sandstone to a mudstone unit, with the basal contact possibly representing a flooding surface. The section also gradually cleans upwards to the sandstones seen at the base of core 2 (Figures 2.21a, 2.22 and 2.23).

The overlying succession of facies S4 is again interpreted as multiple hyperpycnal events depositing sand, based on their sharp, coarse grained bases and fining-upward character. The gradational passage into facies S2a suggests a deepening of the system to a prodelta depositional environment. The sandstone interbeds are sharp-based and absent of bioturbation indicating they are most likely storm deposits. The increase in bioturbation at the top of the succession is a result of a progradation of the delta and subsequent lobe-switching.

Conglomerate (facies C1) at the base of core 1 is interpreted as the upper part of a transgressive lag. The alternation between coarse and fine-grained sandstone laminae just above the conglomerate reflects fluctuation in sediment supply and process during the abandonment of the delta lobe. The overlying succession of facies S2b suggests depositional in a prodelta environment with repeated events of sandy storm deposits. Upwards, the system seems to shallow, as sandstone event beds become less common

and bioturbated mudstone becomes sandier upwards. Coarsening-upwards sandstones (facies S2c) are capped by another trangressive lag (facies C1) representing the time of shallowest water before the transgression. Above the sharp contact with the overlying mudstone (facies S2b) is the maximum flooding surface. Lithic clasts from the underlying bed were bioturbated into the mudstone beds as the system deepened back into a prodelta environment. Further deepening of the system is represented by predominantly unbioturbated, weakly laminated mudstones of facies M1, interpreted as being deposited in a distal prodelta environment.

CHAPTER 3: PETROGRAPHY AND CHEMICAL MINERALOGY

3.1 Introduction

The polarizing microscope and electron microprobe were used to investigate chemical variations within the diagenetic minerals of interest, mainly clay and carbonate minerals. The small-scale, and often intergrown nature of the clay minerals made them particularly difficult to discriminate using a petrographic microscope, therefore back-scattered electron images produced by the microprobe, in addition to point analyses, were useful in investigating textural, chemical and age relationships between diagenetic phases. All depths in text and on figures are measured below Kelly bushing unless otherwise indicated.

3.2 Methods

Polished thin sections of representative plug samples were vacuum-impregnated with blue epoxy, cut and polished at Vancouver Petrographics. Diagenetic minerals were identified using a polarizing microscope. Electron microprobe work was conducted at the Dalhousie University Regional Electron Microprobe and Image Analysis Facility using a JEOL-8200 electron microprobe with five wavelength spectrometers and a Noran 133 eV energy dispersion detector. The beam was operated at 15 kV and 20 nA, using a beam diameter of about 1μm. The energy dispersive spectrometer (EDS) was used for quick recognition of minerals, and for identifying minerals that contain elements not being analyzed for, such as sulfur and barium, found in drilling mud contaminant containing barium sulphate (barite). Back-scattered electron images and X-ray maps were very useful in investigating textural relationships between diagenetic phases.

Thin sections provided by Exxon Mobil were used to look at intervals for which probe thin sections were not available. These thin sections are vacuum impregnated with blue epoxy to define the porosity. Thin sections were stained for carbonate and feldspars minerals. The staining method followed the techniques of Friedman (1959) for carbonate minerals and Houghton (1980), for feldspars minerals. Half of the slide was etched with hydrochloric acid and a mixture of alzerian red ($C_{14}H_7O_7SNa$) and potassium ferricyanide ($K_3(Fe(CN)_6)$) was applied. The combined stain colored calcite a pinkish red, ferroan calcite a bluish-purple, ankerite a turquoise-blue and left dolomite unstained. The other half of the slide was etched with hydrofluoric acid and sodium cobaltinitrite ($Na_3Co(NO_2)_6$) was applied, staining alkali feldspar yellow to distinguish it from the unstained plagioclase.

Limited scanning electron microscopy (SEM) was performed by Exxon Mobil (Core Laboratories, 1999d) to investigate the types of clays that were beyond the resolution of the polarizing microscope. These images have been somewhat useful in interpreting the paragenetic sequence.

3.3 Results

The diagenetic minerals identified in thin sections are: the clay minerals chlorite, illite and kaolinite; carbonate minerals including calcite, ferroan, manganoan, and magnesian calcite, ankerite, and siderite; and other diagenetic minerals including silica, pyrite and rutile (Appendices 3 to 7). The diagenetic cements present within samples from the Venture and Thebaud fields are presented in Table 1. Electron microprobe analyses were not conducted on sample SP30 of Venture 4, because the sample was

mounted on two slides during polishing and was too thick to fit into the sample holder used in the electron microprobe.

Table 3.1: Diagenetic cements and textures seen in thin section*

well	plug	measured depth (average, m)	true vertical depth (subsea)	clays		carbonates			silica	pyrite	diagenetic albite**	grain dissolution
				chlorite	kaolinite	Ankerite	ferroan Calcite	siderite				
Thebaud C-74	P2	3864.68	3825.59	x	-	-	x	-	x	-	-	x
Thebaud C-74	P3	3865.66	3826.59	x	-	-	x	-	x	x	-	x
Thebaud C-74	P7	3876.81	3837.68	x	x	-	x	-	-	x	Cal	x
Thebaud C-74	P10	3879.67	3840.59	x	x	-	x	-	-	x	-	-
Thebaud C-74	P11	3881.70	3842.62	x	x	-	x	-	x	-	-	x
Thebaud C-74	P12	3883.07	3844.01	x	x	-	x	-	x	-	Cal	x
Thebaud C-74	P13	3902.73	3863.78	x	x	-	x	x	x	-	Cal	x
Thebaud C-74	P14	3905.24	3866.28	x	x	-	-	-	x	-	-	x
Thebaud C-74	P16	3906.86	3867.58	x	x	x	-	-	x	x	-	x
Thebaud C-74	P17	3908.02	3869.07	x	x	-	x	x	x	-	-	x
Thebaud C-74	P18	3908.77	3869.82	x	x	-	x	x	x	-	-	x
Thebaud C-74	P19	3910.00	3871.04	x	-	-	x	-	x	-	-	x
Thebaud C-74	P20	3911.74	3872.73	x	-	-	-	-	x	-	-	x
Thebaud C-74	P21	3912.49	3873.49	x	x	-	-	-	-	-	-	-
Thebaud C-74	P22	3913.84	3874.82	x	x	-	-	-	-	-	-	-
Thebaud C-74	P23	3914.45	3875.45	x	x	-	x	-	-	-	-	x
Thebaud C-74	P24	3915.82	3876.84	x	x	-	-	-	x	-	-	-
Thebaud C-74	P25	3917.17	3878.23	x	x	-	-	-	-	-	-	x
Thebaud C-74	P26	3918.73	3879.47	x	x	-	-	-	x	x	-	-
Thebaud C-74	P27	3920.15	3881.19	x	x	-	-	-	x	x	-	-
Thebaud C-74	P29	3922.09	3883.11	x	x	-	x	-	x	-	Cal	x
Thebaud C-74	P30	3924.59	3885.61	x	x	-	x	-	x	x	Cal	-
Thebaud C-74	P31	3926.24	3887.23	x	x	-	-	-	x	-	-	-
Venture 1	SP5	4591.63	4393.52	-	x	x	-	-	x	x	Ank	x
Venture 1	SP28	4598.47	4398.98	-	x	x	-	-	-	x	-	-
Venture 1	SP35	4601.05	4401.09	x	-	x	-	-	x	-	Ank	x
Venture 1	SP51	4606.47	4405.30	x	-	-	x	x	x	-	Kfs	x
Venture 1	SP76	4614.99	4412.13	x	-	-	x	-	x	-	-	x
Venture 3	SP5	4871.74	4615.67	-	-	-	x	-	-	-	-	x
Venture 3	SP8	4872.64	4616.59	-	-	-	x	x	-	x	-	-
Venture 3	SP25	4878.71	4622.61	x	-	-	-	-	-	x	-	x
Venture 3	SP38	4882.53	4626.47	x	-	x	-	-	-	-	-	x
Venture 3	SP49	4885.76	4629.69	x	-	x	-	-	x	-	-	x
Venture 3	SP54	4887.86	4631.80	-	-	-	-	-	-	-	-	-
Venture 4	SP2	5341.42	4401.16	x	-	x	x	x	x	x	-	x
Venture 4	SP22	5371.87	4426.11	-	x	-	x	-	-	x	-	x
Venture 4	SP25	5373.02	4427.02	x	-	-	x	-	x	x	-	-
Venture 4	SP30	5374.93	4428.64	x	-	-	-	-	x	x	-	-
Venture 4	SP50	5381.56	4434.09	x	-	x	-	-	x	-	-	x
Venture 4	SP56	5383.42	4435.65	x	-	-	x	-	x	x	-	x
Venture 4	SP61	5384.83	4436.80	x	-	-	-	-	x	x	-	-
Venture 4	SP68	5387.69	4439.15	-	-	-	x	-	-	x	-	-
Venture 4	SP74	5389.45	4440.61	x	-	x	-	-	-	x	-	x
Venture 4	SP80	5391.67	4442.44	x	-	x	-	-	-	x	Ank	x
Venture 4	SP87	5394.06	4444.39	x	-	x	-	-	-	x	-	x
Venture 4	SP90	5395.40	4445.52	x	-	-	-	-	-		Kfs	x

*x = present in thin section; - = absent

** Ank = albite in ankerite cement; Cal = albite in ferroan calcite cement; Kfs=albitization of detrital K-feldspar

3.3.1 Clay minerals

The fibrous and thin nature of clays (chlorite and illite in particular) make them difficult to analyze using the electron microprobe, and the majority of the analyses yielded total amounts below the acceptable limits for electron microprobe chemical analyses of such minerals. In order to compare between analyses with lower or higher than the acceptable totals, such analyses were recalculated. Analyses of dominantly chlorite were recalculated to a total of 85% and analyses of dominantly illite were recalculated to a total of 90%.

Chlorite analyses often contained small amounts of other elements, commonly Ti, Ca, Na, K, indicating that the chlorite is mixed with rutile, calcite, albite and most commonly, illite. The fine-grained chlorite can intergrow with other diagenetic clay minerals. In such cases, the microprobe beam, with a diameter 1-2 μm, can analyze minor amounts of the intergrown minerals. Such analyses have been named for their dominant component. For example, a chlorite analysis with minor potassium and titanium (<1%) would be named "chlorite" with the contaminant minerals placed in brackets "(illite, rutile)". If the analyses yielded quantities in sub-equal amounts, the analyses were given both mineral names, for example, chlorite+illite.

3.3.2 Chlorite: mode of occurrence in thin section

Back-scattered electron (BSE) images (Appendices 3 to 6) and electron microprobe analyses (Appendix 7) were used to recognize five groups of chlorite on the basis of morphology. The classification of the mode of occurrence of chlorite follows Ehrenberg (1993).

Group 1: Chlorite rims on grains (Figures 3.1 and 3.2)

Diagenetic chlorite rims on grains are composed of chlorite mixed with illite, rutile or calcite either in subequal amounts or as minor components (Figure 3.3). The rims, usually <10 μm thick, are made up of fibrous crystals of chlorite, usually oriented perpendicular to the grain surface. They tend to be thicker on embayed grain surfaces (Figure 3.1A) and absent where framework grains are in direct contact with each other. Chlorite rims preserve grain shapes after detrital grains, such as K-feldspar, that have become corroded or completely dissolved (white box, Figure 3.3C).

Some chlorite rims overlie detrital clay, which is present as dark coatings on grains or as matrix clay (Figures 3.1 and 3.2) in clean sandstones. The clay coatings are present at grain contacts between detrital grains and vary in thickness, usually most thick along embayed surfaces (Figure 3.1). The coating preserves the original framework grain shape after the development of diagenetic cements, such as quartz overgrowths or diagenetic chlorite rims (Figure 3.1A).

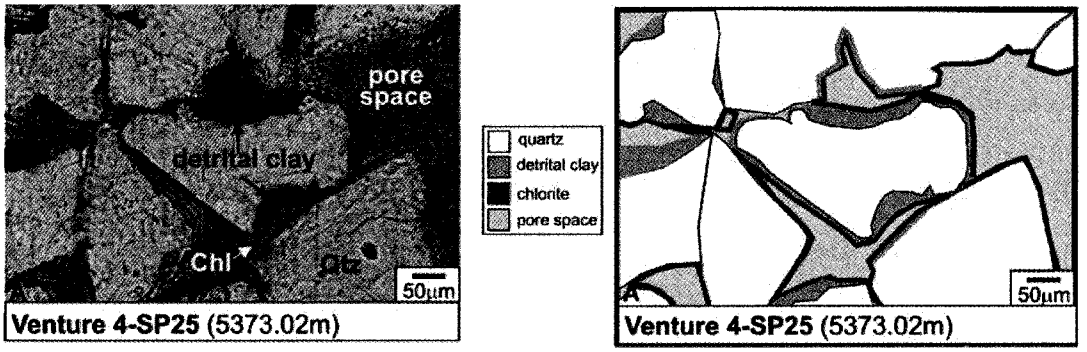

Figure 3.1: A) Microphotograph of dark brown detrital clay coatings on quartz grains (ppl). The coatings are rimmed by diagenetic chlorite; **B)** cartoon of microphotograph to illustrate the distribution of the clays.

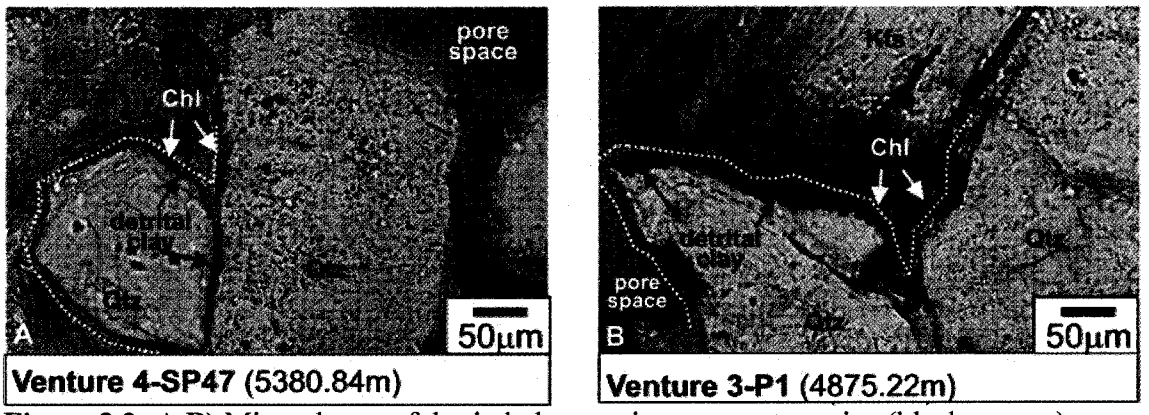

Figure 3.2: A,B) Microphotos of detrital clay coating on quartz grains (black arrows) with diagenetic chlorite rims (ppl). Note the lack of pore-filling cements, and therefore excellent porosity (>26% measured from plugs).

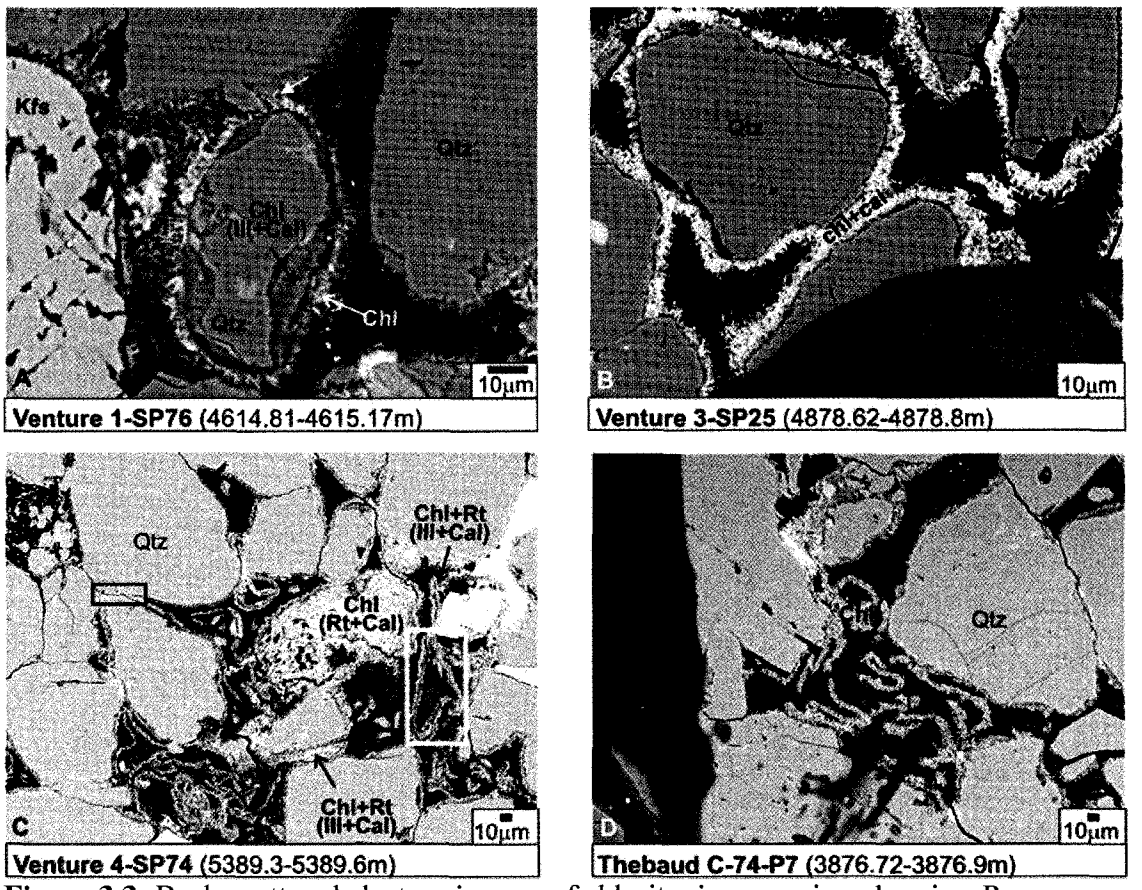

Figure 3.3: Back-scattered electron images of chlorite rims on mineral grains. Pore-filling cements are absent and high pore space is high in all images. **A)** Quartz grain with an inner rim of chlorite (illite+calcite), coated by an outer rim of chlorite; **B)** well-developed, continuous rims of chlorite+calcite rimming quartz grains. The crystals are oriented perpendicular to the grain surface; **C)** mixture of chlorite and rutile (with minor illite and calcite) in places preserving the original shapes of dissolved grains (white box). Chlorite rims are absent at contact surfaces between quartz grains (black box); **D)** chlorite coating on detrital grains and within pore space.

Group 2: Expanded mica grains (Figure 3.4)

Chloritized mica grains have an inflated or swollen appearance and may be split along cleavage planes (Figure 3.4D). Some grains are more expanded at the edges, giving a fan-like appearance (Figure 3.4C). The mica grains are occasionally lined with chlorite rims (Figure 3.4D).

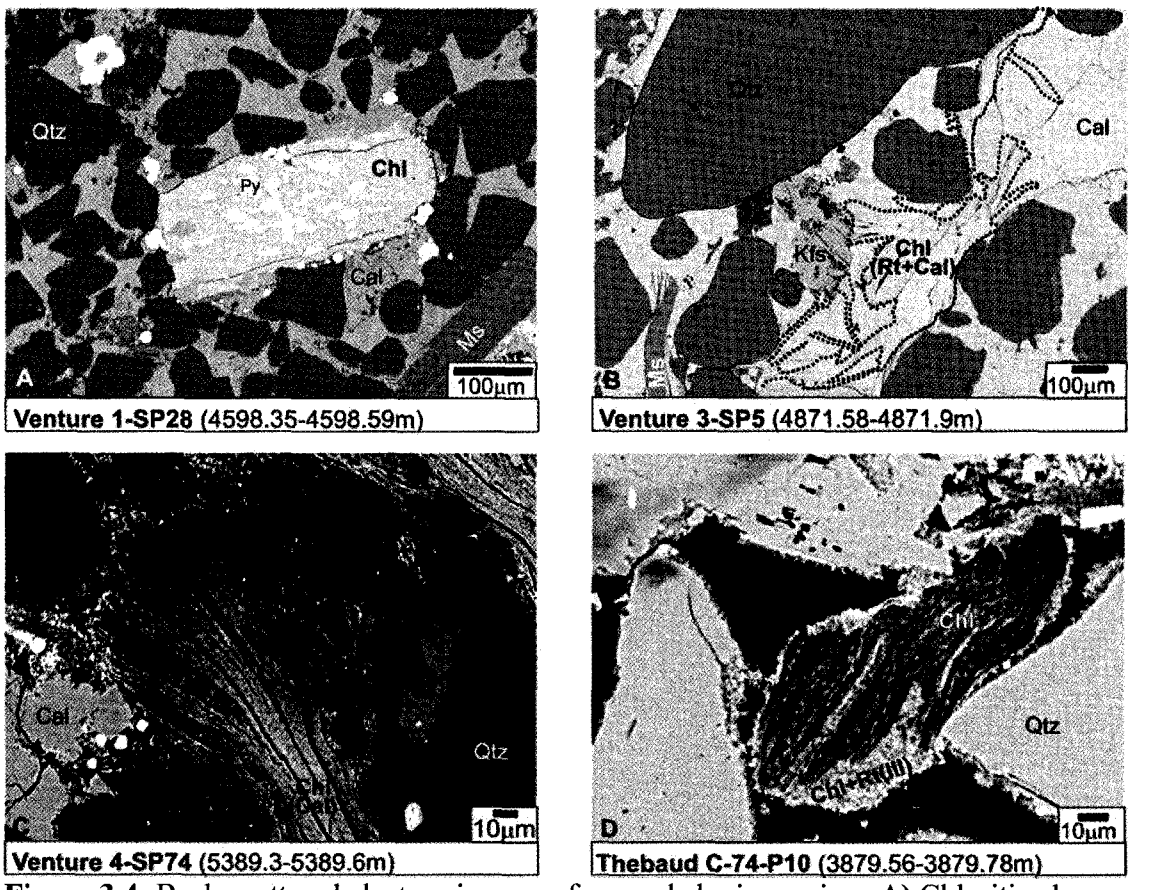

Figure 3.4: Back-scattered electron images of expanded mica grains. **A)** Chloritized mica grain (identified as biotite in thin section) with pyrite developed along cleavage planes. The grain is uniformly expanded throughout; **B)** chloritized mica grains (outlined by dashed line)set in calcite cement. The grains are expanded more at the edges; **C)** chloritized mica grain with extensive fanning along edges; **D)** chloritized mica irregularly expanded along cleavage planes, creating microporosity within the grain. The grain, as well as other framework grains, is rimmed by chlorite mixed with rutile.

Group 3: Pore-filling clays (Figure 3.5)

Pore-filling clays occur as random masses of chlorite, commonly mixed with illite, and in places with calcite or albite. The clays pervade available pore space between framework grains. Pore-filling clays are found in samples with well developed chlorite rims and those with quartz overgrowths.

In Venture 4, sample SP80 (5391.51-5391.83m), pore filling chlorite occurs as tiny spherules of <10 µm in diameter (Figure 3.5C). This is interpreted as either altered

volcanic ash or as fecal pellets altered to chlorite during diagenesis. The morphology of the aggregates, with larger, brighter spherules concentrated in layers could represent original layers in the ash. Enough ash in the sandstone would cause changes in geophysical well logs, however a thin bentonite ash bed may not be resolved in most logs. Ash has a contrasting density to the sandstone because it is comprised of minerals that are more dense than quartz which is the dominant mineral in these sandstones. This causes an increase in the bulk density log and the density log run over the core (Schlumberger, 1989). Ash layers also have elevated amounts of uranium and thorium causing a spike in the gamma ray logs (Schlumberger, 1989).. The corresponding well logs for Venture 4 show sharp increases in density values, sonic travel time and resistively values consistent with ash in the sandstone, however the gamma log is does not increase (Figure 3.6). However there are not thin sections in the interval just above sample SP80 to confirm this hypothesis.

Alternatively, this interval is sparsely bioturbated, and the shape of the pore as a whole in Figure 3.5C is similar to that of a horizontal cross-section through a burrow trace. In this case the chlorite would have formed from fecal matter filling the burrow trace (McIlroy et al., 2003; Needham et al., 2005).

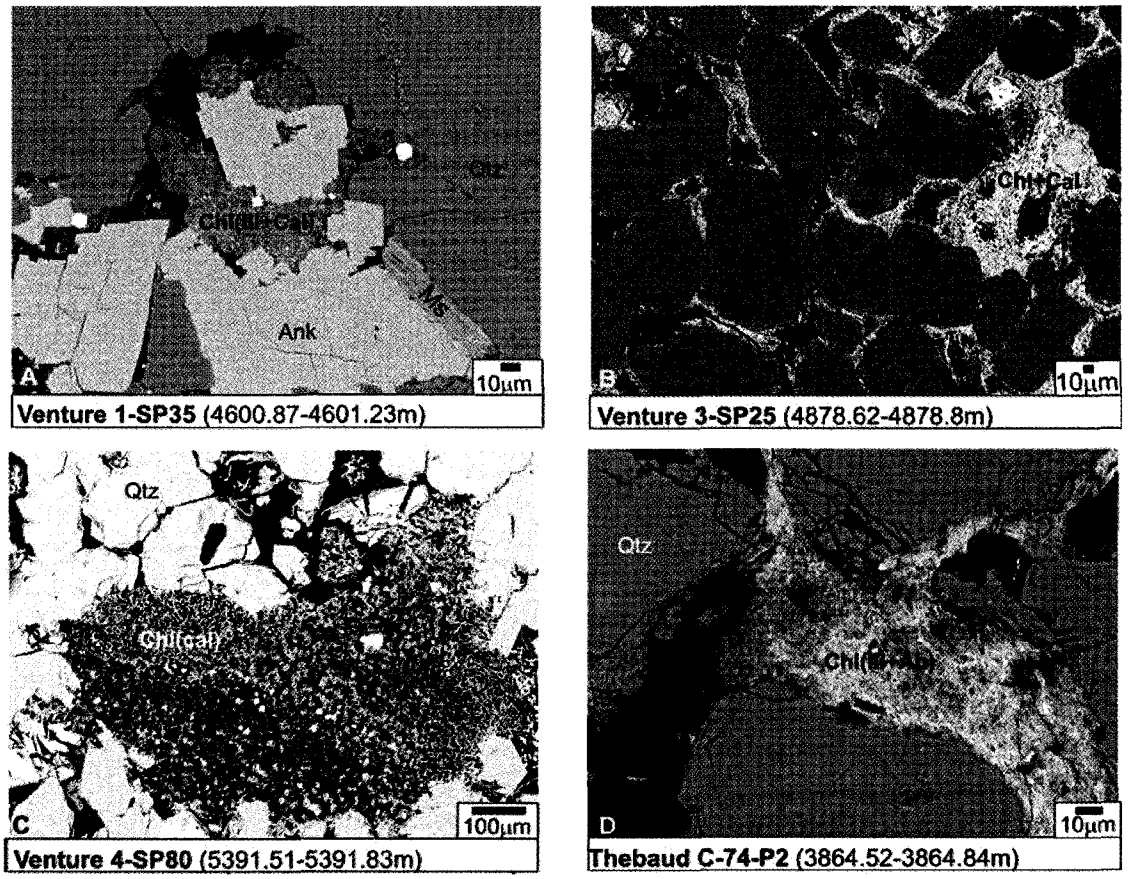

Figure 3.5: Back-scattered electron images of pore filling chlorite. **A)** Chlorite, with minor illite and calcite, occurs as pore filling cement with ankerite; **B)** chlorite and calcite rimming detrital grains and filling pore space; **C)** chlorite with trace calcite from an altered ash clast or fecal pellet, forming tiny spherules within an intraclast; **D)** chlorite, illite and trace albite growing into and filling the pore space between detrital quartz grains.

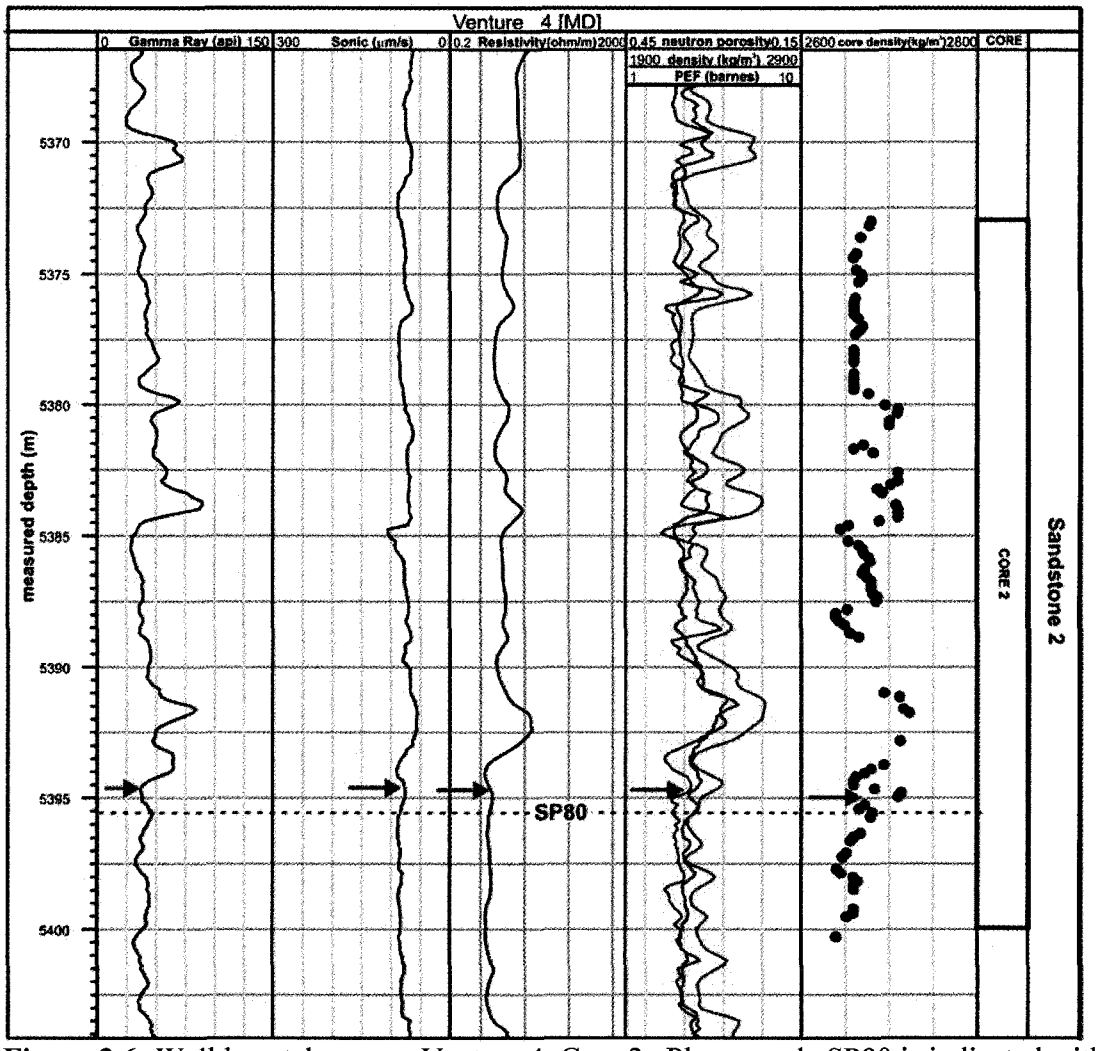

Figure 3.6: Well logs taken over Venture 4, Core 2. Plug sample SP80 is indicated with dashed line (sample was depth corrected by matching core gamma to wireline gamma ray log). Red arrows indicate an increase in sonic travel time, resistivity, core and log density just above SP80, however there is a drop in gamma ray values. This anomaly may have been caused by ash in the unsampled interval.

Group 4: Grain replacement (Figure 3.7)

Chlorite, generally mixed with illite, is seen replacing framework grains, in addition to mica, in many samples. The chlorite and illite crystals are randomly oriented and occasionally mixed with silt-sized quartz or feldspar grains (Figure 7C). Often the original grain shape is preserved and the pseudomorphed grain may be rimmed by chlorite (Figure 3.7B).

Mixtures of chlorite and calcite or chlorite and illite have partially replaced intergranular cements in igneous rock fragments (Figure 3.7D).

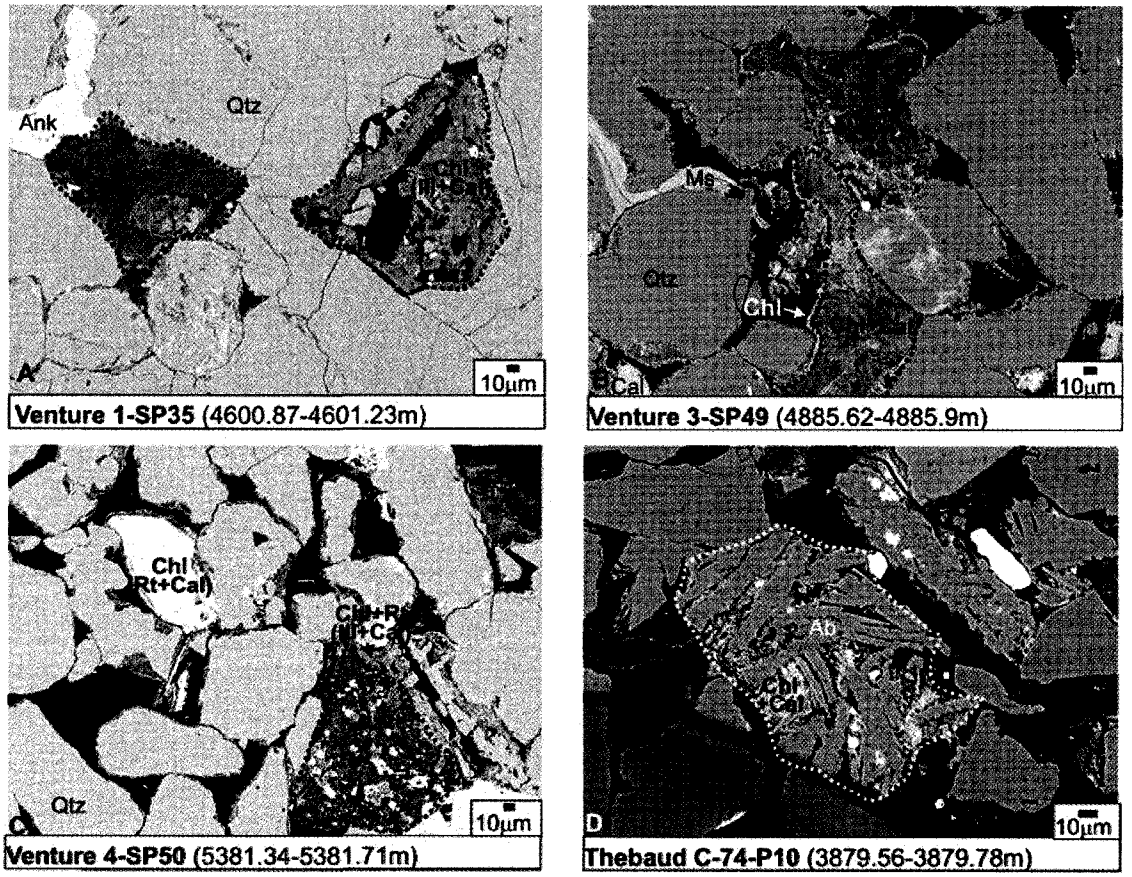

Figure 3.7: Back-scattered electron images of grain replacement by chlorite (outlined in images by dashed lines). **A)** Chlorite with minor illite and calcite has completely replaced a detrital grain; **B)** compacted detrital clay replaced by subequal amounts of chlorite and calcite and rimmed by chlorite; **C)** a pellet of mixed clays and silt sized quartz and pyrite grains; **D)** chlorite and calcite replacing parts of an apparent lithic clast composed mostly of albite laths.

Group 5: Coated grains (Figure 3.8)

Concentric layers of mixed clays, composed of chlorite with minor amounts of illite and calcite, surround framework grains such as quartz (Figure 3.8A), or lithic clasts, typically made up of albite laths (Figure 3.8D). Some coated grains have a hollow center where the framework grain has been dissolved after the layers of clay were accreted (Figure 3.8C). The coatings are up to 50 μm in total thickness. The individual layers of

the coating have different grey scales in back-scattered electron images (e.g., Figure 3.8B) and analyses of these visually different layers show that they vary in the ratio of illite to chlorite. Coated grains are seen exclusively in samples from Thebaud C-74, less commonly in the upper cores (3862.40 to 3906.86m measured depth), and more common in the coarser grained, poorly sorted intervals (3907.87 to 3917.17m measured depth) of facies S4. These beds were deposited during high-energy events, and the ooids most likely developed from mechanical accretion of the clay layers as detrital grains are being deposited. The coated grains provide evidence that the clay mineral precursor to chlorite can form very early.

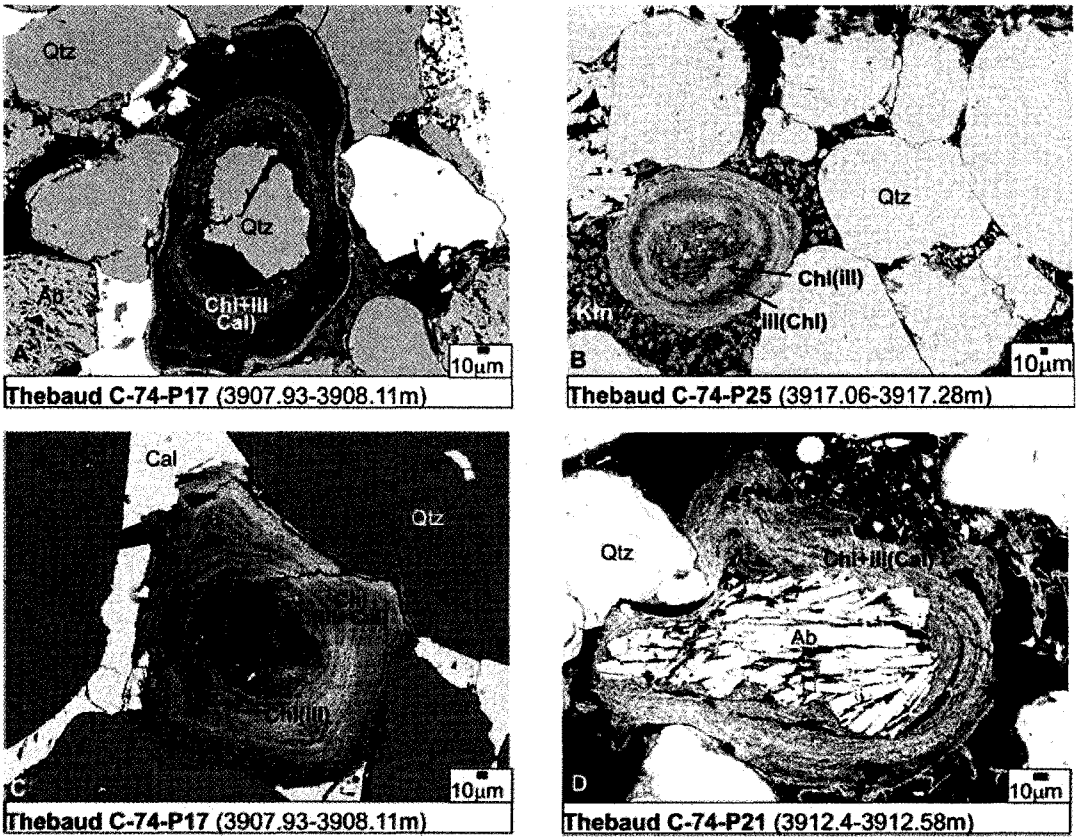

Figure 3.8: Back-scattered electron images of coated grains. **A)** Layers of chlorite and illite coating a corroded detrital quartz grain. Despite the different levels of brightness in the coating, analyses yielded similar compositions from core to edge of the coating; **B)** alternating concentric layers of dominantly chlorite with minor illite and of illite with traces of chlorite surrounding a core of clay with silt-sized detrital grains (probably a pellet or an intraclast); **C)** a dissolved grain with thick chlorite rims, with traces of illite and calcite; **D)** a lithic clast composed of parallel-oriented albite laths coated by a mixture of chlorite and illite. The coating is very thin where detrital quartz is in contact with the clast.

The FeO (total) and (K_2O) values from selected electron microprobe analyses of chlorite and illite (recalculated data, Appendix 7) were plotted separately for each of the five described petrographic groups (Figure 3.9) (Ehrenberg, 1993). FeO and K_2O values vary linearly for all groups, from the end members of iron-rich chlorite and illite, suggesting that these minerals, chlorite and illite, occur as discrete minerals, rather than being any kind of a mixed-layer mineral. In the latter case the analyses would have plotted as a cluster. Numerous mixed chlorite-illite areas examined in thin section and

back-scattered electron images also provide the impression that these minerals occur as discrete phases in widely varying proportions (e.g., Figure 3.9) rather than being mixed-layer minerals.

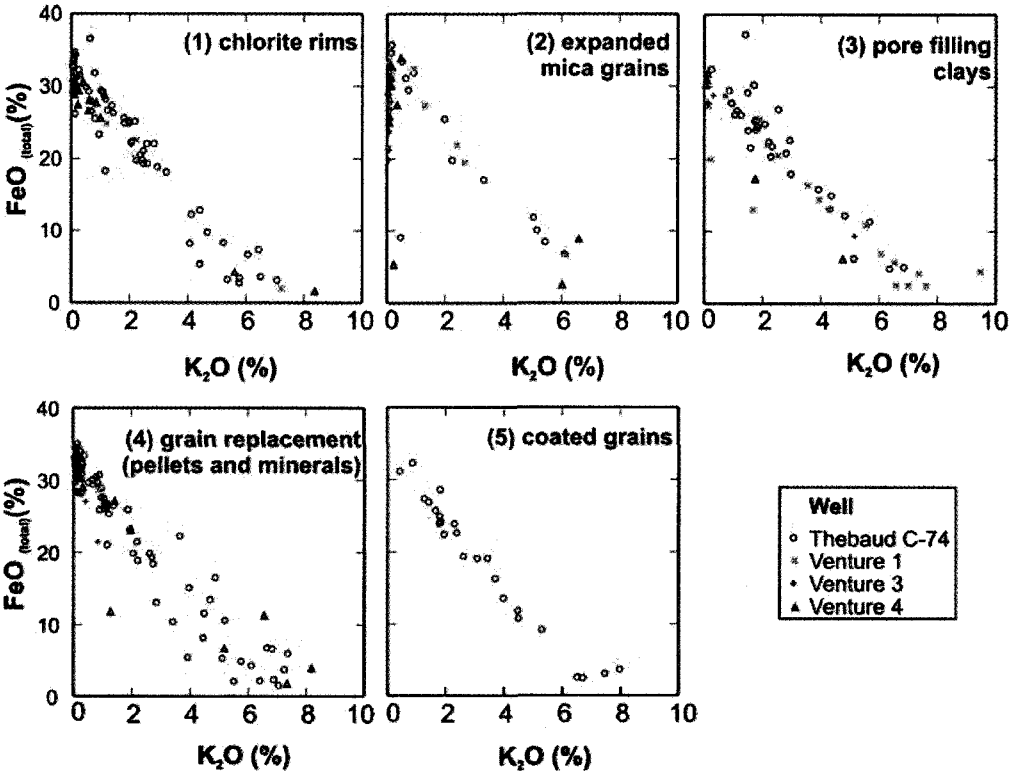

Figure 3.9: Selected electron microprobe analyses of chlorite and illite classified by mode of occurrence in thin section. The data plotted on this figure are those in Appendix 7.

Most chlorite rim analyses consist of >60% chlorite, but a few are illite with <50% chlorite. Most expanded mica grains are >95% chlorite, but a few analyses have 20-80% illite. Pore-filling clays consist of chlorite, illite or mixtures of chlorite and illite.

For the more pure chlorite analyses (49 in total) the atomic formulae were calculated on the basis of 28 oxygen ions (Appendix 8). Iron and magnesium were plotted against tetrahedral aluminum in order to investigate how the Fe/Mg ratio varies by well (Figure 3.10A) and petrographic chlorite morphology classification (Ehrenberg, 1993) (Figure 3.10B). There seem to be no trends with petrographic type, with the

exception of the expanded mica grains having higher magnesium values (lower Fe/Mg ratios) than analyses from other petrographic groups, suggesting that the chloritized mica is a more magnesium-rich mineral than the other forms chlorite.

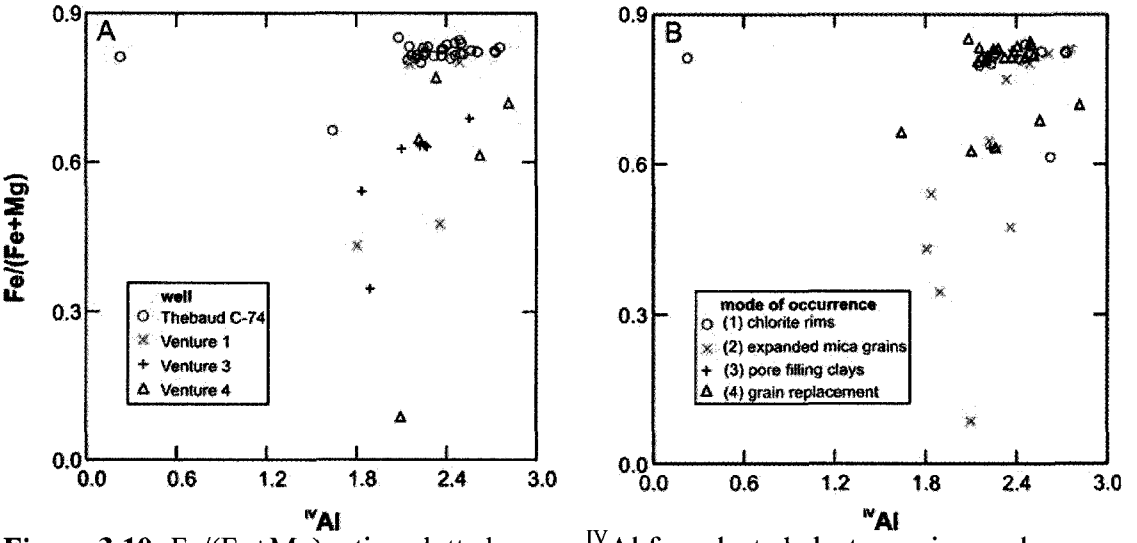

Figure 3.10: Fe/(Fe+Mg) ratios plotted verses ^{IV}Al for selected electron microprobe analysis of relatively pure chlorite, **A)** by well; **B)** by mode of occurrence of chlorite in thin section. The data plotted on this figure are those in Appendix 8.

The Fe/(Fe/Mg) ratios were also plotted at subsea true vertical depth (SSTVD) (Figure 3.11). For the Thebaud C-74 well (3830 to 3890m SSTVD) these ratios are constant, whereas in the Venture wells they vary widely with depth (4398 to 4632 m SSTVD). There does not seem to be any correlation between petrographic type and Fe/(Fe/Mg) ratios, implying the grain replacing chlorite does not have a different composition as determined by the original grain composition.

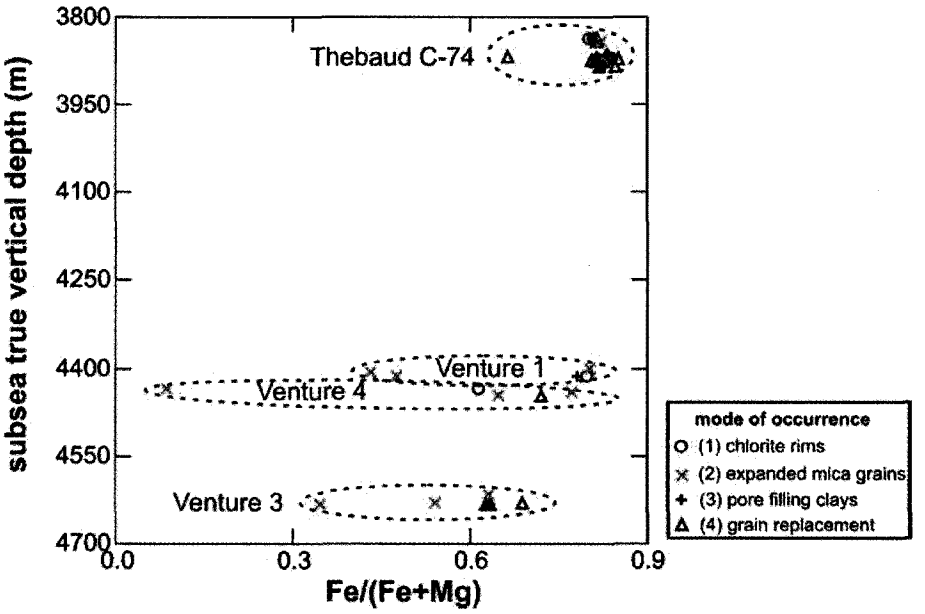

Figure 3.11: The Fe/(Fe/Mg) ratios of selected chlorite analyses plotted at true vertical depth (subsea) for all studied wells. The data plotted on this figure are those in Appendix 8)

3.3.3 Kaolinite

Kaolinite forms aggregates of loosely-packed booklets that fill available pore-space. It is most visible in samples that have well-developed pore space, such as samples P22 to P27 (measured porosity values >18%). In samples where porosity values are low due to compaction of framework grains during burial, kaolinite will develop in secondary pore space created by the dissolution of detrital grains. Kaolinite is used as a general term however it may actually be dickite because of its often blocky habit. The burial depths of the samples (3.8 to 4.7 km SSTVD) would also be sufficient to generate temperatures needed to convert kaolinite to dickite (>100 C).

Kaolinite cement predates silica cementation (Figures 3.12A,B) and postdates the formation of chlorite rims on detrital grains (Figure 3.12C,D). It is difficult to determine if it is earlier or later than carbonate cementation since the two cement types were rarely observed in direct contact in thin section, however since ferroan calcite is later than

quartz overgrowths in some samples (Figure 3.12A), kaolinite must have developed earlier than at least some of the ferroan calcite since it predates the silica cementation. Grain dissolution may have resulted in kaolinite and ferroan calcite, yielding additional silica available to form overgrowths on detrital quartz grains.

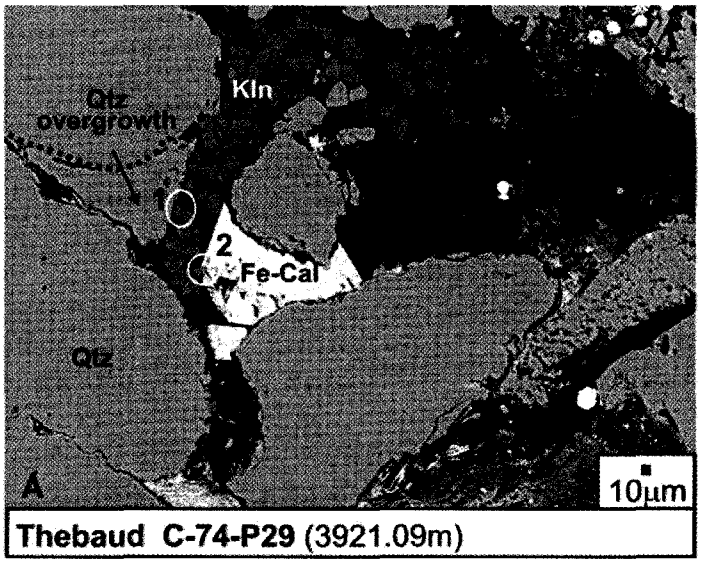

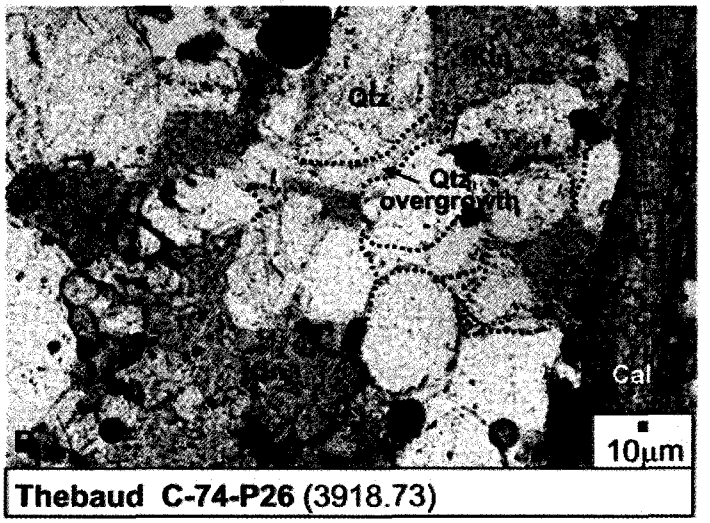

Figure 3.12: Kaolinite in back-scattered electron image (A,C) and microphotograph (ppl) (B,D). **A)** Detrital quartz grains with overgrowths (dashed black lines) and with pore filling kaolinite and ferroan calcite. The silica cement formed after the kaolinite as the overgrowths have grown into the kaolinite (1), cross-cutting the booklets. The ferroan calcite has also grown after the kaolinite (2); **B)** kaolinite cement partially filling available pore space between detrital grains. Silica overgrowths have locally cemented pore space.

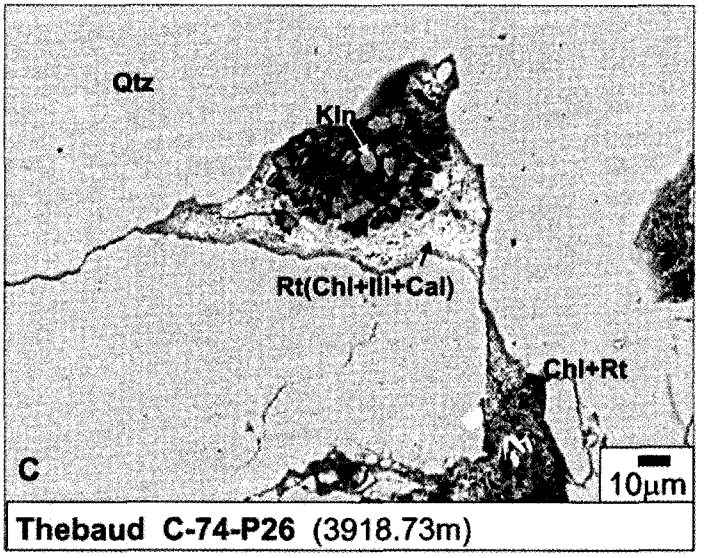

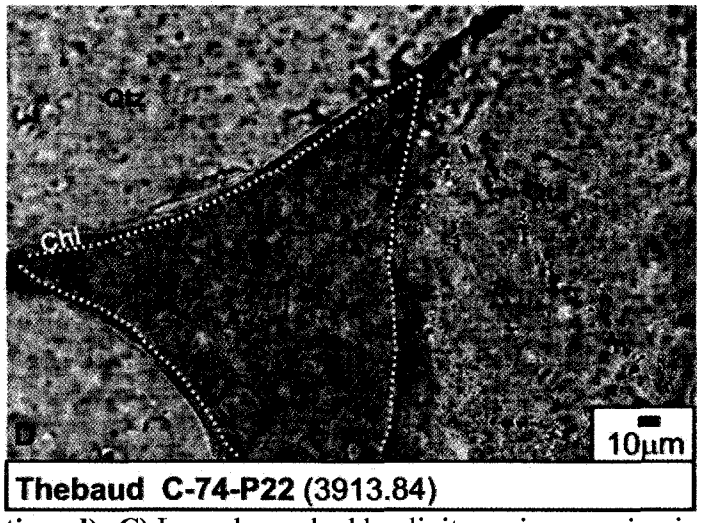

Figure 3.12 (continued): C) Loosely-packed kaolinite grains growing in pore space, after the formation of a pore rim mixture of rutile, chlorite and calcite; **D)** chlorite rims on detrital quartz grains, kaolinite cement fills the pore and formed after the chlorite rims or at least the precursor of the chlorite rims (dashed white line).

3.3.4 Carbonates

Some carbonate analyses had high CaO values as a result of not using a carbonate standard during calibration of the electron microprobe prior to analyses, since the majority of analyses were conducted on silicate minerals. Such analyses, with CaO values > 34% in ankerite, >57% in calcite varieties were corrected by a factor of 0.88 to bring the values to a more acceptable range (indicated in Appendices 7 and 9).

The atomic formulae for carbonate analyses were calculated on the basis of 6 oxygen atoms (Appendix 9). The relative abundance of calcium, iron and magnesium cations were plotted in a calcium-iron-magnesium ternary diagram (Figure 3.13). Nomenclature fields were created by plotting carbonate analyses, representing a wide range of chemical variations of calcite (ferroan, magnesian varieties), ankerite, dolomite, siderite, and magnesite from Chang et. al, (1996). Carbonate analyses from the studied wells plotted on the classification diagram as siderite, ankerite, ferroan calcite, magnesian calcite and calcite. Manganoan calcite was also identified in the samples but it does not appear on this classification diagram.

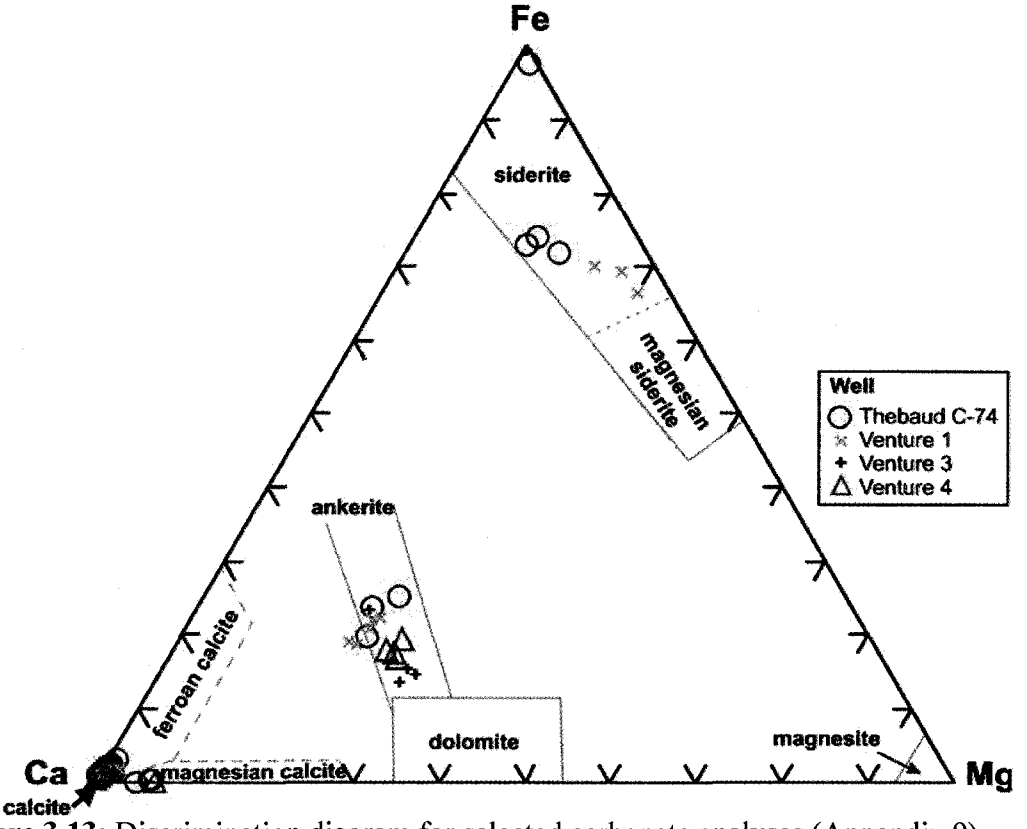

Figure 3.13: Discrimination diagram for selected carbonate analyses (Appendix 9). Structural formulae were calculated from electron microprobe data on the basis of 6 oxygen atoms. Nomenclature fields (grey solid and dotted lines) were created by plotting carbonate analyses representing a wide range of chemical variations (Chang et al., 1996).

Pure calcite ($CaCO_3$) is fairly uncommon and mostly occurs as biogenic fragments, not as diagenetic cements. Manganoan calcite (>1% MnO) was identified in two samples (Figure 3.14) and is interpreted as a bioclast.

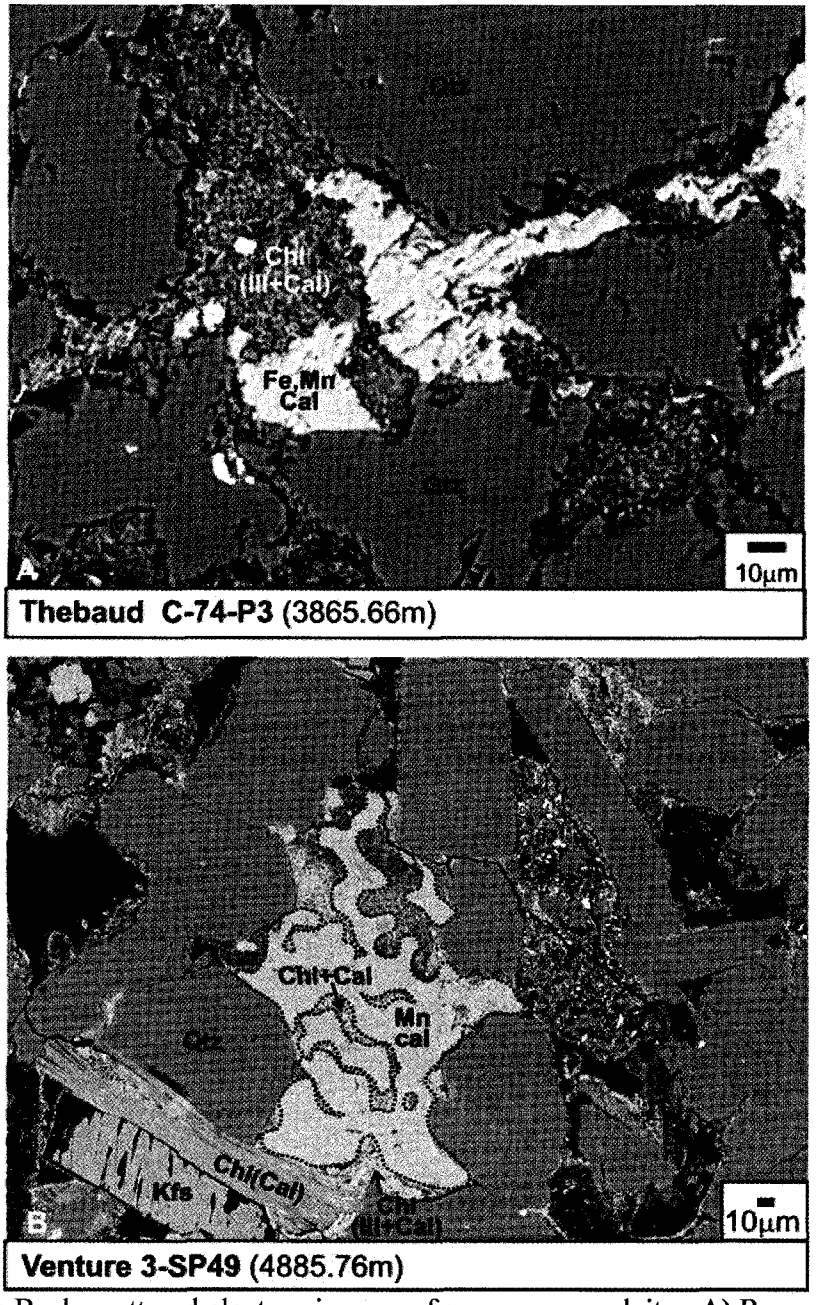

Figure 3.14: Back-scattered electron images of manganoan calcite. **A)** Ragged crystals of ferroan, manganoan calcite with a mixture of chlorite, illite and calcite; **B)** manganoan calcite bioclast (outlined with dashed black line) with a mixture of chlorite and calcite growing in the partially dissolved areas.

Magnesian calcite (>1% MgO) is commonly found as bioclasts or as corroded, porous patches within ferroan calcite cement (Figure 3.15). The magnesian calcite grains are interpreted as earlier grains that have partially dissolved as they have abundant corrosion surfaces and are porous (Figure 3.15B). Ferroan calcite and magnesian calcite have formed interlayered concentric growths around the patches of magnesian calcite. The alternation of the two varieties of calcite shows that the availability of Fe or Mg cations determined which species of calcite, ferroan or magnesian, developed. The textures seen, especially oscillatory growth, suggests that there was varying supply of these two cations during diagenesis.

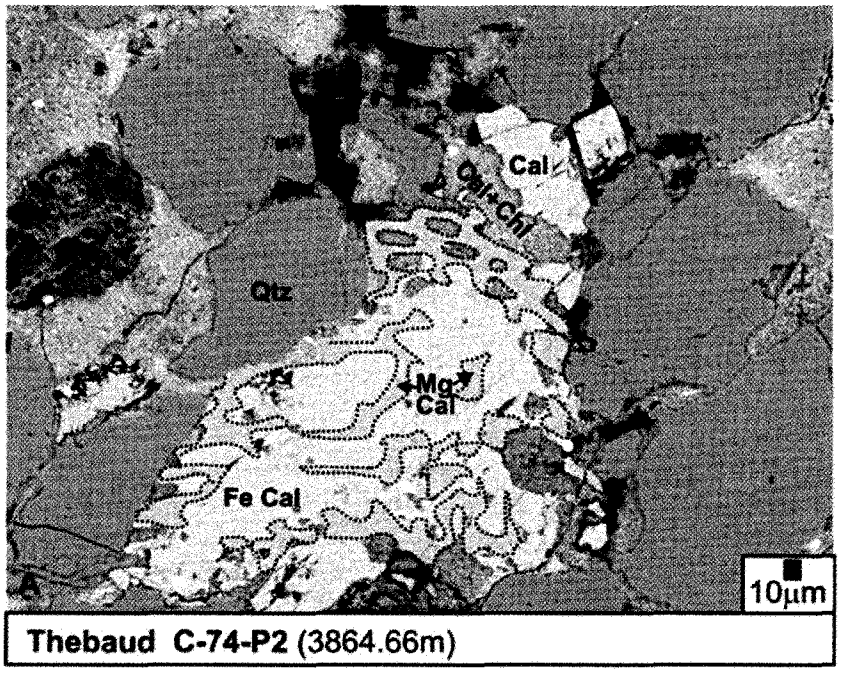

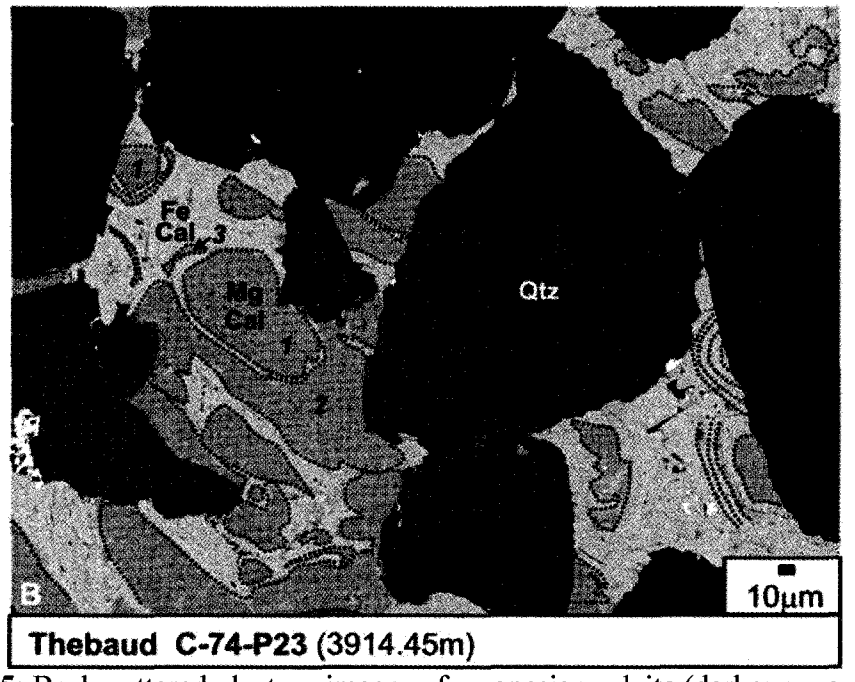

Figure 3.15: Backscattered-electron images of magnesian calcite (darker grey, outlined with dashed black line) and ferroan calcite (lighter grey). **A)** Partially dissolved magnesian calcite being replaced by ferroan calcite; **B)** patches of porous magnesian calcite encompassed by alternating concentric growths of ferroan and magnesian calcite cement (dashed black lines). The numbers indicate the oscillatory growths of the magnesian calcite

Ferroan calcite (>1% FeO) is the main carbonate identified in the studied samples, in particular within samples from Thebaud C-74, where it often occurs as a pervasive, pore-filling cement.

Ankerite occurs in each studied well, but it is rare in Thebaud C-74. Ankerite generally present as small patches of blocky crystals, usually with mixed clay lining fractures within the grain and along the rim (Figure 3.16). Ankerite is also seen partially filling pore spaces (Figure 14, Appendix 4 and Figure 16, Appendix 5).

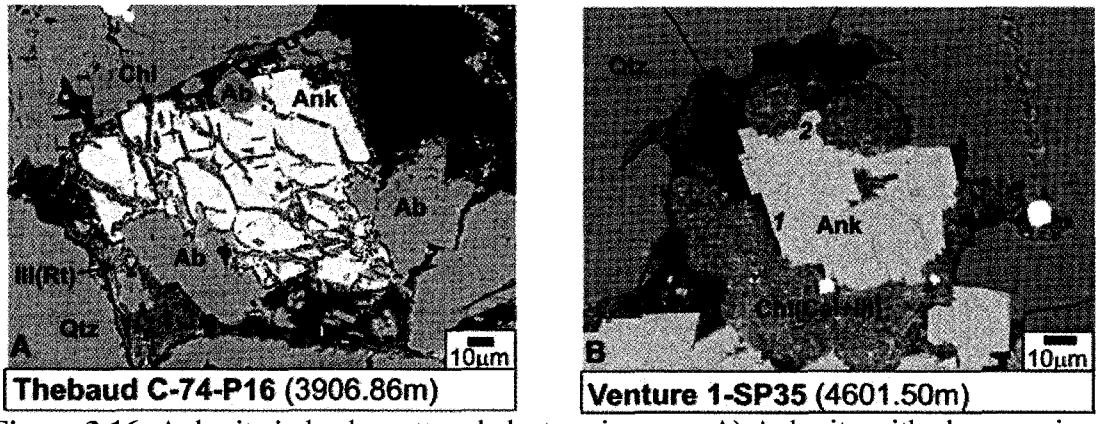

Figure 3.16: Ankerite in back-scattered electron images. **A)** Ankerite with clay growing along fractures; **B)** rhombohedral ankerite crystal with well-developed crystal faces where growth was into pore space (1); elsewhere the ankerite engulfs apparently early chlorite spherules (2).

Siderite was identified in Thebaud C-74 and Ventures 1 and 3 wells. It occurs as detrital intraclasts, and in the form of fine-grained masses of cement between grains (Figure 3.17E,F), or partially replacing minerals, such as mica (Figure 3.17).

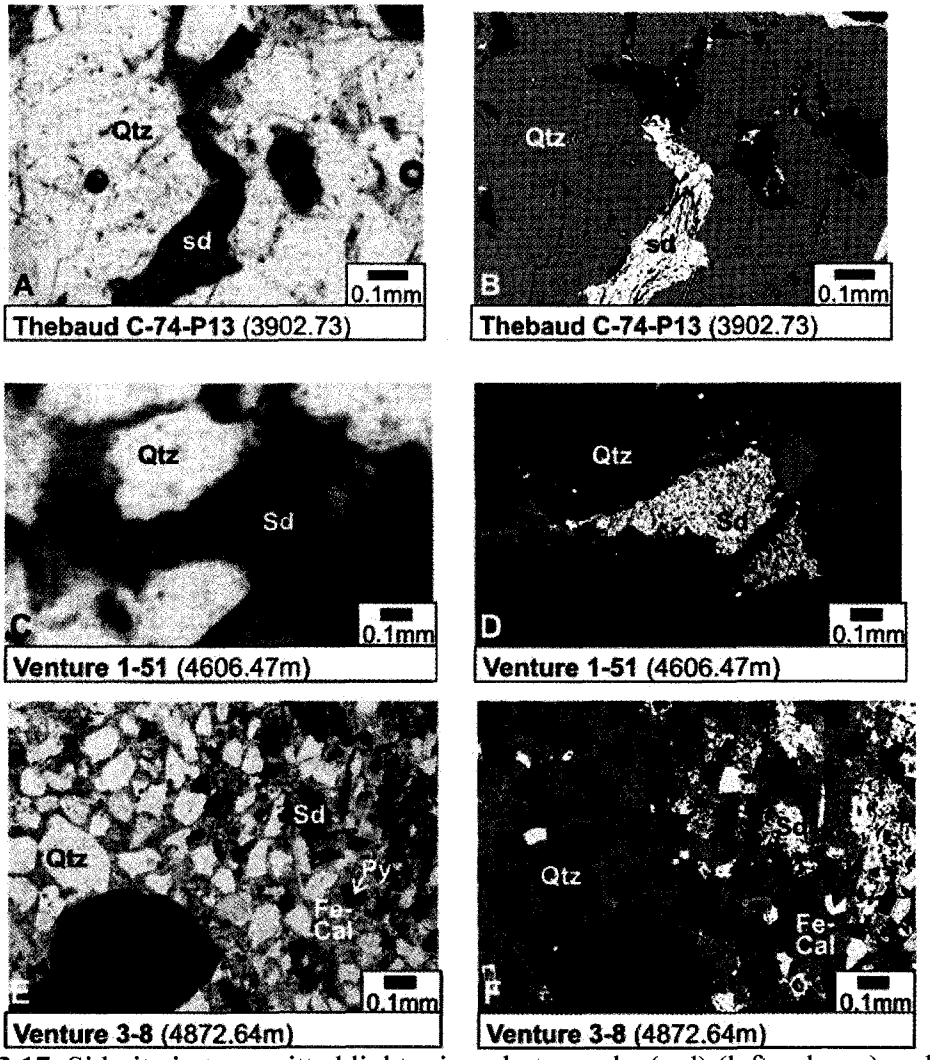

Figure 3.17: Siderite in transmitted light microphotographs (ppl) (left column) and back-scattered electron images (right column). **A, B)** siderite crystals replacing ?mica; **C, D)** fine grained siderite replacing a framework grain; **E, F)** early diagenetic corroded siderite within later ferroan calcite.

3.3.5 Silica cement

Quartz cement is present as overgrowths on detrital quartz grains and as pore-filling cement (Figure 3.18). The cement partially or completely fills the primary porosity preserved during deposition and results in low porosity and permeability (e.g., Blatt, 1979). Clay coats that adhered to sand grains during deposition mark the original grain boundaries after extensive silica overgrowths have developed (Figure 3.18B).

Compaction of detrital quartz grains has caused dissolution along grain contacts and the reprecipitation of silica as cement (e.g.,McBride, 1989) (Figure 3.18A).

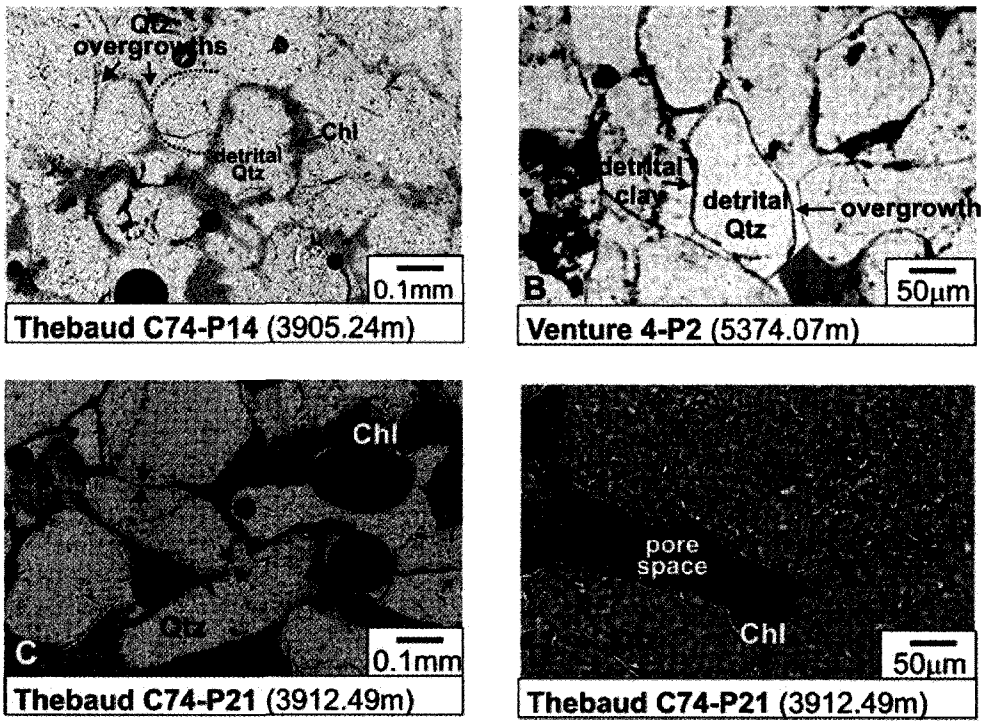

Figure 3.18: Silica cementation in thin section (ppl). **A)** Compaction of detrital quartz grains has significantly reduced porosity. Quartz overgrowths have developed and filled some pore space (outlined with dashed black line); chlorite rims around some grains have prevented quartz overgrowths from forming and preserved detrital grain boundary; **B)** dusty rims of detrital clay show the grain boundary prior to the quartz overgrowths; **C,D)** Quartz grains with well-developed chlorite rims and good porosity. Black arrows indicate contact dissolution between quartz grains where chlorite rims are absent

3.3.6 Other diagenetic minerals (pyrite, rutile)

Pyrite is present as replacing grains, as framboids of small aggregates of round grains associated with clay minerals, or lining cleavage planes of expanded mica grains (Figure 3.4A). Cubic pyrite crystals are also seen mixed with aggregates of clays (illite, chlorite). Pyrite is a minor constituent, making up, at the most, less than 1% of the thin sections.

Tiny diagenetic rutile crystals, <1μm in diameter, are often mixed with diagenetic pore-lining and pore-filling clays, such as chlorite and illite, resulting in electron microprobe analyses with up to 39% TiO_2 (Figures 19C,D). Rutile is rarely seen in lithic clasts (Figure 3.19A), where it is partially dissolved (Figure 3.19B).

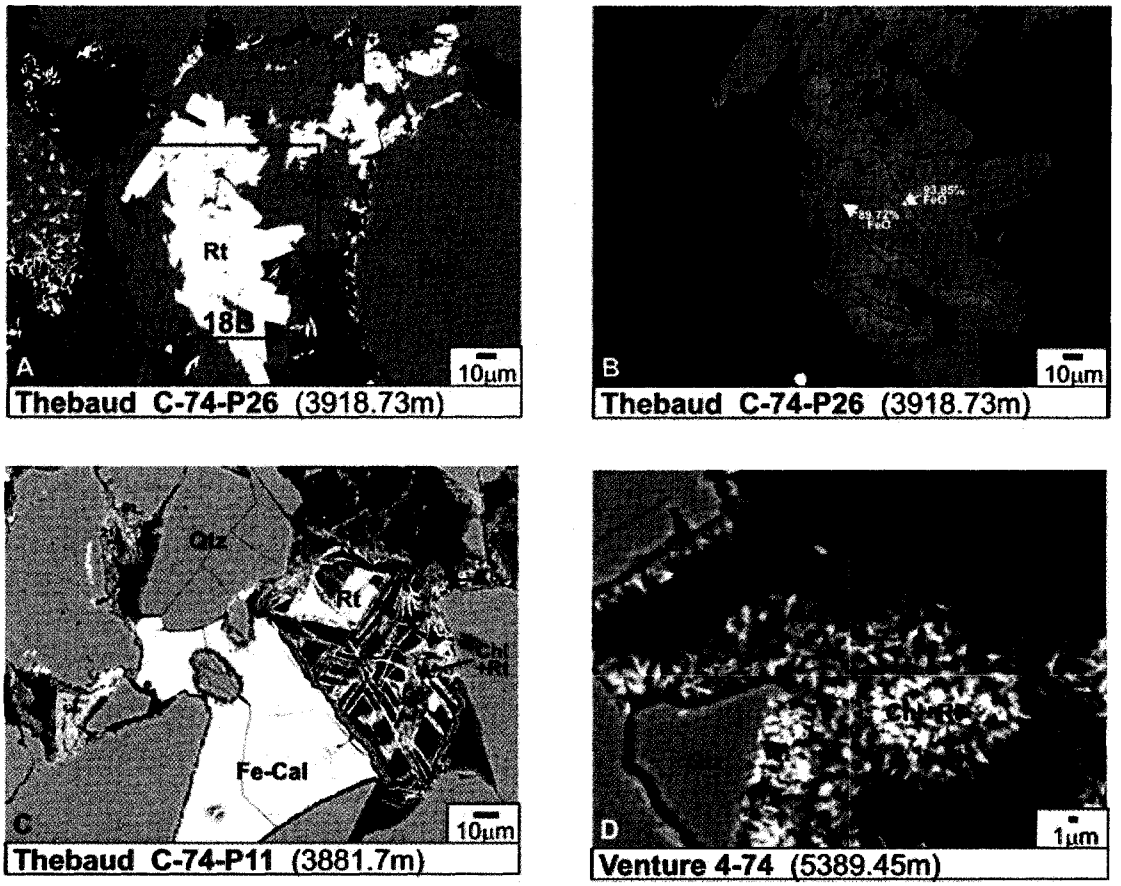

Figure 3.19: Back-scattered electron images of rutile. **A)** Clast of albite laths and diagenetic rutile; **B)** close-up of rutile with contrast decreased to highlight the compositional variations in the crystals, the lighter areas are more iron rich (outlined with a dashed black line, the darker areas are less iron rich; **C)** diagenetic rutile resulting from partially dissolved detrital ilmenite grain. Chlorite and rutile with minor illite rimsthe grain; **D)** mixture of chlorite and rutile lining and filling pore space.

3.4 Sequence of diagenetic events

Based on grain textures and relationships between diagenetic minerals observed in thin section (Table 1) and in back-scattered electron images and electron microprobe chemical analyses (Appendices 3 to 7), the following diagenetic sequence is suggested.

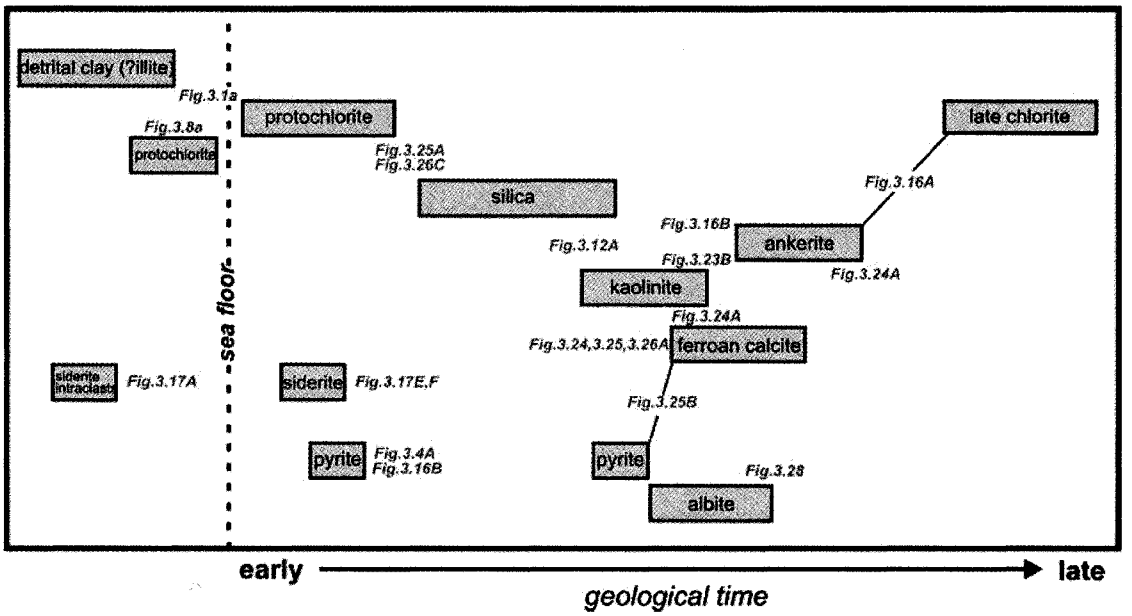

Figure 3.20: Paragenetic sequence in sandstones from the Venture and Thebaud fields. Numbers in parentheses refer to figures showing the relationships.

Chlorite rims are rarely seen associated with other pore-filling cements. Where pervasive pore-filling silica or carbonate cement is present, chlorite rims are usually very poorly developed or absent. The preservation of framework grain boundaries (generally lithic clasts or K-feldspar) by the chlorite rims after partial or complete dissolution indicates that the chlorite rims developed prior to the breakdown of framework grains (Figure 3.3C).

In places, chlorite rims developed early and are encased in carbonate cement (Figure 3.21B). However, elsewhere carbonate cement is seen in direct contact with detrital grains and appears to be going into dissolution, with chlorite growing along the edges of the carbonate cement (Figure 3.21A, 23A).

Electron microprobe analyses of illite have FeO values up to 14% (Figure 3.8A) suggesting mixing with chlorite in concentric layers of coated grains. Such illite is either detrital or formed synchronously with chlorite or protochlorite (Figure 3.4 to 3.8). Illite

is also present as a detrital clay coating on framework grains. Expanded mica grains also show mixed mica and chlorite, apparently due to neoformation of chlorite or protochlorite during alteration of mica.

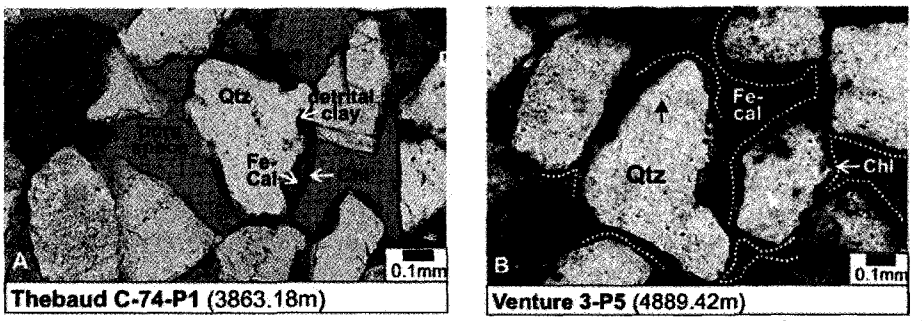

Figure 3.21: Microphotographs of ferroan calcite and chlorite rims (ppl). **A)** Detrital quartz grain with partial ferroan calcite coating and chlorite rim, ferroan calcite formed earlier than chlorite rim; **B)** chlorite rims along quartz grains. Later ferroan calcite fills pore space overgrowing chlorite rims.

Ankerite cement (stained turquoise-blue in unpolished thin sections) develops as patches in pore space and in direct contact with detrital grains suggesting that the ankerite formed early (Figure 3.22). In microphotographs, it may appear corroded along grain boundaries and cleavage planes (Figure 3.23).

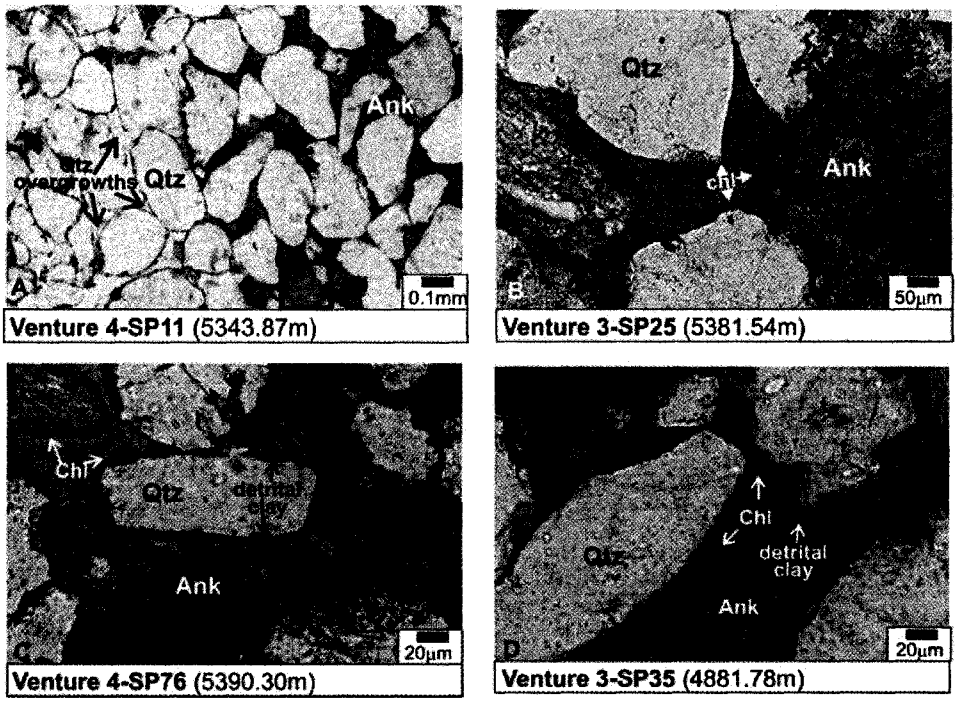

Figure 3.22: Microphotographs of ankerite cement (stained turquoise-blue) in thin section (ppl). **A)** Ankerite cement filling pore space between detrital quartz grains (right in microphoto). Extensive silica overgrowths on quartz grains (opposite half of the microphotograph) have grown into available pore space destroyed all primary porosity. A dissolved framework grain (black box) has created secondary porosity in the ankerite cement, however this may be a result of "grain plucking" during thin section polishing; **B)** chlorite rimming quartz grains and ankerite cement; **C)** detrital quartz grain coated with detrital clay. Ankerite cement is in direct contact with the clay coating. Diagenetic chlorite is growing along the clay coating but is not present between the clay coating and the ankerite; **D)** ankerite fragment coated with clay, with diagenetic chlorite growing on the clay coating.

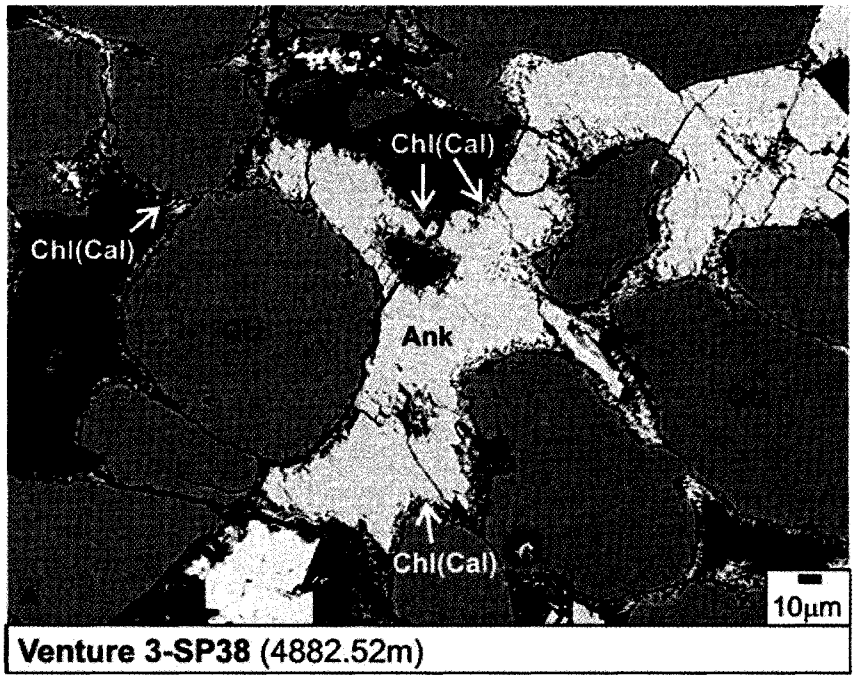

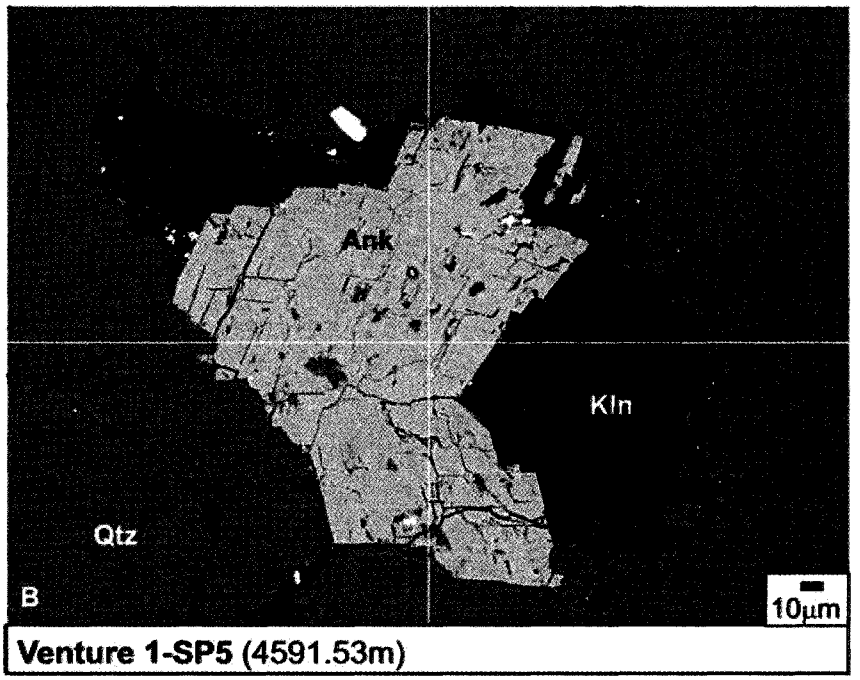

Figure 3.23: Back-scattered electron images of ankerite in thin section. **A)** Ankerite cement growing between detrital quartz grains. The ankerite encases chlorite rims that had formed on detrital grains. The grains have dissolved completely leaving chlorite lining the dissolution holes in the ankerite cement; **B)** ankerite and kaolinite cement growing in a pore within compacted quartz grains. The ankerite cement edges intersect and cross-cut the kaolinite booklets indicating that the ankerite formed later than the surrounding kaolinite.

A second type of carbonate cementation, ferroan calcite, is either seen independent of other cements, or growing at the same time as ankerite (Figure 3.24A,B). In some samples it is pervasive, completely filling all primary pore space between grains (Figure 3.25B). The calcite cemented available pore space and prevented further compaction of the rock. This is interpreted as an early-formed calcite cement as the degree of compaction of the framework grains is low (Figure 3.25B). Back-scattered electron images demonstrate that ferroan calcite developed early in some samples and shows similar textural characteristics to the ankerite cement, being in direct contact with framework grains, in contrast later chlorite rims form along the edges of the carbonate cement (Figure 3.21A, 3.25B). This is particularly common in Thebaud C-74, where ferroan calcite is the dominant carbonate cement. Ferroan calcite has developed later in the paragenetic sequence as well, where the degree of compaction is much higher and other diagenetic cements have developed, such as silica. Figure 3.25A shows ferroan calcite cement has formed after silica overgrowths on quartz grains.

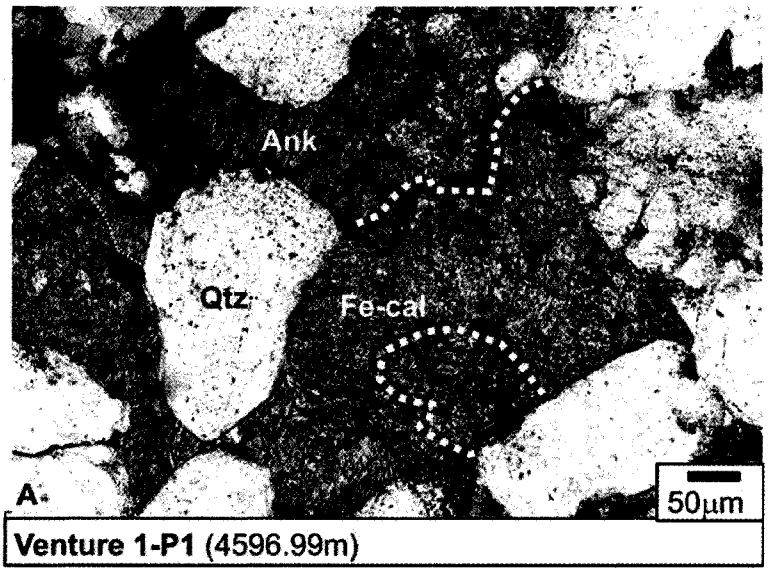

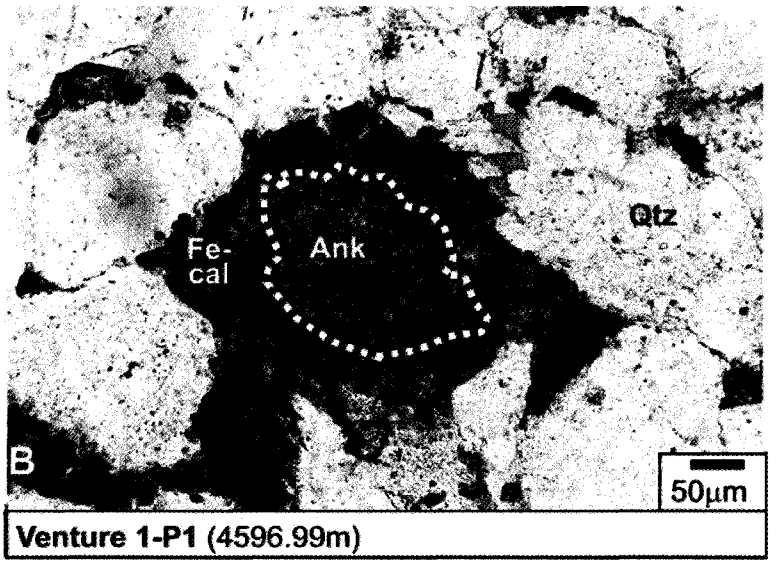

Figure 3.24: Carbonate cement in microphotography (ppl). Ankerite is stained turquoise-blue and ferroan calcite a bluish-purple; the contact between the two cements is indicated with a dashed white line. **A)** Ankerite and ferroan calcite cement; **B)** ferroan calcite in direct contact with detrital grains, ankerite has formed in the centre of the pore, perhaps a dissolved patch within the ferroan calcite.

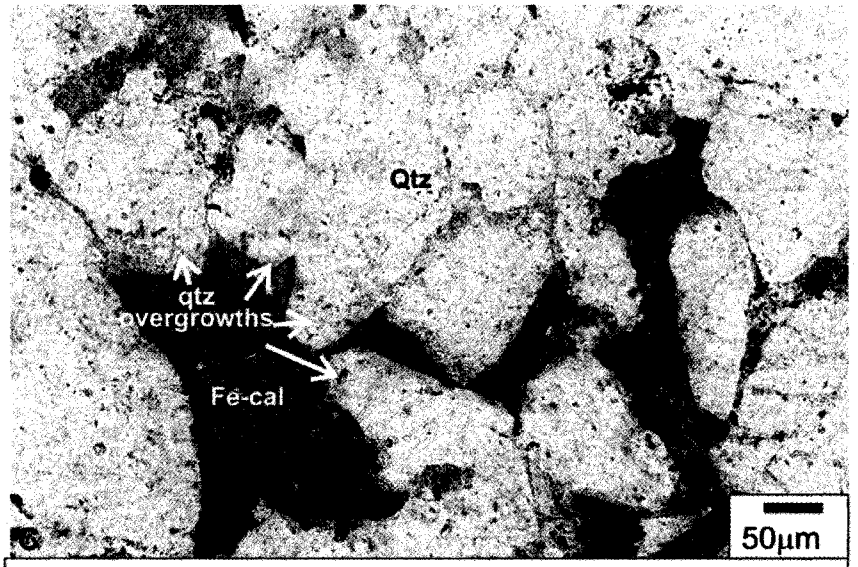

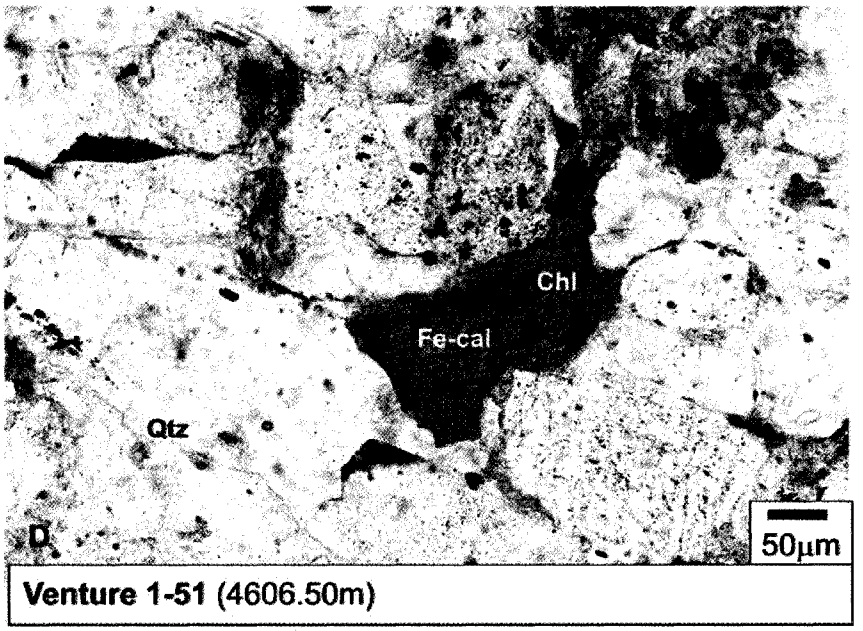

Figure 3.24 (continued): C) Quartz grains with overgrowths and ferroan calcite cement growing over the silica overgrowths; **D)** ferroan calcite intergrown with chlorite.

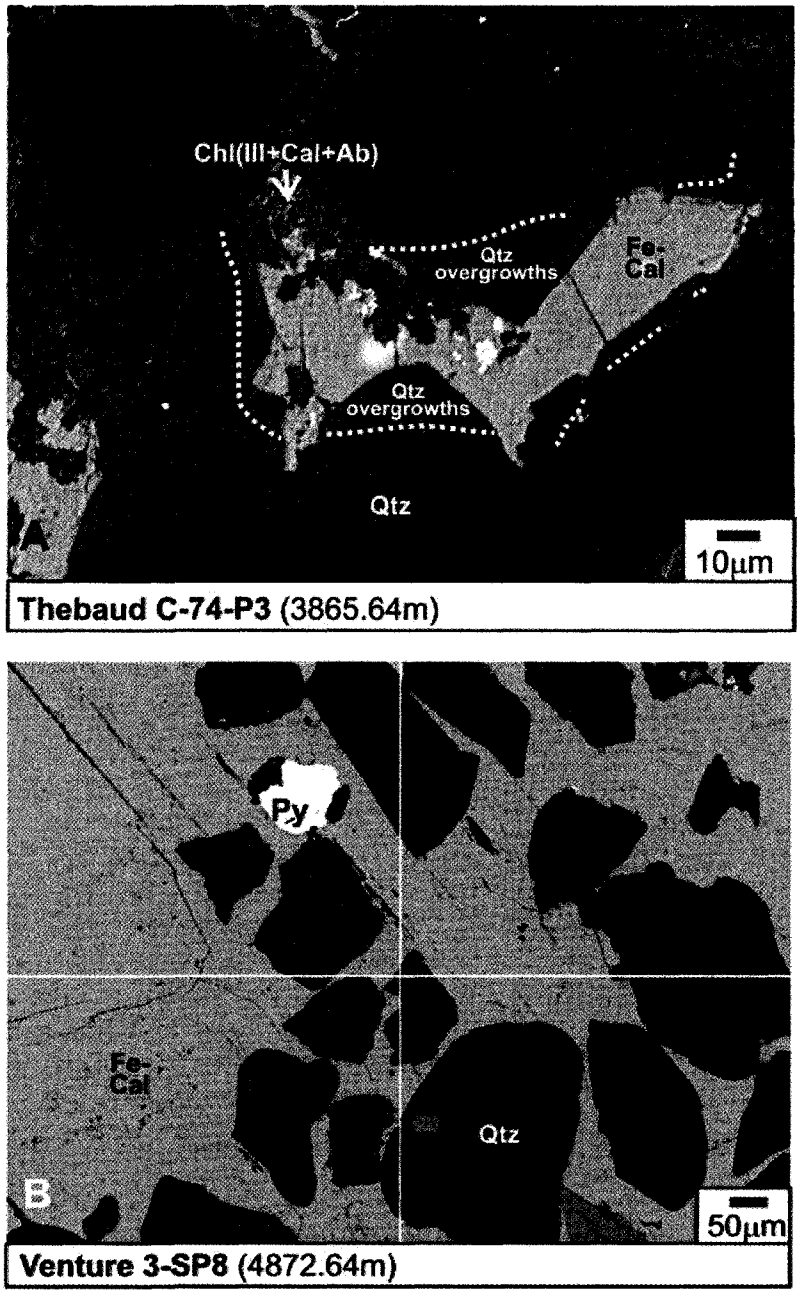

Figure 3.25: Back-scattered electron images of ferroan calcite. **A)** Ferroan calcite cement formed around quartz overgrowths indicating that it had developed later than the overgrowths; the sample is fairly well-compacted also indicating the sample has been subjected to some level of compaction prior to the development of the ferroan calcite cement; **B)** pervasive, pore-filling ferroan calcite and framboidal pyrite.

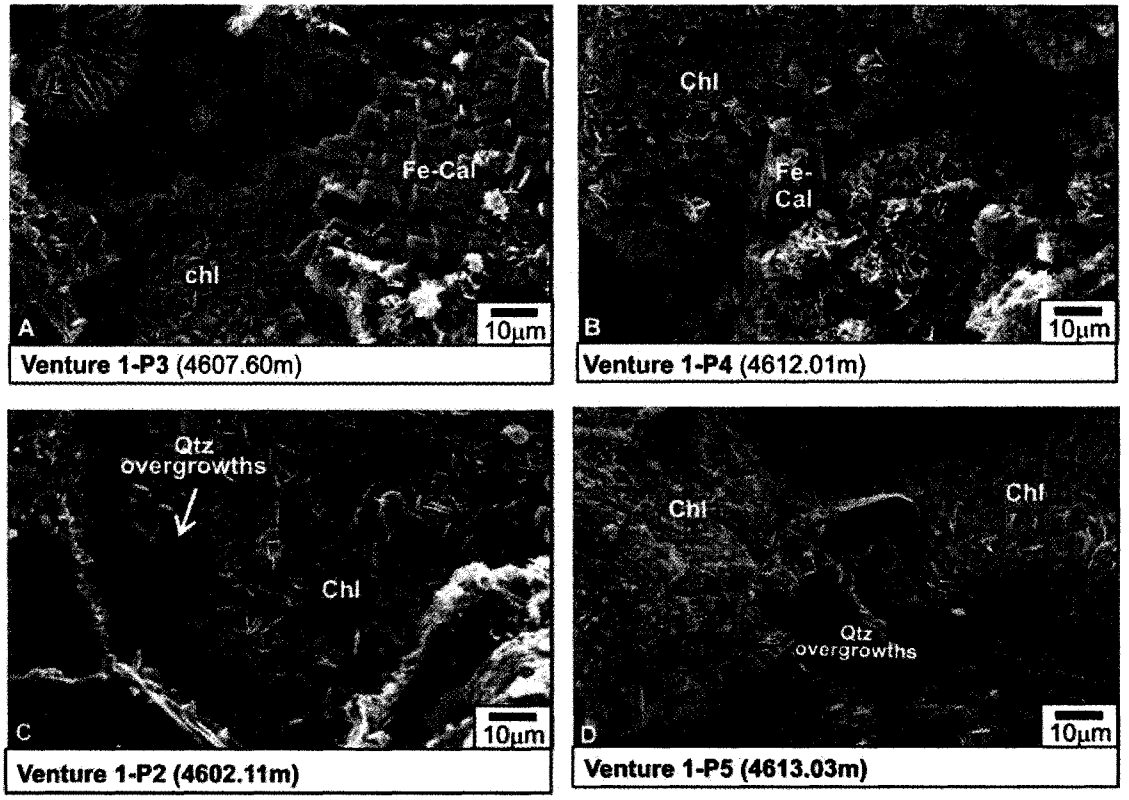

Figure 3.26: SEM microphotographs of diagenetic phases (modified from Core Laboratories, 1999d). **A, B)** Chlorite rims lining framework grains. Ferroan calcite forms clean, well developed crystals and is not rimmed by chlorite; **C, D)** chlorite rims on framework grains. Quartz overgrowths seem to have formed where chlorite rims are thin, discontinuous or absent, the overgrowths lack chlorite rims and are interpreted as a later diagenetic phase.

Diagenetic framboidal pyrite developed early in the paragenetic sequence. Tiny crystals often appear corroded and are encased in later cements, such as ferroan calcite (Figure 3.25B). Siderite cementation has developed early in the diagenetic sequence, prior to chlorite rims and silica cements. Siderite cement and detrital grains replaced by siderite are present in samples later cemented by silica or clay cements (Figure 3.17A)

Silica cementation, as already mentioned, occurred later in the sequence, either as overgrowths on detrital quartz grains or pore-filling cement (Figure 3.24C and Figure 3.26C,D). The overgrowths are particularly obvious where partial detrital clay coating ("dusty rims") had formed prior to cementation, preserving the original grain boundary

(Figure 3.18B). Silica cementation predates ferroan carbonate and postdates chlorite rims (Figure 3.26C,D).

Partial or complete dissolution of framework grains (mainly feldspar) seems to have occurred throughout the diagenetic history of these rocks. In other samples, partial or total dissolution of the grains occurred after the development of grain-rimming clays, preserving the original grain shape.

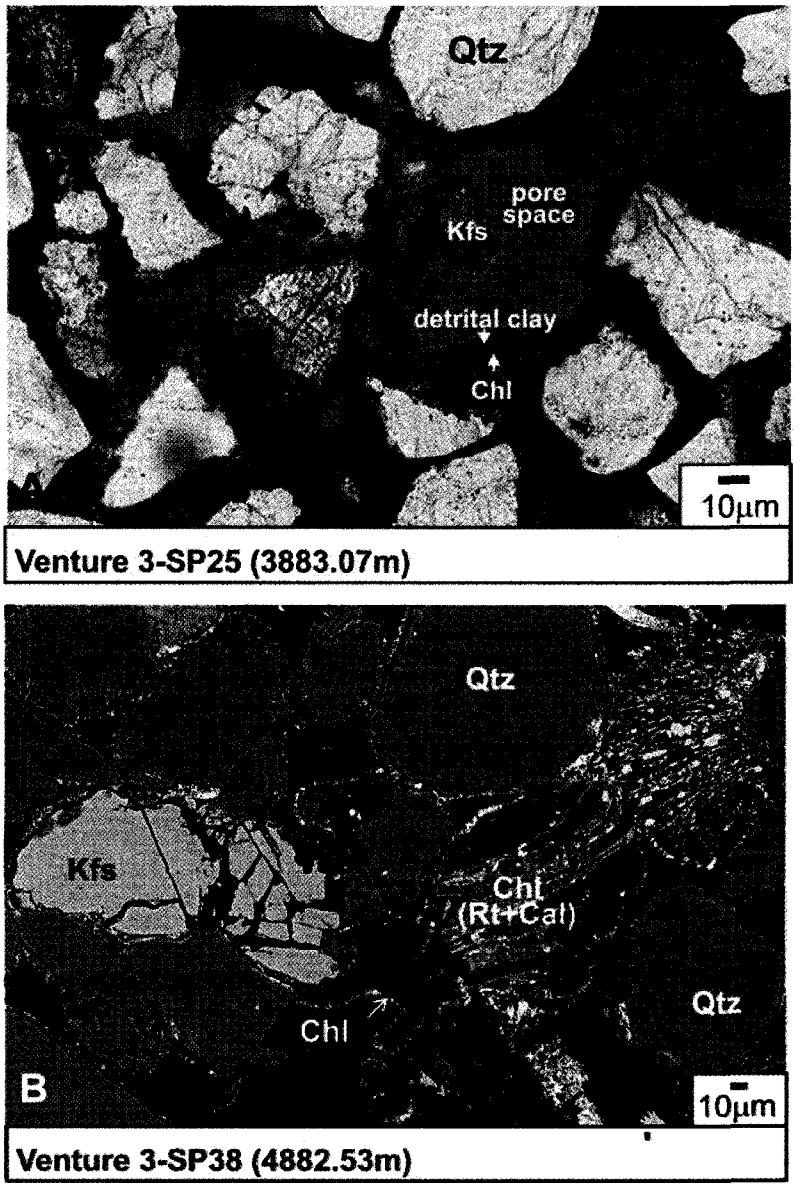

Figure 3.27: Grain dissolution in microphotograph (ppl) and back-scattered electron image. **A)** Secondary porosity created by the near complete breakdown of a K-feldspar grain. A detrital clay coating and diagenetic chlorite rim developed prior to the dissolution; **B)** well-developed chlorite rims on framework grains. K-feldspar and mica grains have partially dissolved.

Albitization of framework grains occurs late in the paragenetic sequence. Detrital feldspar grains, mostly K-feldspar, partially dissolve and albite precipitates during albitization, resulting in volume reduction, usually as patches or along cleavage planes (Figure 3.28A). The K-feldspar grains are partially or completely dissolved and the

available pore space is cemented with late ferroan calcite. Diagenetic albite grains are therefore commonly seen within ferroan calcite cement as clean, euhedral crystals (Figure 3.28B).

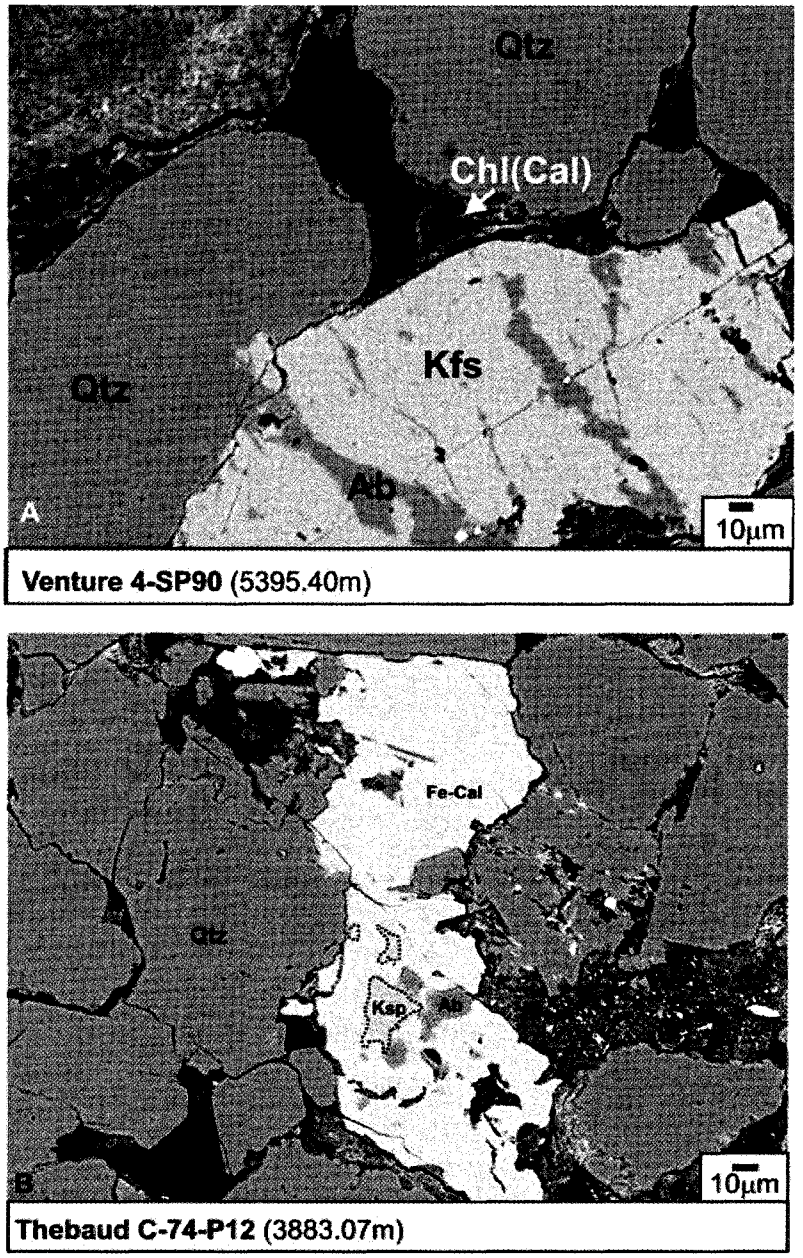

Figure 3.28: Backscattered-electron images of diagenetic albite. **A)** Diagenetic albite forming patches within a detrital K-feldspar grain; **B)** fragments of K-feldspar and albite grains associated with probably late ferroan calcite cement.

3.5: X-ray maps

Electron microprobe analysis of chlorite has shown that it is often mixed with minor amounts of other elements not found in chlorite, most commonly K, Ca, Na or Ti. X-ray maps using these elements were produced to investigate the distribution of illite, calcite, albite, and rutile within chlorite cement.

Igneous clasts, composed of albite laths with interstitial patches of chlorite, were identified in several of the samples. Microprobe analyses of these patches show that the chlorite is either mixed with illite, calcite and/or rutile. For example, analysis 162 in Thebaud C-74 sample P7 shows the area between albite laths as being dominantly chlorite, with minor illite and albite (2.85% K_2O and 2.73% Na_20) (Figure 3.29). Analysis 178 from sample P10 identifies patches within a similar clast as being a mix of chlorite and calcite with minor albite (20.85% CaO and 0.49% Na_2O) (Figure 3.30).

Pore-filling clays were also identified in thin section. Electron microprobe analysis of pore-filling clay from Thebaud C-74 P7 show that such an area is composed of a mixture of clays and other diagenetic minerals: illite (4.13% K_2O), chlorite (12.30% FeO, 2.39% MgO), rutile (3.02% TiO_2), albite (0.51% Na_2O) and 0.09% CaO (analysis 172) (Figure 3.31).

X-ray maps were produced of the chlorite patches within the igneous clasts and of the pore-filling clays. The maps show the distribution of K, Ca, Na, Si and Ti, elements identified from microprobe spot analyses of the corresponding mapped areas. Potassium, indicative of illite, seems to be evenly distributed in micron-sized spots within the chlorite and does not occur as large discrete patches in the cement (Figures 3.29 and 3.30). CaO, a proxy for calcite, is not evenly distributed within the chlorite cement, but

concentrated in patches 2-30μm in size (Figures 3.30 and 3.31). Na_2O distribution, used to indicate the prescence of albite laths 10μm wide and 50μm long in the lithic clasts, (Figures 3.29 and 3.30) but is absent between laths. Na_2O also appears to be present as 1μm patches within pore-filling cement in Figure 3.31. Rare, 1-2μm spots of Ti, indicate that rutile crystals are present in the lithic clasts (Figure 3.29) and may be up to 8μm in length (Figure 3.30). Rare 1-2μm spots are irregularly distributed in the pore-filling cement in Figure 3.31.

The X-ray maps therefore show that the chlorite patches within the lithic clasts and between albite laths are accompanied by 3-10μm size patches of calcite and rutile, whereas potassium appears more evenly distributed in sub-micron spots (Figure 3.30). The maps also show that pore-filling chlorite may also contain dispersed 1μm crystallites of illite and larger, irregular patches of calcite. Rutile may also occur in 1-3μm irregular patches.

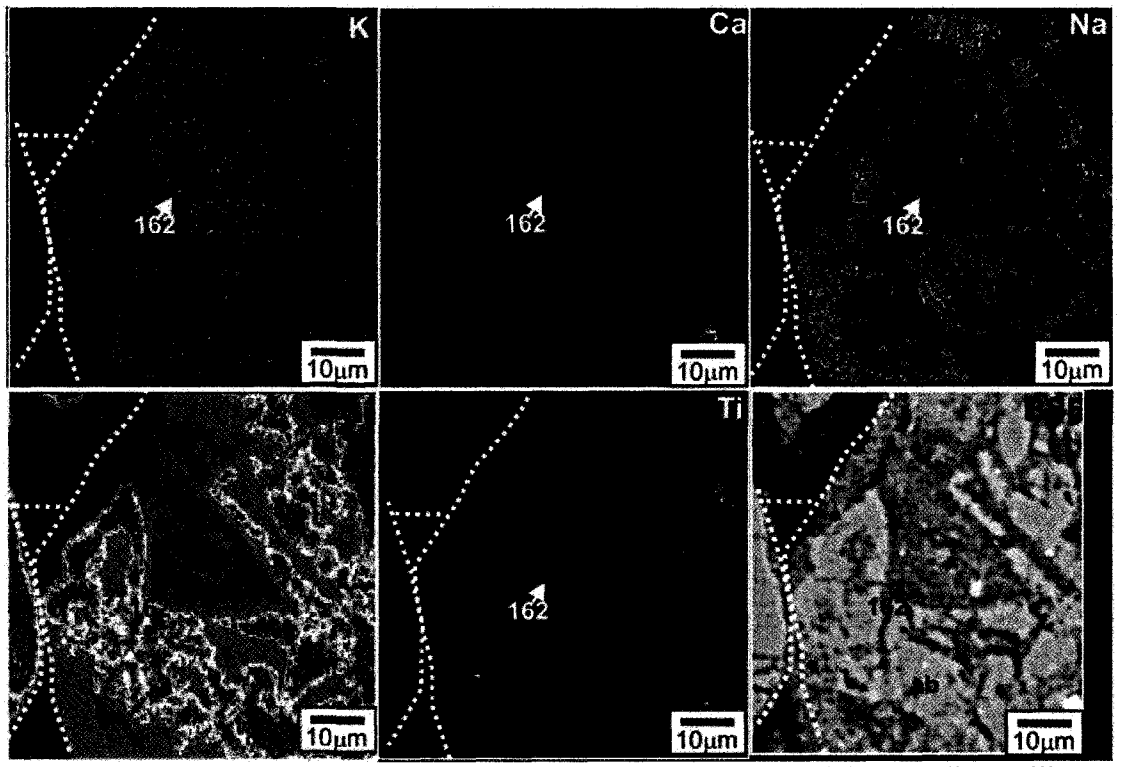

Figure 3.29: X-ray map showing the distribution of potassium, calcium, sodium, silica and titanium within chlorite cement patches between albite laths. The corresponding back-scattered electron image and the position of the microprobe analysis (162, Appendix 7) are also shown for reference (Thebaud C-74, P7, 3876.81m measured depth).

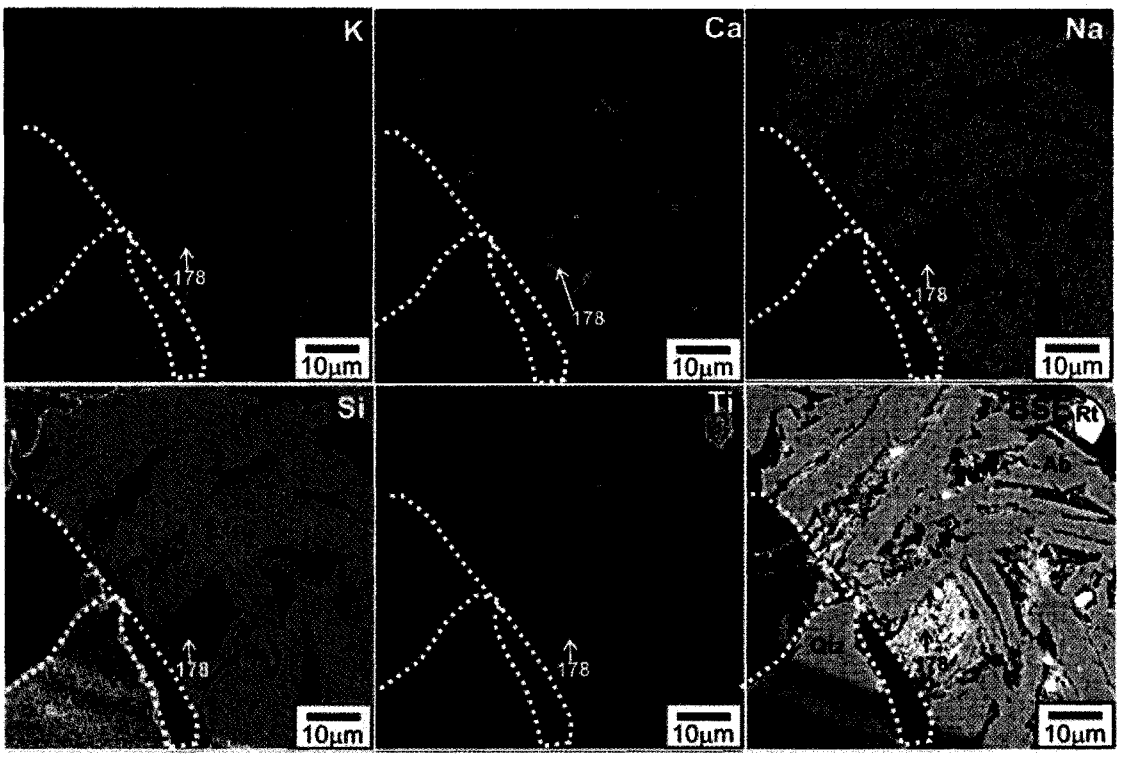

Figure 3.30: X-ray map showing the distribution of potassium, calcium, sodium, silica and titanium within chlorite cement patches between albite laths. The corresponding back-scattered electron image and the position of the microprobe analysis (178, Appendix 7) are also shown for reference (Thebaud C-74, P10, 3879.67m measured depth).

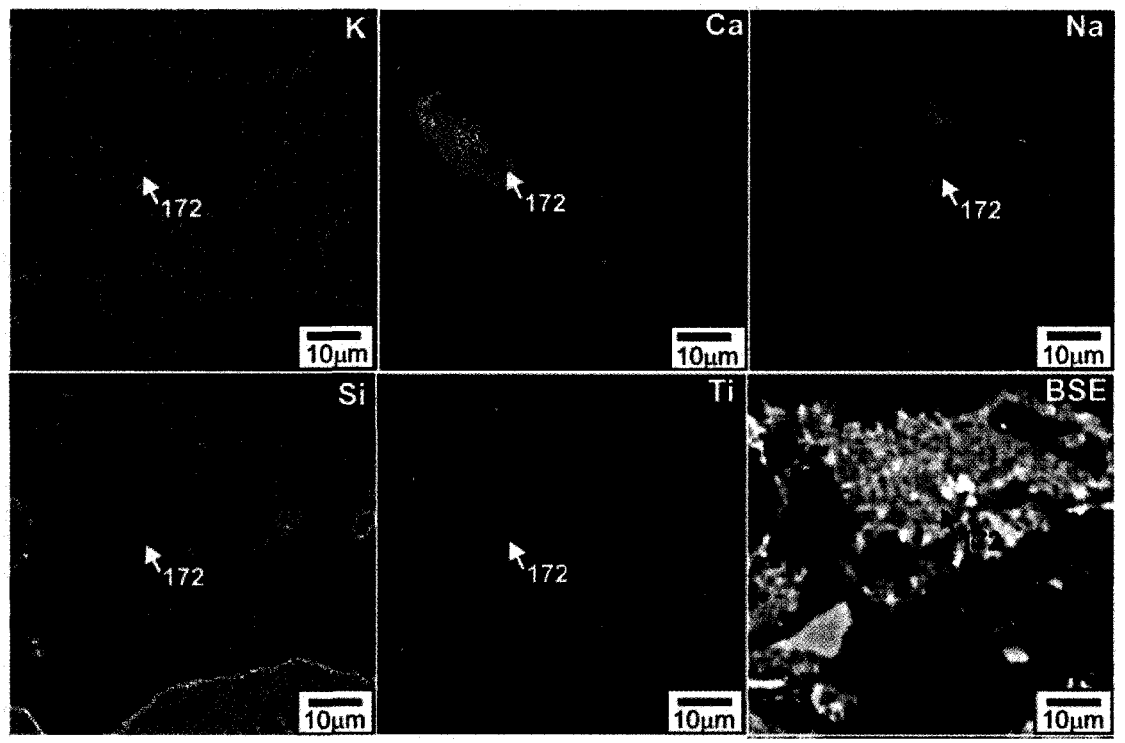

Figure 3.31: X-ray map showing the distribution of potassium, calcium, sodium, silica and titanium within pore-filling chlorite cement The corresponding back-scattered electron image and the position of the microprobe analysis (172, Appendix 7) are also shown for reference (Thebaud C-74, P7, 3876.81m measured depth).

CHAPTER 4: X-RAY DIFFRACTION

4.1 Introduction

Quantitative X-ray diffraction analyses were performed on the <2μm fraction from plug samples in order to identify the clay minerals present. The diffractogram patterns were also used to distinguish subtypes of clay minerals, such as iron-rich chlorite from magnesium rich chlorite. X-ray diffraction analyses were conducted on Thebaud C-74 sample P23 and P19. The <63μm fraction of sample P19 was lost during sieving. Sample P23 is a poorly sorted conglomerate and because of the limited amount of bulk sample available for separation, it was determined there would not be enough clay to produce a smear slide for analyses. Depths in text and on figures are measured below Kelly bushing unless otherwise indicated.

4.2 Methods

4.2.1 Sample Preparation

Each plug sample was prepared for X-ray diffraction using the techniques of Ryan and Hillier (2002). A portion of each small plug sample, weighing approximately 30 to 50g, was cut off the end and sawed into centimeter-sized pieces. The pieces were thoroughly washed in distilled water and dried with Kim Wipes. Rock chips were placed inside a thick plastic sleeve for protection and, using a small hammer, gently crushed to a fine powder, being careful not to grind the samples. As the bag became tattered, the partially crushed rocks were transferred to a new plastic sleeve and further crushed, until the material was completely disaggregated. For well-indurated (usually silica cemented) samples, a heavy iron crusher was used to crush each sample (Figure 4.1). The sediment was wet-sieved to separate the <63 μm fraction. The <63 μm fraction was suspended in a

1% Calgon solution ($(NaPO_3)13{\bullet}Na_2O$) (to prevent flocculation) in 250 ml bottles and placed on shaker table for approximately 90 minutes.

The <2 μm fraction was separated using settling tubes (Figure 4.2A). These tubes are modified 1000 ml graduated cylinders that contain a spigot placed 20 cm below the top 1000 ml graduation mark. Settling rates and timed intervals were used to obtain the desired <2 μm fraction (approximately 16 hours depending on the laboratory temperature). The suspended sediment from above the spigot, which consists of only <2 μm sediment, was tapped off into a 500 ml centrifuge bottle (Figure 4.2B). Most of the samples are poor in clay and therefore the remaining sediment below the spigot was resuspended and the same process was repeated to acquire the most <2 μm fraction from the sample. One ml of a 0.5 N MgCl solution was added to flocculate the tapped off material and the solution was centrifuged for 90 minutes at 3000 rpm to allow for decanting of the supernatant. The samples were dried slowly at 40 C for approximately two weeks. A net sample weight was calculated and the material was transferred into 50 ml conical tubes, centrifuged and decanted.

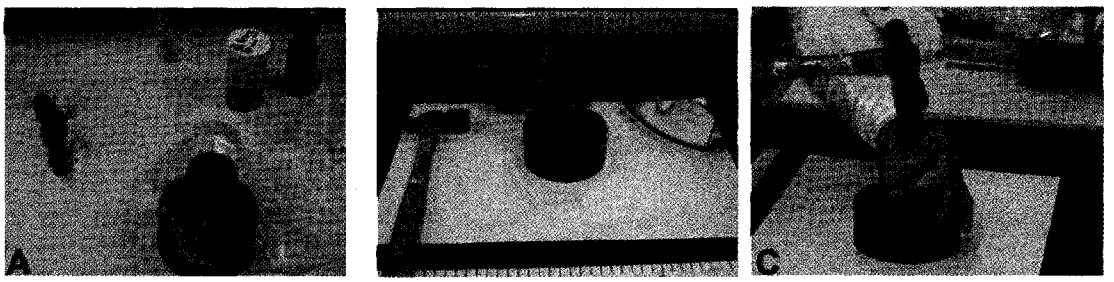

Figure 4.1: Equipment used for disaggregating well-indurated samples. **A)** Partially crushed sample was placed inside iron crusher, lined with thick plastic; **B,C)** The crusher was reassembled and a hammer was used to apply force to the crusher.

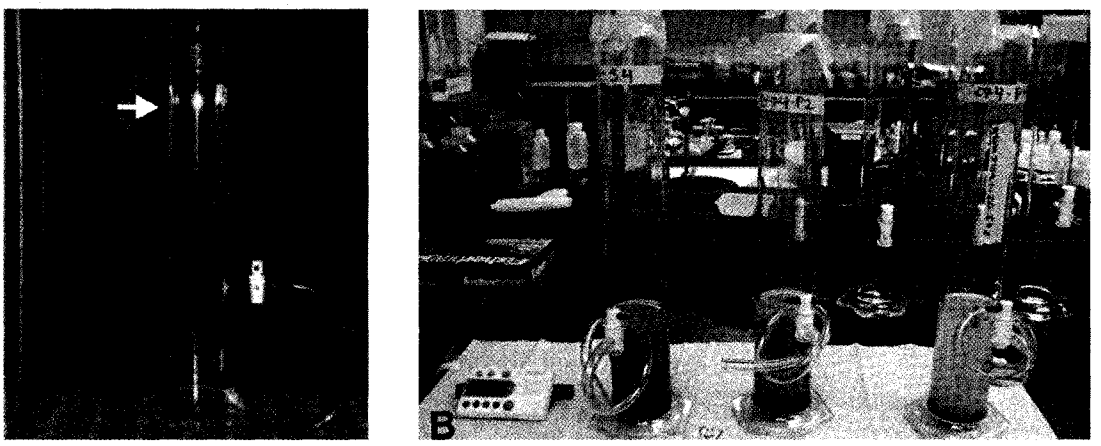

Figure 4.2: Modified graduated cylinders used for separating the <2 μm sediment fraction. **A)** Empty 1000 ml graduated cylinder with a spigot placed 20 cm below the top 1000 ml graduation mark (white arrow); **B)** Modified graduated cylinders the first round of 16 hours of settling. Suspended sediment from above the spigot has been tapped off. The settling process was repeating twice, each time the tubes were filled with distilled water to the 1000 ml mark, the sediment below the spigot was resuspended and allowed to settle for an additional 16 hours, and tapped off.

Samples that were large enough were split roughly in half. Each sample was mixed thoroughly to homogenize any layering created during centrifuging. The mass of the <2 μm fraction was determined for each split sample at room temperature and humidity. For each split, 5% of the clay mass (rounded to three decimal places) was calculated and the same amount of zincite (ZnO) standard was added to one of the split samples. Material that did not have zincite added was set aside. After carefully weighing out the amount of zincite to be added to each sample in a room with little air movement, the zincite was suspended in distilled water using the sonic bath. Distilled water was also added to the clay samples and clumps were disaggregated using a sonic bath. The suspended zincite was added to the clay sample. The samples were recentrifuged for 90 minutes and the supernatant was decanted, to obtain a clay sample with the consistency of soft butter. For samples that were particularly difficult to decant, the fume hood was used to evaporate enough excess water to achieve the necessary consistently to make the

slide. Some samples required a second centrifuge, as zincite would collect as a film on the inside of the conical tubes.

4.2.2 X-ray diffraction analysis

Using a diamond carbide pen, glass slides were cut into one inch squares and labeled on the underside. The slides were washed in laboratory soap, rinsed in distilled water and dried with Kim Wipes and under the fume hood. Using the sample with 5 % zincite added, a smear slide was produced by spreading each sample thinly across the slides in one direction, using a piece of photographic film to create a thin, even surface on which platy clay minerals were oriented. Air-dried samples were run in a Siemens Kristaloflex diffractometer (Co Kα radiation source) using a "standard clay" run with patterns recorded between 2 and 52 2 theta (θ) with 0.02 steps and a 1.0 second count per step. Samples were run a second time using a "short clay" run with patterns recorded between 28.5 to 30.5 2θ at increments of 0.004 steps and 1.0 second counts per step, to expand the partially overlapping kaolinite and chlorite peaks, at 3.53 and 3.57Å, respectively.

4.2.3 Glycolation

Slide mounts of six samples (Thebaud C-74 P2, Thebaud C-74 P3, Thebaud C-74 P16, Venture 3 SP49, Venture 3 SP54 and Venture 4 SP2) were placed in a large desiccator and exposed to an ethylene glycol vapor overnight. Each sample was analyzed immediately after being removed from the desiccator using a "glycol" run, with patterns recorded between 2 and 17 2θ with 0.02 step and 3.0 second counts per step.

4.2.4 Thermal treatments

Four samples (Thebaud C-74 P2, Thebaud C-74 P11, Thebaud C-74 P16 and Venture 3 SP54) were heat treated to further characterize the clay minerals present. Residual sample was stirred vigorously and placed in the sonic bath to homogenize the material. Samples were mounted onto heat resistive slides made of thick (0.2 mm) glass cut into one inch squares and were heated overnight in steps of 110 , 300 , 500 and 650 C, running the "standard clay" run after each heating session (2 - 52 2θ, 0.02 steps, with a 1.0 second count per step).

Peak areas and d-spacings were determined using EVA, an X-ray diffraction spectrum analyses program (Bruker AXS, 2007) (Table 4.1).

4.3 Clay identification

The most common clays identified in the samples were chlorite, illite, kaolinite, and less frequently, trace amounts of smectite (Table 4.1). X-ray diffractograms are found in Appendices 10 to 13.

Table 4.1: Peak areas determined using X-ray diffraction software.

	top measured depth (m)	bottom measured depth (m)	peak area									
			(001) chlorite	(001) illite	chlorite/smectite	(001) kaolinite (002) chlorite	(003) chlorite	quartz	(002) kaolinite	(004) chlorite	zincite	zincite
D-spacing (Å)			*14*	*10*	*7.8*	*7.09*	*4.72*	*4.26*	*3.58*	*3.53*	*2.81*	*2.47*
Thebaud C-74 P2	3864.52	3864.84	6.73	12.09	2.14	125.08	24.05	0.61	0.00	79.14	5.14	1.48
Thebaud C-74 P3	3865.56	3865.75	1.33	13.66	1.53	59.71	12.85	0.37	0.00	35.15	2.00	0.64
Thebaud C-74 P7	3876.72	3876.90	2.14	2.32	0.86	53.62	7.78	0.36	0.00	29.40	1.65	0.65
Thebaud C-74 P10	3879.56	3879.78	1.56	1.62	0.49	49.18	4.83	0.00	4.11	21.48	1.04	0.46
Thebaud C-74 P11	3881.59	3881.80	1.99	2.83	0.59	55.76	8.48	0.50	10.20	34.69	2.64	1.25
Thebaud C-74 P12	3882.96	3883.17	1.98	6.55	1.10	65.67	9.62	0.48	0.00	39.17	2.35	0.81
Thebaud C-74 P13	3902.65	3902.81	0.37	4.25	0.00	8.20	1.39	1.43	2.13	4.75	1.31	1.20
Thebaud C-74 P14	3905.10	3905.37	0.00	2.37	0.48	30.18	3.63	0.50	9.66	15.81	1.41	0.90
Thebaud C-74 P16	3906.75	3906.97	0.60	8.37	0.51	27.01	2.00	0.47	10.66	9.37	0.92	0.68
Thebaud C-74 P17	3907.93	3908.11	2.55	6.95	1.42	67.04	11.55	0.49	15.06	42.73	3.16	1.42
Thebaud C-74 P18	3908.65	3908.88	4.55	4.94	1.51	84.21	14.99	0.52	0.00	61.86	4.94	1.68
Thebaud C-74 P20	3911.66	3911.82	2.56	1.73	0.68	51.38	7.32	0.00	0.00	27.97	1.01	0.76
Thebaud C-74 P21	3912.40	3912.58	4.12	1.30	0.66	61.67	8.54	0.00	13.16	33.19	2.18	1.23
Thebaud C-74 P22	3913.73	3913.95	1.69	0.76	0.64	26.65	3.20	0.00	10.41	12.90	1.81	0.68
Thebaud C-74 P24	3915.74	3915.90	2.29	1.06	0.96	43.90	4.85	0.26	12.50	23.67	2.81	0.90
Thebaud C-74 P25	3917.06	3917.28	2.89	1.08	0.74	55.84	7.22	0.00	21.18	28.18	3.06	1.15
Thebaud C-74 P26	3918.64	3918.82	1.11	2.22	0.73	35.76	5.00	1.25	9.98	18.12	1.90	1.02
Thebaud C-74 P27	3920.04	3920.25	4.05	2.30	1.02	65.05	9.07	0.51	22.35	36.97	2.83	1.42
Thebaud C-74 P29	3921.98	3922.20	2.40	2.25	0.86	55.11	7.47	0.53	19.41	28.88	2.07	0.80
Thebaud C-74 P30	3924.50	3924.67	2.49	2.36	0.68	50.37	6.49	0.68	13.39	22.56	1.60	0.72
Thebaud C-74 P31	3926.15	3926.33	0.00	9.52	1.19	42.38	5.60	0.36	19.08	21.15	1.43	1.16
Venture 1 SP05	4591.48	4591.77	0.00	5.28	0.00	1.95	0.00	0.84	0.23	2.02	0.47	0.55
Venture 1 SP28	4598.35	4598.59	0.00	4.62	0.00	2.93	0.35	1.09	1.05	2.05	0.71	0.88
Venture 1 SP35	4600.87	4601.23	1.73	3.54	0.43	23.97	4.17	1.73	0.00	17.43	1.98	1.50
Venture 1 SP51	4606.32	4606.61	0.00	5.53	0.00	12.23	2.46	0.72	0.00	7.86	1.03	0.69
Venture 1 SP76	4614.81	4615.17	3.27	2.90	0.81	45.40	8.80	0.75	0.00	31.51	3.28	1.37
Venture 3 SP05	4871.58	4871.90	2.66	3.33	0.45	30.68	5.55	0.77	0.00	20.31	0.00	1.52
Venture 3 SP08	4872.58	4872.70	2.25	1.58	0.26	20.17	4.00	0.54	0.00	15.93	0.00	1.94
Venture 3 SP25	4878.62	4878.80	8.94	0.96	0.54	50.71	13.02	0.34	0.00	35.56	0.00	5.00
Venture 3 SP38	4882.37	4882.68	5.13	0.81	0.00	24.54	5.14	0.30	0.00	11.87	0.38	0.99
Venture 3 SP49	4885.62	4885.90	13.50	1.40	0.96	71.07	20.96	0.46	0.00	54.89	0.00	8.54
Venture 3 SP54	4887.39	4888.32	1.35	12.83	0.00	10.98	4.53	0.29	0.00	7.53	0.46	0.91
Venture 4 SP02	5341.32	5341.52	0.00	4.64	0.00	2.98	0.57	1.64	0.77	1.90	0.93	1.04
Venture 4 SP22	5371.77	5371.97	0.86	2.04	0.00	18.15	2.50	0.61	0.00	12.84	1.40	1.25
Venture 4 SP25	5372.85	5373.18	4.41	1.83	0.74	47.61	8.29	0.00	0.00	27.38	2.11	0.53
Venture 4 SP30	5374.79	5375.06	7.06	2.71	1.06	73.63	15.07	0.37	0.00	51.25	5.13	0.88
Venture 4 SP50	5381.34	5381.77	5.89	1.72	1.02	63.82	13.19	0.39	0.00	46.84	4.89	1.19
Venture 4 SP56	5383.28	5383.56	3.86	2.38	0.71	37.06	6.78	0.40	0.00	26.08	2.73	1.10
Venture 4 SP61	5384.68	5384.98	5.19	2.25	0.92	48.66	9.41	0.21	0.00	32.65	3.02	0.86
Venture 4 SP68	5387.54	5387.83	1.32	1.19	0.26	15.33	2.46	0.57	0.00	9.87	1.19	1.09
Venture 4 SP74	5389.30	5389.60	7.75	0.97	1.35	64.29	13.66	0.20	0.00	47.76	4.92	0.99
Venture 4 SP80	5391.51	5391.83	4.91	0.80	0.74	54.61	11.21	0.00	0.00	38.70	3.38	0.92
Venture 4 SP87	5393.96	5394.15	5.06	1.59	0.71	54.28	12.34	0.38	0.00	41.82	4.53	1.12
Venture 4 SP90	5395.23	5395.57	5.04	0.69	0.68	50.87	9.66	0.17	0.00	35.01	3.31	1.09

4.3.1 Chlorite

Chlorite is recognized by characteristic (001) (14Å), (002) (7Å), (003) (4.7Å) and (004) (3.53Å) peaks (Moore and Reynolds, 1997). The relative intensities of different chlorite peaks on an X-ray diffractogram can provide information about the types of

chlorite that are present. Chlorite enriched in iron or other heavy metals have low intensity odd order peaks ((001), (003) and (005)) compared to even order peaks (002) and (004) (Figure 4.3A). Magnesium-rich chlorite show more symmetrical peak intensities (Figure 4.3B).

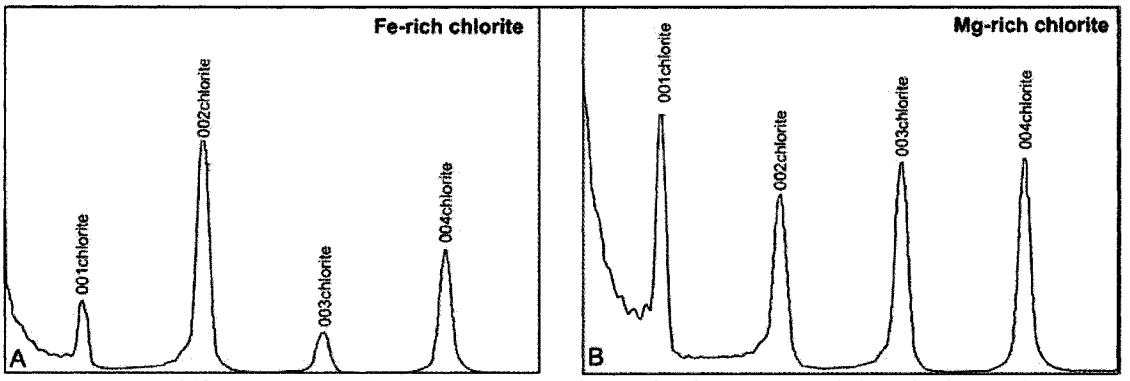

Figure 4.3: Diffractograms showing the peak intensity in **A)** iron-rich chlorite and **B)** magnesium-rich chlorite (modified from Moore and Reynolds, 1997).

Peak area ratios of the (001)/(004) peaks vary between samples, indicating variation in the abundance of Fe-rich chlorite. In general, the diffractogram patterns for samples with well formed chlorite rims have low odd order peaks ((001), (003) and (005)) compared to the even order peaks ((002) and (004)) (Figure 4.4) (Moore and Reynolds, 1997). Such chlorites are iron-rich. Nevertheless, the three samples with particularly high (001)/(004) peak ratios (i.e. the most Mg-rich chlorite) are classified as having well developed chlorite rims. Taking all samples as a whole, there is no strong relationship between (001)/(004) peak area ratio and the quality of chlorite rims. There is a weak correlation between samples with the higher (001)/(004) peak ratio and those with well-developed chlorite rims.

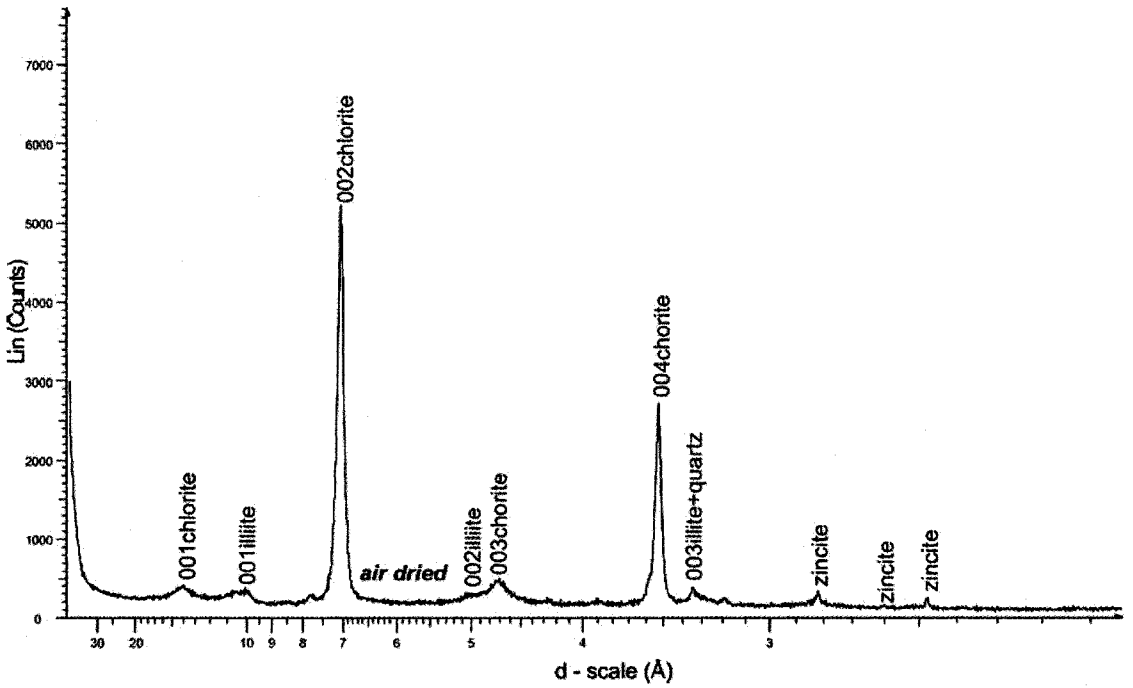

Figure 4.4: An example of a diffractogram of a sample containing iron rich chlorite. In thin section this sample has well developed chlorite rims and excellent porosity (24.3%) (Thebaud C-74, P10 3879.56 - 3879.78 m).

Although samples in general have weak odd peaks compared to even peaks (Figure 4.4), the (001) and (003) ratios vary considerably among samples. Moore and Reynolds (1997) noted that if iron distribution is symmetrical on the silicate and hydroxide sheets, the (001) and (003) peaks have equal intensities. If (001)>(003) chlorite peak intensity, then enrichment is on the silicate layer, whereas (001)<(003) chlorite peak intensity indicates enrichment on the hydroxide layer (Moore and Reynolds, 1997). In general the studied samples show enrichment on the hydroxide sheet, with ratios varying from 0 to 0.69. One sample (V3-38) has a ratio of 0.99 suggesting symmetrical iron distribution.

The chlorite peaks were unaffected by 110 and 300 C heating. At 500 C, the intensity of the 14Å peak increased and the peak sharpened, the intensity of the 7Å and 3.53Å peaks was significantly weakened and the peaks were shifted to 13.7, 6.92 and

3.45Å respectively. Since three of the heat-treated samples did not display a kaolinite (003) peak at 2.4Å, the shift is believed to be genuine and not a result of the destruction of kaolinite (which overlaps with the chlorite (002) and (004) peaks) causing an apparent shift of peaks. The (003) chlorite peak at 4.7Å peak collapses at 500 C. All chlorite peaks are destroyed at 650 C.

In summary, chlorite identified by X-ray diffraction from the Venture and Thebaud fields is generally iron rich, evident by the low intensity of the odd to even peak ratios. The iron enrichment is in the silicate sheet, with diffractograms showing low (001)/(003) peak ratios.

4.3.2 Kaolinite

Kaolinite was difficult to distinguish from chlorite because of overlap between the kaolinite (001) peak (~7.18Å) with the chlorite (002) peak (~7.08Å) and the kaolinite (002) peak (~3.58Å) with the chlorite (004) peak (~3.53Å). However, where kaolinite was previously identified in thin section, the diffractogram for the sample showed a separation of the kaolinite (002) and chlorite (004) peaks as well as a weak kaolinite (003) peak at ~2.4Å. The presence of kaolinite was also confirmed by collapse of all peaks at 500 C heat treatment (Figure 4.5)

4.3.3 Illite

Illite is characterized by a strong (001) peak at 10.1Å. When illite forms mixed-layer clays, the d-spacing of the series of basal reflectors, which for pure illite is (001) = 10Å , (002) = 5Å etc, is no longer in an integral sequence. To investigate whether illite was interstratified with other clay minerals such as smectite, the ratio of the d-spacing (001) and (002) reflectors was calculated (Table 4.2). Unmixed, pure illite would have a

ratio value of 2.0. Ratio values within the sample set were greater than 2.00, ranging from 2.01 to 2.09 indicating that illite shows some degree of interstratification with other clay minerals (Weaver, 1956). There was no correlation between the ratio values and either depth or between well.

In some samples, there appears to be an illite-smectite montmorillonite mixed-layer clay, characterized by greater breadth of the 10Å, giving the peak a much gentler slope on the left side, compared to the steep one on the right side (Figure 4.5). Upon glycolation, this mixed-layer clay peak shifted causing the 10Å peak to narrow in breadth and sharpened and increase intensity (Figure 4.5). Similar behavior was seen at when samples were heated to 110 C. However, the lack of a strong smectite peak at 17Å on glycolation indicates that smectite is present in very small quantities.

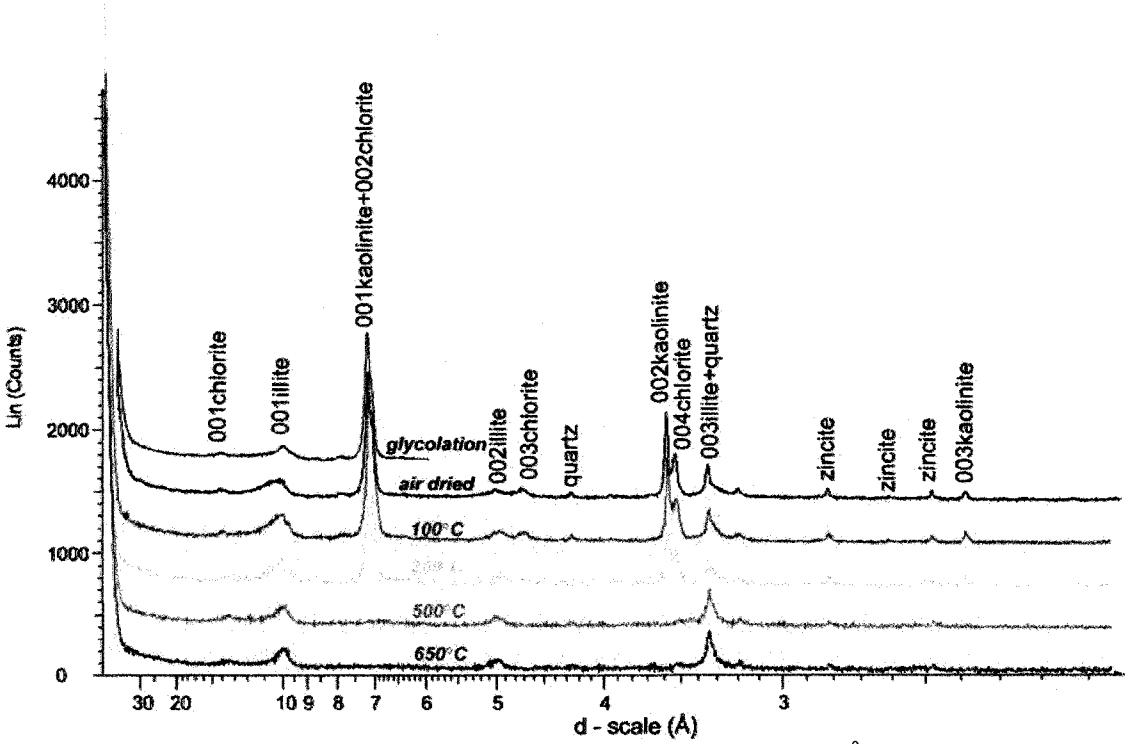

Figure 4.5: Example of the sharpening of the (001) illite peak at 10Å during glycolation (blue curve) and 110 C heating (green curve). Note that at 500 C, kaolinite was destroyed and the large chlorite peak at 3.54Å decrease in intensity and shifted to 3.45Å (Thebaud C-74, P16, 3906.75 - 3906.97m).

Aluminum-rich illite

It has been shown that the ratio of peak areas of the (002) to the (001) reflector is a reasonable indication of the octahedral composition of illite (Esquevin, 1969; Jackson, 1977). Aluminum-rich illites have ratios of >0.4, whereas magnesium and iron-rich illite have low ratios of <0.15. Electron microprobe analysis show that illite is enriched in aluminum, ranging from 20 to 30 %, with most analyses having >24% Al_2O_3. (002)/(001) ratio values range from 0.41 to 1.97, with only two samples, Thebaud C-74 P27 and P16 having lower values of 0.29 and 0.31, respectively. This range indicates that the illite is enriched in aluminum (Table 4.2).

Table 4.2: Parameters for characterizing illite from X-ray diffraction patterns.

Well	Top depth (m)	Top depth (m)	Plug	(001) d-spacing (Å)	(002) d-spacing (Å)	(001) d-spacing / (002) d-spacing	(001) peak area	(002) peak area	(001) peak area / (002) peak area
Thebaud C-74	3864.52	3864.84	P2	10.12	4.96	2.04	312.80	454.80	1.45
Thebaud C-74	3865.56	3865.75	P3	10.18	4.97	2.05	347.80	263.50	0.76
Thebaud C-74	3876.72	3876.90	P7	10.18	4.91	2.07	65.33	105.00	1.61
Thebaud C-74	3879.56	3879.78	P10	10.49	5.02	2.09	48.70	41.59	0.85
Thebaud C-74	3881.59	3881.80	P11	10.05	4.83	2.08	90.61	129.40	1.43
Thebaud C-74	3882.96	3883.17	P12	10.16	4.90	2.08	165.70	176.90	1.07
Thebaud C-74	3902.65	3902.81	P13	10.29	5.00	2.06	97.90	74.33	0.76
Thebaud C-74	3905.10	3905.37	P14	10.08	4.98	2.03	69.55	75.71	1.09
Thebaud C-74	3906.75	3906.97	P16	10.16	5.00	2.03	184.10	54.28	0.29
Thebaud C-74	3907.93	3908.11	P17	10.21	4.97	2.06	202.30	209.90	1.04
Thebaud C-74	3908.65	3908.88	P18	10.14	4.91	2.07	133.20	253.50	1.90
Thebaud C-74	3911.66	3911.82	P20	10.15	4.90	2.07	55.62	109.40	1.97
Thebaud C-74	3912.40	3912.58	P21	10.07	4.93	2.04	53.03	87.12	1.64
Thebaud C-74	3913.73	3913.95	P22	10.07	4.96	2.03	30.87	32.49	1.05
Thebaud C-74	3915.74	3915.90	P24	10.20	4.97	2.05	40.24	36.11	0.90
Thebaud C-74	3917.06	3917.28	P25	10.13	5.00	2.03	44.16	39.60	0.90
Thebaud C-74	3918.64	3918.82	P26	10.19	4.98	2.05	58.53	68.53	1.17
Thebaud C-74	3920.04	3920.25	P27	10.16	-	-	66.93	-	-
Thebaud C-74	3921.98	3922.20	P29	10.20	4.91	2.07	51.39	86.99	1.69
Thebaud C-74	3924.50	3924.67	P30	10.18	4.96	2.05	60.32	64.58	1.07
Thebaud C-74	3926.15	3926.33	P31	10.23	4.98	2.06	246.90	165.30	0.67
Venture 1	4591.48	4591.77	5	10.42	5.01	2.08	272.30	84.82	0.31
Venture 1	4598.35	4598.59	28	10.13	5.00	2.03	159.70	75.18	0.47
Venture 1	4600.87	4601.23	35	10.12	4.98	2.03	114.50	97.17	0.85
Venture 1	4606.32	4606.61	51	10.10	4.98	2.03	171.40	107.80	0.63
Venture 1	4614.81	4615.17	76	10.07	4.97	2.02	98.44	93.78	0.95
Venture 3	4871.58	4871.90	5	10.15	4.97	2.04	94.12	69.95	0.74
Venture 3	4872.58	4872.70	8	10.26	4.98	2.06	59.72	34.16	0.57
Venture 3	4878.62	4878.80	25	9.99	4.94	2.02	36.25	15.01	0.41
Venture 3	4882.37	4882.68	38	10.10	4.97	2.03	30.48	12.73	0.42
Venture 3	4885.62	4885.90	49	9.97	4.93	2.02	28.93	48.97	1.69
Venture 3	4887.39	4888.32	54	10.17	5.01	2.03	326.00	138.40	0.42
Venture 4	5341.32	5341.52	2	10.11	4.98	2.03	144.70	94.50	0.65
Venture 4	5371.77	5371.97	22	10.07	4.97	2.02	75.22	64.47	0.86
Venture 4	5372.85	5373.18	25	10.05	4.94	2.03	66.28	78.42	1.18
Venture 4	5374.79	5375.06	30	10.06	4.98	2.02	80.62	120.70	1.50
Venture 4	5381.34	5381.77	50	10.06	4.99	2.01	54.19	68.86	1.27
Venture 4	5383.28	5383.56	56	10.06	4.98	2.02	64.76	63.57	0.98
Venture 4	5384.68	5384.98	61	10.04	4.96	2.02	68.37	79.22	1.16
Venture 4	5387.54	5387.83	68	10.07	4.97	2.02	42.60	31.14	0.73
Venture 4	5389.30	5389.60	74	10.16	4.97	2.04	50.96	62.09	1.22
Venture 4	5391.51	5391.83	80	10.13	4.97	2.04	29.02	35.81	1.23
Venture 4	5393.96	5394.15	87	10.12	4.97	2.04	48.53	81.40	1.68
Venture 4	5395.23	5395.57	90	10.14	4.96	2.04	36.49	64.31	1.76

CHAPTER 5: WHOLE ROCK GEOCHEMISTRY

5.1 Introduction

Whole rock geochemistry was conducted on the suite of small plug samples representing a range of stratigraphic levels, petrographic types, porosity and permeabilites. The geochemical data was combined with: thin section observations and classification, X-ray diffraction peak areas, as well as porosity and permeability data obtained from Exxon Mobil. The data set was subjected to statistical analysis to investigate the relationship between the mineralogy and the chemistry of the samples. A whole rock geochemical analysis was not conducted on Thebaud C-74 sample P23 because it is a poorly sorted conglomerate with granules and pebble-sized grains. All depths in text and on figures are measured below Kelly bushing unless otherwise indicated.

5.2 Methods

30 to 50 grams of representative sample was removed from each plug using a rock saw and cut into small pieces, one to two centimeters wide. The pieces were brushed vigorously with a toothbrush, rinsed in deionized water and dried with Kimwipes. The pieces were initially crushed using a hammer, and then pulverized in a ball mill. Sample powders were sent to Activation Laboratories in Ancaster, Ontario, for analysis of major, minor, trace and rare earth elements (REE).

Seven sandstone types are distinguished using a polarizing microscope (Figure 5.1): (1) well sorted with chlorite rims; (2) well sorted with chlorite rims and pore-filling clays; (3) carbonate-cemented; (4) partially dissolved carbonate-cemented with chlorite rims; (5) silica-cemented; (6) muddy; and (7) poorly sorted from transgression surfaces.

Each sample was also classified based on the quality (abundance and thickness) of chlorite rims seen in thin section.

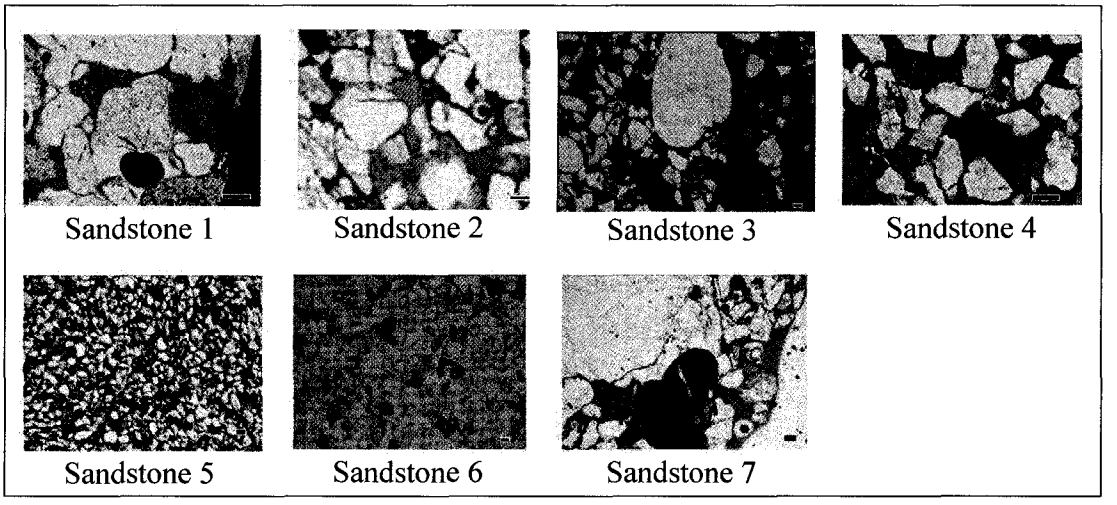

Figure 5.1: Sandstone types seen in thin section (bars are equal to 100 μm).

5.3 Results

Whole rock geochemical data, consisting of major elements (reported in weight percent as oxides), trace and rare earth elements (REE) (in parts per million (ppm)) are given in Table 5.1.

Variation in element abundance is strongly controlled by the mineralogy of the samples. SiO_2 is present principally in quartz, the predominant framework mineral, but also in feldspar, detrital and diagenetic phyllosilicates mica, chlorite, other and clay minerals. Al_2O_3 is in feldspar, ferromagnesian minerals and clays. Thus, because SiO_2 and Al_2O_3 are the two dominant oxides present, they inversely covary as a result of analyses being presented as percentages. Other elements, principally in framework grains, include NaO_2 and K_2O in feldspars, together with CaO, which also occurs in calcite cement. Elements such as Mn and Sr are also significant components of carbonate minerals. Minor or trace elements in heavy minerals include TiO_2 in rutile, Zr and Hf in

zircon, and Cr in chromite. Elements predominantly found in diagenetic cements include CaO in carbonate cements, MgO and $Fe_2O_{3(T)}$ in some carbonate cements and chlorite, and P_2O_5 in francolite. SiO_2 is also present in some sandstones as silica cement.

5.4 Statistical analysis of geochemical and other data

5.4.1 Approach

The statistical analysis package SYSTAT version 11 was used to apply a variety of statistical methods to a suite of selected data: element abundances for SiO_2, Al_2O_3, Fe_2O_3 (total), MnO, MgO, CaO, Na_2O, K_2O, TiO_2, P_2O_5, Sc, V, Cr, Co, Ni, S, Ga, As, Rb, Sr, Y, Zr, Nb, Cs, Ba, La, Ce, Nd, Eu, Tb, Dy, Er, Tm, Yb, Lu, Hf, Ta, Pb, Th, and U), together with abundance of chlorite rims (categorized from thin sections into four groups from 1 (none) to 4 (excellent or well developed)), core plug sample porosity and permeability, and chlorite peak areas from the X-ray diffractograms (Table 5.1).

5.4.2 Correlation Matrices

The production of a correlation matrix (Table 5.2), using the whole rock geochemical data, thin section observations, core petrophysical measurements and X-ray diffraction data shows the following associations between elements:

The ranked estimate of the quality of chlorite rims (Table 5.2) correlates positively with porosity measured on core plugs ($R^2 = 0.89$). This confirms the basic assumption of this thesis, that chlorite rims act to significantly preserve porosity during diagenesis, and also suggests that the ranking of chlorite rim type is reasonably robust.

Permeability determined from core plugs correlates positively with Ba ($R^2 = 0.846$), but not as strongly with any other element. Neither does Ba correlate strongly

with geochemically similar elements such as K. Therefore this correlation with permeability is interpreted to result from invasion of permeable strata by drilling mud.

Fe_2O_3 (total), Al_2O_3, MgO, Sc, V, Ni and Ga show positive intercorrelations (R^2 values > 0.7), interpreted to result from the presence of chlorite within samples. There is a positive correlation ($R^2 = 0.70$) between the ratio of (001) to (004) chlorite peak areas and MgO, indicating the presence of Mg-rich chlorite in some samples.

Silica shows strong negative correlations with MnO ($R^2 = -0.84$), CaO ($R^2 = -0.92$), and Sr ($R^2 = -0.86$). This is comparable to thin section observations, where extensive silica cement and carbonate cement are rarely seen together. In addition, CaO correlates negatively with Na_2O ($R^2 = -0.74$), with Na probably principally in albite. K_2O shows a high positive correlation with Rb ($R^2 = 0.98$) and Cs ($R^2 = 0.85$) and is probably present in potassium feldspar.

TiO_2 and P_2O_5 correlate positively with each other ($R^2 = 0.91$) and with Sc, V, Nb, La, Ce, Nb, Eu, Tb, Dy, Ta and U (R^2 values > 0.78). TiO_2 also correlates positively with Cr, Y, Zr, Tm, Yb, Lu, Hf and Th (R^2 values > 0.82)

5.4.3 Principal component analysis: all data

Principal component analysis (PCA) was initially conducted to obtain ideas that could be followed up by more rigorous testing. Six principal components explained about 90 percent of the variation in the data (Table 5.3).

Table 5.1: Whole rock geochemical data for plug samples.

well	sample	industry sand	top measured depth (m)	bottom measured depth (m)	mean grain size* (µm)	Udden-Wentworth grain-size**	matrix* (%)	sandstone type*	chlorite rims*	porosity† (%)	permeability‡ (mD)	(001)/(004) chlorite XRD peak area	SiO_2 (%)	Al_2O_3 (%)	Fe_2O_3 (total) (%)	MnO (%)	MgO (%)	CaO (%)	Na_2O (%)	K_2O (%)	TiO_2 (%)	P_2O_5 (%)	LOI (%)	Total (%)
Thebaud C-74	P2	Sandstone A	3864.52	3864.84	136	fL	20	6	4	12.8	0.32	0.09	82.34	5.33	4.65	0.01	0.57	0.82	1.23	0.48	0.72	0.08	2.71	98.94
Thebaud C-74	P3	Sandstone A	3865.56	3865.75	160	fL	20	6	4	11.5	0.02	0.04	81.18	6.46	4.67	0.02	0.61	1.20	0.83	0.86	0.81	0.09	3.49	100.20
Thebaud C-74	P7	Sandstone A	3876.72	3876.90	136	fL	30	4	4	24.6	83.1	0.07	85.05	5.21	3.95	0.02	0.44	0.99	1.23	0.42	0.70	0.09	2.16	100.20
Thebaud C-74	P10	Sandstone A	3879.56	3879.78	152	fL	1	4	4	24.3	99.7	0.07	87.59	4.74	3.21	0.01	0.38	0.43	1.13	0.39	0.71	0.08	1.67	100.30
Thebaud C-74	P11	Sandstone A	3881.59	3881.80	136	fL	1	4	4	23.4	80.5	0.06	85.91	4.48	2.93	0.01	0.36	0.60	1.33	0.42	1.00	0.09	1.63	98.75
Thebaud C-74	P12	Sandstone A	3882.96	3883.17	128	fL	1	4	3	17.4	2.45	0.05	85.38	4.27	2.82	0.01	0.36	0.92	1.39	0.42	0.79	0.10	2.21	98.66
Thebaud C-74	P13	Sandstone A	3902.65	3902.81	320	mL	trace	5	2	10.5	2.1	0.08	88.70	2.43	1.55	0.02	0.12	1.92	1.26	0.12	0.29	0.06	2.70	99.18
Thebaud C-74	P14	Sandstone B	3905.10	3905.37	240	fU	trace	2	2	14.8	13.7	0.00	90.45	2.71	1.22	0.02	0.12	1.22	1.20	0.21	0.34	0.06	1.77	99.31
Thebaud C-74	P16	Sandstone B	3906.75	3906.97	200	fL	5	2	2	11.6	1.06	0.06	90.43	3.81	1.66	0.01	0.13	0.43	1.12	0.34	0.45	0.07	1.88	100.30
Thebaud C-74	P17	Sandstone B	3907.93	3908.11	ps	-	0	3	2	8.9	0.66	0.06	75.63	2.64	2.85	0.10	0.31	9.05	0.54	0.28	0.28	0.04	8.15	99.87
Thebaud C-74	P18	Sandstone B	3908.65	3908.88	ps	-	3	4	3	12.9	1.37	0.07	86.28	2.71	3.12	0.02	0.29	1.70	1.05	0.19	0.35	0.04	2.89	98.64
Thebaud C-74	P19	Sandstone B	3909.92	3910.07	280	mL	trace	4	3	10.3	0.37	n/a	89.45	1.95	2.00	0.01	0.17	1.41	0.99	0.18	0.37	0.08	1.94	98.56
Thebaud C-74	P20	Sandstone B	3911.66	3911.82	220	fU	1-3	1	4	20.3	30.4	0.09	90.01	3.14	2.73	0.00	0.29	0.32	1.14	0.13	0.59	0.06	1.04	99.45
Thebaud C-74	P21	Sandstone B	3912.40	3912.58	400	mU	1-3	2	4	24.3	524	0.12	90.31	3.24	2.00	0.01	0.19	0.32	1.37	0.25	0.34	0.07	1.11	99.22
Thebaud C-74	P22	Sandstone B	3913.73	3913.95	420	mU	1-3	2	4	24.4	896	0.13	89.29	2.29	2.25	0.03	0.21	0.59	0.94	0.13	0.26	0.05	2.01	98.09
Thebaud C-74	P24	Sandstone B	3915.74	3915.90	320	mL	2	2	2	19	236	0.10	91.31	2.40	2.16	0.03	0.18	0.33	0.98	0.01	0.25	0.05	1.50	99.21
Thebaud C-74	P25	Sandstone B	3917.06	3917.28	ps	-	1	2	3	21.8	558	0.10	91.83	2.34	1.84	0.02	0.17	0.42	0.95	0.18	0.28	0.05	1.20	99.28
Thebaud C-74	P26	Sandstone B	3918.64	3918.82	ps	-	5-7	2	2	8.6	0.96	0.06	89.80	2.55	1.66	0.01	0.12	1.05	1.12	0.12	0.26	0.05	1.94	98.61
Thebaud C-74	P27	Sandstone B	3920.04	3920.25	136	fL	25	2	2	11.8	0.13	0.11	84.71	6.00	4.28	0.01	0.46	0.26	1.26	0.28	0.76	0.11	2.02	100.20
Thebaud C-74	P29	Sandstone B	3921.98	3922.20	ps	-	-I	-	3	11.9	2.93	0.08	85.07	3.48	1.70	0.03	0.17	2.93	1.30	0.25	0.39	0.07	3.29	98.66
Thebaud C-74	P30	Sandstone B	3924.50	3924.67	168	fL	30	2	2	11	0.16	0.11	81.77	5.86	4.13	0.02	0.38	1.02	1.75	0.23	0.61	0.12	3.16	99.03
Thebaud C-74	P31	Sandstone B	3926.15	3926.33	168	fL	20	2	2	11	0.13	0.00	78.70	7.61	3.88	0.02	0.41	0.52	1.93	0.79	0.85	0.14	3.77	98.59
Venture 1	SP5	Samdstone 2	4591.48	4591.77	240	fU	trace	4	1	7.1	0.16	0.00	91.63	1.68	1.71	0.02	0.16	0.49	0.73	0.24	0.71	0.09	1.62	99.08
Venture 1	SP28	Samdstone 2	4598.35	4598.59	120	vfU	0	3	1	1.3	0	0.00	63.93	2.23	2.30	0.08	0.36	16.71	0.22	0.54	0.56	0.09	13.21	100.20
Venture 1	SP35	Samdstone 2	4600.87	4601.23	280	mL	3 10	4	2	7.2	0.12	0.10	86.42	2.40	2.56	0.05	0.53	1.95	0.72	0.35	0.47	0.11	3.13	98.68
Venture 1	SP51	Samdstone 2	4606.32	4606.61	232	fU	10	4	1	6.7	0.04	0.00	83.38	5.21	3.88	0.03	0.60	1.11	0.42	1.17	0.54	0.15	3.70	100.20
Venture 1	SP76	Samdstone 2	4614.81	4615.17	136	fL	1	1	3	13.3	0.26	0.10	85.69	4.84	4.03	0.01	0.72	0.33	0.97	0.73	0.47	0.13	2.13	100.10
Venture 3	SP5	Samdstone 3	4871.58	4871.90	ps	-	0	3	1	3.4	0	0.13	61.97	1.82	1.84	0.08	0.57	18.23	0.24	0.31	0.39	0.11	14.93	100.50
Venture 3	SP8	Samdstone 3	4872.58	4872.70	ps	-	5	3	1	2.8	0	0.14	55.18	2.58	3.37	0.17	0.71	20.01	0.35	0.40	1.35	0.34	15.41	99.88
Venture 3	SP25	Samdstone 3	4878.62	4878.80	168	fL	10	4	4	21.8	23.3	0.25	77.24	4.95	6.46	0.03	1.50	1.69	0.85	0.58	1.73	0.47	4.21	99.71
Venture 3	SP38	Samdstone 3	4882.37	4882.68	176	fL	5	4	4	25.4	3.63	0.43	82.14	4.12	5.13	0.03	1.31	1.26	0.84	0.45	1.24	0.37	3.34	100.20
Venture 3	SP49	Samdstone 3	4885.62	4885.90	128	fL	5	4	4	21.8	9.56	0.25	78.78	5.37	6.10	0.03	1.93	1.35	0.88	0.68	0.95	0.33	3.94	100.30
Venture 4	SP2	Samdstone 2	5341.32	5341.52	240	fU	1	5	2	5.57	1.22	0.00	91.27	2.74	1.28	0.01	0.15	0.19	0.77	0.64	0.27	0.07	1.28	98.66
Venture 4	SP22	Samdstone 2	5371.77	5371.97	144	fL	1	3	1	3.1	0.03	0.07	65.58	3.17	2.97	0.19	0.65	13.48	0.31	0.70	0.68	0.16	12.16	100.00
Venture 4	SP25	Samdstone 2	5372.85	5373.18	128	fL	1-3	4	4	21.8	23.3	0.16	84.00	4.21	3.64	0.02	0.67	1.63	0.72	0.77	1.07	0.20	3.58	100.50
Venture 4	SP30	Samdstone 2	5374.79	5375.06	144	fL	5	1	3	18.7	5.35	0.14	83.06	4.54	3.96	0.01	0.72	0.52	1.05	0.72	0.98	0.18	2.62	98.35
Venture 4	SP50	Samdstone 2	5381.34	5381.77	184	fU	5	4	3	20.9	56.9	0.13	83.04	3.41	3.23	0.07	0.80	1.89	1.02	0.58	0.76	0.19	4.19	99.17
Venture 4	SP56	Samdstone 2	5383.28	5383.56	160	fL	1-3	3	1	6.5	0.04	0.15	67.96	2.28	1.92	0.15	0.35	14.14	0.30	0.52	0.68	0.17	12.00	100.50
Venture 4	SP61	Samdstone 2	5384.68	5384.98	128	fL	15	4	3	21.1	11.2	0.16	83.39	4.26	3.54	0.02	0.69	1.13	1.04	0.87	1.21	0.28	3.03	99.45
Venture 4	SP68	Samdstone 2	5387.54	5387.83	128	fL	10	4	1	1.9	0.03	0.13	54.72	3.57	4.35	0.28	0.85	18.28	0.29	0.58	1.07	0.29	15.94	100.20
Venture 4	SP74	Samdstone 2	5389.30	5389.60	152	fL	15-20	4	4	24.6	15.8	0.16	79.48	3.85	4.06	0.03	0.79	1.63	0.98	0.55	3.07	0.59	3.73	98.75
Venture 4	SP80	Samdstone 2	5391.51	5391.83	168	fL	15	4	4	20.8	16.2	0.13	77.44	4.24	4.72	0.08	1.15	2.46	1.09	0.67	2.06	0.48	4.76	99.15
Venture 4	SP87	Samdstone 2	5393.96	5394.15	136	fL	5	4	4	21.5	10.3	0.12	81.05	4.92	4.57	0.02	0.88	0.90	1.08	0.85	0.91	0.31	3.16	98.65
Venture 4	SP90	Samdstone 2	5395.23	5395.57	176	fL	7	2	4	23.5	38.3	0.14	82.25	4.60	4.03	0.01	0.77	0.79	1.14	0.87	1.37	0.42	2.87	99.10

*estimated from thin section; ps=poorly sorted

**Udden-Wentworth grain-size classification scheme (Wentworth, 1922).

†from core plugs calculated by Core Laboratories using Boyle's Law and helium ga

‡from core plugs calculated by Core Laboratories measured using a steady state routine gas permeameter and a "hassler type" core hol

Table 5.1 (continued) Whole rock geochemical data for plug samples.

well	sample	Sc (ppm)	V (ppm)	Cr (ppm)	Co (ppm)	Ni (ppm)	S (%)	Ga (ppm)	As (ppm)	Rb (ppm)	Sr (ppm)	Y (ppm)	Zr (ppm)	Nb (ppm)	Cs (ppm)	Ba (ppm)	La (ppm)	Ce (ppm)	Nd (ppm)	Eu (ppm)	Tb (ppm)	Dy (ppm)	Er (ppm)	Tm (ppm)	Yb (ppm)	Lu (ppm)	Hf (ppm)	Ta (ppm)	Pb (ppm)	Th (ppm)	U (ppm)
Thebaud C-74	P2	5.00	56.00	140.00	6.00	26.00	0.23	8.00	11.00	20.00	140.00	18.20	417.00	24.80	0.90	275.00	30.60	72.30	26.20	0.90	0.62	3.42	1.97	0.29	1.90	0.29	9.90	1.78	6.00	4.82	1.30
Thebaud C-74	P3	7.00	74.00	130.00	8.00	26.00	0.35	10.00	13.00	33.00	169.00	20.20	463.00	29.80	1.50	175.00	36.50	84.30	29.90	1.04	0.70	3.88	2.27	0.34	2.33	0.35	11.60	2.17	7.00	6.84	1.71
Thebaud C-74	P7	4.00	38.00	120.00	7.00	30.00	0.28	10.00	0.00	13.00	91.00	18.60	488.00	30.90	0.50	675.00	26.60	55.20	22.20	0.83	0.60	3.34	2.03	0.31	2.01	0.33	12.10	2.13	10.00	4.78	1.50
Thebaud C-74	P10	4.00	41.00	140.00	9.00	25.00	0.13	8.00	0.00	13.00	73.00	17.20	495.00	26.90	0.50	739.00	26.80	55.20	21.50	0.76	0.51	3.02	1.87	0.30	1.97	0.31	12.20	2.08	10.00	4.99	1.46
Thebaud C-74	P11	4.00	47.00	200.00	8.00	21.00	0.18	7.00	0.00	13.00	67.00	23.30	1076.00	27.80	0.40	437.00	30.30	64.50	25.50	0.87	0.67	4.09	2.76	0.44	3.04	0.52	25.80	2.17	9.00	6.23	2.26
Thebaud C-74	P12	2.00	34.00	140.00	6.00	18.00	0.21	7.00	0.00	14.00	137.00	22.30	878.00	24.40	0.50	175.00	26.90	56.10	22.90	0.79	0.63	3.67	2.43	0.39	2.66	0.44	19.00	1.89	7.00	5.59	1.97
Thebaud C-74	P13	0.00	11.00	90.00	8.00	23.00	0.44	3.00	13.00	6.00	73.00	7.30	188.00	13.00	0.20	165.00	10.70	23.00	9.66	0.43	0.26	1.39	0.76	0.12	0.75	0.11	4.00	1.05	18.00	2.00	0.73
Thebaud C-74	P14	2.00	19.00	90.00	6.00	14.00	0.28	3.00	5.00	6.00	56.00	7.40	178.00	14.60	0.20	468.00	10.70	23.10	8.85	0.42	0.22	1.31	0.81	0.13	0.85	0.13	4.30	1.07	12.00	2.26	0.57
Thebaud C-74	P16	3.00	30.00	90.00	8.00	18.00	0.65	4.00	7.00	10.00	93.00	8.40	216.00	17.00	0.30	223.00	14.60	31.30	12.00	0.47	0.25	1.47	0.97	0.15	0.99	0.16	5.30	1.38	11.00	2.97	0.75
Thebaud C-74	P17	4.00	23.00	70.00	3.00	13.00	0.43	4.00	8.00	8.00	396.00	14.60	166.00	10.50	0.30	118.00	16.20	37.60	16.10	0.86	0.51	2.83	1.33	0.19	1.17	0.17	4.00	0.77	5.00	2.64	0.64
Thebaud C-74	P18	3.00	31.00	110.00	4.00	16.00	0.58	4.00	8.00	7.00	136.00	10.80	367.00	11.80	0.30	201.00	15.70	35.10	14.30	0.52	0.33	1.84	1.02	0.16	1.05	0.16	7.20	0.91	4.00	3.69	0.81
Thebaud C-74	P19	2.00	21.00	120.00	3.00	13.00	0.33	3.00	0.00	5.00	91.00	9.10	313.00	9.00	0.20	354.00	12.40	27.90	12.00	0.59	0.32	1.68	1.00	0.15	1.03	0.17	7.40	0.78	6.00	2.56	0.92
Thebaud C-74	P20	3.00	33.00	160.00	2.00	19.00	0.08	6.00	0.00	7.00	72.00	13.50	550.00	17.90	0.20	1041.00	18.00	39.00	15.00	0.55	0.38	2.41	1.56	0.25	1.69	0.27	12.20	1.36	4.00	4.04	1.25
Thebaud C-74	P21	3.00	23.00	90.00	3.00	17.00	0.14	4.00	0.00	5.00	76.00	7.90	137.00	18.20	0.20	1457.00	13.20	27.50	10.00	0.42	0.22	1.36	0.85	0.13	0.85	0.13	3.30	1.42	5.00	2.62	0.60
Thebaud C-74	P22	2.00	18.00	110.00	3.00	15.00	0.14	3.00	0.00	4.00	392.00	6.90	114.00	13.90	0.10	11670.00	10.90	22.50	8.28	0.29	0.19	1.16	0.72	0.11	0.76	0.12	3.10	1.14	8.00	2.18	0.51
Thebaud C-74	P24	0.00	18.00	120.00	3.00	19.00	0.14	3.00	0.00	4.00	154.00	5.40	113.00	13.20	0.10	4240.00	10.30	21.00	7.44	0.29	0.15	0.96	0.60	0.10	0.63	0.09	2.70	1.04	8.00	1.97	0.47
Thebaud C-74	P25	0.00	16.00	110.00	3.00	15.00	0.08	3.00	0.00	4.00	74.00	5.70	149.00	14.40	0.10	1654.00	10.50	21.60	7.62	0.28	0.16	1.03	0.68	0.11	0.74	0.11	3.70	1.12	5.00	2.22	0.53
Thebaud C-74	P26	3.00	21.00	90.00	3.00	16.00	0.40	3.00	0.00	4.00	80.00	6.20	166.00	11.40	0.20	277.00	8.41	17.00	6.00	0.25	0.16	1.03	0.69	0.11	0.78	0.13	3.50	0.92	4.00	1.76	0.41
Thebaud C-74	P27	5.00	48.00	120.00	4.00	28.00	0.06	12.00	0.00	11.00	107.00	12.60	370.00	31.90	0.40	91.00	24.10	49.20	18.20	0.69	0.39	2.39	1.54	0.24	1.60	0.26	9.40	2.60	4.00	4.31	1.24
Thebaud C-74	P29	2.00	25.00	110.00	2.00	12.00	0.09	4.00	0.00	5.00	93.00	12.30	156.00	20.10	0.20	173.00	13.20	28.60	11.60	0.85	0.38	2.31	1.25	0.18	1.14	0.16	3.90	1.52	0.00	2.71	0.60
Thebaud C-74	P30	3.00	40.00	90.00	13.00	33.00	0.79	9.00	10.00	9.00	127.00	10.90	260.00	29.50	0.30	125.00	20.80	41.80	15.30	0.64	0.33	2.06	1.27	0.19	1.26	0.20	5.80	2.63	25.00	3.96	0.98
Thebaud C-74	P31	6.00	64.00	110.00	11.00	30.00	1.08	11.00	6.00	25.00	140.00	16.00	370.00	33.30	0.90	223.00	32.20	64.90	22.50	0.91	0.49	2.91	1.92	0.30	1.96	0.30	8.60	3.11	20.00	5.44	1.44
Venture 1	SP5	2.00	40.00	190.00	4.00	15.00	0.69	3.00	0.00	10.00	71.00	9.80	489.00	25.40	0.20	132.00	20.10	39.50	14.70	0.54	0.29	1.64	1.03	0.16	1.10	0.18	10.30	1.71	10.00	3.00	1.18
Venture 1	SP28	2.00	28.00	120.00	4.00	15.00	0.78	3.00	0.00	18.00	466.00	9.80	297.00	17.10	0.50	82.00	17.10	32.90	12.80	0.52	0.29	1.67	1.09	0.17	1.14	0.19	7.70	1.12	4.00	2.98	1.15
Venture 1	SP35	6.00	56.00	130.00	4.00	16.00	0.18	4.00	0.00	12.00	108.00	11.40	263.00	14.70	0.40	90.00	27.90	56.40	21.40	0.94	0.42	2.22	1.13	0.17	1.07	0.16	6.00	1.05	0.00	2.78	0.89
Venture 1	SP51	5.00	59.00	90.00	11.00	33.00	0.86	7.00	6.00	39.00	105.00	10.90	156.00	16.60	1.00	149.00	20.50	41.70	16.30	0.85	0.38	2.07	1.21	0.18	1.13	0.17	4.20	1.07	16.00	3.71	1.07
Venture 1	SP76	5.00	50.00	70.00	6.00	31.00	0.05	7.00	0.00	25.00	111.00	7.40	109.00	15.80	0.70	156.00	14.30	29.60	11.10	0.51	0.24	1.37	0.83	0.13	0.81	0.12	2.60	0.89	4.00	3.06	0.83
Venture 3	SP5	3.00	44.00	50.00	5.00	10.00	0.22	3.00	5.00	10.00	348.00	9.50	109.00	16.90	0.30	106.00	18.10	36.90	14.40	0.80	0.34	1.82	0.93	0.13	0.82	0.12	2.60	1.04	3.00	1.95	0.68
Venture 3	SP8	6.00	129.00	140.00	26.00	20.00	0.64	5.00	13.00	14.00	436.00	19.60	360.00	58.70	0.40	82.00	50.40	103.00	39.70	2.18	0.81	3.90	1.90	0.27	1.70	0.25	9.30	3.91	25.00	4.08	2.28
Venture 3	SP25	8.00	232.00	140.00	14.00	29.00	0.09	10.00	0.00	18.00	308.00	19.90	400.00	71.30	0.50	599.00	70.60	136.00	49.20	2.37	0.83	4.27	2.10	0.30	1.92	0.28	9.90	4.24	9.00	4.92	2.36
Venture 3	SP38	7.00	126.00	110.00	12.00	25.00	0.06	7.00	0.00	15.00	240.00	14.60	264.00	54.50	0.50	356.00	44.30	86.10	31.20	1.51	0.55	2.86	1.47	0.21	1.36	0.20	6.30	3.11	5.00	4.01	1.60
Venture 3	SP49	7.00	117.00	70.00	17.00	34.00	0.11	8.00	0.00	21.00	256.00	13.30	175.00	38.00	0.60	201.00	36.50	71.80	25.80	1.32	0.55	2.85	1.38	0.19	1.23	0.18	4.30	2.14	6.00	4.08	1.27
Venture 4	SP2	3.00	35.00	70.00	4.00	16.00	0.48	4.00	0.00	20.00	75.00	6.00	93.00	9.20	0.40	124.00	12.10	24.30	9.71	0.48	0.21	1.12	0.58	0.08	0.54	0.08	1.90	0.59	6.00	1.54	0.48
Venture 4	SP22	4.00	53.00	100.00	5.00	16.00	0.12	5.00	0.00	21.00	538.00	12.80	248.00	21.20	0.60	110.00	22.60	44.30	18.20	1.04	0.46	2.43	1.29	0.19	1.26	0.19	6.50	1.43	5.00	3.31	1.14
Venture 4	SP25	6.00	81.00	180.00	9.00	28.00	0.11	6.00	0.00	25.00	206.00	20.00	552.00	35.30	0.70	198.00	32.30	62.90	24.90	1.33	0.69	3.77	2.04	0.32	2.14	0.33	13.80	2.05	8.00	5.38	1.88
Venture 4	SP30	5.00	74.00	150.00	10.00	33.00	0.16	7.00	0.00	25.00	194.00	13.80	368.00	29.70	0.80	211.00	30.40	58.30	21.00	0.90	0.43	2.54	1.58	0.25	1.64	0.25	9.90	1.82	9.00	4.47	1.58
Venture 4	SP50	4.00	70.00	130.00	5.00	19.00	0.05	5.00	0.00	21.00	201.00	15.20	300.00	30.20	0.50	192.00	29.20	54.80	19.90	1.01	0.45	2.55	1.36	0.19	1.20	0.19	6.60	1.55	3.00	3.36	1.18
Venture 4	SP56	4.00	41.00	120.00	3.00	11.00	0.07	4.00	0.00	17.00	427.00	19.80	261.00	25.90	0.40	108.00	25.20	51.50	20.30	1.14	0.63	3.69	1.80	0.25	1.54	0.23	6.70	1.57	3.00	2.95	1.04
Venture 4	SP61	7.00	107.00	210.00	8.00	27.00	0.07	7.00	0.00	25.00	222.00	16.00	617.00	42.10	0.70	207.00	43.00	82.70	29.80	1.26	0.52	2.95	1.81	0.28	1.90	0.31	14.40	2.37	5.00	5.41	1.93
Venture 4	SP68	6.00	115.00	220.00	8.00	22.00	0.14	8.00	0.00	21.00	853.00	22.40	696.00	35.70	0.70	103.00	51.80	89.60	32.70	1.54	0.74	3.96	2.16	0.33	2.24	0.34	18.00	2.31	5.00	5.16	2.11
Venture 4	SP74	9.00	223.00	680.00	11.00	21.00	0.01	8.00	0.00	19.00	257.00	36.00	2258.00	115.00	0.60	186.00	80.60	164.00	62.40	2.73	1.16	6.41	4.05	0.63	4.48	0.75	47.50	6.01	4.00	11.40	4.95
Venture 4	SP80	8.00	159.00	400.00	11.00	29.00	0.04	8.00	0.00	23.00	252.00	29.80	986.00	84.80	0.60	255.00	58.90	114.00	44.60	2.11	0.96	5.44	3.17	0.48	3.21	0.49	24.50	4.16	6.00	7.13	3.27
Venture 4	SP87	6.00	73.00	120.00	8.00	33.00	0.06	7.00	0.00	27.00	227.00	13.10	276.00	36.20	0.70	206.00	31.70	56.70	19.60	0.93	0.42	2.41	1.39	0.21	1.35	0.20	6.50	1.78	4.00	3.47	1.30
Venture 4	SP90	7.00	129.00	190.00	9.00	32.00	0.07	7.00	0.00	26.00	223.00	17.50	543.00	55.10	0.70	201.00	40.40	75.50	27.90	1.34	0.57	3.22	1.88	0.28	1.93	0.29	12.60	2.74	6.00	4.76	2.03

*estimated from thin section; ps=poorly sorted

**Udden-Wentworth grain-size classification scheme (Wentworth, 1922).

[I]from core plugs calculated by Core Laboratories using Boyle's Law and helium ga

[II]from core plugs calculated by Core Laboratories measured using a steady state routine gas permeameter and a "hassler type" core hol

Table 5.2: Correlation matrix of whole rock geochemical data, thin section observations, core petrophysical measurements and X-ray diffraction data.

variables	sandstone types	chlorite rims	porosity	permeability	(001)/(004) chlorite XRD peak area	SiO_2	Al_2O_3	$Fe_2O_{3(T)}$	MnO	MgO	CaO	Na_2O	K_2O	TiO_2	P_2O_5	Sc	V	Cr	Co	Ni	S	Ga	As	Rb	Sr	Y	Zr	Nb	Cs	Ba	La	Ce	Nd	Eu	Tb	Dy	Er	Tm	Yb	Lu	Hf	Ta	Pb	Th	U
sandstone types	1																																											
chlorite rims	0.356	1																																											
porosity	0.448	**0.885**	1																																									
permeability	-0.019	0.272	0.400	1																																									
(001)/(004) chlorite XRD peak area	0.152	0.408	0.456	0.057	1																																								
SiO_2	0.463	0.425	0.512	0.305	-0.174	1																																							
Al_2O_3	0.159	0.407	0.283	-0.255	0.084	0.053	1																																						
$Fe_2O_{3(T)}$	0.179	0.476	0.326	-0.265	0.547	-0.257	**0.724**	1																																					
MnO	-0.328	-0.521	-0.535	-0.130	0.083	**-0.291**	0.027	1																																					
MgO	0.196	0.355	0.272	-0.267	**0.704**	-0.375	0.401	**0.852**	0.183	1																																			
CaO	-0.560	-0.608	-0.645	-0.188	0.016	**-0.392**	-0.118	**0.855**	0.070	1																																			
Na_2O	0.346	0.477	0.515	0.113	-0.094	0.619	0.521	0.098	-0.659	-0.176	**-0.814**	1																																	
K_2O	0.068	0.115	0.003	-0.359	0.061	-0.283	0.552	0.538	0.080	0.529	0.019	-0.181	1																																
TiO_2	0.236	0.360	0.339	-0.257	0.441	-0.298	0.307	0.590	0.125	**0.802**	0.025	0.002	0.407	1																															
P_2O_5	0.242	0.291	0.296	-0.298	0.613	-0.384	0.243	0.649	0.227	**0.774**	0.108	-0.127	0.484	**0.908**	1																														
Sc	0.144	0.368	0.305	-0.374	0.480	-0.342	0.542	**0.782**	0.133	**0.781**	0.012	-0.072	0.670	**0.775**	**0.901**	1																													
V	0.238	0.323	0.270	-0.260	0.581	-0.363	0.308	**0.713**	0.188	**0.780**	0.071	-0.122	0.467	**0.914**	**0.951**	**0.844**	1																													
Cr	0.261	0.288	0.300	-0.089	0.148	-0.091	0.057	0.234	0.070	0.219	-0.054	0.040	0.160	**0.854**	0.652	0.490	0.641	1																											
Co	0.106	0.090	0.064	-0.284	0.388	-0.394	0.400	0.575	0.170	0.603	0.156	0.002	0.365	0.548	0.617	0.553	0.631	0.188	1																										
Ni	0.372	0.428	0.388	-0.247	0.265	0.068	**0.826**	**0.778**	-0.277	0.561	-0.398	0.387	0.593	0.378	0.433	0.554	0.427	0.104	0.540	1																									
S	-0.121	-0.529	-0.554	-0.210	-0.547	-0.053	0.081	-0.228	-0.032	-0.368	0.110	0.077	0.001	-0.295	-0.341	-0.250	-0.297	-0.277	0.174	-0.033	1																							
Ga	0.192	0.393	0.271	-0.302	0.209	-0.110	**0.915**	**0.809**	-0.113	0.498	-0.241	0.384	0.478	0.500	0.408	0.651	0.494	0.244	0.426	**0.765**	-0.080	1																					
As	-0.302	-0.220	-0.397	-0.214	-0.242	-0.151	0.132	-0.021	0.040	-0.194	0.152	0.076	-0.086	-0.174	-0.219	-0.090	-0.144	-0.214	0.321	0.021	0.553	0.010	1																				
Rb	0.079	0.102	-0.044	-0.411	0.036	-0.288	0.576	0.571	0.100	0.522	0.016	-0.186	**0.978**	0.412	0.460	0.664	0.462	0.187	0.364	0.614	0.017	0.515	-0.011	1																			
Sr	-0.341	-0.337	-0.368	-0.026	0.255	**-0.392**	-0.197	0.206	**0.868**	0.341	**0.859**	-0.656	0.195	0.241	0.354	0.281	0.331	0.128	0.172	-0.160	-0.122	-0.023	-0.067	0.189	1																		
Y	0.146	0.352	0.252	-0.303	0.246	-0.375	0.355	0.527	0.252	0.448	0.128	-0.003	0.380	**0.853**	0.671	0.690	**0.704**	**0.764**	0.409	0.266	-0.274	0.556	-0.064	0.409	0.293	1																	
Zr	0.285	0.335	0.315	-0.183	0.086	-0.091	0.178	0.260	0.015	0.184	-0.069	0.137	0.162	**0.819**	0.555	0.464	0.574	**0.930**	0.201	0.118	-0.238	0.361	-0.177	0.185	0.071	**0.842**	1																
Nb	0.225	0.369	0.367	-0.193	0.502	-0.286	0.299	0.599	0.112	0.617	0.017	0.035	0.340	**0.981**	**0.927**	**0.756**	**0.920**	**0.806**	0.586	0.384	-0.286	0.493	-0.137	0.340	0.224	**0.798**	**0.741**	1															
Cs	-0.034	0.201	-0.039	-0.350	-0.003	-0.281	0.596	0.815	0.043	0.443	-0.024	-0.053	**0.947**	0.361	0.322	0.654	0.390	0.162	0.330	0.594	0.044	0.630	0.192	**0.905**	0.137	0.454	0.215	0.292	1														
Ba	-0.031	0.203	0.304	**0.845**	0.059	0.244	-0.232	-0.189	0.087	-0.209	-0.156	0.053	-0.344	-0.222	-0.202	-0.309	-0.210	-0.070	-0.232	-0.197	-0.149	-0.257	-0.156	-0.348	0.087	-0.265	-0.187	-0.171	-0.338	1													
La	0.231	0.325	0.257	-0.286	0.510	-0.421	0.354	**0.703**	0.254	**0.708**	0.122	-0.082	0.447	**0.945**	**0.905**	**0.844**	**0.959**	**0.713**	0.615	0.398	-0.285	0.569	-0.103	0.458	0.367	**0.846**	0.694	**0.932**	0.444	-0.239	1												
Ce	0.192	0.351	0.258	-0.290	0.481	-0.395	0.375	0.699	0.211	0.679	0.099	-0.060	0.428	**0.942**	**0.871**	**0.842**	**0.941**	**0.722**	0.615	0.382	-0.265	0.582	-0.005	0.448	0.318	**0.886**	**0.716**	**0.928**	0.467	-0.243	**0.992**	1											
Nd	0.188	0.337	0.245	-0.301	0.458	-0.407	0.342	0.668	0.231	0.655	0.123	-0.081	0.412	**0.947**	**0.863**	**0.826**	**0.929**	**0.742**	0.608	0.351	-0.264	0.586	-0.033	0.430	0.322	**0.881**	**0.743**	**0.930**	0.442	-0.252	**0.986**	**0.998**	1										
Eu	0.127	0.219	0.159	-0.315	0.574	-0.517	0.238	0.638	0.360	**0.711**	0.255	-0.225	0.438	**0.914**	**0.911**	**0.824**	**0.945**	0.662	0.664	0.311	-0.252	0.453	-0.042	0.438	0.431	**0.820**	0.620	**0.913**	0.381	-0.266	**0.954**	**0.956**	**0.966**	1								
Tb	0.113	0.319	0.195	-0.340	0.351	-0.464	0.390	0.617	0.314	0.576	0.201	-0.112	0.421	**0.872**	**0.749**	**0.770**	**0.801**	0.697	0.542	0.304	-0.262	0.560	0.008	0.447	0.363	**0.970**	**0.751**	**0.834**	0.484	-0.269	**0.909**	**0.929**	**0.948**	**0.913**	1						
Dy	0.120	0.354	0.239	-0.325	0.310	-0.411	0.382	0.595	0.264	0.527	0.147	-0.041	0.408	**0.867**	**0.715**	**0.746**	**0.760**	**0.725**	0.479	0.309	-0.278	0.585	-0.029	0.436	0.315	**0.990**	**0.791**	**0.822**	0.480	-0.280	**0.883**	**0.905**	**0.925**	**0.871**	**0.991**	1					
Er	0.166	0.398	0.302	-0.285	0.199	-0.289	0.433	0.531	0.136	0.410	0.030	0.102	0.377	**0.990**	**0.843**	**0.876**	**0.885**	**0.787**	0.401	0.323	-0.247	0.613	-0.070	0.406	0.193	**0.985**	**0.881**	**0.795**	0.471	-0.252	**0.828**	**0.854**	**0.875**	**0.775**	**0.938**	**0.970**	1				
Tm	0.196	0.407	0.320	-0.296	0.183	-0.248	0.428	0.495	0.100	0.360	-0.001	0.139	0.352	**0.845**	**0.809**	0.638	0.650	**0.799**	0.366	0.312	-0.242	0.603	-0.056	0.376	0.159	**0.971**	**0.903**	**0.777**	0.450	-0.238	**0.796**	**0.825**	**0.947**	**0.734**	**0.910**	**0.946**	**0.996**	1			
Yb	0.199	0.412	0.328	-0.249	0.142	-0.215	0.415	0.470	0.076	0.333	-0.026	0.154	0.334	**0.842**	0.596	0.619	0.636	**0.821**	0.341	0.300	-0.243	0.585	-0.104	0.363	0.140	**0.958**	**0.924**	**0.771**	0.437	-0.222	**0.783**	**0.810**	**0.831**	**0.711**	**0.889**	**0.930**	**0.989**	**0.998**	1		
Lu	0.219	0.405	0.337	-0.232	0.104	-0.171	0.390	0.417	0.040	0.279	-0.052	0.177	0.297	**0.820**	0.554	0.599	0.594	**0.829**	0.297	0.265	-0.233	0.557	-0.129	0.333	0.101	**0.935**	**0.945**	**0.743**	0.394	-0.209	**0.744**	**0.772**	**0.795**	0.566	**0.853**	**0.899**	**0.975**	**0.989**	**0.995**	1	
Hf	0.273	0.341	0.313	-0.187	0.094	-0.133	0.208	0.295	0.058	0.213	-0.039	0.117	0.197	**0.831**	0.568	0.493	0.590	**0.923**	0.228	0.152	-0.254	0.399	-0.186	0.221	0.111	**0.873**	**0.994**	**0.751**	0.252	-0.171	**0.719**	**0.738**	**0.764**	0.644	**0.764**	**0.825**	**0.911**	**0.931**	**0.949**	**0.985**	1	
Ta	0.185	0.325	0.323	-0.182	0.446	-0.293	0.414	0.610	0.098	0.540	0.011	0.156	0.286	**0.894**	**0.834**	**0.714**	**0.864**	**0.740**	0.651	0.407	-0.152	0.633	-0.032	0.274	0.187	**0.791**	**0.723**	**0.959**	0.289	-0.162	**0.910**	**0.916**	**0.913**	**0.872**	**0.825**	**0.917**	**0.911**	**0.784**	**0.796**	**0.780**	**0.736**	1	
Pb	0.007	-0.232	-0.155	-0.070	-0.189	-0.062	0.277	0.028	-0.014	-0.133	0.006	0.302	-0.017	-0.007	-0.036	-0.109	-0.020	-0.134	0.613	0.308	0.643	0.175	0.593	0.000	-0.133	-0.037	-0.095	0.047	0.018	-0.011	0.001	0.015	0.017	0.038	0.006	-0.013	-0.004	-0.007	-0.018	-0.029	-0.066	0.219	1	
Th	0.226	0.456	0.359	-0.249	0.183	-0.161	0.526	0.571	-0.012	0.402	-0.120	0.196	0.412	**0.860**	0.624	0.589	0.664	**0.818**	0.402	0.417	-0.190	0.660	-0.039	0.448	0.085	**0.905**	**0.898**	**0.796**	0.540	-0.224	**0.803**	**0.835**	**0.844**	**0.716**	**0.855**	**0.887**	**0.949**	**0.955**	**0.982**	**0.955**	**0.913**	**0.815**	0.017	1	
U	0.241	0.352	0.306	-0.262	0.299	-0.300	0.313	0.528	0.143	0.488	0.047	0.020	0.383	**0.967**	**0.903**	**0.797**	**0.925**	**0.883**	0.501	0.335	-0.254	0.514	-0.131	0.402	0.229	**0.921**	**0.907**	**0.920**	0.392	-0.229	**0.907**	**0.916**	**0.932**	**0.864**	**0.906**	**0.914**	**0.936**	**0.933**	**0.934**	**0.922**	**0.924**	**0.896**	0.016	**0.929**	1

indicates positive correlation >0.7

indicates negative correlation >-0.7

Table 5.3: Rotated loading matrix (varimax).

	Units	1	2	3	4	5	6	7
chlorite rims	rank 1-4	0.310	-0.593	0.130	0.296	-0.334	-0.292	0.311
porosity	%	0.273	-0.645	-0.007	0.341	-0.314	-0.405	0.159
permeability	MD	-0.171	-0.119	-0.224	-0.061	-0.120	-0.897	-0.023
(001)/(004) chlorite peak area	ratio	0.076	0.028	-0.083	0.859	-0.271	-0.098	0.163
SiO_2	wt. %	-0.199	-0.891	-0.127	-0.210	-0.135	-0.121	-0.121
Al_2O_3	wt. %	0.219	-0.367	0.659	0.156	0.242	0.080	0.482
Fe_2O_3 (total)	wt. %	0.300	-0.043	0.545	0.628	0.023	0.025	0.368
MnO	wt. %	0.113	0.929	-0.038	0.074	0.016	-0.003	0.054
MgO	wt. %	0.200	0.130	0.410	0.800	-0.158	0.079	0.114
CaO	wt. %	0.022	0.951	-0.127	0.009	0.086	0.109	0.004
Na_2O	wt. %	0.099	-0.803	-0.082	-0.078	0.222	-0.041	0.337
K_2O	wt. %	0.192	0.108	0.911	0.160	-0.041	0.122	-0.158
TiO_2	wt. %	0.840	0.014	0.165	0.483	-0.017	0.044	-0.138
P_2O_5	wt. %	0.575	0.118	0.220	0.719	-0.063	0.034	-0.205
Sc	ppm	0.512	0.071	0.527	0.549	-0.074	0.147	0.042
V	ppm	0.610	0.099	0.241	0.706	-0.020	0.055	-0.138
Cr	ppm	0.907	-0.055	-0.033	0.098	-0.118	-0.054	-0.277
Co	ppm	0.282	0.098	0.227	0.633	0.577	0.052	0.018
Ni	ppm	0.126	-0.362	0.666	0.417	0.224	0.013	0.212
S	ppm	-0.188	0.055	0.106	-0.320	0.786	0.153	-0.190
Ga	ppm	0.416	-0.211	0.541	0.261	0.152	0.097	0.513
As	ppm	-0.083	0.103	-0.003	-0.101	0.738	0.157	0.187
Rb	ppm	0.220	0.118	0.928	0.129	0.001	0.137	-0.122
Sr	ppm	0.151	0.895	0.094	0.202	-0.083	-0.190	0.061
Y	ppm	0.917	0.139	0.177	0.170	-0.056	0.085	0.189
Zr	ppm	0.967	-0.092	-0.009	-0.011	-0.082	0.027	-0.083
Nb	ppm	0.779	-0.008	0.096	0.575	0.032	0.007	-0.121
Cs	ppm	0.273	0.073	0.886	0.031	0.066	0.141	0.143
Ba	ppm	-0.152	-0.044	-0.171	-0.047	-0.053	-0.919	-0.021
La	ppm	0.750	0.147	0.230	0.574	0.008	0.056	-0.007
Ce	ppm	0.778	0.118	0.221	0.537	0.035	0.066	0.023
Nd	ppm	0.806	0.136	0.191	0.508	0.034	0.078	0.017
Eu	ppm	0.696	0.265	0.156	0.608	0.026	0.110	-0.056
Tb	ppm	0.842	0.218	0.202	0.336	0.000	0.111	0.170
Dy	ppm	0.878	0.161	0.200	0.265	-0.032	0.103	0.203
Er	ppm	0.942	0.028	0.202	0.128	-0.022	0.068	0.192
Tm	ppm	0.954	-0.009	0.189	0.080	-0.027	0.053	0.184
Yb	ppm	0.963	-0.033	0.180	0.054	-0.034	0.038	0.159
Lu	ppm	0.968	-0.066	0.149	0.004	-0.042	0.032	0.135
Hf	ppm	0.977	-0.056	0.028	-0.003	-0.084	0.015	-0.043
Ta	ppm	0.785	-0.032	0.063	0.527	0.206	-0.006	0.024
Pb	ppm	0.005	-0.069	0.034	0.070	0.945	-0.091	0.024
Th	ppm	0.915	-0.115	0.293	0.126	0.026	0.024	0.122
U	ppm	0.928	0.033	0.168	0.301	0.011	0.032	-0.068

Based upon the rotated loading scores, the components were interpreted as follows:

Component 1 explains the largest part of the total variance (38 %). It has strong loadings for TiO_2 (0.84), Cr (0.91), Zr (0.97), La (0.75), Ce (0.78), Nd (0.81), Tb (0.84), Dy (0.88), Er (0.94), Tm (0.95), Yb (0.96), Lu (0.97). Zr is present principally in zircon, REEs in monazite, Cr in chromite and TiO_2 in rutile, all detrital heavy minerals known from Cretaceous sandstone samples of the Scotian Basin. Other than Cr, none of these elements are mobile under diagenetic conditions. This component therefore seems to represent variation in abundance of heavy minerals in different sandstones.

Component 2 (12% of total variance) shows strong loadings for MnO (0.93), CaO (0.95), and Sr (0.89), together with strong negative loadings for SiO_2 (-0.89) and Na_2O (-0.80). The dominance of CaO, Sr and MnO suggests that this loading represents the variation in abundance of carbonate cement (whether calcite, ferroan calcite, ankerite or dolomite). The lack of a strong loading for MgO or Fe_2O_3 results from these elements also being abundant in other minerals such as chlorite.

Component 3 (12 % of total variance) represents the presence of K-feldspar in the samples, with strong loadings for Al_2O_3 (0.66), K_2O (0.91), Rb (0.93), Cs (0.89). Clay minerals, such as illite, kaolinite and chlorite are also represented by the high loadings on Al_2O_3 and K_2O.

Component 4 (15 % of total variance) demonstrates high loading values for (001)/(004) chlorite X-ray diffraction peak area (0.86), Fe_2O_3 (0.63) and MgO (0.80) reflecting not only the presence of chlorite but because of the strong loading on X-ray diffraction peak area, indicates that the chlorite is iron rich.

Component 5 (7 % of total variance) has strong loadings on S (0.79), As (0.74) and Pb (0.95), all of which are present in sulphide minerals.

Component 6 accounts for a small percentage of the total variance (5%) and represents drilling mud contaminant producing strong negative loadings for permeability (-0.89) and Ba (-0.92).

5.4.4 Principal component analysis: detrital signature

A new PCA was run for elements predominantly found in detrital minerals, and omitting elements that are significantly influenced by early diagenesis. In addition, the number of REE was reduced because in the PCA their strong correlation may bias the analysis towards the REE. The following elements were used: TiO_2, Sc, Cr, Co, Y, Zr, Nb, La, Ce, Yb, Hf, Ta, Th, and Ni (Table 5.4).

Table 5.4: Rotated loading matrix (varimax) using elements predominantly found in detrital minerals.

	Unit	1	2
TiO_2	wt.%	0.802	0.557
Sc	ppm	0.448	0.765
Cr	ppm	0.938	0.107
Co	ppm	0.113	0.864
Y	ppm	0.857	0.373
Zr	ppm	0.975	0.083
Nb	ppm	0.731	0.605
La	ppm	0.689	0.671
Ce	ppm	0.712	0.654
Yb	ppm	0.974	0.118
Ta	ppm	0.700	0.630
Th	ppm	0.861	0.398
Ni	ppm	0.010	0.788

In this PCA, two components explained 88 percent of the variation in the data. Based upon the component loadings plot, elements cluster into three groups (Figure 5.2): (a) Zr, Hf, and Cr; (b) TiO_2, Y, and the REE; (c) Ni, Co, and Sc. The first group consists

of elements concentrated in ultrastable heavy minerals such as zircon and chromite. The second group represents minerals with a granitic or metamorphic source including ilmenite, monazite and garnet. The last group represents minerals of a mafic source.

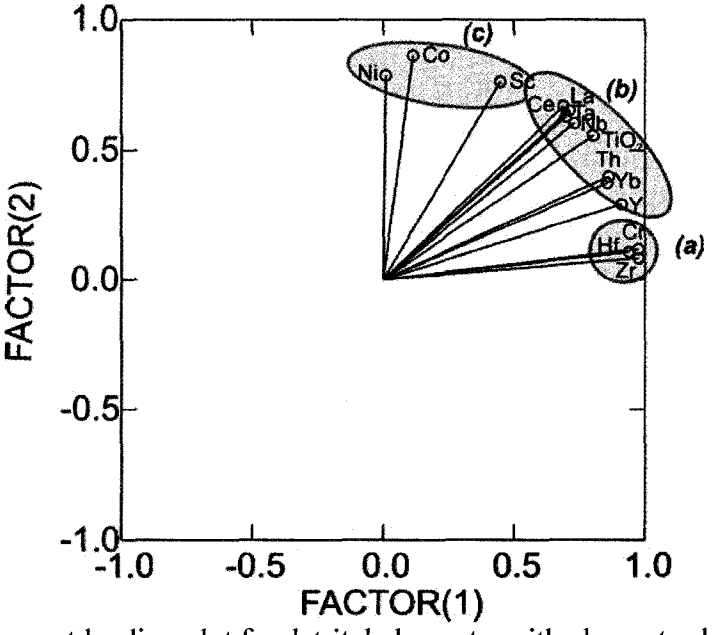

Figure 5.2: Component loading plot for detrital elements, with elements clustering into groups representing three sources: (a) mafic; (b) granitic or metamorphic source; and (c) ultrastable heavy minerals.

5.4.5 Correlation between Titanium and Phosphorus

Correlation methods described earlier in this chapter have identified a significant relationship between phosphorus and titanium. The PCA shows a strong positive correlation between the two, and the correlation matrices reveals that each correlates with the other more strongly than with any other element. Furthermore, well-developed chlorite rims correlate with P_2O_5 and TiO_2, in particular in the type 4 sandstones, those with dissolved carbonate cement and chlorite rims.

Logistic Regression

A logistic regression analysis was conducted in order to investigate the relationship of chlorite rims with titanium and phosphorus. The data fits the regression

curve well ($\beta_{constant}$: -2.609 (±0.858), $\beta_{titanium}$: 2.666 (±1.039), $\beta_{phosphorus}$: 6.723 (±2.783); $p_{titanium}$ = 0.01, $p_{phosphorus}$= 0.016), indicating that as titanium and phosphorous values increase, there is a high probability of finding well developed chlorite rims (Figure 5.3).

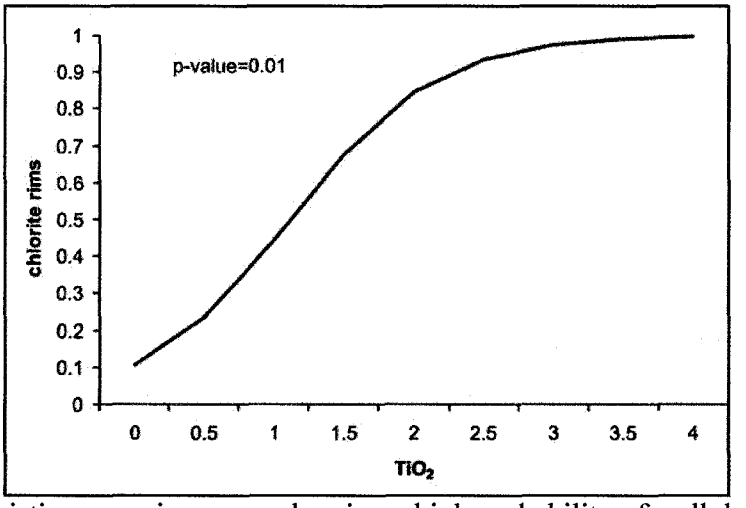

Figure 5.3: Logistic regression curve showing a high probability of well developed chlorite rims in samples with high titanium.

5.5 Stratigraphic variation in geochemistry

5.5.1 Stratigraphic variations in elements predominantly in cement

Iron, magnesium and potassium generally covary with each other down section. These elements represent the varying amounts of illite, kaolinite and chlorite cement. These inversely covary with CaO and MgO, representing carbonate cement (Figures 5.4 to 5.15).

In Thebaud C-74, Fe, Mg and K are higher in the samples from Sandstone A and the lower part of Sandstone B (Figure 5.4). This agrees with stratigraphic and petrographic observations, where sandstones from this interval have muddy bioturbation and substantial clay cement (mainly pore filling) in thin section. Samples from the lower part of Sandstone A and upper part of Sandstone B are generally clean and clay cement is pore lining rather than pore filling. CaO and MgO values are low down section with the

exception of a spike in values for sample P17 (3911.15 m corrected measured depth), the sole carbonate cemented sample in Thebaud C-74. The elevated iron values in this sample are consistent with microprobe analysis showing the carbonates are ferroan calcite and ankerite (Figure 5.4).

In the Venture wells, Fe_2O_3, MgO and K_2O values increase down section within Sandstone 2 and inversely covary with CaO and MgO (Figures 5.5 and 5.6). This agrees with thin section observations that samples dominated by carbonate cement are generally poor in clay cement. In the lower part of Sandstone 2 in Venture 4, K_2O inversely co-varies with Fe_2O_3 and MgO, possibly indicating a higher ratio of illite to chlorite cement (Figure 5.6).

CaO and MgO values are low in Sandstone 2. Samples from this interval have minor amounts of carbonate cement (mostly ferroan calcite or ankerite), with the exception of sample 56 in Venture 4 (5387.37 m corrected measured depth), where the sandstone contains abundant ferroan calcite cement.

As would be expected, samples from Limestone 3 have the highest values of CaO (18-20%) and MnO (0.08-0.17%) of the sample set. Sandstone 3 shows similar trends as Sandstone 2 for elements found in clay minerals, with Fe_2O_3 MgO and K_2O values gradually increasing down section, where the samples have well-developed pore-lining clays (Figure 5.6).

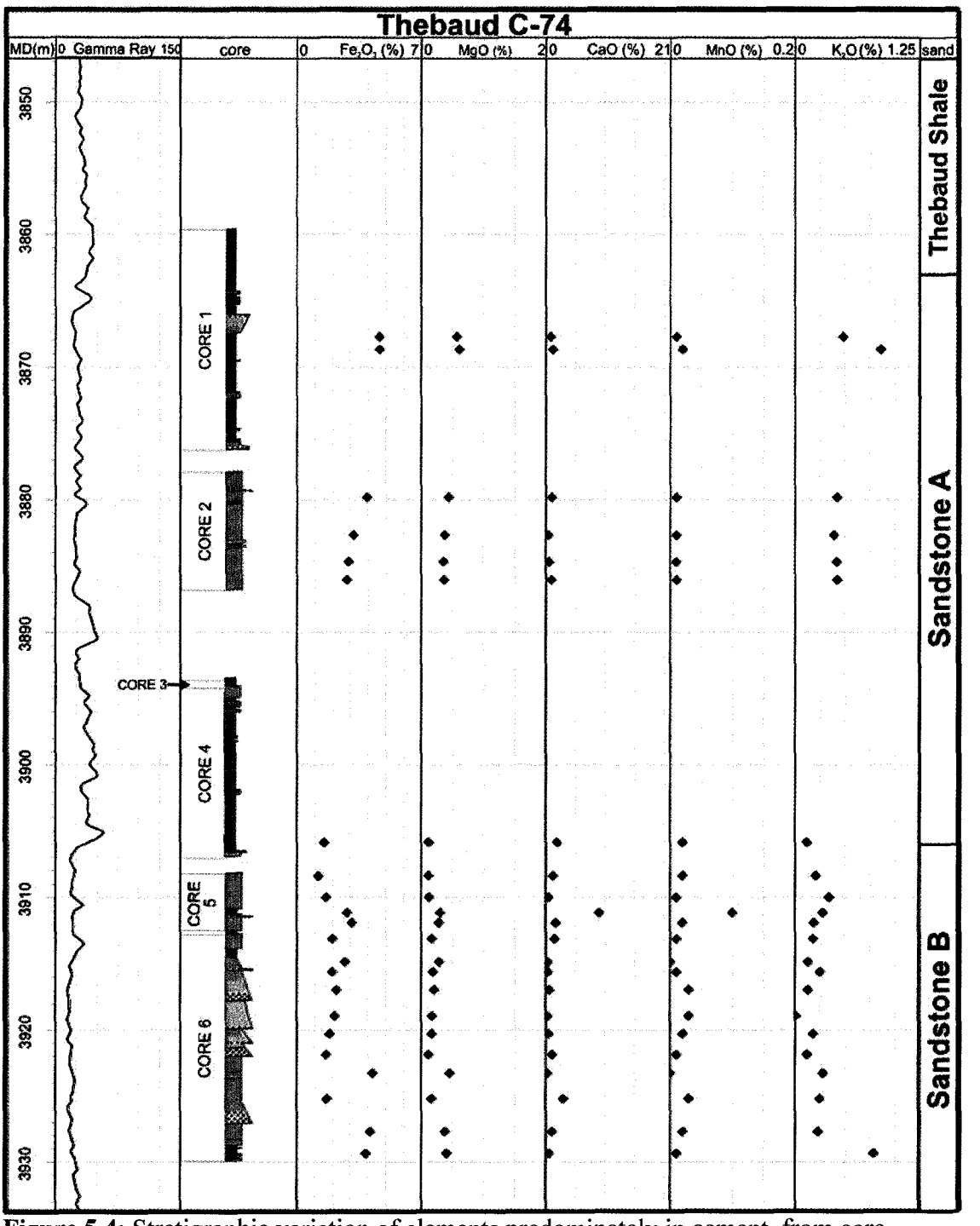

Figure 5.4: Stratigraphic variation of elements predominately in cement, from core samples in Thebaud C-74.

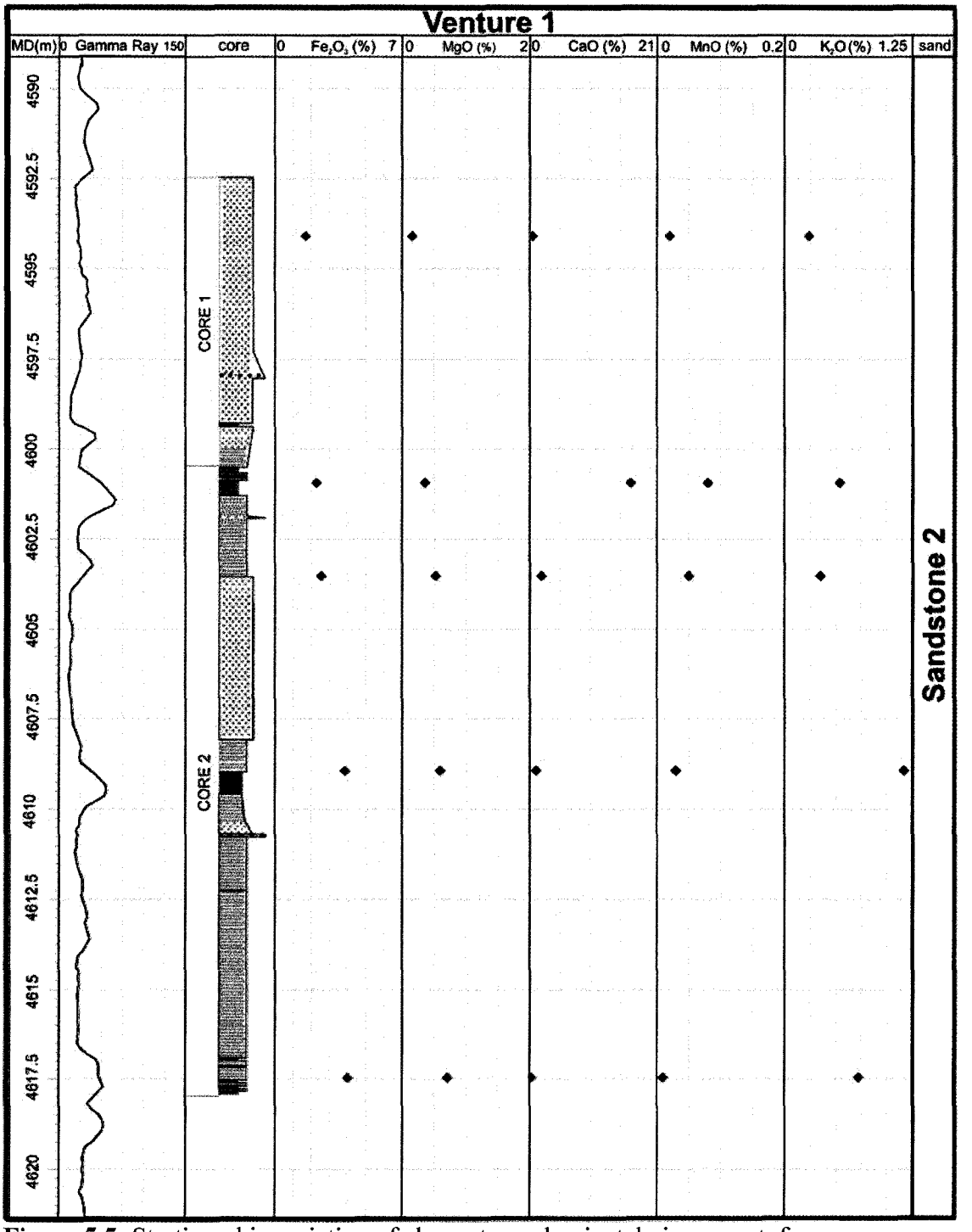

Figure 5.5: Stratigraphic variation of elements predominately in cement, from core samples in Venture 1.

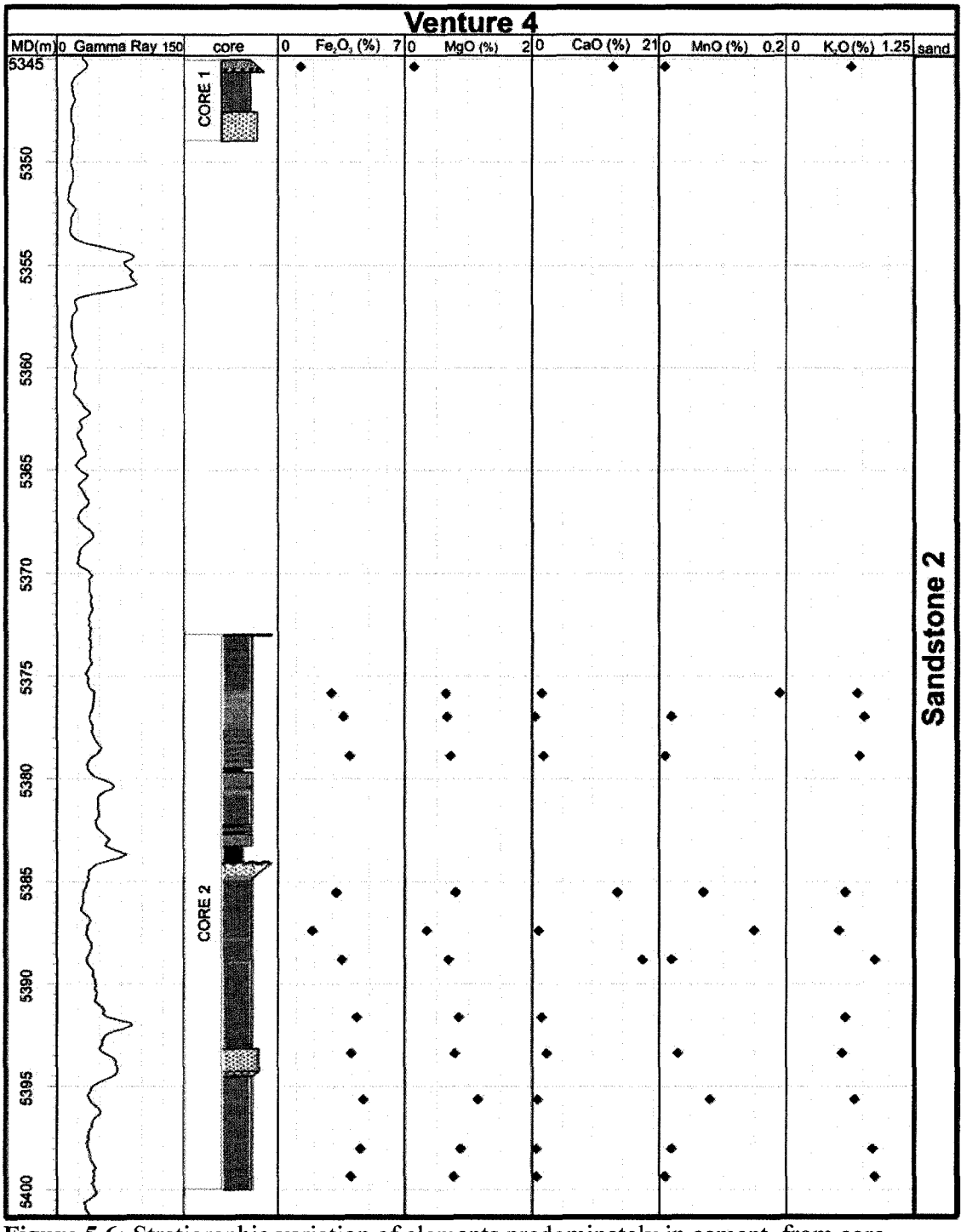

Figure 5.6: Stratigraphic variation of elements predominately in cement, from core samples in Venture 4.

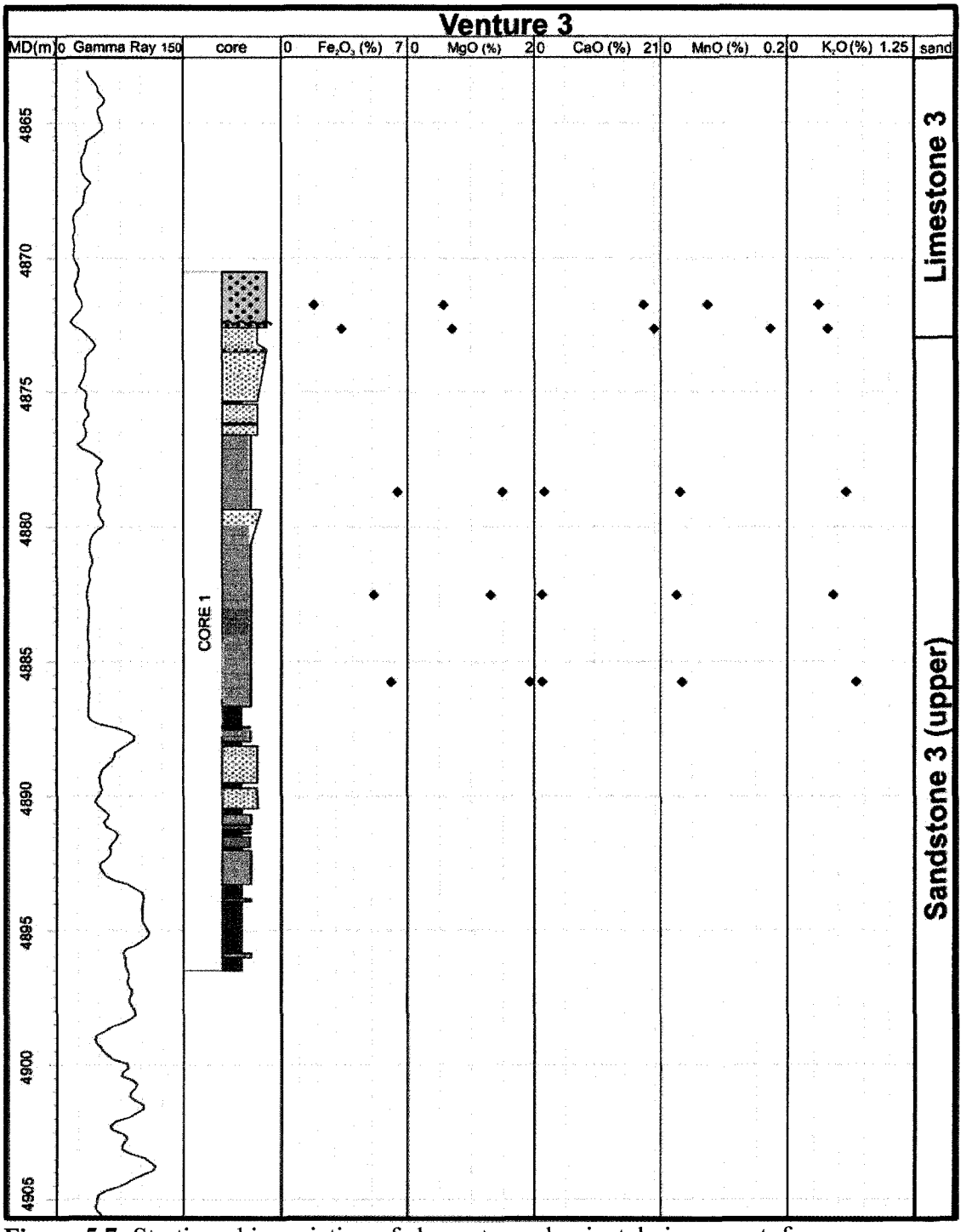

Figure 5.7: Stratigraphic variation of elements predominately in cement, from core samples in Venture 3.

5.5.2 Stratigraphic variation of titanium and phosphorous

Titanium and phosphorus covary with each other down section. Both elements have low values in Thebaud Sandstones A and B (0.25-1% TiO_2, 0.04-0.14% P_2O_5) (Figure 5.8).

In the lower part of Venture Sandstone 2 (Figures 5.9 and 5.10) and the upper part of Sandstone 3, however, the titanium values are consistently high (0.39-3.1% TiO_2, 0.11-0.59 % P_2O_5) (Figures 5.9 to 5.11).

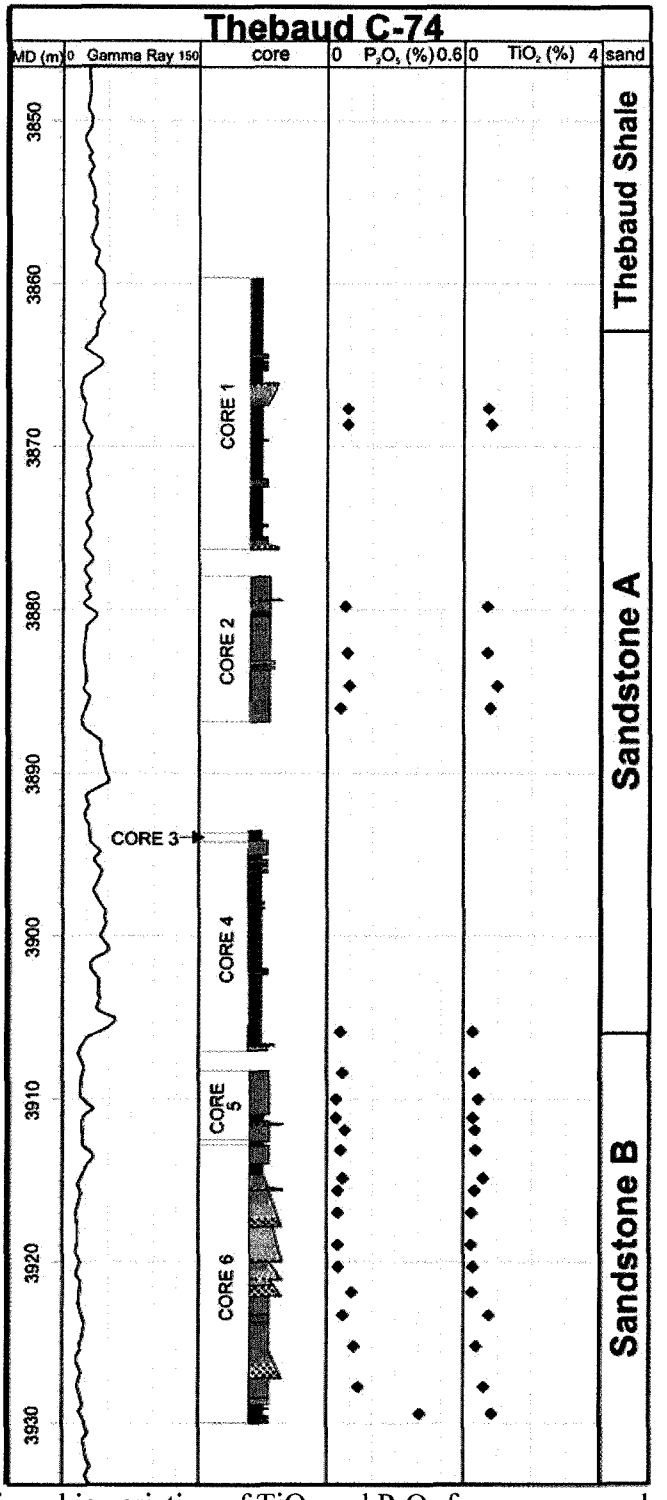

Figure 5.8: Stratigraphic variation of TiO_2 and P_2O_5 from core samples in Thebaud C-74.

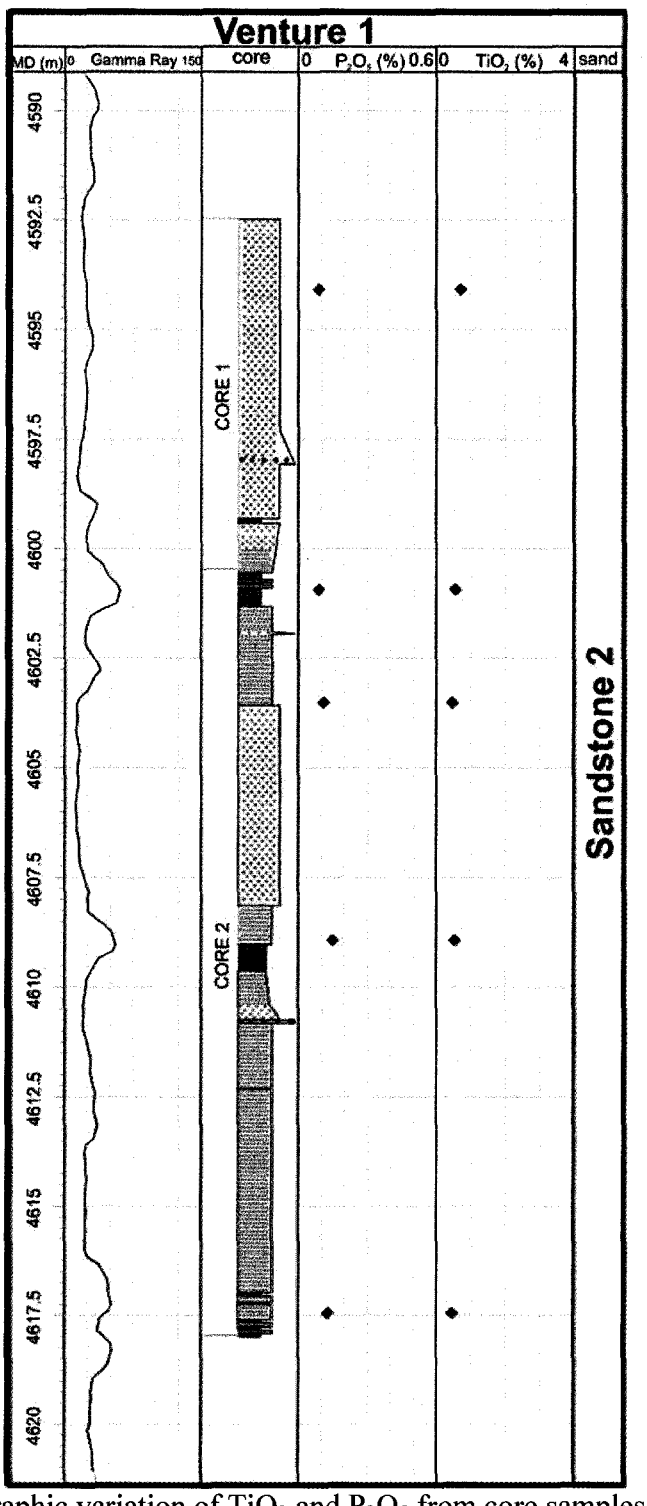

Figure 5.9: Stratigraphic variation of TiO_2 and P_2O_5 from core samples in Venture 1.

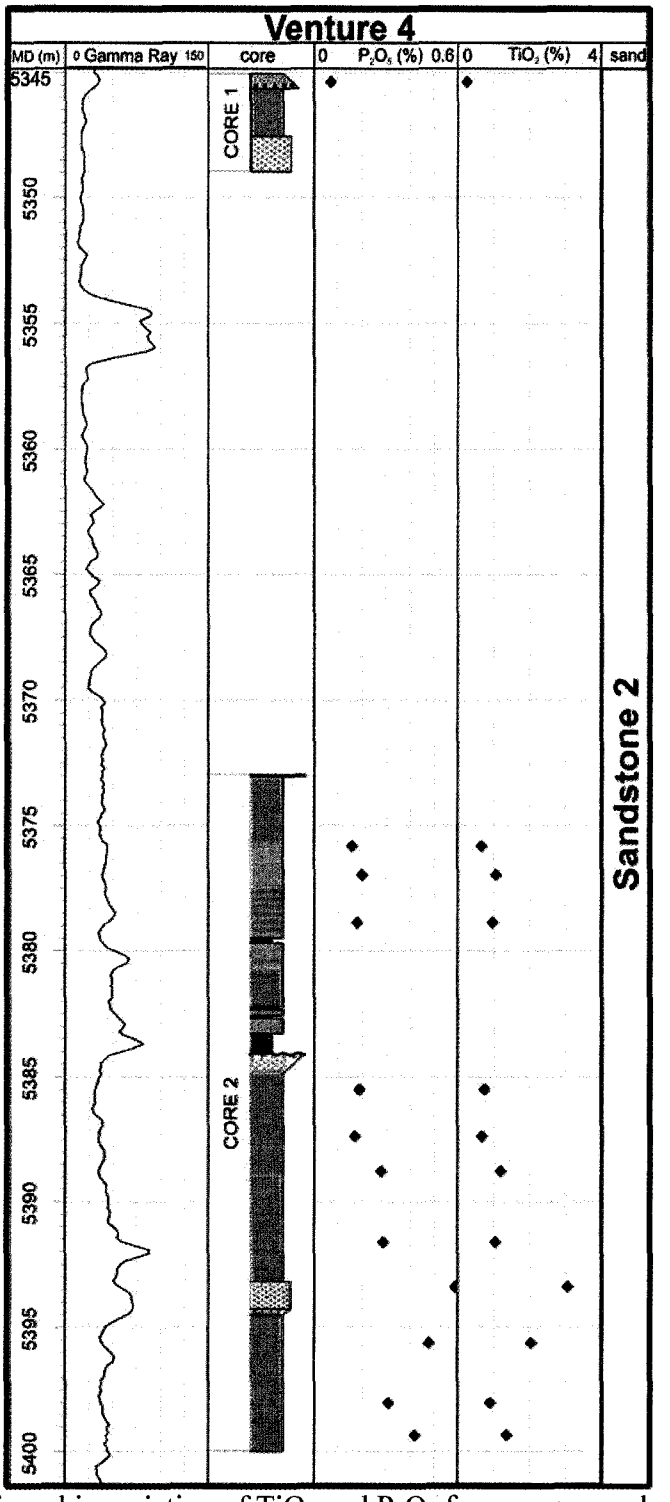

Figure 5.10: Stratigraphic variation of TiO_2 and P_2O_5 from core samples in Venture 4.

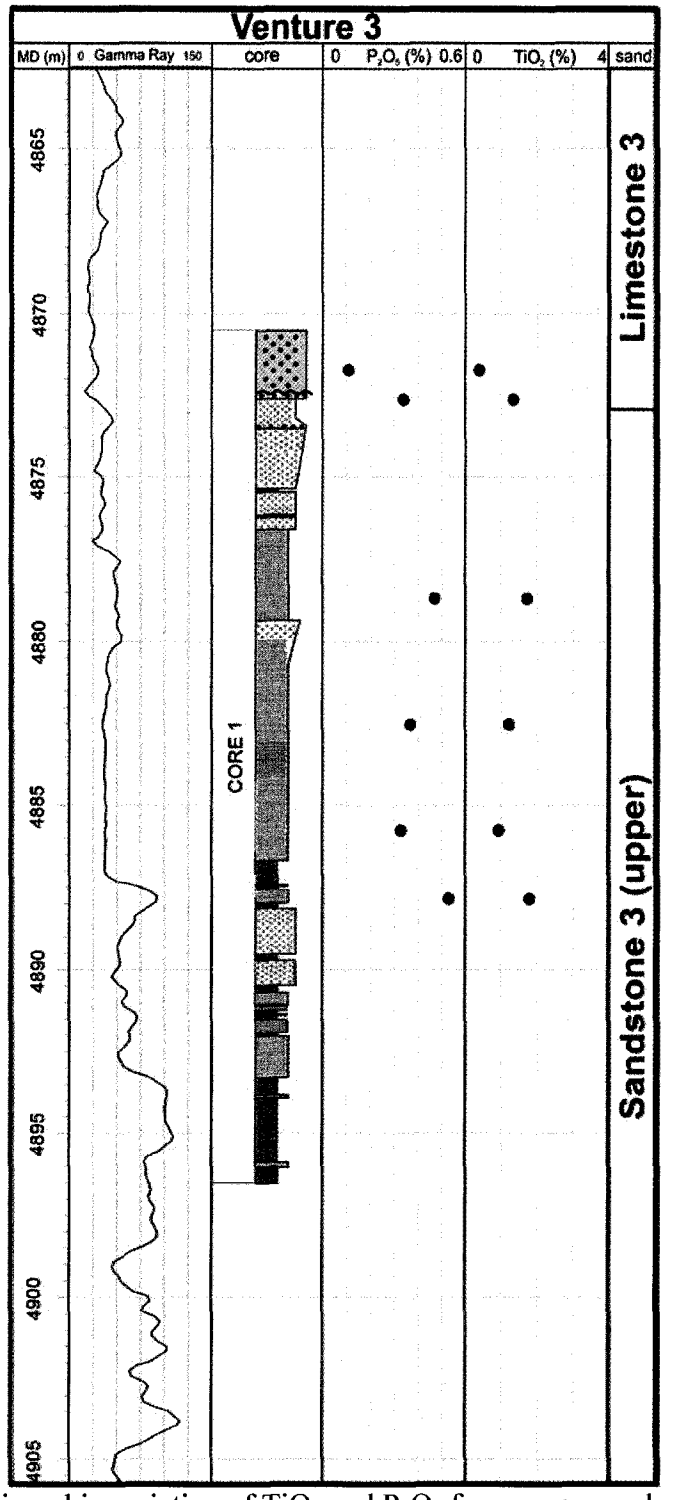

Figure 5.11: Stratigraphic variation of TiO_2 and P_2O_5 from core samples in Venture 3.

5.5.3 Stratigraphic variations in other elements found predominantly in detrital minerals

Elements representing minerals from different sources as identified by factor analysis in section 5.4.4 covary with each other down section. These are: the ultrastable heavy minerals (Zr, Hf and Cr), granitic or metamorphic minerals (TiO_2, Y and REE) and mafic minerals (Ni, Co and Sc)

In Thebaud C-74, elements within each group generally have high values in Sandstone A and lower values in the upper part of Sandstone B (Figure 5.12). Values show a slight increase in the lower part of Sandstone B. The consistently low values in the upper Sandstone B may reflect a difference in source, or more likely a change in the maturity or sorting of source material for this particular interval, which is characterized by interpreted as sandstones interpreted to be deposited by repeated flooding events into the shoreface.

In the lower part of Sandstone 2 in Venture 4, Cr, Zr, Hf, TiO_2, Y and HREE values gradually increase, with a spike in values at 5393.4 m corrected measured depth (sample SP74) (Figure 5.14). The upper part of Venture Sandstone 2 in Venture 1 has high values for these elements that decrease down section (Figure 5.13).

Values for Sc, Co and Ni show the opposite trend in the upper part of Sandstone 2, with values gradually increasing down section (Figure 5.13). In the lower part of Sandstone 2, like elements from ultrastable and granite/metamorphic minerals, elements in mafic minerals gradually increase to the base of the core (Figure 5.14). This trend is interpreted as representing the top Sandstone 2 having a mixed source, with a more mafic influence depositing the base of Sandstone 2 (Figure 5.14).

Elements found in detrital minerals from base of Venture Limestone 3 (sample SP5, top of Venture 3) co-vary with each other. The mixture of elements from different sources may reflect the intense reworking that formed the base of this unit (Figure 5.15).

Within Venture Sandstone 3, values of elements representing the ultrastable heavy minerals and a granitic/metamorphic source increase upwards. Values for elements concentrated in mafic minerals decrease up section. Similar to Venture Sandstone 2, Sandstone 3 are interpreted as having more of a mafic source, with less influence from other sources (Figure 5.15).

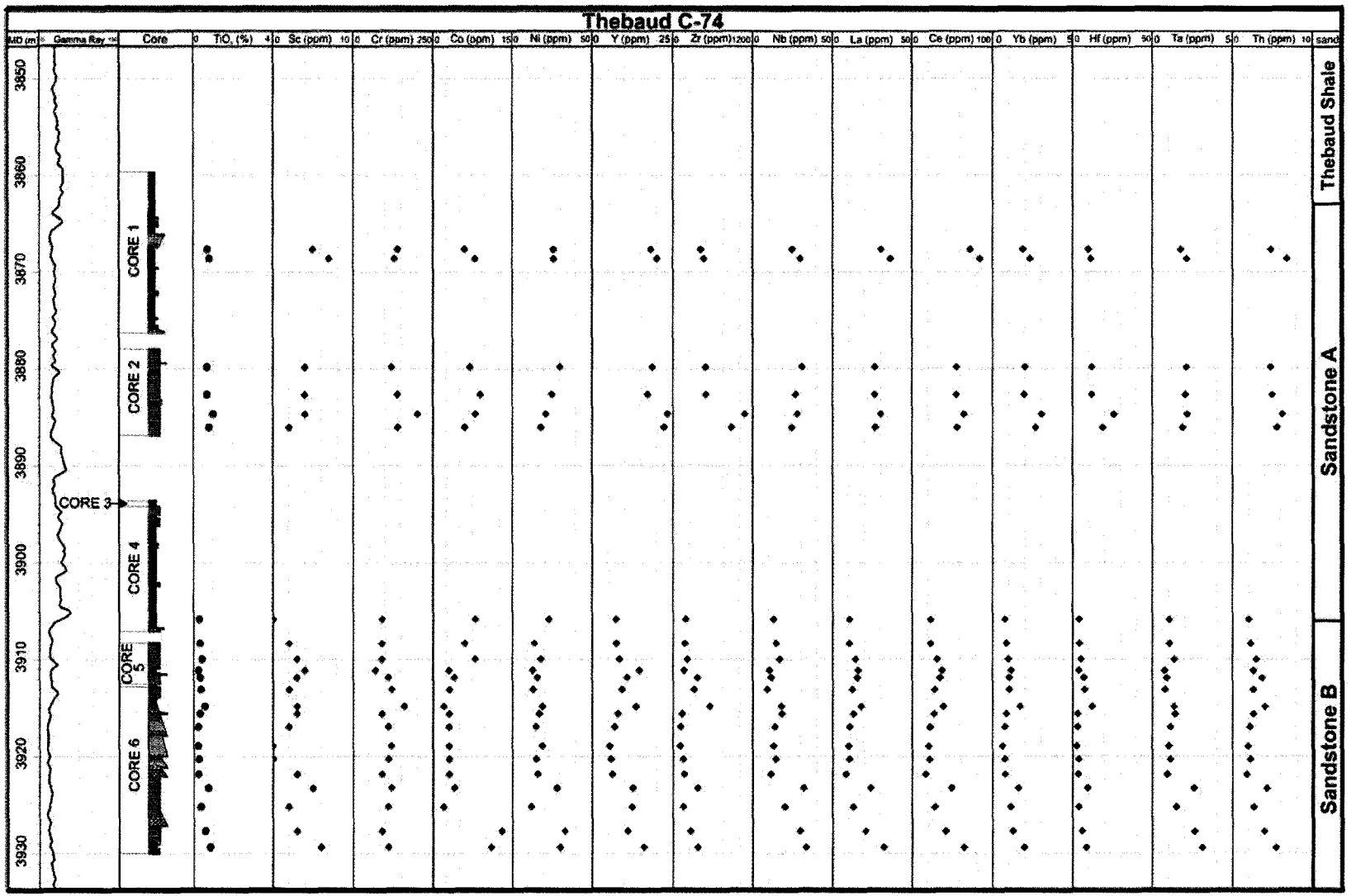

Figure 5.12: Stratigraphic variation of elements found predominately in detrital minerals, from core samples in Thebaud C-74

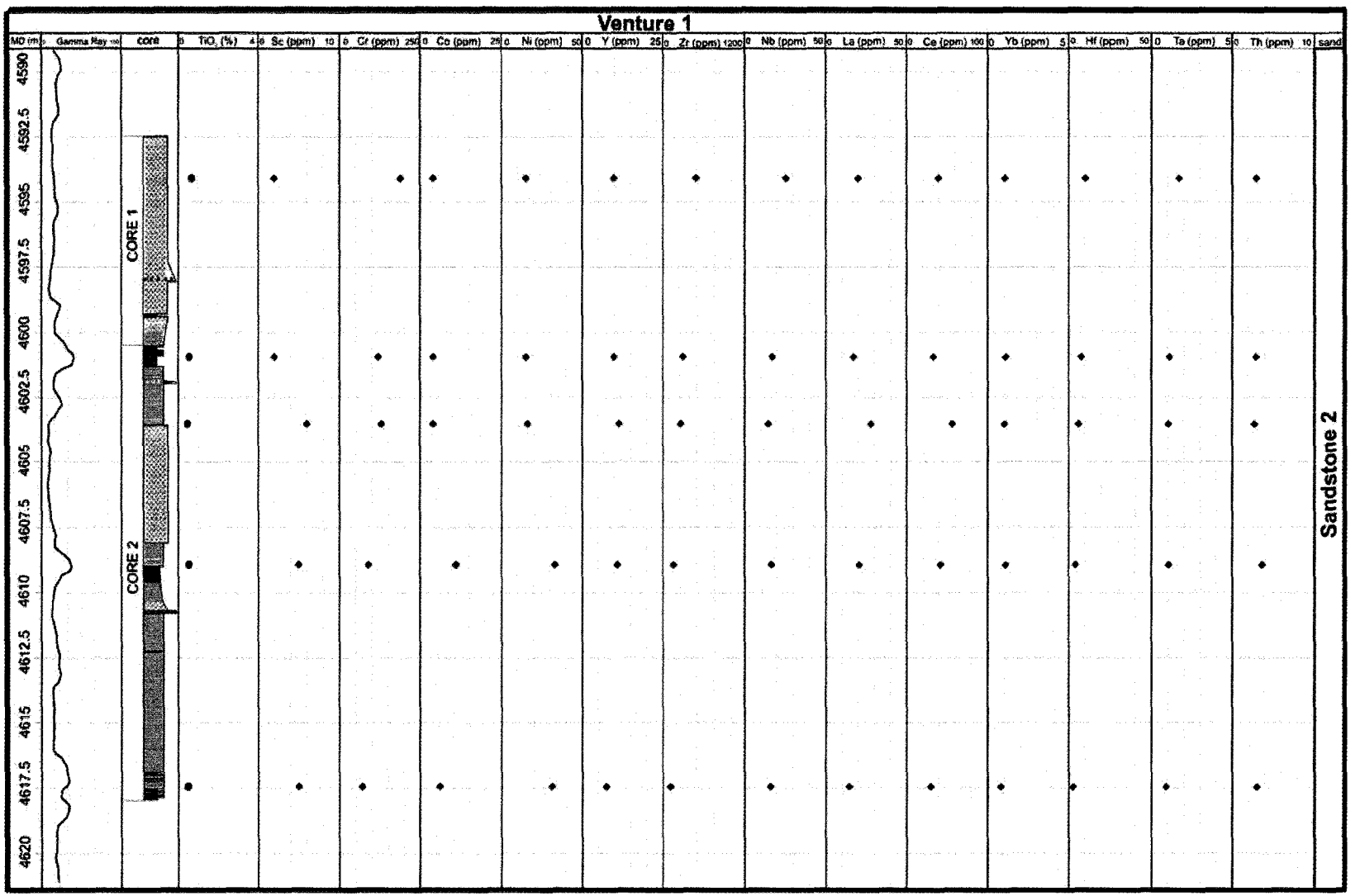

Figure 5.13: Stratigraphic variation of elements found predominately in detrital minerals, from core samples in Venture 1.

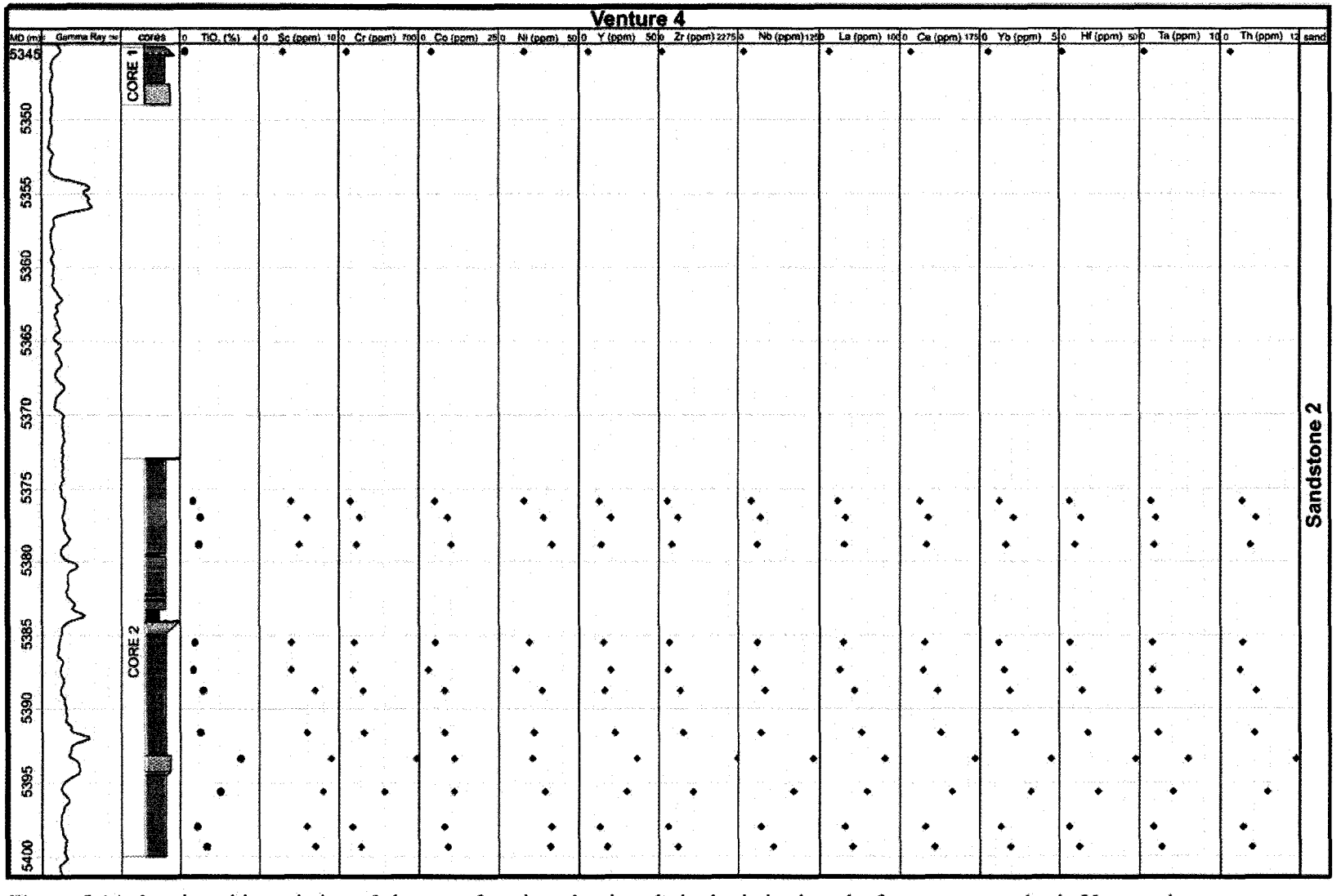

Figure 5.14: Stratigraphic variation of elements found predominately in detrital minerals, from core samples in Venture 4.

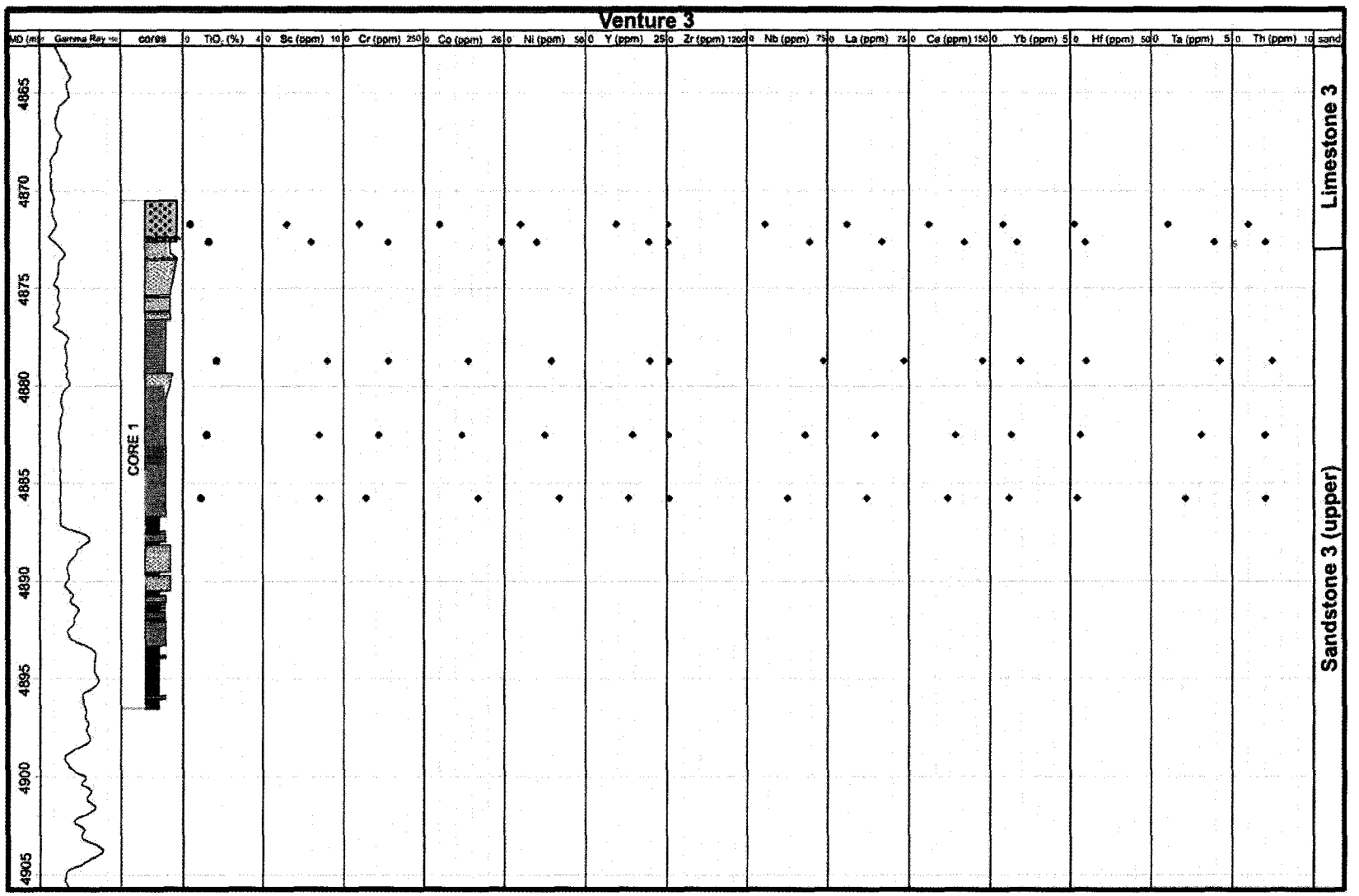

Figure 5.15: Stratigraphic variation of elements found predominately in detrital minerals, from core samples in Venture 3.

CHAPTER 6: DISCUSSION

6.1 Introduction

There are two hypotheses for the timing of chlorite diagenesis in sandstone reservoirs: it is an early burial diagenetic feature (e.g., Ehrenberg, 1993) or a late diagenetic feature (e.g., Hutcheon, 1990). The formation of chlorite is dependant on the availability of iron in the diagenetic environment. Previous work in the Norwegian section of the North Sea has shown that the presence of iron-rich detrital clay (berthierine) will facilitate the formation of diagenetic iron-rich chlorite (chamosite) during burial (Ehrenberg, 1993; Ryan and Hillier, 2002; Aagaard et al., 2000). The alternate hypothesis is supported by Hutcheon (1990) and Jansa and Noguera (1990) who argued that the chlorite is a later diagenetic mineral, formed by clay-carbonate reaction between kaolinite and ankerite during the influx of basin fluids.

6.2 The diagenetic sequence

Diagenetic minerals identified in the sandstone samples include chlorite, illite, kaolinite, pyrite, siderite, several varieties of calcite, and ankerite.

Chlorite is present as four different morphologies in thin section: pore-rimming, pore-filling, replacing framework grains (including mica grains) and as thick, concentric grain coatings (Figures 3.3 to 3.5, and 3.7). The chlorite commonly rims detrital mixed clays that coat framework grains (Figures 3.1 and 3.2). Electron microprobe analyses of chlorite record between 22 and 32% FeO (total), averaging about 30% FeO. Chlorite analyses are often mixed with minor amounts of K_2O, Na_2O, CaO and TiO_2. X-ray diffraction shows that the iron enrichment is on the silicate sheet (Figure 4.4). Chlorite appears to form early during burial diagenesis as it is often encased in later carbonate or

clay cement (Figure 3.26).

Pore-filling chlorite commonly contains dispersed 1μm crystallites of illite (Figure 3.29). By comparing K_2O and FeO graphically (Figure 3.9), combined with study of backscattered electron images of mixed chlorite/illite areas in thin section (e.g., Figure 3.8), it seems that the two minerals occur as discrete phases and not as mixed-layer minerals. Electron microprobe analyses and X-ray diffractograms indicate that illite is enriched in aluminum, with most analyses having >24% Al_2O_3. X-ray diffractograms also show illite as having a very low degree of interstratification with other clay minerals (Figure 4.5 and Table 4.2). Textural relationships (Figure 3.29 to 3.31) show that illite formed during the later stages of diagenesis, after the formation of pore-filling chlorite or kaolinite.

Kaolinite is present as loosely packed booklets (Appendix 6, Figure 44). In a few samples, kaolin mineral morphology changes from a booklet to a blocky morphology that may indicate that the kaolinite has changed to dickite (Appendix 6, Figure 117). Kaolinite generally fills large primary pore space or secondary porosity created by the dissolution of detrital grains (e.g., Appendix 6, Figure 105), forming after chlorite development, but before calcite or ankerite cement.

Diagenetic framboidal pyrite developed early in the paragenetic sequence, forming framboids that are encased in later carbonate cements

Silica cementation developed later in the sequence, as overgrowths on detrital quartz grains or pore-filling cement. Silica cementation predates some ferroan carbonate and postdates chlorite rims (Figure 3.26C, D) and is the one of the major porosity reducing processes in the Sable Subbasin.

Albitization also predated carbonate cementation. Detrital K-feldspar grains that have developed patches of albite are later partially dissolved and replaced by ferroan calcite or ankerite (Fig. 3.28B).

Ferroan, manganoan and magnesian calcite, ankerite and siderite were identified in the samples forming both early and late diagenetic phases. Siderite is present as detrital intraclasts and as early diagenetic cement. Ferroan calcite and ankerite are seen as early in the paragenetic sequence as chlorite rims (Figure 3.21A) and also as a late feature, encasing the earlier diagenetic cements (Figure 3.23A).

The hypothesis that chlorite is a late diagenetic feature was tested by comparing the presence of well-developed chlorite rims with other diagenetic features to see if there was any correlation. Factor analysis suggests that the overall quality of chlorite rims does not correlate well with diagenetic features such as carbonate cement or sulphides. No correlation was found between quality of chlorite rims and petrographic sandstone type (Table 5.2, Figures 5.1 and 6.1 to 6.4). These observations suggest that chlorite was independent of the other diagenetic phases and not formed later from influx of basinal fluids.

6.3 Stratigraphic distribution of chlorite

Figures 6.1 to 6.4 show the stratigraphic distribution of the quality of chlorite rims (with 1 being the lowest and 4 being the highest) and the seven sandstone types (Figure 5.1). Chlorite rims are found in samples in all study wells and in each sandstone studied: Sandstones 2 and 3 (Venture 1, 3 and 4) and Sandstones A and B (Thebaud C-74). Chlorite is present locally within subfacies S2a, S2b, S3 and S4. These sandstone facies have varying levels of bioturbation and are interpreted as being deposited in both the

mouthbar/delta front and prodelta at varying proximity to the distributary channel (Figure 6.5 and Figure 6.6).

Chlorite rims are not present in sandstone samples from facies S1, interpreted as being deposited in a distributary channel. The distinctive feature of S1 is the sparse bioturbation and evidence of relatively rapid deposition. The general lack of bioturbation may have had an influence on the amount of detrital clay rims that developed on sand grains. Experimental work by Needham et al. (2005) has shown that sediment ingestion and excretion can produce iron-rich detrital clays coatings on grains. The lack of chlorite rims in facies S1, despite its general similarity to other sandstone facies, may be due to a lack of bioturbation, which is thought to produce or concentrate iron rich clay coatings which later would recrystallize to chlorite. Chlorite was also absent from mudstone and limestone intervals (facies M1, M2 and L1).

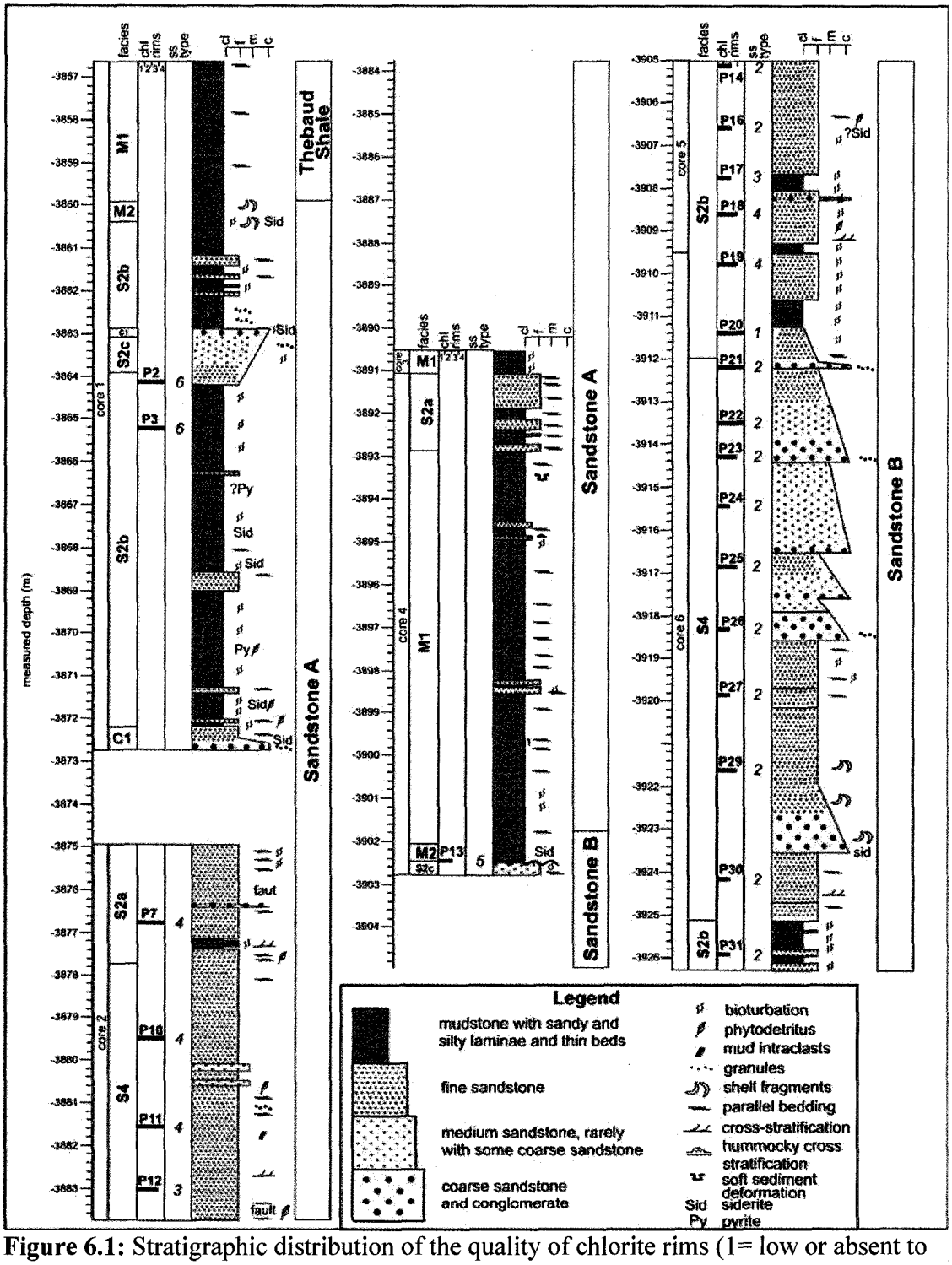

Figure 6.1: Stratigraphic distribution of the quality of chlorite rims (1= low or absent to 4 =well formed) and the seven sandstone types estimated from thin section in samples from Thebaud C-74.

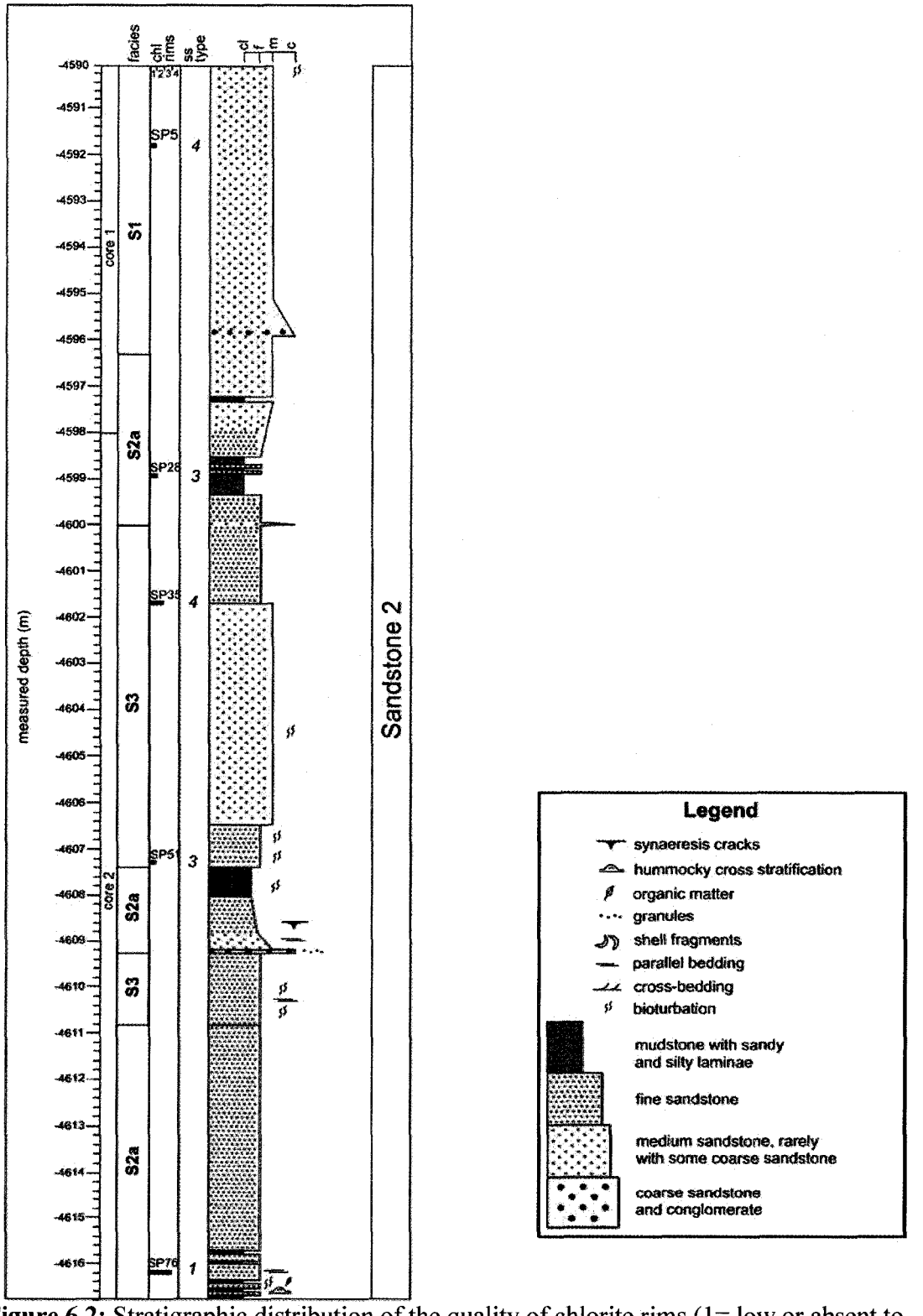

Figure 6.2: Stratigraphic distribution of the quality of chlorite rims (1= low or absent to 4 =well formed) and the seven sandstone types estimated from thin section in samples from Venture 1

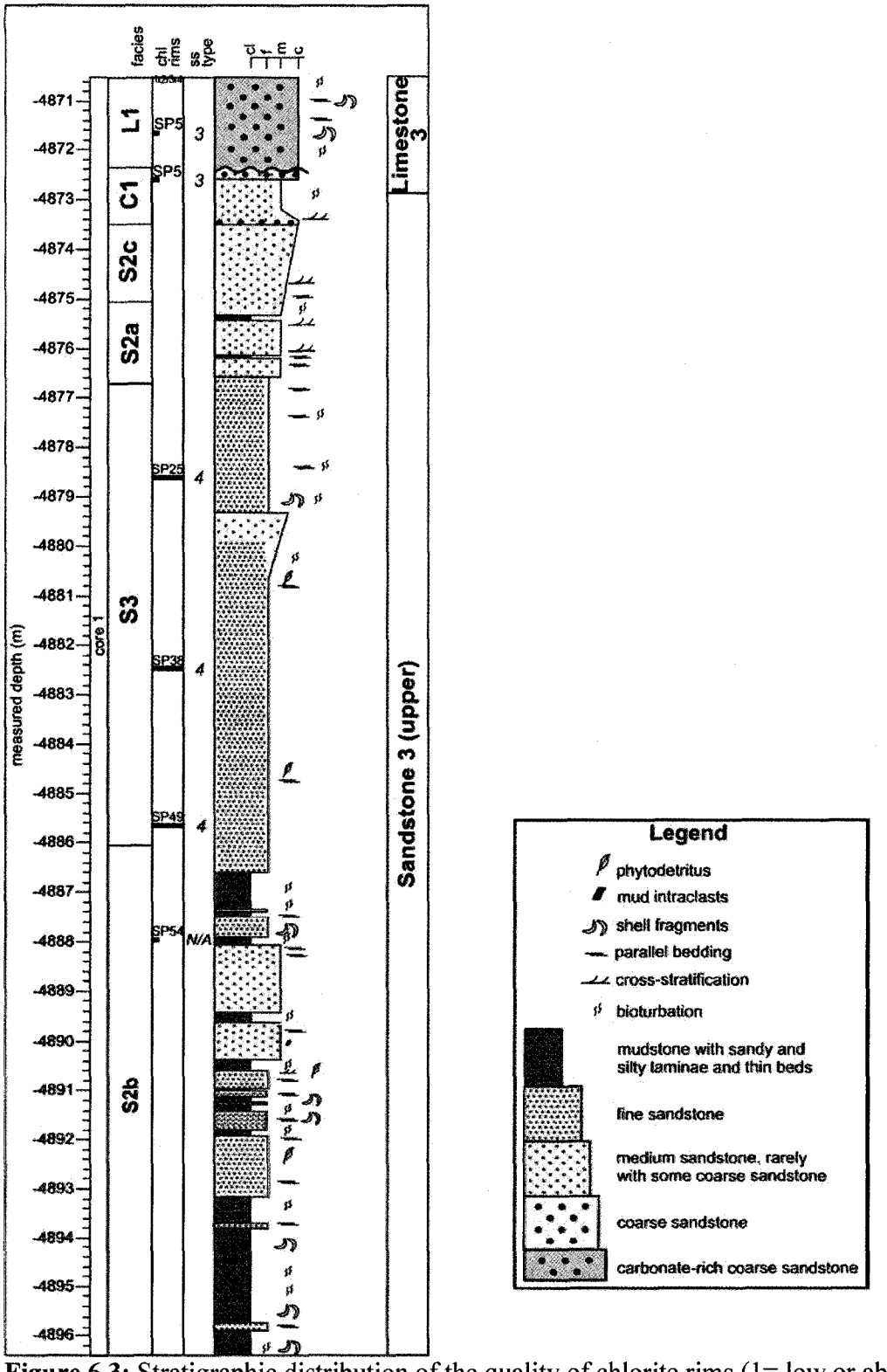

Figure 6.3: Stratigraphic distribution of the quality of chlorite rims (1= low or absent to 4 =well formed) nd the seven sandstone types estimated from thin section in samples from Venture 3.

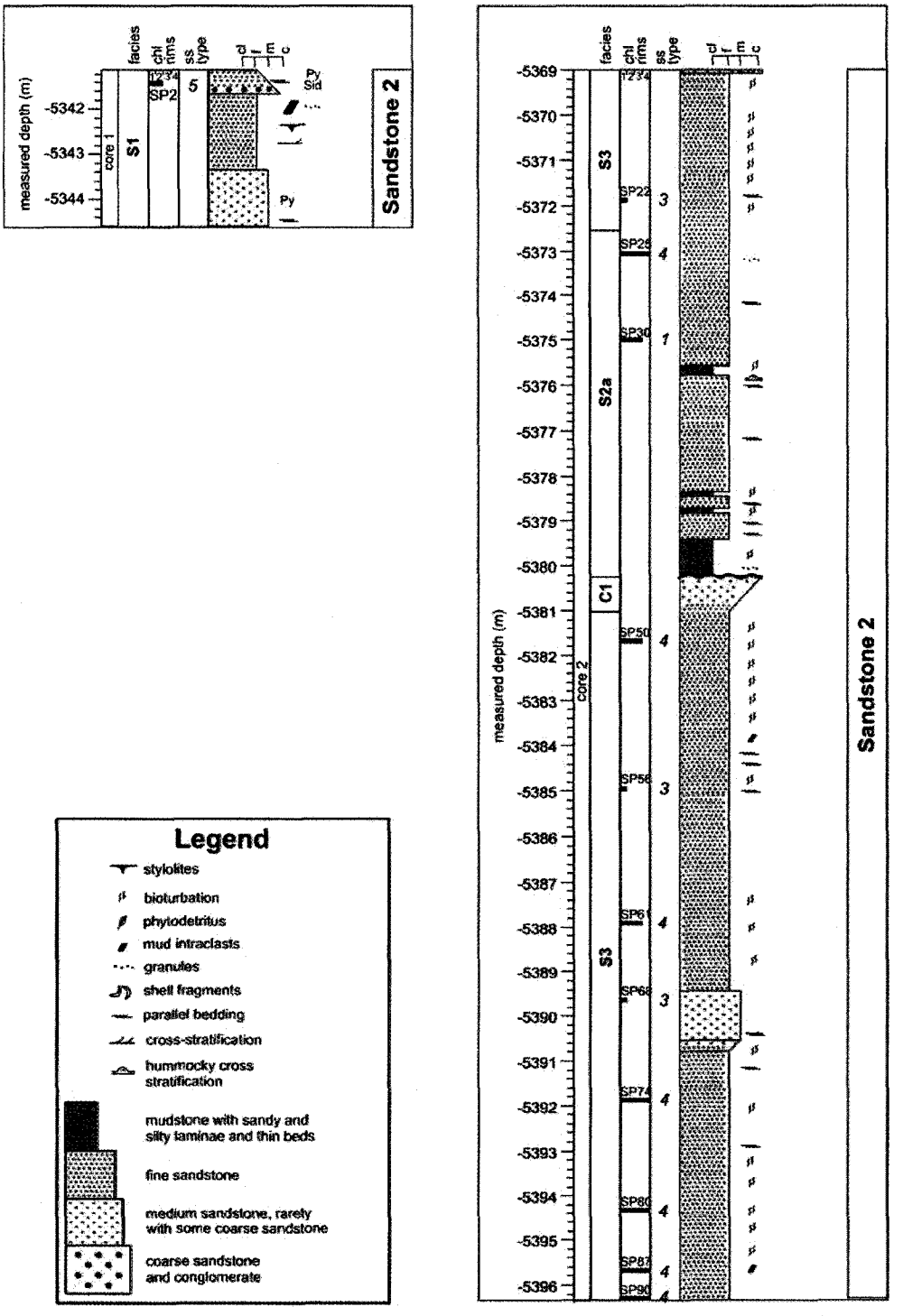

Figure 6.4: Stratigraphic distribution of the quality of chlorite rims (1= low or absent to 4 =well formed) and the seven sandstone types estimated from thin section in samples from Venture 4.

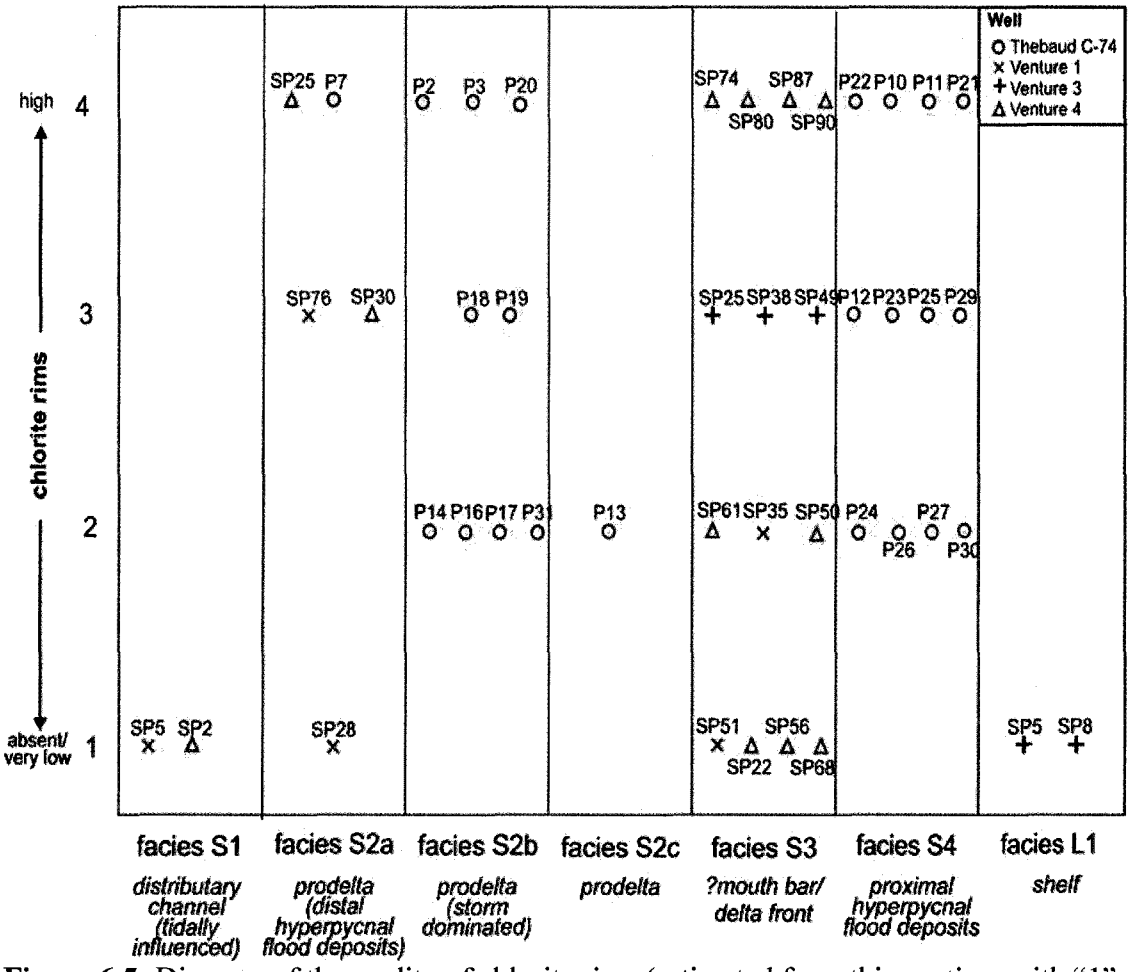

Figure 6.5: Diagram of the quality of chlorite rims (estimated from thin section, with "1" being absent to very low and "4" being well-developed) versus the depositional facies (estimated from core).

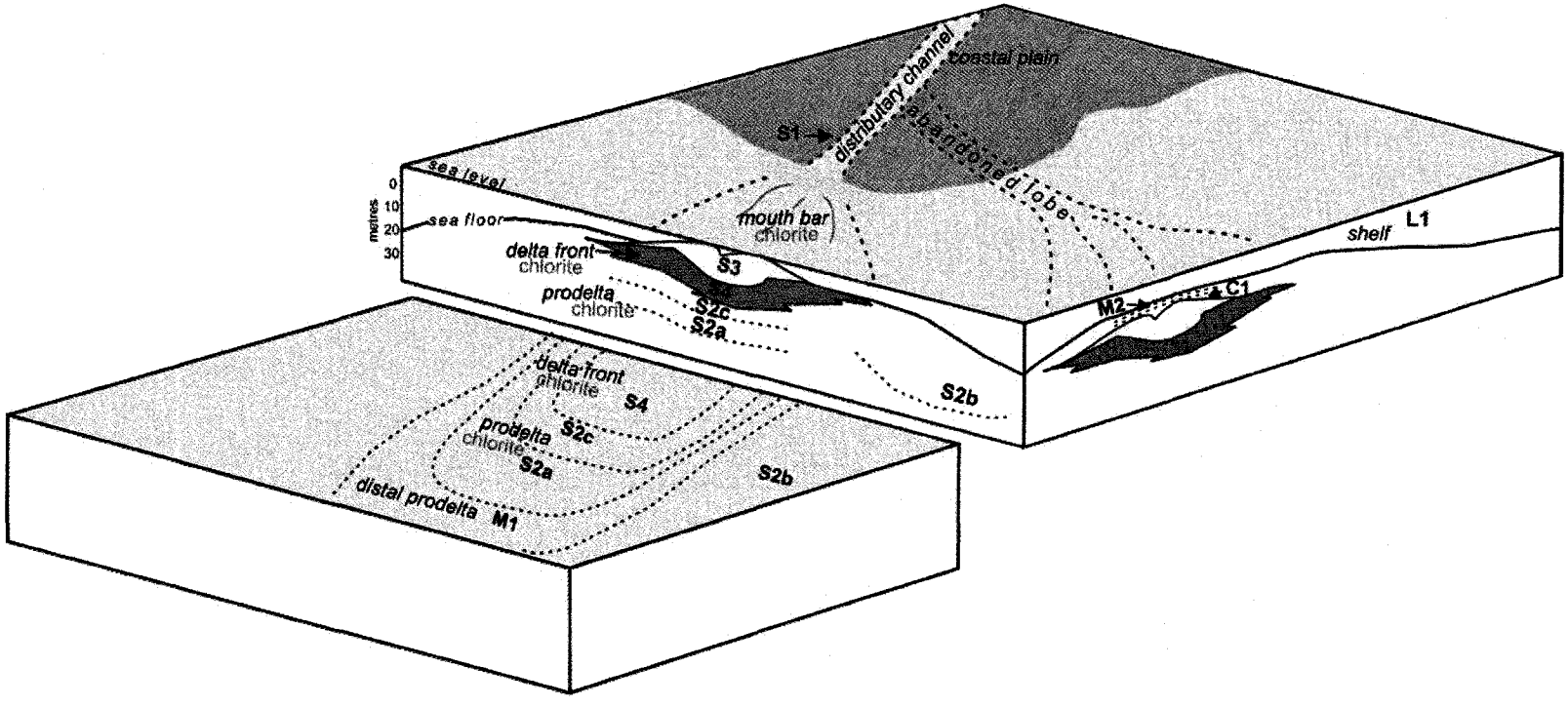

Figure 6.6: A summary cartoon of the distribution of the facies seen in core, relative to deltaic depositional and early diagenetic environments in the Sable Subbasin.

There does not seem to be a correlation between overpressure and chlorite rims or chlorite-rich grains. Samples from Sandstone 2, which is above the top of the overpressure and therefore hydropressured, have well-developed rims (e.g., Venture 4, SP74, SP80), comparable to samples below the top of overpressure, such as those observed in Sandstones 3 or Sandstone A and B (e.g., Venture 3, SP38).

The depth of burial of samples is 3800-3900 m for Thebaud C-74 and 4300-4700 m for the Venture wells (SSTVD). Measured temperatures for both wells do not exceed 160°C in drill stem tests (Figure 6.7B). The diagenetic assemblage and the observed order of the paragenetic sequence are consistent with the observed depth and temperature of the wells (Figures 3.20 and 6.7). For example, Worden and Burley (2003) showed that late ankerite forms at similar or higher temperatures than silica cement, illite cement and late albite, T>100°C, which is consistent with textures seen in thin sections (Figure 3.25A), where some ferroan carbonates formed later than quartz overgrowths and partially dissolved albitized K-feldspar grains (Figure 3.28B).

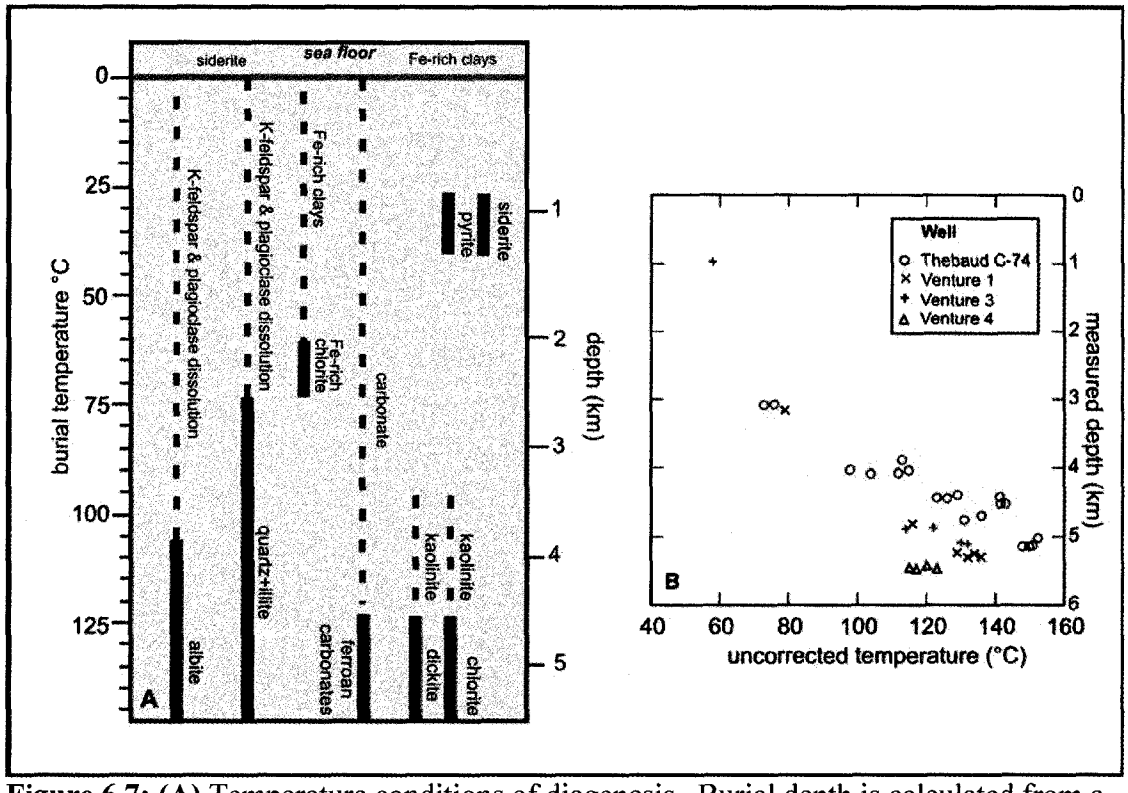

Figure 6.7: (A) Temperature conditions of diagenesis. Burial depth is calculated from a geothermal gradient of 30°C/km (modified from Burley and Worden, 2003); **(B)** uncorrected temperature data measured from well logs during drilling. Depths are measured, uncorrected for well deviation during drilling.

6.4 Timing of the formation of diagenetic chlorite

Jansa and Noguera (1990) and Hutcheon (1990) have suggested that diagenetic chlorite formed during late diagenesis, as a result of fluids moving through the basin, resulting in the removal of early calcite cement, producing reaction between kaolinite and carbonate minerals to create chlorite.

Jansa and Noguera also claim to have seen a dramatic increase in chlorite rims with the overpressured reservoirs. Although chlorite rims are well-developed in samples from the overpressured zones, such diagenetic chlorite rims are also found above the top of overpressure in Ventures 1 and 4 (i.e., Sandstone 2, above 4500m SSTVD).

Petrographic evidence is lacking in samples used in this study for the reaction of

carbonate and kaolinite to produce chlorite. Chlorite rims are commonly surrounded or encased with well-developed booklets of kaolinite, indicating that the chlorite predates kaolinite (Figure 3.12D). Kaolinite and carbonate minerals are rarely seen in contact. Where they do co-exist in a sample, the two do not exhibit dissolution textures that would indicate a chlorite-forming reaction. Ferroan calcite and ankerite are demonstrably developed late in the paragenetic sequence (Figure 3.25A). Hutcheon (1990) reported SEM images of chlorite coatings on ferroan calcite crystals, which he interpreted as ferroan calcite reacting to form chlorite. Similar textures seen in thin sections and back-scattered electron images, however, show that there is more than one generation of carbonate cement (Figure 3.21). Hutcheon's SEM image may represent an early generation of ferroan calcite, which developed prior to chlorite diagenesis, with the crystal face acting as a substrate for chlorite development, similar to a detrital framework grain.

Petrographic evidence from microphotographs, back-scattered electron images and electron microprobe analyses support the hypothesis that diagenetic chlorite formed early as rims on framework grains, in a manner similar to studies in the North Sea (Ehrenberg, 1993), South Texas (Hillier, 1994) and the US Gulf Coast (Ryan and Reynolds, 1996). Grain rimming chlorite in some sandstones overlies a thin detrital clay layer that is coating the framework grain (Figure 3.2). This clay coating was rarely thick enough to be analyzed with the microprobe beam, however the few available analyses show that the coating consists of a mixture of clays with an iron component. This detrital clay component may have acted as a chlorite precursor (e.g. as described by Aagaard et al., 2000) and changed to chlorite during early burial diagenesis. Diagenetic chlorite

mimics the inferred petrographic textures of the precursor clay; it is thickest at embayed or corroded surfaces where the clay accumulated during accretion (Figure 3.1). Chlorite, however, is absent at compacted contacts between framework grains indicating that some compaction or at least abrasion occurred before chlorite formation.

6.5 Sea-floor Diagenetic Environment

Statistical analysis on whole rock geochemical data from sandstone samples shows that P_2O_5 correlates strongly with TiO_2, and each correlates with the other more strongly than with any other element. Samples identified as having well-developed chlorite rims also correlate with P_2O_5 and TiO_2 (Table 5.1 and 5.2). Logistic regression analysis of chlorite with P_2O_5 and TiO_2 shows a strong relationship between the two. As titanium and phosphorus values increase, there is an increasingly high probability of finding well developed chlorite rims (Figure 5.3).

Phosphorus is an important early diagenetic element and its precipitation is favoured by an environment rich in iron (e.g. Burns, 1997). Titanium is much more stable and immobile during diagenesis. During sedimentary transport and deposition, titanium-rich ilmenite will alter to pseudorutile, and then to rutile, in doing so releasing available iron (Pe-Piper et al. 2005). In the early diagenetic environment (at seafloor or very shallow burial), the released available Fe facilitates diagenetic phosphorite formation, where the sedimentation rate is low. The conditions that favour precipitation of phosphate may include an abrupt change in sedimentation rate, such as at a transgression surface that then favours phosphate diagenesis in the underlying 10 m or so (Burns, 1997).

Available Fe also facilitates the formation of very early diagenetic odinite or berthierine at the seafloor (Ehrenberg, 1993; Hillier, 1994; Ryan and Reynolds, 1996; Aagaard et al., 2000; Burley and Worden, 2003), which has been shown to alter to chlorite during diagenesis. It can be suggested then that abundant detrital ilmenite supplied available Fe to the very early seafloor diagenetic system. This iron supply facilitated growth of diagenetic berthierine at the seafloor, coating framework grains. The berthierine or other iron-rich clays later recrystallized to iron-rich chlorite on burial to form the chlorite rims. The chlorite rims helped preserve high porosities leading to better petroleum reservoirs. The fact that some clay coatings are unaltered to chlorite indicates that there is a range of clay coatings of variable suitability as a precursor. Other iron-rich minerals, including siderite intraclasts and pyrite, are present in samples with abundant chlorite rims. The presence of other iron-rich minerals may indicate that there is an additional supply of iron present allowing their formation (i.e., growth of early diagenetic pyrite, very early ferroan calcite).

6.6 Conclusions:

From analytical work, in particular petrographic work, it can be argued that a precursor iron-rich clay has diagenetically altered to form chlorite rims during early burial diagenesis, before widespread precipitation of pore-filling kaolinite and quartz overgrowths. The main arguments for this conclusion are:

1. The lack of chlorite rims in facies S1, despite other things being equal, may be due to the depositional environment not favouring formation of early Fe-rich clay coatings. The distinctive feature of S1 is the sparse bioturbation and relatively rapid deposition.

2. The quality of the final chlorite rim appears to depend on the seafloor diagenetic environment. This is apparent from the correlation between the quality of chlorite rims and phosphorus concentration. Phosphate is characteristically mobile during sea-floor diagenesis, but stable during burial diagenesis. The conditions that favour precipitation of phosphate, which are ideal for forming Fe-rich clay coatings, may also make some Fe-rich clay coatings a better precursor than others for the burial diagenetic conversion to chlorite.

REFERENCES:

Aagaard, P., Jahren, J.S., Harstad, A.O., Nilsen, O., and Ramm, M. 2000. Formation of grain-coating chlorite in sandstones. Laboratory synthesized vs. natural occurrences. Clay Minerals, **35**(1): 261-269.

Al-Ramadan, K.A., Hussain, M., Imam, B., and Saner, S. 2004. Lithologic characteristics and diagenesis of the Devonian Jauf sandstone at Ghawar Field, eastern Saudi Arabia. Marine and Petroleum Geology, **21**(10): 1221-1234.

Baker Hughes 1999a. Final Well Report: SOE Venture 1.

Baker Hughes 1999b. Final Well Report: SOE Venture 3.

Baker Hughes 1999c. Final Well Report: SOE Venture 4.

Blatt, H. 1979. Diagenetic processes in sandstones. *In* Aspects of Diagenesis, (ed.) P.A. Scholle and P.R.Schluger; Society of Economic Paleontologists and Mineralogists Special Publication **26**, p. 141-158.

Bruker AXS 2007. DIFFRACplus EVA (software).

Burley, S., and Worden, R. 2003. Sandstone Diagenesis: Recent and Ancient. Blackwell Publishing Ltd, Malden, MA.

Burns, S.J. 1997. Early diagenesis in Amazon Fan sediments *In* Proceedings of the Ocean Drilling Program, Scientific Results, (ed.) R.D. Flood, Piper, D.J.W., Klaus, A., and Peterson, L.C. **155**, p. 497-504.

Canada Nova Scotia Offshore Petroleum Board 1997. Technical summaries of Scotian Shelf: significant and commercial discoveries.

Chang, L.L.Y., Howie, R.A., and Zussman, J. 1996. Rock-forming minerals: volume 5B: non-silicates: sulphates, carbonates, phosphates, halides. Geological Society, London.

Core Laboratories 1999a. Core analyses report for Sable Offshore Energy Incorporated, SOE Venture 1.

Core Laboratories 1999b. Core analyses report for Sable Offshore Energy Incorporated, SOE Venture 3.

Core Laboratories 1999c. Core analyses report for Sable Offshore Energy Incorporated, SOE Venture 4.

Core Laboratories 1999d. Reservoir quality study of the Missisauga Sand 2 (TS,XRD,SEM)

Cummings, D.I. 2004. Sedimentology and Stratigraphy of an Ancient Progradational Terrigenous Clastic Shelf Margin, Missisauga Formation (Upper Jurassic-Lower Cretaceous), Offshore Nova Scotia, Canada. Ph.D. Thesis, University of Ottawa, Ottawa, Ontario Canada. 238p.

Cummings, D.I., and Arnott, R.W.C. 2005. Growth-faulted shelf-margin deltas: a new (but old) play type, offshore Nova Scotia. Bulletin of Canadian Petroleum Geology, **53**(3): 211-236.

Drummond, K.J. 1992. Geology of Venture, a geopressured gas field, offshore Nova Scotia. Giant Oil and Gas Fields of the Decade 1978-1988 AAPG Memoir, **54**: 55-72.

Ehrenberg, S.N. 1993. Preservation of Anomalously High-Porosity in Deeply Buried Sandstones by Grain-Coating Chlorite - Examples from the Norwegian Continental-Shelf. Bulletin, American Association of Petroleum Geologists, **77**(7): 1260-1286.

Ehrenberg, S.N., Dalland, A., Nadeau, P.H., Mearns, E.W., and Amundsen, H.E.F. 1998. Origin of chlorite enrichment and neodymium isotopic anomalies in Haltenbanken sandstones. Marine and Petroleum Geology, **15**(5): 403-425.

Esquevin, J. 1969. Influence de la composition chimique des illites sur leur cristallinité. Bulletin Centre de Recherches de Pau **3**: 147-153.

Ferlt, W.H. 1976. Abnormal Formation pressures. Elsevier Scientific Publishing Co., New York.

Friedman, G.M. 1959. Identification of carbonate minerals by staining methods. Journal Sedimentary Petrology, **29**: 87-98.

Given, M.M. 1977. Mesozoic and early Cenozoic geology of Offshore Nova Scotia. Bulletin of Canadian Petroleum Geology, **25**(1): 63-91.

Grigsby, J.D. 2001. Origin and growth mechanism of authigenic chlorite in sandstones of the lower Vicksburg Formation, South Texas. Journal of Sedimentary Research, **71**(1): 27-36.

Hillier, S. 1994. Pore-lining chlorites in siliciclastic reservoir sandstones - electron-microprobe, SEM and XRD data, and implications for their origin. Clay Minerals, **29**(4): 665-679.

Houghton, H.F. 1980. Refined techniques for staining plagioclase and alkali feldspars in thin section. Journal of Sedimentary Petrology, **50**: 629-631.

Hutcheon, I. 1990. Clay-Carbonate reactions in the Venture Area, Scotian Shelf, Nova Scotia, Canada *In* Fluid-mineral interactions: a tribute to H.P. Eugster, (ed.) R.J. Spencer and I.M. Chou; The Geochemical Society; Special Publication no. 2, pp. 199-212.

Jackson, T.A. 1977. A relationship between crystallographic properties of illite and chemical properties of extractable organic matter in pre-Phanerozoic and Phanerozioc sediments. Clays and Clay Minerals, **25**: 187-195.

Jansa, L.F., and Noguera-Urrea, V.H. 1990. Geology and diagenetic history of overpressured sandstone reservoirs, Venture gas field, offshore Nova-Scotia, Canada. Bulletin, American Association of Petroleum Geologists, **74**(10): 1640-1658.

Ketzer, J. 2002. Diagenesis and Sequence Stratigraphy. an integrated approach to constrain evolution of reservoir quality in sandstones. Acta Universitatis Upsaliensis. 30 pp.

McBride, E.F. 1989. Quartz Cement in Sandstones - a Review. Earth-Science Reviews, **26**(2): 69-112.

McIlroy, D., Worden, R.H., and Needham, S.J. 2003. Faeces, clay minerals and reservoir potential. Journal of the Geological Society, **160**: 489-493.

McIver, N. 1972. Mesozoic and Cenozoic stratigraphy of the Nova Scotia Shelf. Canadian Journal of Earth Science, **9**: 54-70.

Mobil Oil Canada Limited 1986. Final well report: Thebaud C-74.

Moore, D.M., and Reynolds, R.C. 1997. X-Ray Diffraction and the Identification and Analysis of Clay Minerals. New York : Oxford University Press, 332 pp.

Mudford, B.S., and Best, M.E. 1989. Venture gas-field, offshore Nova-Scotia - case study of overpressuring in region of low sedimentation rate. Bulletin, American Association of Petroleum Geologists, **73**(11): 1383-1396.

Needham, S.J., Worden, R.H., and McIlroy, D. 2005. Experimental production of clay rims by macrobiotic sediment ingestion and excretion processes. Journal of Sedimentary Research, **75**(6): 1028-1037.

Odin, G.S. 1988. Green Marine Clays. Elsevier, Amsterdam.

Pe-Piper, G., Piper, D.J.W., and Dolansky, L. 2005. Alteration of ilmenite in the Cretaceous sandstones of Nova Scotia, southeastern Canada. Clays and Clay Minerals, **53**(5): 490-510.

Pe-Piper, G., and Mackay, R.M. 2006. Provenance of Lower Cretaceous sandstones onshore and offshore Nova Scotia from electronmicroprobe geochronology and chemical variation of detrital monazite. Bulletin of Canadian Petroleum Geology, 54(4): 366-379.

Pittman, E.D. and Lunsden, D.N. 1968. Relationship between chlorite coatings on quartz grains and porosity, Spiro Sand, Oklahoma. Journal of Sedimentary Research, **38**: 668-770.

Reimer, C. 2002. Missisauga Formation at the Venture field: proximal delta and shallow marine reservoirs (abstract). *In* Core Conference guide book. Halifax, NS. Petroleum Society of CIM, pp. 65-76.

Rossi, C., Kalin, O., Arribas, J., Iglesia, A., and Bartrina, T. 2003. Effect of authigenic grain-coating chlorite on the resistivity and reservoir quality of the Lower Carboniferous RKF sandstones (Rhourde El Krouf Field, Berkine Basin, Algeria). *In* AAPG International Conference. Barcelona, Spain, p. 24.

Ryan, P.C., and Reynolds, R.C. 1996. The origin and diagenesis of grain-coating serpentine-chlorite in Tuscaloosa Formation sandstone, US Gulf Coast. American Mineralogist, **81**(1-2): 213-225.

Ryan, P.C., and Hillier, S. 2002. Berthierine/chamosite, corrensite, and discrete chlorite from evolved verdine and evaporite-associated facies in the Jurassic Sundance Formation, Wyoming. American Mineralogist, **87**(11-12): 1607-1615.

Sable Offshore Energy 1996. Development Plan Application.

Salem, A.M., Ketzer, J.M., Morad, S., Rizk, R.R., and Al-Aasm, I.S. 2005. Diagenesis and reservoir-quality evolution of incised-valley sandstones: evidence from the Abu Madi gas reservoirs (upper Miocene), the Nile Delta Basin, Egypt. Journal of Sedimentary Research, **75**(4): 572-584.

Shimeld, J. 2004. A comparison of salt tectonic subprovinces beneath the Scotian Slope and Laurentian Fan. *In* Salt-sediment interactions and hydrocarbon prospectivity: Concepts, applications and case studies for the 21st century. Gulf Coast Society Section of the Society of Economic Paleontologists and Mineralogists, 24th Annual Bob F. Perkins Research Conference, extended abstracts volume, Houston.

Schlumberger 1989. Log Interpretation Principles/Applications. Schlumberger Educational Services, Houston.

Schlumberger. 2004. Petrel (software).

Wade, J.A., and MacLean, B.C. 1990. The geology of the southeastern margin of Canada, Chapter 5 *In* Geology of the Continental Margin of Eastern Canada, (ed.) M.J. Keen and G.L. Williams; Geological Survey of Canada, Geology of Canada. no. 2, pp. 167-238 (also Geological Society of America, The Geology of North America, v.I-1).

Weaver, C.E. 1956. The distribution and identification of mixed-layer clays in sedimentary rocks. American Mineralogist, **41**: 202-221.

Williams, H., and Grant, A.C. 1998. Tectonic Assemblages Map, Atlantic Region, Canada. 1:3,000,000 scale.Geological Survey of Canada Open File.

Williamson, M.A. 1995. Overpressures and hydrocarbon generation Sable Subbasin, offshore Nova Scotia. Basin Research, **7**(1): 21-34.